

**Late-orogenic, mantle-derived, bimodal
magmatism in the southern Adelaide Foldbelt,
South Australia**

by

Simon P Turner

B.Sc. Hons. (Adelaide 1986)

Submitted in fulfilment of the requirement
for the degree of Doctor of Philosophy

*Department of Geology and Geophysics
The University of Adelaide
South Australia*

May, 1991

Table of Contents

Abstract	page
Statement of originality	I-III
Acknowledgements	IV
	V

Chapter 1. Introduction

1.1. General introduction	1
1.2. Source regions and thermal requirements for magma generation	2
1.3. Geological setting and previous work	5
1.4. Thesis outline	9

Chapter 2. Petrogenesis of late-orogenic layered gabbros at Black Hill, South Australia: Part 1. Mineral chemistry and crystallization conditions

2.1. Introduction	12
2.2. Geological setting	12
2.3. Layering, convection and recharge	14
2.4. Petrography	22
2.4.1. Gabbro-norites and potassic gabbro-norites	24
2.4.2. Pyroxene monzonites and anorthosites	24
2.4.3. Troctolites and peridotites	26
2.4.4. Olivine gabbros	28
2.4.5. Norites	28
2.4.6. Coarse zones	29
2.4.7. Granophyres	29
2.5. Mineral Chemistry	29
2.5.1. Feldspars	31
2.5.2. Pyroxenes	32
2.5.3. Olivines	36
2.5.4. Amphibole	39
2.5.5. Biotite	42
2.5.6. Oxides	45

2.5.7. Olivine-plagioclase symplectites	49
2.6. Discussion of crystallization conditions	51
2.7. Conclusions and problematic lithologies	52

Chapter 3. Petrogenesis of late-orogenic layered gabbros at Black Hill, South Australia: Part 2. Geochemical and isotopic constraints on fractionation, assimilation and the source

3.1. Introduction	56
3.2. Geochemistry	57
3.2.1. Analytical techniques	57
3.2.2. Major and trace element geochemistry	57
3.2.3. Rare earth elements	67
3.2.4. Radiogenic isotopes	68
3.3. Petrogenesis	72
3.3.1. Phase equilibria constraints	72
3.3.2. Composition of the parental magma	75
3.3.3. Combined assimilation and fractionation (AFC)	77
3.3.4. Source implications	87
3.3.5. Chamber recharge and the norites	90
3.3.6. Origin of the granophyric sills	91
3.4. Discussion	93

Chapter 4. Source and evolution of A-type granites and volcanics from the Padthaway Ridge, South Australia: implications for A-type genesis

4.1. Introduction	96
4.2. Geological setting	96
4.3. Field relations	98
4.3.1. Granitic rocks	98
4.3.2. Volcanic rocks	99
4.3.3. Taratap Adamellite	99
4.4. Petrography	100
4.4.1. Hypersolvus granites	100
4.4.2. Subsolvus granites	103
4.4.3. Volcanics	104

4.5. Mineral chemistry and crystallization conditions	105
4.5.1. Pyroxene	105
4.5.2. Amphibole	108
4.5.3. Biotite	110
4.5.4. Quartz-fayalite-oxide assemblage	111
4.5.5. Feldspars	112
4.6. Geochemistry and isotopes	112
4.7. Characteristics of A-types and a comparison with the Padthaway Suite	119
4.8. Models for A-type genesis	123
4.8.1. The melt depleted granulite model	124
4.8.2. A basalt fractionation model	127
4.9. Petrogenesis of the Padthaway Suite	130
4.9.1. Implied quaternary quartz-feldspar relationships	130
4.9.2. The role of fluorine	131
4.9.3. Isotopes and source compositions	133
4.10. Concluding remarks	135

Chapter 5. The Mannum Granite: magma mingling, diffusion and implications for the origin of A-type magmas

5.1. Introduction	136
5.2. Age constraints	136
5.3. Field relationships	137
5.4. Petrography and microtextures	139
5.5. Geochemical and isotopic variation	144
5.6. Discussion of the origin of the enclaves	154
5.7. Enclave - granite interaction	155
5.7.1. Thermal and physical constraints on mixing	156
5.7.2. Post mingling diffusion	158
5.8. Compositional relationships between the enclaves and granite	162
5.9. Conclusions and a model for the Mannum Granite	164

Chapter 6. Some thermal and isostatic constraints on late-orogenic magmatism

6.1. Introduction	167
6.2. Geophysical considerations	168
6.2.1. Isostatic consequences	170

6.2.2. Thermal consequences	173
6.3. Petrological considerations	174
6.4. Discussion	175
6.5. Implications for the evolution of the late-orogenic bimodal province in the southern Adelaide Foldbelt	176
6.5.1. Evidence for exhumation and possible uplift	176
6.5.2. A lithospheric mantle source	177

References	179
-------------------	-----

Appendices

- A. Analytical techniques and uncertainties
- B. Complete listing of analyses of Black Hill gabbros
- C. Complete listing of analyses of granites and granophyres from Black Hill
- D. Drill hole logs from Black Hill
- E. Copies of papers and abstracts referred to in the text:
 - E1) Foden, J.D., Turner, S.P., and Morrison, R.S., 1990: Tectonic implications of Delamerian magmatism in South Australia and western Victoria. In: Jago, J.B., and Moore, P.J., (Eds.), 1990: The evolution of a Late-Precambrian - Early Palaeozoic rift complex: The Adelaide Geosyncline. *Geol. Soc. Aust., Spec. Publ.*, 16, pp 465-482.
 - E2) Turner, S.P., Foden, J.D., and Cooper, J., 1989: Post Delamerian magmatism: tectonic controls on magma chemistry and evidence for post Delamerian extension. SGTSG conference, *Geol. Soc. Aust. Abst.* no. 24, pp 155-156.
 - E3) Foden, J.D., Turner, S.P., and Michard, A., 1989: Isotopic studies and lithospheric growth in the Adelaide Foldbelt. SGTSG conference, *Geol. Soc. Aust. Abst.* no. 24, pp 47-48.
 - E4) Turner, S.P., and Foden, J.D., 1990: Post Delamerian magmatism - is lithospheric thinning guilty? Tenth AGC, *Geol. Soc. Aust. Abst.* no. 25, pp 262-263.
 - E5) Turner, S.P., Foden J.D., and Sandiford, M., 1990: Evidence for involvement of an enriched lithospheric mantle source in late-orogenic bimodal magmatism, South Australia. 7th Int. Conf. Geochron. Cosmochron. & Isotope Geol. *Geol. Soc. Aust. Abstr.* 27: 103.
 - E6) Foden, J.D., Turner, S.P., and Michard, A., 1990: Proterozoic lithospheric enrichment and its profound influence on the isotopic

composition of Phanerozoic magmas. 7th Int. Conf. Geochron. Cosmochron. & Isotope Geol. *Geol. Soc. Aust. Abstr.* 27: 34

E7) Turner, S.P., and Foden, J.D., 1990: The nature of mafic magmatism during the development of the Adelaide Geosyncline and the subsequent Delamerian orogeny. In: Parker, A.J., Rickwood, P.C., and Tucker, D.H. (eds.) *Mafic dykes and emplacement mechanisms*. Proc. 2nd Int. Dykes Conf., IGCP publ. # 23, Balkema, Rotterdam, pp. 431-434.

Erratum: IMA ruling titanite should have been used instead of sphene.

List of Figures

Fig. 1.1. Map showing locations of lithologies referred to in the text	7
Fig. 1.2. Spidergram illustrating differences between syn- and late-orogenic granites	8
Fig. 2.1. Geological map of the Black Hill intrusive complex	13
Fig. 2.2a & b. Cross sections of the Black Hill and Cambrai plutons	15-16
Fig. 2.3a-d. Photos of layering within the gabbros	17
Fig. 2.4a & b. Summarized drill core logs for the Black Hill and Cambrai plutons	19-20
Fig. 2.5a-h. Photomicrographs of the gabbros	25
Fig. 2.5i-p. Photomicrographs of the gabbros	27
Fig. 2.6. Ternary feldspar diagram for the gabbros	31
Fig. 2.7. Cr vs Mg# for pyroxenes	34
Fig. 2.8a & b. Quaternary pyroxene diagrams and olivine compositional range	36
Fig. 2.9a-d. Photomicrographs of pigeonites and symplectites	35
Fig. 2.10. Ni vs Mg# in olivines	38
Fig. 2.11. Silica activity diagram	39
Fig. 2.12. Tetrahedral Al vs Na + K for amphiboles	41
Fig. 2.13. Quaternary diagram for amphiboles	41
Fig. 2.14. TiO ₂ vs Mg# for biotites	42
Fig. 2.15. Total Al vs Al co-ordination for biotites	44
Fig. 2.16. Mg# vs Cl in biotites	45
Fig. 2.17. Oxygen fugacity vs temperature diagram	47
Fig. 2.18. Al vs FeO for spinels	48
Fig. 2.19. Cr# vs Mg# for chromian spinels	48
Fig. 3.1. AFM plot for the Black Hill gabbros	60
Fig. 3.2. Mg# variation diagrams	61-63
Fig. 3.3. Chondrite normalized rare earth plots	67
Fig. 3.4. Nd-Sm isochron for potassic gabbronorite BHG-1	70
Fig. 3.5. ϵ_{Nd} vs initial $^{87}Sr/^{86}Sr$	71
Fig. 3.6a-c. Projections in the ol-pl-cpx-qtz tetrahedron	73
Fig. 3.7. MORB normalized spidergram for the parental magma	76
Fig. 3.8. MgO variation diagrams with TRACE5 modelled trends	78-80
Fig. 3.9. ϵ_{Nd} vs K ₂ O	81
Fig. 3.10. Initial $^{87}Sr/^{86}Sr$ vs SiO ₂	82
Fig. 3.11. Spidergram showing modelled vs actual pyroxene monzonite	85
Fig. 3.12. ϵ_{Nd} vs initial $^{87}Sr/^{86}Sr$ with calculated AFC trend	86

Fig. 3.13. Spidergram showing modelled vs actual granophyre	92
Fig. 4.1. Map of the Padthaway suite with the +10 milligal anomaly	97
Fig. 4.2a-h. Photomicrographs from the Padthaway Suite	102
Fig. 4.3. Inferred crystallization sequence for the Marcollat Granite	103
Fig. 4.4. Quaternary pyroxene diagram	105
Fig. 4.5. Quaternary amphibole plot	109
Fig. 4.6. Alkali's vs tetrahedral Al in amphiboles	109
Fig. 4.7. Ti vs total Al for amphiboles	109
Fig. 4.8. Aluminium co-ordination vs Al ₂ O ₃ for biotites	110
Fig. 4.9. Oxygen fugacity vs temperature	111
Fig. 4.10. Ternary feldspar diagram	112
Fig. 4.11. Selected SiO ₂ variation diagrams for the Padthaway Suite	113
Fig. 4.12. MORB normalized spidergram	117
Fig. 4.13. Chondrite normalized rare earth diagram	117
Fig. 4.14. Ga/Al vs Zr+Nb+Y+Ce	123
Fig. 4.15. A-type normalized spidergrams for partial melt and fractionation models	125
Fig. 4.16. CIPW normative plot with fluorine minima	132
Fig. 4.17. εNd vs initial ⁸⁷ Sr/ ⁸⁶ Sr for the Padthaway Suite	133
Fig. 4.18. A-type normalized spidergrams for granophyre and modelled A-type	134
Fig. 5.1a-h. Field and petrographic photos	138
Fig. 5.2a & b. Rare earth variation in sphenes	142
Fig. 5.3. SiO ₂ variation diagrams	145
Fig. 5.4. Chondrite normalized rare earth diagram	151
Fig. 5.5. Enclave trace element profiles	155
Fig. 5.6. Calculated temperature - viscosity variation diagram for Mannum	157
Fig. 5.7. Calculated diffusion profiles	160
Fig. 5.8a & b. Actual and calculated Zr profiles	161
Fig. 5.9. Zr/Nb profile	162
Fig. 5.10. P ₂ O ₅ vs MgO with interpreted trends	163
Fig. 5.11. εNd vs initial ⁸⁷ Sr/ ⁸⁶ Sr for the granite and enclaves	164
Fig. 5.12. Cartoon of the suggested model for the magmatic relationships	166
Fig. 6.1. Cartoon illustrating the evolution of a convergent orogen	169
Fig. 6.2. Schematic density and vertical stress vs depth diagrams	170
Fig. 6.3a & b. Potential energy and temperature variations on the <i>fc-fl</i> plane	172
Fig. 6.4. Schematic illustration of deformation paths on the <i>fc-fl</i> plane	173

List of Tables

Table 2.1. Summarized petrography for the Black Hill gabbros	23
Table 2.2. Representative feldspar analyses	30
Table 2.3. Representative pyroxene analyses	33
Table 2.4. Representative olivine analyses	37
Table 2.5. Representative amphibole analyses	40
Table 2.6. Representative biotite analyses	43
Table 2.7. Representative oxide analyses	46
Table 2.8. Analyses of symplectite components	50
Table 2.9. Average pressure estimates from "Thermocalc"	53
Table 3.1. Representative geochemical analyses from Black Hill	58-59
Table 3.2. Nd and Sr isotope analyses from Black Hill	69
Table 3.3. Results of AFC modelling using "TRACE5"	84
Table 3.4. Potential contaminants and mixing calculations	88
Table 4.1. Estimated modal analyses for the Padthaway Suite	101
Table 4.2. Selected microprobe analyses	106-107
Table 4.3. Geochemistry of samples from the Padthaway Ridge	114-115
Table 4.4. Rare earth and Nd, Sr isotopic analyses of selected samples	118
Table 4.5. Characteristics of A-type rocks	120
Table 4.6. Geochemistry of silicic rocks from large mafic intrusions	122
Table 4.7. Modelling of partial melts from mafic I-type granites	126
Table 4.8. Two stage, least squares modelling of basalt to A-type fractionation	128
Table 5.1. Selected microprobe analyses for the Mannum Granite and enclaves	140
Table 5.2. Microprobe analyses of sphenes	143
Table 5.3. Geochemistry of samples from Mannum	146-150
Table 5.4. Rare earth and Nd, Sr isotopic analyses of selected samples	152-153

Abstract

Late-orogenic magmas are common to many foldbelts, suggesting a causal link between this thermal pulse and the cessation of deformation. An investigation of such a late-orogenic magmatic suite is made in the southern Adelaide Foldbelt which forms part of the large Late Proterozoic - Early Cambrian Adelaide Geosyncline deformed by the Cambro-Ordovician Delamerian Orogeny. During this orogeny the foldbelt was intruded firstly by a 516-490 Ma syn-orogenic (or deformed) group of magmas and subsequently by a 490-487 Ma late-orogenic (or undeformed) group, these two suites having marked chemical and isotopic differences. The late-orogenic suite is bimodal with mafic dykes and plutons accompanied by high-silica granites and rhyolites. It is argued that these mafic and felsic intrusives are both thermally and compositionally related.

The mafic rocks of the late orogenic suite are exemplified by several layered gabbroic plutons outcropping at Black Hill near the eastern side of the Mt Lofty Ranges. Lithologies include troctolites, peridotites, olivine gabbros and gabbro-norites. The mineralogy of these gabbros shows that they crystallized in high level magma chambers from a continental tholeiitic magma. Like layered gabbroic intrusions in other parts of the world they contain a plagioclase plus two pyroxene assemblage with an olivine compositional hiatus. Crystallization occurred under high temperature, low pressure, low fO_2 conditions producing a trend of moderate iron enrichment followed by silica enrichment after the appearance of magnetite. Geochemical and isotopic constraints indicate that the magma underwent fractional crystallization combined with assimilation of the amphibolite grade metasedimentary wall rocks. The greatest contamination occurred near the margins of the plutons resulting, amongst other things, in silica and marked potassium enrichment to produce potassic gabbro-norites and pyroxene monzonites. The effect of contamination was to displace the magma from the two pyroxene-plagioclase cotectic resulting in the formation of anorthosites and the stabilization of pigeonite. Geochemical and isotopic evidence is interpretable in terms of 5-20% contamination but such a scenario requires that the initial magma (and therefore probably also the source) be enriched in incompatible elements.

High-silica, potassium-rich rhyolites and rapakivi granites have been examined near Black Hill at Mannum and from the Padthaway Ridge. These form a probable felsic end of the suite and are characterised by low Al_2O_3 and CaO contents and high LREE, Zr, Nb, Y and Ga contents identifying them as A-type magmas. Although various petrogenetic models have been proposed for A-types, their high incompatible/compatible element ratios are most readily obtainable by extended fractionation of mantle derived basaltic magma. Such a model is supported by data from the Padthaway A-types. They

tend towards one feldspar (hypersolvus) varieties and typically contain Fe-rich biotite and ferrohastingsite. Less common are fayalite-hedenbergite assemblages and some samples contain relicts of pigeonite and magnesian-augite. These latter pyroxenes are not in equilibrium with their host rocks and indicate polybaric crystallization from mafic parental magma. The mineral assemblages show that this parental magma was hot (>960 °C), relatively anhydrous and consequently able to undergo extensive fractionation when it reached the water-undersaturated granite minimum. Progressive development of low Sr, Al_2O_3 , CaO concentrations and negative Eu anomalies support this interpretation. Again plausible crystallization models suggest the need for the mafic parent to be enriched in incompatible elements.

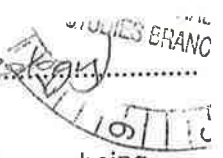
Granophyres from the Black Hill plutons are compositionally similar to the Padthaway Ridge rocks and gravity data suggests both these and Black Hill overlie an extensive tract of mafic plutons. Also located on the gravity high and belonging to the same suite is the A-type Mannum Granite which preserves evidence for contemporaneity of the mafic and felsic magmas. This granite contains numerous dioritic enclaves whose compositions contribute to a tholeiitic fractionation trend similar to the Black Hill gabbros. The droplet-like shapes and microtextures of these enclaves along with geochemical and isotopic data suggest that they and their host granite formed contemporary magmas and that the enclaves may represent draw-up from an underlying layered mafic chamber. The available evidence suggests that despite the high temperatures of both mafic and felsic magma, the viscosity contrast after thermal equilibration was too high for unrestricted mixing and only mingling and diffusion took place.

The range of Nd and Sr isotopic compositions of all of these silicic rocks are virtually indistinguishable from the mafic ones consistent with other data suggesting a common source. Overall ϵ_{Nd} varies from +5 to -4 and initial $^{87}Sr/^{86}Sr$ from 0.7035 to 0.7065 so that the entire suite has an isotopic range which is like some parts of the so-called enriched mantle sampled by ocean island basalts. In conjunction with their geochemistry this suggests derivation from an enriched source with relatively little crustal contribution, particularly from the evolved Archaean and Proterozoic material likely to characterize the lower crust in this region. However, a model involving crustal contamination of asthenospheric melts cannot be conclusively rejected although it requires quite high assimilation rates ($>30\%$) to produce the incompatible trace element concentrations. One potential source is subcontinental lithospheric mantle that was previously enriched by infiltration of small partial melts from the asthenosphere. Enriched mantle xenoliths suggest the existence of such a source and T_{DM} Nd model ages for both the late orogenic magmas and many of these mantle xenoliths range from 900 to 1200 Ma which may partially reflect the timing of the enrichment event.

The generation of melts within the subcontinental lithosphere requires a substantial thermal anomaly which is also likely to affect the potential energy of the lithosphere. Following the suggestion of Houseman *et al.* (1981) that mantle lithosphere thickened during convergence may become unstable to convective thinning, theoretical models are outlined which suggest that mantle lithospheric thinning will increase both the potential energy and the thermal budget of the orogen. The increased potential energy accompanying isostatic uplift causes convergent deformation to be terminated or partitioned elsewhere whilst uplift is likely to induce rapid unroofing of the orogen. The increased thermal budget results in the potential for melting in the lower crust and low temperature melting fractions in the mantle lithosphere. Such melts will be relatively anhydrous and able to fractionate extensively to produce silicic differentiates and a bimodal magmatic suite. In the southern Adelaide Foldbelt both the nature of the magmatism and evidence for ca. 10 kms denudation just prior to emplacement of the late-orogenic suite provide some support for such a model. It is suggested that this process may also be responsible for the late-orogenic suites found in other foldbelts. Late-orogenic magmatic episodes may involve considerable new additions to the crust transferring geochemical enrichments from small degree partial melts contained in the mantle lithosphere.

NAME: Simon P. TURNER

COURSE: PhD (Geology)



I give consent to this copy of my thesis, when deposited in the University Library, being available for loan and photocopying.

SIGNED:

DATE: 30/9/91

Statement of Originality:

I hereby certify that this thesis does not incorporate, without acknowledgement, any material which has been previously submitted for a degree or diploma in any university, and to the best of my knowledge and belief, it does not contain any written or published material by another person, except where due reference is made in the text.

12/5/91

Simon Philip Turner
May, 1991

Acknowledgements

The three years, during which this thesis was written have certainly been the best I've ever had and many people deserve hearty thanks. Firstly my supervisor, John Foden, for without his friendship, enthusiasm and help this thesis would not exist. It is also gastronomically fortuitous for me that his many talents extend to superb cooking, though I think John, that it is your turn in our culinary competition (potage de Sandiford?). Numerous ideas in this thesis evolved from long discussions with John. In particular he has managed to create an atmosphere that is a pleasure to work in, though how he always maintained a receptive smile as I interrupted him again and again with yet another problem or manuscript to criticise, not to mention waking him up at 3 in the morning, I don't know - but sincere thanks.

I am also extremely grateful to Mike Sandiford (everyone should jump on a table sometimes!) who first introduced me to many of the geodynamic ideas in this thesis and has shared (helped to make!) many "memorable" moments. Mike has been a wealth of information, inspiration (and employment!) and always has a new way of viewing a problem, not to mention a pertinent comment which may or may not be wanted! I particularly look forward to further work and learning with both John and Mike.

Numerous people from the geology department have become close friends, including some like Peter Haines and Bob Morrison who have now left, and they have also made it a pleasurable environment to work in. A myriad of Fasta Pasta lunches and 5pm sessions were coloured by the presence of these people. Critical technical assistance was provided by many staff including: D. Bruce, G. Trevelyan, P. McDuie, J. Willoughby, J. Stanley, R. Barrett and W. Mussared. I have enjoyed many discussions with geologists from the South Australian Department of Mines and Energy, particularly in the Regional Geology section who were always ready to help. Thanks to Mike Brumby who put in many weekends of help during gravity surveying at Black Hill - mind you I don't like the way he plays tennis. Thanks also to Kurt Stüwe for many lively debates. To my closest friends: Peter, Mike, Simone, Jim, Tania, Dave, Nigel, Graham, Bunge, Nick, Nat & Anna, Andy & Sophia, Alan & Phil, Mike & Libby, Pru & Andrew, I hope I can now spend a bit more time with you all.

Lastly and most importantly I wish to acknowledge the continuous support and encouragement provided throughout this thesis by my parents and particularly Kathy who has helped in almost every aspect of this thesis, put up with all my moods (as well as her own!) and provided much joy on all of our ventures over the last three years -geological and otherwise.



Chapter 1. Introduction

1.1 General introduction

Magmatic rocks found in orogenic belts can provide a record of the chemical and thermal evolution of the deep lithospheric root of the developing orogen. Although the sampled magmatic rocks of continental orogens may be the end product of several generative processes including partial melting, assimilation, fractionation and mixing the association of magmatic suites with particular tectonic settings suggests that not only magma sources but also the extent to which these modifying processes act may at least partially be a function of tectonic setting. This relationship must be complexly related to geodynamic factors and the thermal regime which, for example, control the stress field and thickness of a piece of crust which in turn affects the degree of fractionation and assimilation a magma will achieve on reaching a particular crustal level. An assessment of these contributions from recycled continental crust and the mantle then provides an insight into the generation and evolution of the continental crust.

Most progress in understanding the relationship between geodynamics and magma composition has been made in extensional tectonic settings where the magma composition is related to the degree of extension (McKenzie and Bickle, 1988). The situation is clearly more complex in continental compressional regimes and no unifying theoretical base for understanding of these magma compositions has yet emerged. Magmatic rocks from continental orogens are clearly modified by processes subsequent to their segregation, however, fortunately some geochemical tracers such as the radiogenic isotopes provide a record of the nature of their source regions. It seems likely that studies of particular styles of magmatism (compositional associations, physical processes) can be used to test or further elucidate geodynamic-magmatic relationships though chemical finger-printing alone is prone to misclassifications (eg Arculus, 1987). A potentially useful approach is to establish temporal-spatial relationships between magmatism and other tectonic elements such as metamorphism, deformation and isostatic responses like uplift.

The setting for this thesis is the southern Adelaide Foldbelt, South Australia which records a long history of magmatism from its Late Proterozoic to Cambrian extensional phase of sedimentation right through and beyond the compressional deformation of the Cambro-Ordovician Delamerian Orogeny. This thesis documents a study of the last magmatic episode in this foldbelt: a late-orogenic bimodal magmatic suite such as is common to many continental orogenic foldbelts. As part of the study currently being

undertaken by a number of workers on the orogenic history of this foldbelt this thesis has the following aims:

- 1) to make a detailed description and analysis of the nature of the late-orogenic magmatism in the foldbelt in terms of both magma chemical evolution, physical properties and source characteristics;
- 2) to assess the emplacement styles and interactions between mafic and felsic end members;
- 3) to assess the relative contributions of crust and mantle to the magmas
- 4) to further the understanding of lithospheric scale processes during the Delamerian Orogeny;
- 5) to use the Adelaide Foldbelt example to test current hypotheses on the nature of the source regions of continental magmas.

1.2 Source regions and thermal requirements for magma generation

A central concern in the study of magmatic processes is why the source region undergoes melting and how this source can be identified from the chemical and isotopic characteristics of the magma(s) produced. There can be little doubt for example that the characteristic compositional differences between magma types such as mid ocean ridge basalts (MORB) and ocean island basalts (OIB) reflect fundamental differences in their sources. The compositional range of MORB seems to be explicable in terms of differing degrees of partial melting of depleted mantle which are induced by adiabatic decompression as a consequence of extension of the overlying lithosphere (McKenzie and Bickle, 1988). OIB seem to be derived from a more enriched source, possibly undepleted mantle or mantle fertilized by additions from detached and enriched lithospheric mantle (McKenzie and O'Nions, 1983), and melting is caused by decompression of rising asthenospheric plumes.

Similarly, moving to continental settings, the rift related magmatism that produces continental flood basalts (CFB) and associated dolerite sills has a thermal origin in extension which produces asthenospheric upwelling, decompression and melting. Rifting may be induced by changing tectonic boundary conditions or initiated by a mantle plume (White and McKenzie, 1989). More isolated anorogenic or within-continent magmatism is often bimodal with alkali basalts and alkali-rich, high silica granites that are usually A-types according to the classification of Collins *et al.* (1981). These suites may be analogous to OIB having their thermal origins in mantle plumes. Unlike OIB and MORB

continental crust is an important compositional component in CFB's and within-continent magmas and has a complex isotopic structure which is likely to be complimentary to the depleted mantle reservoir (eg Allegre, 1987). Subcontinental lithospheric mantle is also a likely compositional component being long lived enough to develop chemical and isotopic anomalies through the infiltration of asthenospheric melts (McKenzie, 1989; Hawkesworth *et al.*, 1990). Studies of mantle xenoliths confirm that much of the lithospheric mantle has isotopic and elemental enrichment relative to depleted mantle or MORB-like source regions (eg Menzies and Murthy, 1980; Menzies 1983). Allegre *et al.* (1981; 1982) suggest that this enriched lithospheric mantle is a fundamental component in CFB's and some like the Karoo may be almost entirely sourced in old enriched lithospheric mantle (Ellam and Cox, 1989). CFB's are likely to be contaminated during ascent through the crust and their trace element and isotopic enrichment is likely to have its origins partly in the crust and partly in enriched subcontinental lithosphere as is argued by Cox and Hawkesworth (1984) for the Deccan Traps basalts.

Sources and thermal requirements are more controversial for continental silicic magmas. In at least some continental orogenic settings granitic rocks can be characterized by their source rocks into I- and S-types, being derived from igneous and metasedimentary sources respectively (Chappell and White, 1974), however such classifications are not always clear cut (eg White *et al.*, 1986) and the cause of melting is less obvious. The thermal conductivity of rocks is low and the maximum radiogenic heating of thickened crust will only be attained if the crust is thickened for periods approaching that of the thermal time constant which is proportional to the square of the length scale of the perturbation (Turcotte and Schubert, 1982). The attainment of these potential temperatures requires times of at least the same order of magnitude as the lifetime of orogens and theoretical modelling suggests that conductive heating of orogenically thickened crust is therefore often unlikely to be sufficient to cause partial melting unless the mantle lithosphere is dramatically thinned (Sandiford and Powell, 1990). For this reason the thermal origin of orogenic granitic rocks is one of considerable debate, one alternative to crustal thickening being the generation of granitic magmas by the intrusion of basalt (Huppert and Sparks, 1988). Hildreth (1981) used similar arguments along with chemical and isotopic evidence to suggest that all lithospheric magmatism is fundamentally basaltic. In other words asthenospheric input is required on thermal grounds and is often present as a compositional end member as well so that S-type granites may grade downwards into I-type granites and ultimately to basaltic roots. Isotopic data from the I- and S-type granitic suites of the Lachlan Foldbelt which suggests mixing of two dominant components (McCulloch and Chappell, 1982; Gray, 1984) may be consistent with this hypothesis. Unfortunately direct observational evidence for the mafic magma is typically absent. This may be because the combination of thickened crust,

compressional stress regime and production of buoyant silicic magmas by fractionation and crustal melting preclude these mafic magmas from reaching the same structural levels as the granites.

Of particular geodynamic interest are magmatic rocks intruded immediately following convergent deformation in many continental orogens (often called "post-tectonic" magmas). These late orogenic magmatic suites also have a heat source problem since they intrude after compressional deformation and crustal thickening have ceased. The emplacement of these as convergent deformation ceases suggests a causal link between the thermal pulse and the cessation of deformation. Conceivably deformation may cease because the external driving forces cease or alternatively because internal outward directed buoyancy forces come to equal and oppose these driving forces (Sandiford and Powell, 1990). Unfortunately neither of these mechanisms provides a satisfactory reason for the thermal perturbation causing the magmatism. One potential solution to this lies in the suggestion by Houseman *et al.* (1981) that orogenically thickened subcontinental lithospheric mantle may become unstable and be displaced by hot convecting asthenosphere with the result that the uppermost mantle and overlying crust become rapidly heated. As shown by England and Houseman, (1988), Molnar, (1988) Sandiford, (1989) and Sandiford and Powell, (1990), lithospheric thinning and the consequent isostatic uplift increase the potential energy stored in the orogen which may produce buoyancy forces capable of terminating deformation independently of the behaviour of the driving forces. This would make the lithospheric mantle a likely source for late-orogenic magmas. Another possibility is that injection of basalt from the asthenosphere which would thicken the lithosphere and (depending on its density) produce uplift (McKenzie, 1984) capable of opposing convergence. In this case asthenospheric mantle is a likely compositional end-member.

It seems that distinguishing magma sources may constrain which models are appropriate. Whilst experimental petrology provides constraints on possible source regions (eg Wyllie, 1984) radiogenic isotopes are clearly invaluable in distinguishing the relative contributions of these sources, in particular much use has been made of combined Nd and Sr isotopic systems (eg Allegre and Othman, 1980; O'Nions, 1984; DePaolo, 1988). Following Thompson *et al.* (1986) and Thompson and Morrison (1988) the combining of isotopic and elemental tracers seems to be the most likely way to distinguish asthenospheric, lithospheric mantle and crustal components in the late-orogenic suite from the southern Adelaide Foldbelt. Such data can then be used along with other tectonic indicators to assess models such as that of Houseman *et al.* (1981) for the thermal origin of the magmas.

1.3 Geological setting and previous work

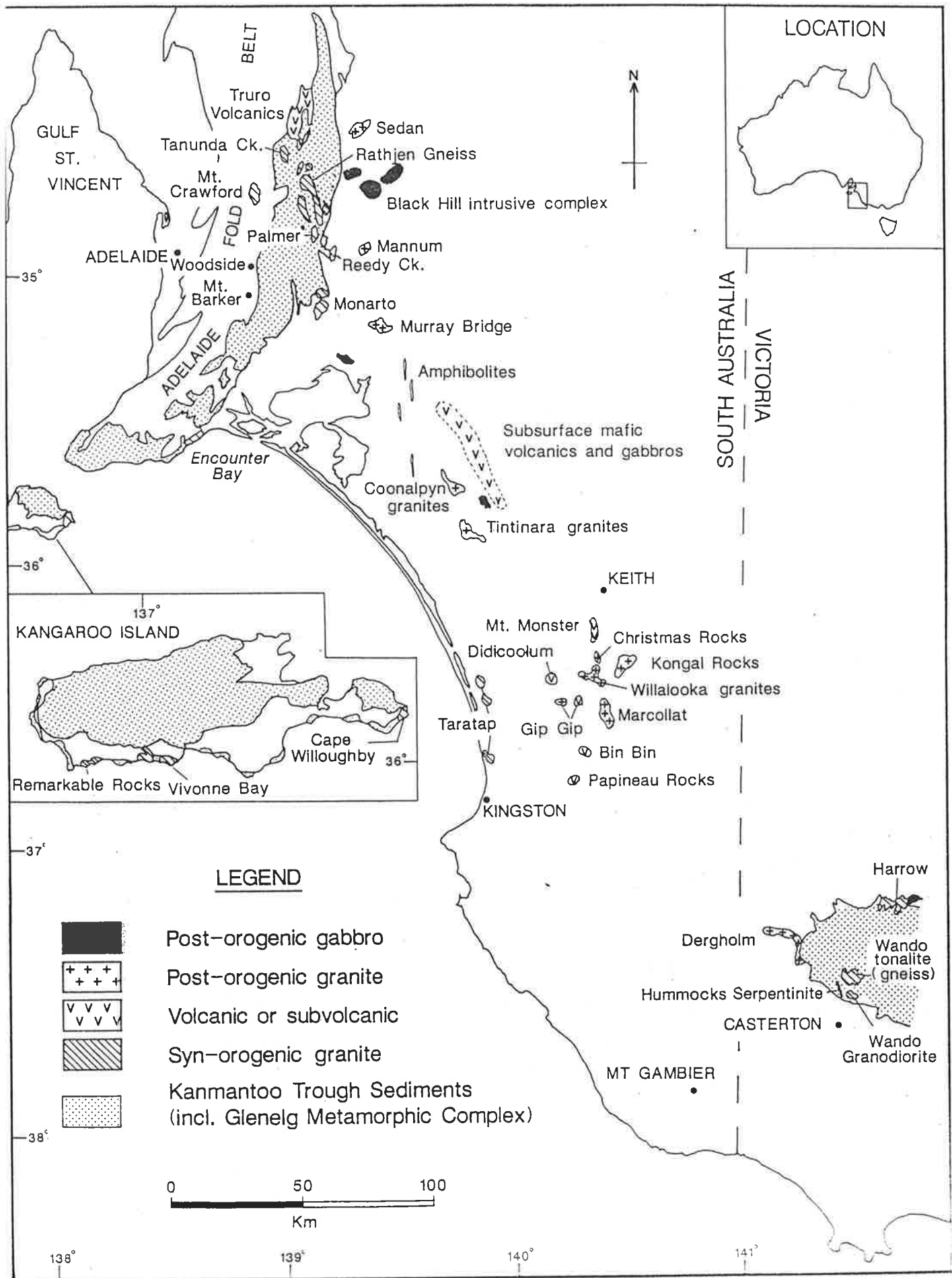
The southern Adelaide Foldbelt forms part of one of the largest and best preserved Late Proterozoic - Early Cambrian Foldbelts in the world extending through most of the length of South Australia. Equivalent age metamorphosed sequences occur in western Tasmania (eg Williams, 1978) and in north Victoria Land, Antarctica (eg Laird and Grindley, 1982) leading various authors to propose an originally contiguous foldbelt extended through South Australia and probably most of Tasmania and Antarctica (the Ross Orogen) as well (eg Ballie, 1985). In South Australia thick sequences of shelf derived sediments deposited during the Late Proterozoic and Early Cambrian were deformed by the Cambro-Ordovician Delamerian Orogeny (Thompson, 1969; Daily *et al.*, 1976). In the eastern exposed sections of the foldbelt in South Australia considered in this thesis (the southern Adelaide foldbelt) the Delamerian Orogeny resulted in complex polyphase deformation and Buchan-style metamorphism (eg Mancktelow, 1979; Sandiford *et al.*, 1990). Magmatic activity, whilst not voluminous, occurred throughout much of the history of the foldbelt (Turner and Foden, 1990b; see appendix E7) from syn-sedimentary mafic dykes and volcanics marking periods of maximum extension to the mafic and silicic activity which spanned the compression of the Delamerian Orogeny. Delamerian intrusives are largely restricted to these higher grade southern outcrops though a significant series of syenogabbros and monzonites have been described by Morrison (1989) from the Peake and Denison Ranges in the northwest of the foldbelt. A recent overview of the foldbelt in South Australia is given in Preiss (1987).

The eastern edge of the southern Adelaide foldbelt is largely hidden by the Tertiary sediments of the Murray Basin. Here the youngest exposed rocks, belonging to the Cambrian Kanmantoo Group are rapidly deposited flysch-like sediments (Milnes, 1982) which may have been deposited in a developing rift (Von der Borch 1980). Recent zircon dating on a tuffaceous layer at the base of the Kanmantoo puts the beginning of this last sedimentation episode at ~526 Ma (Cooper *et al.*, 1990). These are also the most highly metamorphosed and deformed and this unusual feature has recently led to critical re-appraisals of the tectonic history of the foldbelt and the suggestion that the Kanmantoo may be allochthonous (eg Jenkins, 1986; 1990). Deformation involved thrusting and crustal thickening (Mancktelow, 1979; Sandiford *et al.*, 1990) and three fold generations are recognized (eg Offler and Fleming, 1968). However, in contrast to Offler and Fleming (1968) who argued that metamorphism occurred early, Mancktelow (1979) and Sandiford *et al.* (1990) present evidence that peak metamorphism occurred after the first deformation event. The metamorphic grades in the Kanmantoo reach upper amphibolite grade with local development of kyanite-sillimanite assemblages. Sandiford *et al.* (1990) showed that these currently exposed assemblages formed at around 3-5 kbar (10-17 km

depth) so that total crustal thickening is unlikely to have produced crust in excess of 52 km given the current crustal thickness of 30-35km. Noting that at these depths the attained metamorphic conditions of 530-680 °C require a thermal regime in excess of that expected for tectonically thickened crust Sandiford *et al.* (1990) appeal to additional heat supply from syn-tectonic magmas.

This eastern edge of the southern Adelaide Foldbelt contains numerous outcrops of, predominantly granitic, intrusive rocks which are largely restricted in occurrence to the Kanmantoo Group (Fig. 1.1). It had been recognized for some time that these could be divided into syn- and post-deformational suites (eg Milnes *et al.*, 1977; Mancktelow, 1980). Geochronological data (Foden *et al.* in prep) indicates intrusion of the first group spanned 516-490 Ma allowing only a relatively short time (10 Ma) for deposition and deformation of the Kanmantoo Group. Dates for the second group are tightly bracketed at 490-487 Ma (this work; Foden *et al.* in prep) indicating the end of deformation and the intrusion of the later magmas were closely spaced events. Turner (1986) and Foden *et al.*, (1990a; see appendix E1) showed that distinct compositional differences existed between the two suites (Fig 1.2). Foden *et al.* (1990a) referred to these two suites as syn- and post-tectonic in keeping with terminology in much of the literature. However since only convergent strain, rather than "tectonics" or "orogenesis", had "ceased" during intrusion of the second suite, the terms syn-orogenic or syn-deformational and late-orogenic or post-deformational have been adopted in this thesis. In figure 1.1, the syn-orogenic granites include the Tanunda Creek, Cookes Hill and Rathjen gneisses, the Reedy Creek Granodiorite and the Palmer, Monarto, Victor Harbor, Taratap, Cape Willoughby and Remarkable Rocks granites. The post-tectonic granites include the Sedan, Mannum and Murray Bridge Granites as well as the Padthaway Ridge granites at Coonalpyn, Tintinara, Christmas Rocks, Kongal Rocks, Willalooka, Marcollat and Gip Gip and volcanics at Bin Bin, Gip Gip, Mt Monster, Didicoolum and Papineau Rocks. Investigations in western Victoria (Turner, 1986; Turner *et al.*, in prep.) showed that an identical association of early and deformed granodiorites (Wando Granodiorite) and migmatitic granites (Harrow Granodiorite) followed by later, undeformed, true granites (Dergholm Granite) intrude Cambrian amphibolite grade metasediments of the Glenelg River Complex (see Fig. 1.1) which have a similar deformational style to that preserved in the Kanmantoo Group in South Australia. On the basis of these similarities Turner (1986) and Foden *et al.* (1990a) correlated the tectonic evolution of the Glenelg River Province in western Victoria with that of the Kanmantoo in South Australia, the Wilson Terrane in

Overleaf - Figure 1.1 Map showing locations of magmatic rocks and other lithologies referred to in thesis.



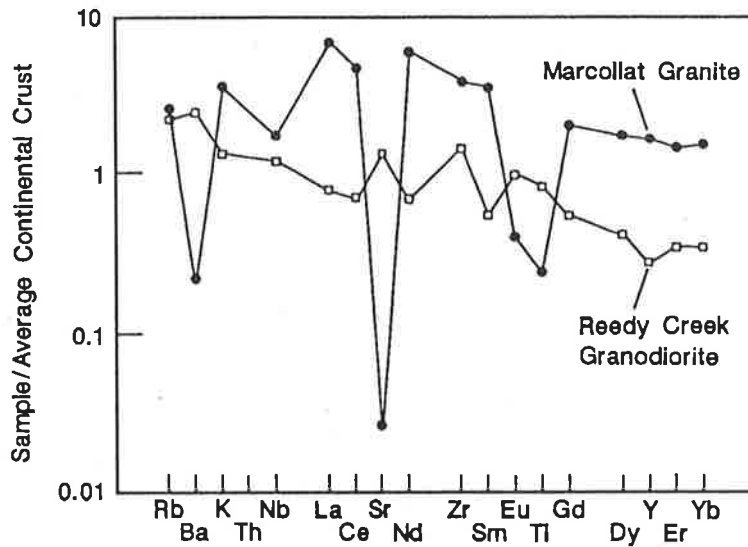


Figure 1.2 Spidergram illustrating the compositional differences between syn-orogenic (Reedy Creek Granodiorite) and late-orogenic (Marcollat Granite) felsic intrusives.

eastern Victoria Land in Antarctica and the early Palaeozoic sequences in western Tasmania.

The earlier, syn-orogenic suite consists of hornblende and biotite bearing tonalites, granodiorites and granites (*sensu stricto*) which are I-types according to the classification of Chappell and White (1974) and often have migmatitic aureoles (eg the Reedy Creek Granodiorite). These rocks have moderate Mg#'s, high compatible trace element concentrations (eg Sc, V, Ni, Sr, Ba) and are poor in incompatible trace elements (eg Zr, Nb, Y, REE). The more mafic I-types have moderately initial $^{87}\text{Sr}/^{86}\text{Sr}$ ratios around 0.7053-0.7083 the S-type aureoles have higher ratios > 0.7110 suggesting significant crustal contamination of relatively primitive magmas. At Vivonne Bay, southern Kangaroo Island, S-type granite is more fully developed in a zoned series of biotite-, garnet- and porphyritic granites which have chemical and isotopic characteristics indicating formation by anatexis of the local metasediments (Mitchell, 1990). The data on the I-type granites are not consistent with derivation from the evolved Proterozoic crustal basement which would have had $^{87}\text{Sr}/^{86}\text{Sr}$ ratios in the range 0.7150-0.7450 at 500 Ma (Foden *et al.*, 1990 and unpublished data). The granites of late-orogenic suite are A-types (see Fig. 1.2) under the classification of Collins *et al.* (1982) and Whalen *et al.* (1987). In contrast to the early suite these are high silica, potassic rapakivi granites which have low Mg#'s and compatible trace element concentrations but high incompatible trace element concentrations and low initial $^{87}\text{Sr}/^{86}\text{Sr}$ ratios (usually < 0.706).

One of the features of the later, post-deformational, suite is that it is compositionally bimodal with the high-silica granites and volcanics being accompanied by gabbroic plutons and dolerite dykes. Gabbroic plutons occur at Black Hill and near

Coonalpyn on the Padthaway Ridge whilst mafic dykes cut the Reedy Creek Granodiorite, the Mannum Granite and outcrop at Mount Pleasant near the Rathjen gneiss and on the Padthaway Ridge. As will be discussed in chapter 6 similar bimodal suites intrude after the end of deformation in many orogenic belts. In light of the interesting composition of the A-types and their apparent close association with mantle derived magmas the bimodal suite seemed to demand further investigation as part of ongoing research on the southern Adelaide Foldbelt. In particular the minimal isotope data base required significant updating. The gabbroic plutons were the least studied at the time and thus formed the starting point for a study which now forms this thesis.

For the purposes of the magmatic rocks studied in this thesis potential source regions include:

- 1) Contemporary depleted mantle with $\epsilon\text{Nd}_{(490 \text{ Ma})} = +9$, $^{87}\text{Sr}/^{86}\text{Sr}_{(490 \text{ Ma})} = 0.70248$.
- 2) Subcontinental lithospheric mantle. Mantle xenoliths from Recent volcanics in South Australia (Mt Gambier, see Fig. 1.1) and western Victoria provide good evidence that the mantle lithosphere here has been enriched for long enough to allow isotopic divergence from the depleted mantle (McDonough and McCulloch, 1987; O'Reilly and Griffin, 1988; Griffin *et al.*, 1988). At 490 Ma ϵNd ranges from +6 to -1.1 whilst $^{87}\text{Sr}/^{86}\text{Sr}$ is 0.7035 to 0.7069.
- 3) Lower crust. Possible lower crustal basement to the exposed upper crustal metasediments and granites is a continuation of the Proterozoic and Archaean gneissic and granulitic terrains exposed to the west on Eyre Peninsula. At 490 Ma these have ϵNd around -16 to -30 (McCulloch, 1987; Daly and Fanning, 1990; Fanning *pers. comm.*) and $^{87}\text{Sr}/^{86}\text{Sr}$ is >0.76 and may exceed 0.8 (Fanning *et al.*, 1980; Webb *et al.*, 1986). Lower crustal and uppermost mantle xenoliths from kimberlites in South Australia suggest that the base of the crust and upper mantle lithosphere is composed of granulites and eclogites (McCulloch *et al.*, 1982; Arculus *et al.*, 1990). These have $\epsilon\text{Nd}_{(490 \text{ Ma})} = -12$ to -21, and $^{87}\text{Sr}/^{86}\text{Sr}_{(490 \text{ Ma})} = 0.7066$ to 0.71196.
- 4) Upper crust represented by the exposed metasediments. ϵNd for the Kanmantoo Group at 490 Ma ~ -12 , $^{87}\text{Sr}/^{86}\text{Sr} \sim 0.7250$.

1.4 Thesis outline

This thesis is based on extensive sampling for petrographic, geochemical and isotopic work. As the majority of outcrops investigated are isolated and surrounded by the Tertiary sediments of the Murray Basin, field maps were not made. Rather, detailed observations of the critical outcrops are described in the relevant sections. All hand specimens, thin sections, polished sections and rock powders are housed in the

University of Adelaide, Department of Geology and Geophysics under the accession number A876-.

The initial incentive of this thesis was to investigate the late-orogenic mafic activity, as exemplified at Black Hill, because least was known about these intrusions and their role in the late evolution of the foldbelt. Consequently much early work was spent logging and analysing the 20 diamond drill holes that intersect these bodies and drill hole logs are presented in appendix D. Chapters 2 and 3 resulting from this work document the interpreted crystallization history and geochemical and isotopic implications of these mafic plutons. However, even as this work proceeded the links with the associated felsic plutons and volcanics became stronger, particularly with recognition of the similarity with granophyres from the mafic plutons, and consequently detailed work was undertaken on the granites and volcanics from the Padthaway Ridge. This forms the basis of chapter 4 which describes these rather unique rocks in detail and also attempts to model their evolution from the mafic parents. Chapter 5 is based on a single, but nevertheless critical outcrop at the Mannum Quarry. It is here that the mafic and felsic end-members of the bimodal suite show evidence of mingling and this chapter establishes their temporal, spatial and chemical consanguinity. Chapter 6 takes a broader view of the data in conjunction with current models for the geodynamics of evolving orogenic belts to try and propose a coherent model for late-orogenic, bimodal magmatic suites. In conclusion it is proposed that the termination of deformation in the Delamerian Orogeny and the emplacement of the late bimodal igneous suite are both manifestations of thinning of the subcontinental mantle lithosphere which occurred in response to the orogenic thickening event.

A number of papers are being published from this work. In particular:

Turner, S.P., Foden, J.D., and Morrison, R.S., 1990: Derivation of A-type magma by fractionation of basaltic magma and an example from the Padthaway Ridge, South Australia. *Contrib. Mineral. Petrol.*, submitted. (based on chapter 4)

Turner, S.P., and Sandiford, M, 1990: Some thermal and isostatic constraints on "post-orogenic" magmatism. *Geology*, submitted. (based on chapter 6)

Foden, J.D., and Turner, S.P., 1990: The Mannum Granite: magma mingling, diffusion and implications for the origin of A-type granites. *Contrib. Mineral. Petrol.*, submitted. (based on chapter 5)

Turner, S.P., 1990: Petrogenesis of late-orogenic layered gabbros at Black Hill, South Australia. *J. Pet.*, submitted. (based on chapters 1 & 2)

Conference abstracts and the precursory publication (Foden *et al.*, 1990) are included in appendix E.

Chapter 2. Petrogenesis of late-orogenic layered gabbros at Black Hill, South Australia: Part 1. Mineral chemistry and crystallization conditions

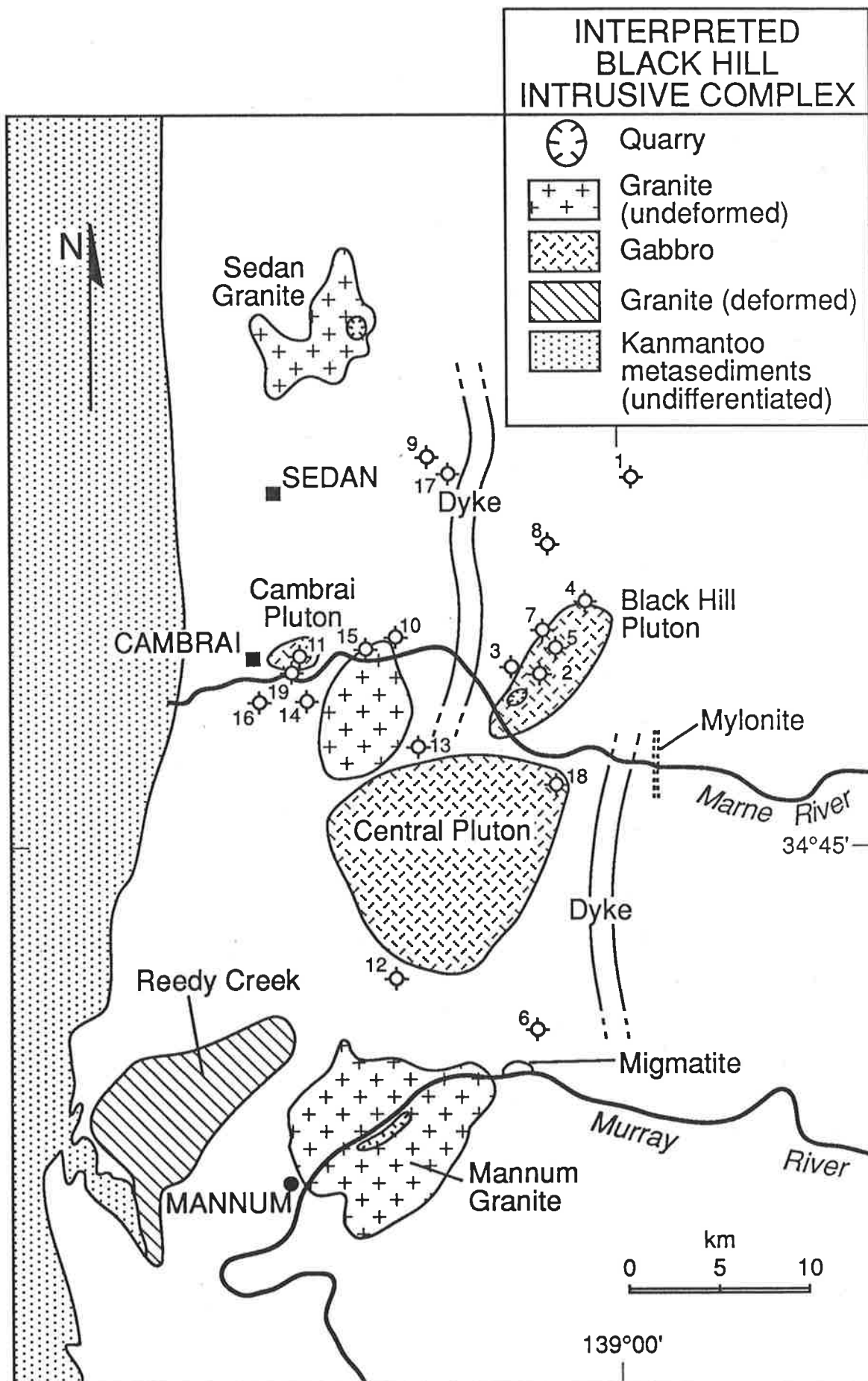
2.1. Introduction

The layered gabbros at Black Hill, which form part of the later, undeformed gabbro-granite complex (cf Chapter 1), lie just to the east of the Kanmantoo outcrop (Fig. 1.1). Milnes *et al.*, (1977) report a Rb-Sr biotite-whole rock isochron from the Black Hill gabbros which gave an age of 487 ± 5 Ma and they also give a K-Ar date on the biotite of 486 Ma indicating that there has been no significant thermal perturbation subsequent to crystallization. A seven point Nd-Sm mineral-whole rock isochron carried out as part of the present study (see chapter 3) yielded an age of 489 ± 10 Ma. Although these gabbros have been quarried for building stone ("Black Imperial Granite") for a long while, the first and only previous study of their petrogenesis was made by Wegmann in 1980. This chapter presents the results of detailed study of over 400 thin sections and probe analyses collected from some 63 polished sections. The varied and well preserved mineralogy of these gabbros allows detailed documentation of their crystallization history which may be applicable to late-orogenic mafic magmatism globally. The compositional evolution of these crystallizing phases carries important implications for the overall chemical evolution of the Black Hill magmas.

2.2. Geological setting

At Black Hill much of the outcrop is covered by Tertiary sediments and the interpretation given in figure 2.1 is based largely on geophysical data. Additionally 19 cored diamond drill holes (Lynch, 1978) intersect the gabbros and granites as well as amphibolite grade metasediments which are assumed to be Kanmantoo Group equivalents intruded by the mafic magma. From aeromagnetic and gravity data layered gabbros comprise at least three plutons however only two of these were extensively intersected by the drilling. These two are here named the Black Hill Pluton, which outcrops and is quarried for building stone, and the Cambrai Pluton. Geophysical data, including detailed gravity surveys by the author were used to constrain the size and shape of the plutons. This work was extended by, and is summarized in Kennedy (1989) who performed 3

Overleaf Figure 2.1. Interpreted geological map of the Black Hill intrusive complex.



⊕ North Broken Hill Ltd Diamond Drill Hole and Number

dimensional modelling of the gravity data showing that the plutons are funnel shaped and taper downwards to 3-3.5km depth where linear magnetic anomalies may represent feeder dykes (Fig. 2.1). The whole area itself lies on the western edge of a major gravity (+10-25 milligals) and magnetic high which is consistent with the presence of a voluminous mafic lopolith at 4-6km depth from which the plutons may extend. The shape of the plutons is consistent with a model in which the mafic magma was transported through the crust in dykes until it reached planes of structural weakness coincident with levels where its buoyancy was capable of supporting the roof rocks. At these levels the magma spread laterally lifting the roof rocks and forming magma chambers. The filling of the chambers would then be likely to have occurred in a number of successive injections through feeder dykes.

Schematic cross-sections of the two plutons (Fig. 2.2a & b) combine geophysical data and drill core logs with mineralogical and geochemical evidence which suggests the present level of exposure is near to the top of the original intrusion(s). The Black Hill Pluton has a area of 20km² and a corresponding volume of about 60km³ whilst the Cambrai Pluton is 4km² and has a volume of 16km³. The Black Hill Pluton consists of an upper (outcropping) roof zone underlain by layered cumulates (lower layered cumulates) with a marginal or border zone consisting of pyroxene monzonites and anorthosites. Dyke or sill-like bodies of granophyric material are also intersected by drill core. Below the lower layered cumulates the undrilled "hidden zone" represents about 60% (vol) of the Black Hill Pluton and somewhat less of the Cambrai Pluton.

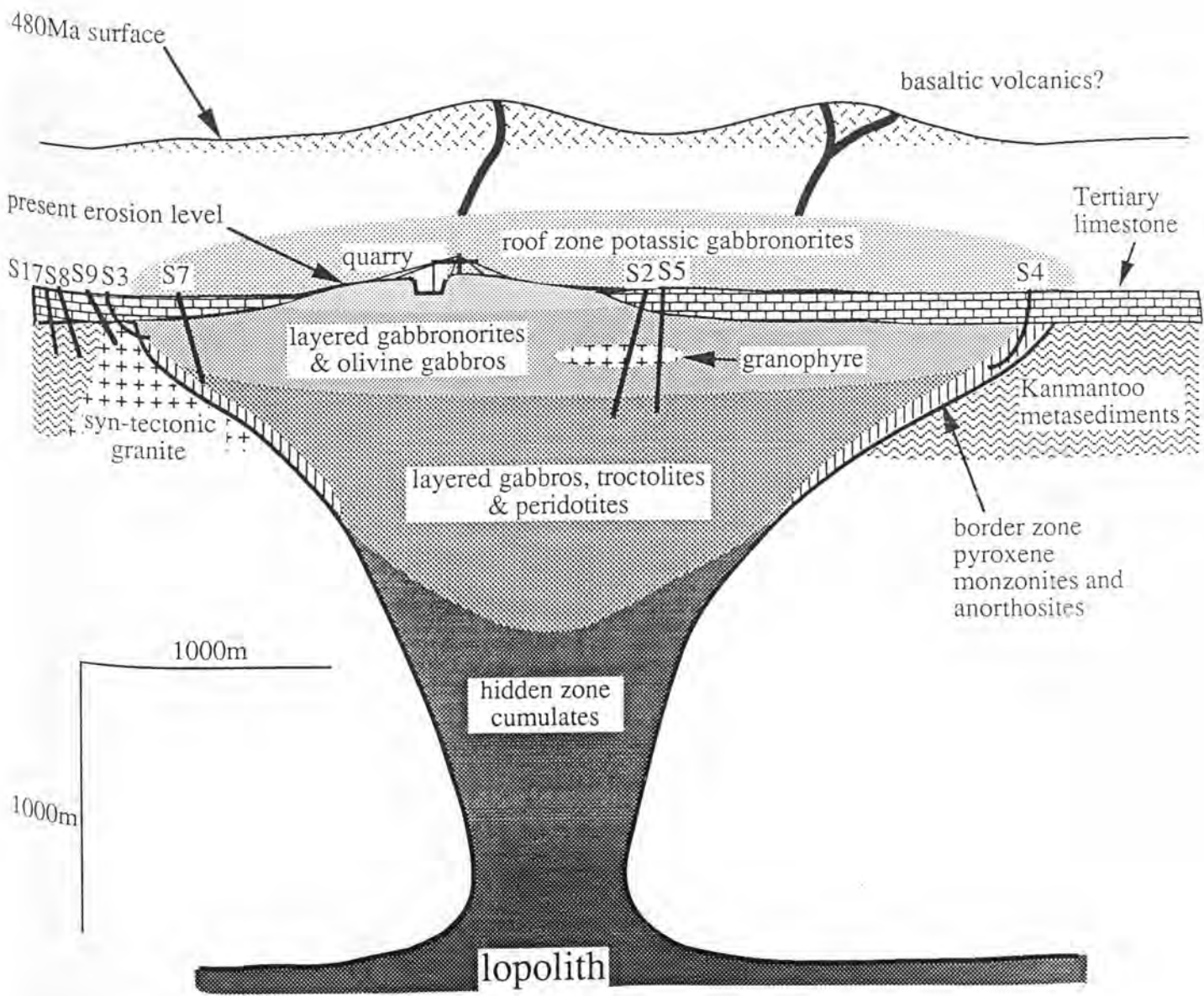
2.3. Layering, convection and recharge

In the outcrop, rhythmic modal layering is defined by pyroxene rich bases grading upwards to lighter, plagioclase rich tops (Figs. 2.3a, b). These layers vary from 0.01-2m in thickness and do not always maintain thickness but may pinch out or coalesce to form larger layers (Fig. 2.3a). This layering is rarely horizontal and may reach dips of up to 60°. In three dimensions the layering is often convex downwards (Fig. 2.3a) and reminiscent of the trough structures described from the Skaergaard intrusion. Streaky or wispy layering, involving thin bands of dark minerals, is quite common as are crossbed structures and truncated layers (Fig. 2.3a).

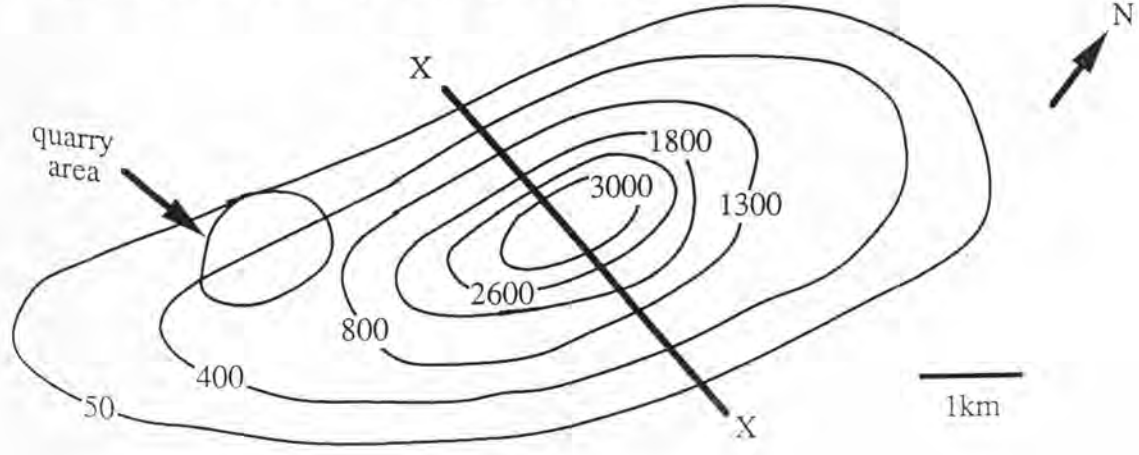
Despite the steep dips in outcrop, in the drill core the gabbros contain a prominent sub-horizontal igneous lamination (Fig. 2.3c), defined by the alignment of plagioclase laths and bands of mafic minerals. Correlation between drill holes suggests that overall

Overleaf Figure 2.2a & b. Schematic cross sections of the Black Hill and Cambrai Plutons based on combined gravity, magnetic and drill hole data.

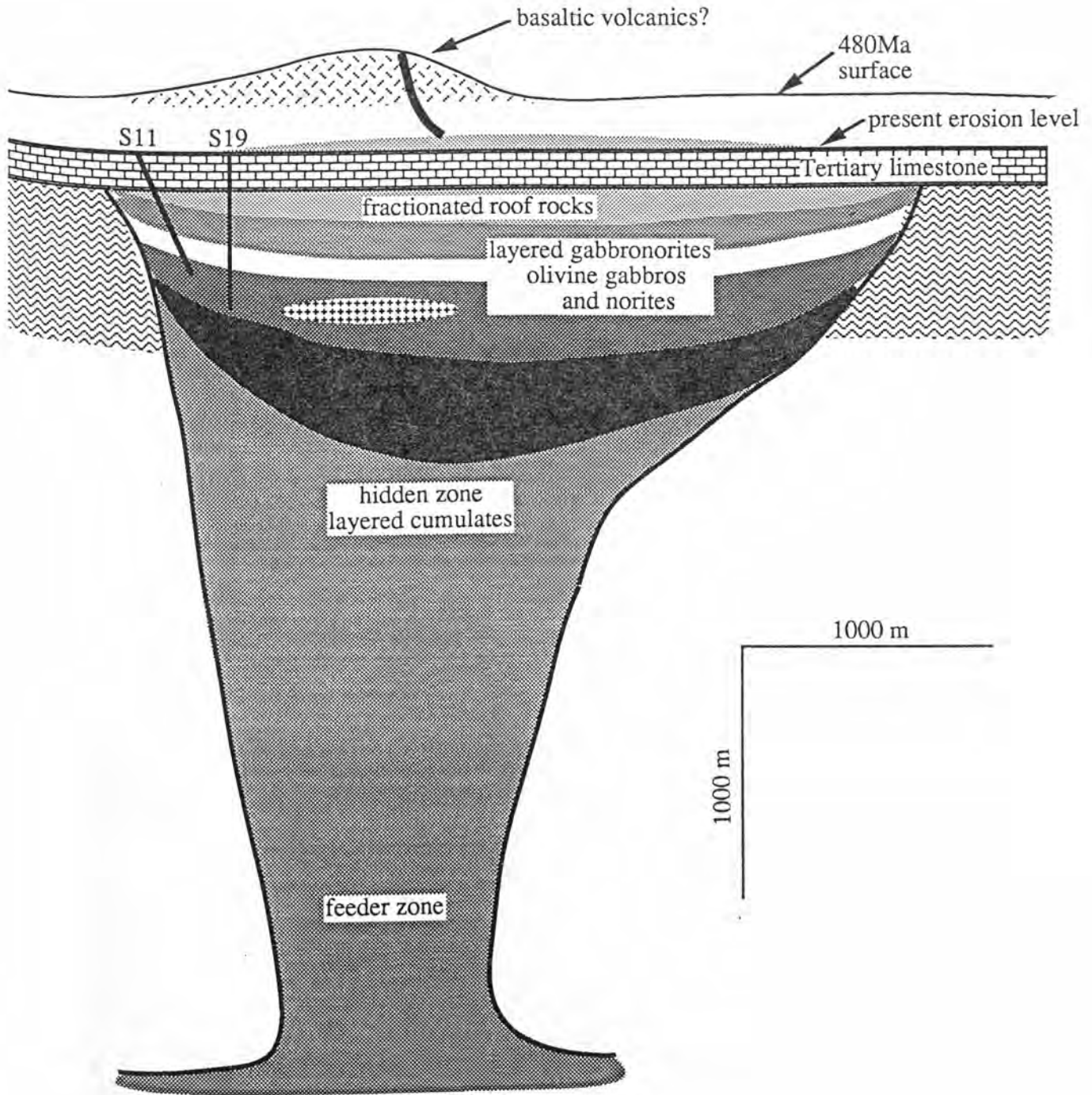
Schematic Black Hill Cross Section



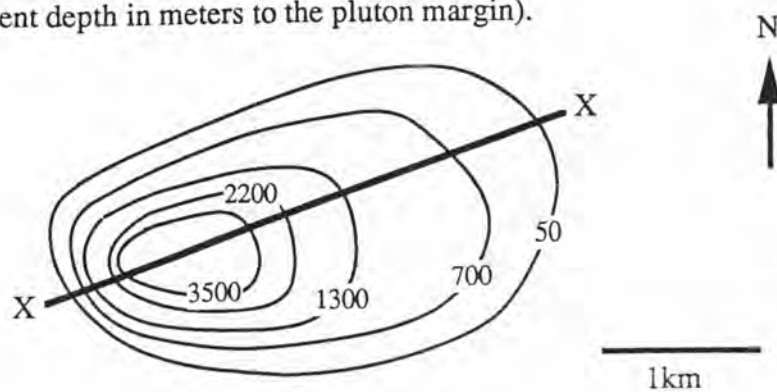
Plan view. (Contours are depths to edge of body in meters)



Schematic Cambrai Cross Section



Plan view (contours represent depth in meters to the pluton margin).



Figures opposite:

- Figure 2.3a.** Meter-high polished block of potassic gabbro from the roof zone of the Black Hill pluton showing modal layering with truncations and some wavy layering. In three dimensions the layers form trough structures.
- Figure 2.3b.** Modal layering in potassic gabbro showing darker pyroxene-rich bases and lighter plagioclase-rich tops. Area is about 30 x 50 cm.
- Figure 2.3c.** Subhorizontal layering in thin section (crossed polars) from drill core (5-575). Note fine grained olivine rich bases to layers in centre of photo. Area is 1.5 x 5 cm.
- Figure 2.3d.** Thin section photograph from drill core (19-869) showing the development of coarse zones of hydrous minerals (actinolite and biotite) at the contact between two cyclic units. Crossed polars, 1.5 x 5 cm.



a



b



c



d

this layering dips shallowly in towards the centre of the plutons. Whilst the outcrop is dominated by potassic gabbro-norites with modal layering, the drill core reveals larger scale cyclical lithological layering in the cumulates. Summary drill core logs for the Black Hill and Cambrai plutons (Fig. 2.4a & b) show repetition of a number of cyclic units. In the Black Hill Pluton these cycles have troctolites with occasional thin peridotite bands at the base overlain by olivine gabbros followed by gabbro-norites. The Cambrai Pluton contains repetitive cycles consisting of olivine gabbros and then norites topped by gabbro-norites. Boundaries between lithological layers are often the site of bands of hydrous minerals termed coarse zones (Fig. 2.3d). Whilst the olivine gabbros and gabbro-norites are indistinguishable between the two plutons the norites would appear to be virtually restricted to the Cambrai Pluton though this may be an artifact of limited drill hole data. The gravity data indicates the drill core did not reach the base of the plutons such that there is a "hidden zone" beneath the lower layered cumulates which might be expected to contain an increased abundance of mafic cumulates such as the troctolites and peridotites.

Cryptic layering which is common to many similar intrusions does not appear to be significant on a broad scale in the layered cumulates, though more detailed sampling would probably reveal fine scale variations within individual cyclic units. There is however a marked change which distinguishes the lower layered cumulates ($Mg\# = 80-85$, Fo_{80}) from the overlying roof zone potassic gabbro-norites ($Mg\# = 56$, Fo_{50}) in the Black Hill Pluton (see Fig. 2.4a).

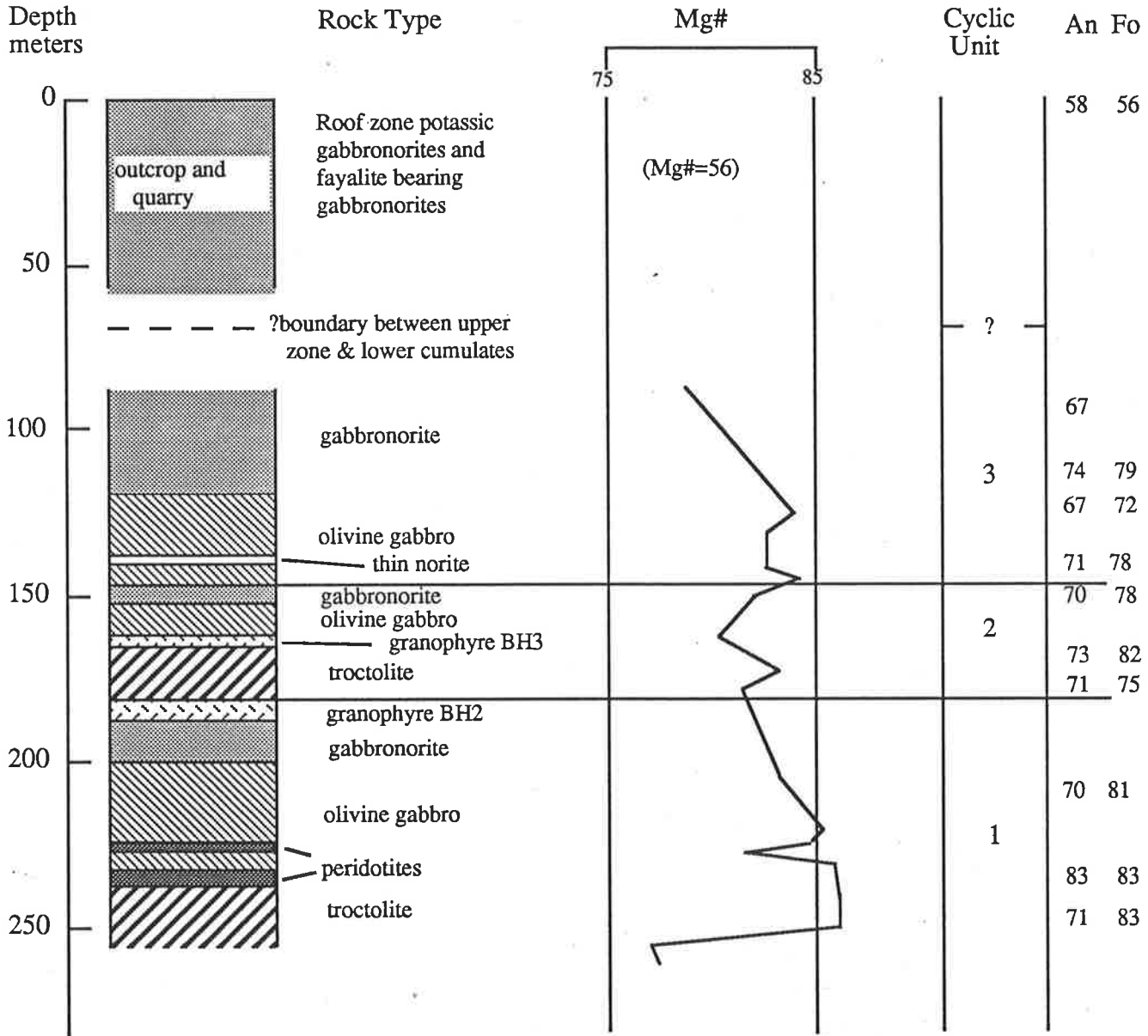
The last few decades have seen many advances in the understanding of magma chamber dynamics in which early concepts of crystal settling have largely been replaced by in situ crystallization at chamber margins to explain layering in igneous rocks. Oscillation around a cotectic (as suggested by Morse, 1979) at the top of a growing crystal pile may provide an explanation of modal layering. McBirney and Noyes (1979) suggest that layering is likely to have formed by oscillatory nucleation and diffusion controlled crystallization occurring at the intrusion margins. Crystallization may occur dominantly in situ at the chamber floor, particularly if convection is efficiently removing heat from the floor. This occurs because the increased pressure at the chamber floor will raise crystallization temperatures of minerals which increases supercooling leading to increased nucleation and growth rates (Turner and Campbell, 1986). At the roof on the other hand, although heat loss will be greater, the liquids will be more evolved due to fractionation and assimilation, with the result that their liquidus is depressed thereby limiting crystallization.

Recent theoretical and experimental work on fluid dynamics indicates that layering

Overleaf Figures 2.4a & b. Summarized drill core logs from the Black Hill and Cambrai Plutons.

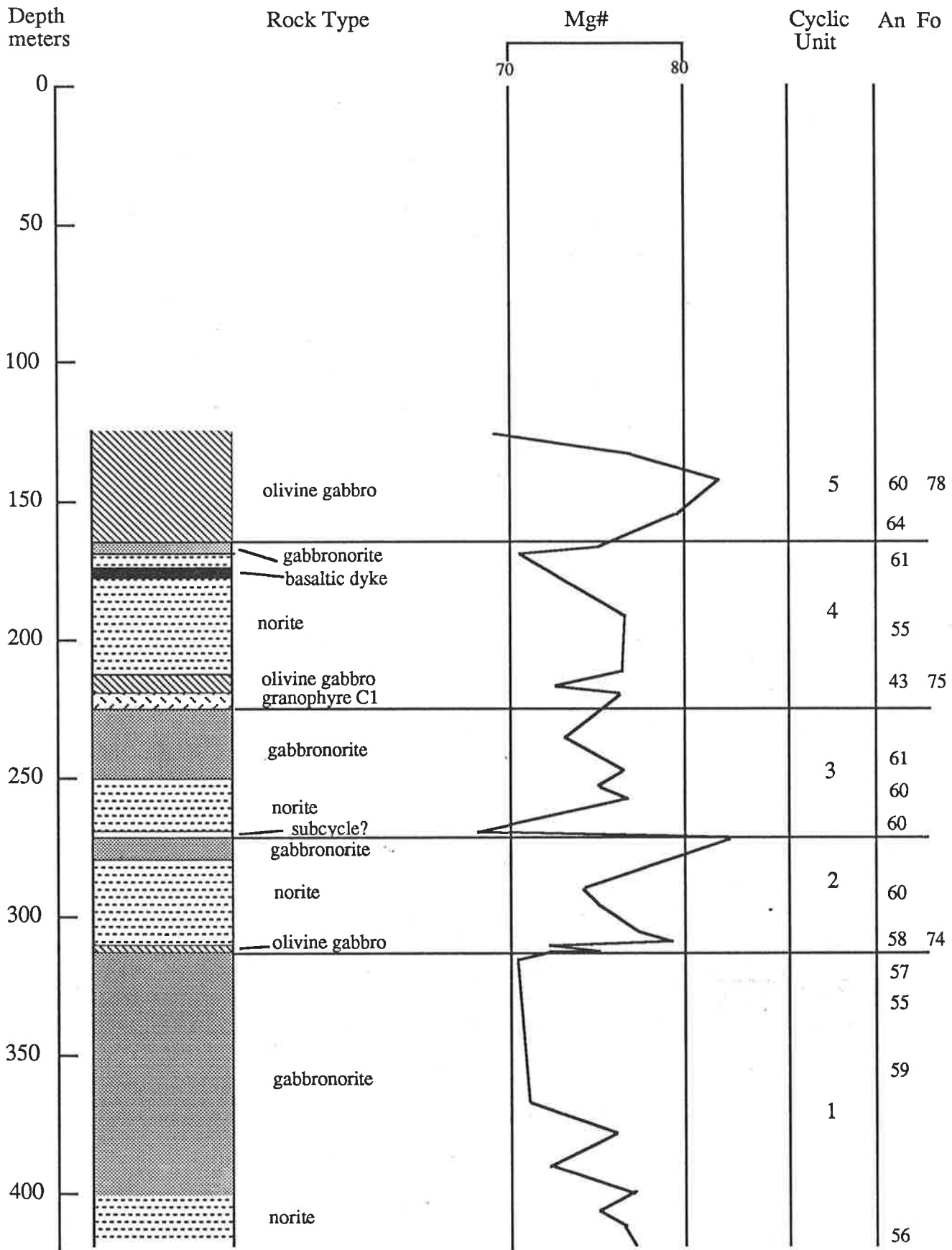
Black Hill Pluton

(synthesis of DDH's S2&S5)



Cambrai Pluton

(synthesis of DDH's S11&S19)



may also be related to injection of fresh magma. For example, depending on the temperature and degree of fractionation (and therefore the density of the resident magma), a fresh injection of primary magma may be relatively lighter and form a layer towards the top of the chamber perhaps also entraining some of the resident magma (Huppert *et al.*, 1986). This may then form a discrete layer or cycle of layers. Alternatively the injected magma may be denser than the resident magma in which case it may pond at the base of the chamber as a discrete layer (Huppert and Sparks, 1980).

From the above discussion it is clear that magma chamber dynamics are likely to be strongly influenced in their early stages by the ability for convective processes to operate. The conditions for thermally driven convection to occur are described by the thermal Rayleigh number:

$$Ra = \rho g \alpha T L^3 / \kappa \nu \dots (\text{eg Turner and Campbell, 1986})$$

where g is the acceleration due to gravity, α is the coefficient of thermal expansion (about $1 \times 10^{-5} \text{ deg}^{-1}$), T is the temperature difference between two boundaries and L is the distance between them, κ is the thermal diffusivity (about $5 \times 10^{-5} \text{ m}^2 \text{ sec}^{-1}$), ρ is the density (about 2.7 kgm^{-3} at $1000 \text{ }^\circ\text{C}$) and ν is the kinematic viscosity (about 10^2 - 10^3 poise for basalt with 2-3% H_2O) (values taken from Murase and McBirney, 1973). For the Black Hill plutons L is (3 - $4 \times 10^3 \text{ m}$) and when raised to the third power will dominate the equation. The Rayleigh number will therefore be well in excess of the 10^3 required for convection to set in and initial turbulent convection ($Ra > 10^6$) is implied. Various other factors such as fresh inputs of hot magma are also likely to induce convection. In particular the compositional Rayleigh number, measuring tendency towards convection produced by compositionally induced density gradients, is likely to be even more important than the thermal Rayleigh number (Sparks *et al.*, 1984, Turner and Campbell, 1986) once fractionation commences.

At Black Hill the truncation of layers and crossbed structures indicates the action of magmatic currents confirming that the magma chambers were in a state of convective motion for some of their pre-solidified history. The outcrop lies near the edge of the Black Hill Pluton and the steep dips of layering may reflect density or convective currents moving down the walls of the magma chamber. Certainly these steep dips argue against an origin of the modal layering by gravitational stratification. The wispy layering suggests redistribution by irregular currents and similar features in the Skaergaard intrusion are restricted to the roof and margins (McBirney and Noyes, 1979) which suggests that the Black Hill outcrop represents the roof zone of the intrusion (see also later discussion).

The magma chambers may also have contained more than one convective cell. As such, models of double diffusive convection are likely to be appropriate. The marked compositional change between the outcropping gabbros and the cumulates intersected in drill core may separate more fractionated magma resident in an upper convective cell from

underlying primitive magma at a temperature, compositional and density interface. Turbulent convection would keep the magma homogenized and continuously supply heat to the roof providing optimum conditions for assimilation of roof rocks. Significantly the roof zone gabbros are highly potassic (see subsequent discussion) consistent with assimilation. Potassium (and volatiles) may also be enriched in such an upper convective cell by double diffusive and or liquid/convective fractionation processes as recently reviewed by Turner and Campbell (1986). Unfortunately there is no drill core from the interval between the potassic gabbro norites and the underlying cumulates.

Formation by processes operating in a closed system would be expected to result in successive cyclic units becoming progressively more fractionated. This is not the case and the repetition of cyclic units in both plutons, as well as reversals in Mg# and the lack of broad scale cryptic variation favours open system processes, specifically recharge with each cyclic unit representing a fresh influx of magma into the chambers. Further evidence for magma chamber recharge processes in Black Hill take the form of narrow, fine grained olivine rich bands at the base of coarse grained olivine gabbros (Fig. 2.3c) which may represent undercooling of an influx of hotter mafic magma against cooler resident magma. Crystallization then occurs on the chamber floor, perhaps with occasional density currents descending from side wall or roof crystallization areas to add to the crystal pile. The beginning of each cyclic unit is marked by an increase in Mg#, consistent with the recharge hypothesis, however this increase is slightly displaced upwards from the lithological boundary. Similar displacements in the Muskox intrusion were explained by Irvine (1980) as resulting from infiltration of the new cyclic unit by more evolved, post cumulus liquids from the units beneath as they are compacted. As will be seen mineralogical evidence suggests low pressure, shallow level crystallization and therefore eruption may well have accompanied recharge episodes, however the current level of exposure means any such extrusive equivalents have been removed.

2.4. Petrography

Table 2.1 gives a petrographic summary for the principle lithologies at Black Hill along with the inferred crystallization order and modal analyses indicating the typical range of mineralogy. Alteration is generally minimal, involving chlorite replacement of biotite and talc replacement of orthopyroxene as well as general uralitization of pyroxenes, and minor sericitization of plagioclase. All samples and thin sections are housed in the Department of Geology and Geophysics at the University of Adelaide under accession number A876-. The sample numbers used here have the drill hole number as their first digit followed by the depth in feet.

Table 2.1. Summarized petrography and modal analyses for Black Hill gabbros (numbers in brackets refer to crystallization order)

Unit	olivine	orthopyroxene	clinopyroxene	plagioclase	hornblende	biotite	oreauces	apatite	alkali feldspar	quartz
Potassic gabbro	- 0.1 (1) rare fayalite inclusions in pyroxene	11.6 (1) 15.3 (1) euhedral to subhedral	17.6 (1) 14.3 (1) euhedral to subhedral	45.8 (1) 53.2 (1) euhedral to subhedral often corroded	0.1 (2) - coronas to px, alteration along px cleavage	3.3 (1) 5.2 (1) discrete foxy-red flakes often intergrown with px	2.5 (1) 3.9 (1) il & mt inclusions particularly in biotite	1.2 (1) 0.9 (1) euhedral as inclusions and discrete	17.8 (2) 4.6 (2) interstitial	- 3.9 (3) interstitial
Gabbro	- 0.2 (1) some iddingsitic relicts	10.8 (1) 9.3 (2) subhedral plates	2.1 (1) 26.6 (2) subhedral plates with occ. plag inclusions	59.6 (1) 49.3 (1) subhedral laths often corroded	13.0 (3) 9.1 (3) coronas to px, alteration along px cleavage	5.4 (3) 3.1 (3) discrete flakes often intergrown with px	2.9 (2) 2.0 (2) il & mt inclusions also sulphides	0.7 (2) 0.4 (2) euhedral, often large prisms	3.5 (4) - interstitial, rare	2 (4) - variable in abundance interstitial
Pyroxene monzonite	- -	7.6 (1) 5 (1) including pigeonite with herringbone exsolution	7 (1) 4 (1) discrete plates and overgrowths on pigeonite	47.1 (1) 39.4 (1) subhedral - euhedral laths often with overgrowths	2 (2) 3.2 (2) alteration to pyroxene	1.8 (2) 1.7 (2) often partially rims pyroxene	1.2 (1) 1.5 (1) ilmenite and magnetite	1 (1) 0.9 (1) large, euhedral ? cumulus also unzoned zircon	28.8 (3) 37.8 (3) interstitial matrix some microperthite	3.5 (4) 6.4 (4) interstitial, with some myrmekitic intergrowths
Anorthosite	- -	0.1 (2) - small subhedral grains	6.3 (2) 3.1 (2) small subhedral grains ? evidence of exsolution	67.9 (1) 79.1 (1) large, complexly zoned laths with overgrowths	5.1 (3) 3.5 (3) in irregular patches often replacing pyroxene	2.5 (3) 3.9 (3) similar to hornblende	2.8 (71) trace inclusions	0.5 (2) trace euhedral	11.6 (4) 8 (4) microcline twinning perthitic & granophyric	2.4 (4) 2.4 (4) interstitial
Norite	- -	50.1 (1) 62.9 (1) small euhedral prisms included in plagioclase	9.5 (3) 1.5 (3) anhedral interstitial with opx and plag inclusions	23.5 (2) 18.6 (2) poikiloblastic interstitial	4.5 (4) 5.8 (4) actinolite alteration of opx intergrown hb & cpx	7.9 (4) 7.3 (4) interstitial and along px margins and cleavage	2.3 (2) 0.7 (2) magnetite, ilmenite and abundant sulphides	0.6 (3) - rare	- - -	1.6 (5) 3.2 (5) variable in abundance interstitial
Olivine gabbro	2.4 (2) 5.8 (2) euhedral often large occ. plag inclusions	4.7 (3) 16.1 (3) coronas on olivine as and poikiloblastic plates	9.9 (3) 26.2 (3) poikiloblastic plates with ol and plag inclusions	69.9 (1) 44 (1) often euhedral with symplectites adj. olivine	11.2 (5) 4.6 (5) patchy actinolite alteration of pyroxene	0.9 (5) 0.9 (5) minor flakes included in rare hornblende	1 (4) 2.3 (4) mt, il sulphides and minor hercynite	- trace -	- - -	- - -
Troctolite	38.7 (1) 12.1 (1) euhedral to subhedral occ. plag inclusions	0.7 (2) - rare thin rims on olivine	7 (2) 1.6 (2) intercumulus and minor poikiloblastic grains	47 (1) 86.3 (1) euhedral with some adcumulus growths	4.2 (3) - actinolite alteration to olivine and pyroxene	trace - rare ? alteration to pyroxene	2.3 (2) trace chromium spinel with minor mt and il	trace trace rare euhedral possibly cumulus grains	- - -	- - -
Peridotite	56.1 (1) 55.5 (1) large subhedral and cumulate	8.7 (2) 9.4 (2) intercumulus and as rims on olivine	22.3 (2) 18.5 (2) intercumulus material	0.2 (2) 5.1 (2) minor and intercumulus near troctolite contacts	4.1 (3) 7.3 (3) actinolite alteration to pyroxene	- -	8.6 (2) 4.2 (2) chromium spinel, mt and minor hercynite	- - -	- - -	- - -
Coarse zone	- -	1 (1) relicts in amphibole	4.9 (1) relicts in amphibole	45.1 (1) large subhedral with patchy twinning	30.5 (2) actinolite and hornblende replacement of pyroxenes	5.1 (2) patchy flakes	4 (1) sulphides and up to 3% hercynite (from reaction?)	trace - large grains, also the first appearance of sphene	- -	9.4 (2) irregular and interstitial
Granophyre	- -	- -	- -	3.3 (1) 3.5 (1) few primary grains, mostly perthite exsolution	- -	1.5 (3) 1.1 (3) rare small slivers probably subsolidus	2.9 (1) 1.0 (1) magnetite and ilmenite	trace trace -	60.2 (2) 50.1 (2) large, often perthitic and sometimes rapakivi	32.1 (1) 44.3 (1) can be included in k-spar also as granophyre

2.4.1. Gabbronorites and potassic gabbronorites

Gabbronorites are the most abundant lithology in the plutons. They typically consist of plagioclase, orthopyroxene and clinopyroxene with minor biotite, hornblende and opaques set amongst interstitial alkali feldspar and minor quartz. Apatite, which can be abundant, and sphene are common accessory phases. These gabbros have relatively non-cumulate textures in which plagioclase and pyroxene appear to have co-precipitated. Plagioclase laths are often highly corroded, particularly in contact with alkali feldspar, indicating resorption. Pyroxene, which occurs in subordinate amounts to plagioclase, forms subhedral plates which occasionally contain inclusions of plagioclase (Fig. 2.5a). Clinopyroxene often exceeds orthopyroxene in content and sometimes contains blebby exsolution of orthopyroxene or vermicular magnetite. Opaques consist of pyrite and equal proportions of ilmenite (with haematite exsolution) and magnetite (which has hercynite exsolution). Biotite occurs as ragged grains often intergrown with or rimming pyroxene or with magnetite cores. Hornblende forms coronas around clinopyroxene and alteration along pyroxene cleavage planes rather than discrete grains. In some cases quartz and alkali feldspar are concentrated into allotriomorphic zones possibly indicating an immiscible relationship (Fig. 2.5c).

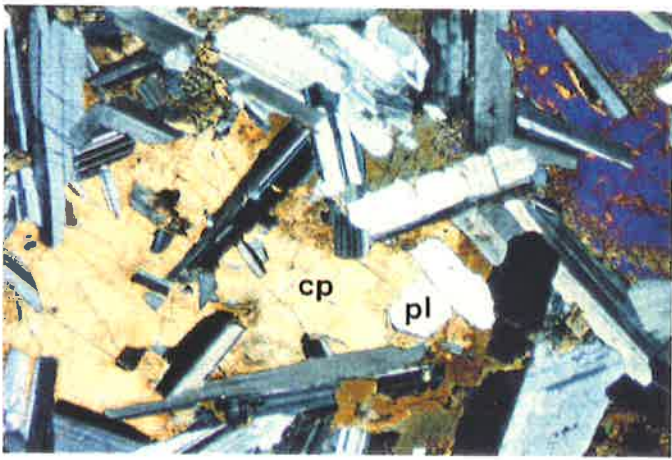
The outcrop of the Black Hill Pluton is a more evolved and potassic variety of gabbronorite with an increased abundance of alkali feldspar and quartz and subequal amounts of ortho- and clinopyroxene. Additionally large flakes of foxy-red biotite are very common and often intimately interfingering with, or even included in orthopyroxene (Fig. 2.5b). Rare fayalitic olivine is also found in these potassic gabbronorites, usually included in orthopyroxene (Fig. 2.5d). The similarity between these rocks and pyroxene monzonites from the intrusion margins along with their chemical and mineralogical distinction from the lower layered cumulates further indicates that they represent rocks from near the upper margins or roof zone of the intrusion. The occurrence of both biotite and alkali feldspar indicates a very high potassium content compared to the other gabbros and could reflect roof and wall rock assimilation. Quartz-feldspar-biotite pods (2-10 cm diameter) found in outcrop are interpreted as forming from late stage, trapped liquids.

2.4.2. Pyroxene monzonites and anorthosites

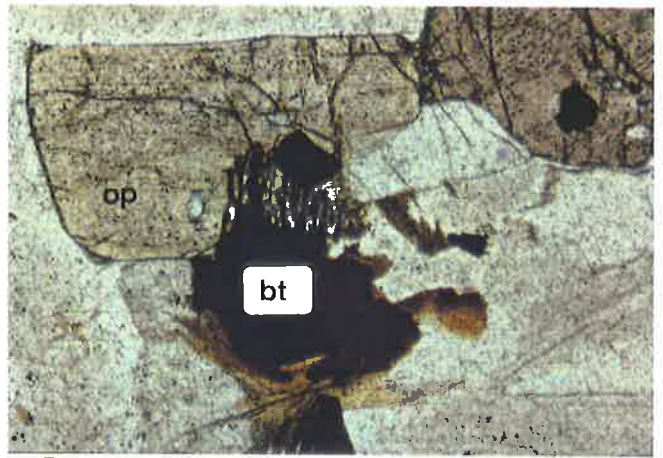
Pyroxene monzonites, that are intersected by a drill hole on the margin of the Black Hill Pluton, are even more fractionated and potassic than the potassic gabbronorites described above. These rocks contain up to 38% alkali feldspar and 6% quartz which surround plagioclase, pyroxene, hornblende and biotite which is less abundant than in the potassic gabbronorites (Fig. 2.5e,f). Additional phases include opaques, ubiquitous euhedral apatite which crystallized early and is found included in both plagioclase and pyroxene, and finally rare, euhedral, unzoned zircon (Fig. 2.5h) which indicates that

Figures opposite:

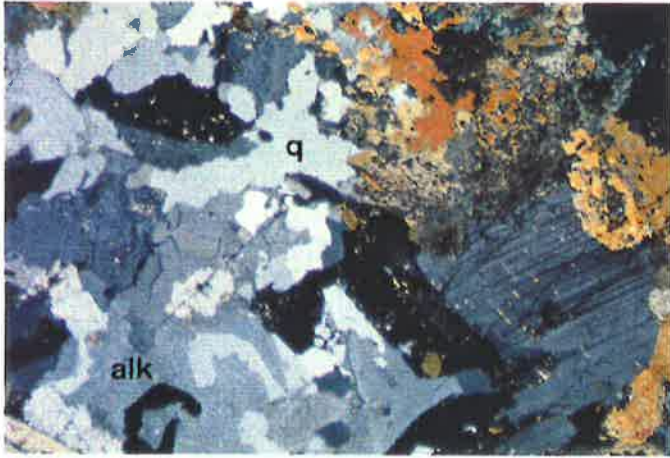
- Figure 2.5a.** Gabbronorite (19-536) with large poikilitic plates of intercumulus clinopyroxene (cp) enclosing cumulus plagioclase. Crossed polars, width of view 4 mm.
- Figure 2.5b.** Textural relationship in a potassic gabbronorite (A171-83) suggesting reaction between liquid and orthopyroxene (op) to produce biotite (bt). Note the opaque grain of magnetite in the core of the biotite. See text for discussion. Plane polarized light, width of view 2 mm.
- Figure 2.5c.** Allotriomorphic patch of interstitial quartz (q) and alkali feldspar (alk) from a potassic gabbronorite (19-1379). Crossed polars, width of view 4 mm.
- Figure 2.5d.** Small relicts of fayalitic olivine (ol) in a roof zone potassic gabbronorite (section 6728 RS94 from SADME) containing clinopyroxene (cp), orthopyroxene (op), plagioclase (pl) and alkali feldspar (alk). Crossed polars, width of view 2 mm.
- Figure 2.5e.** Pyroxene monzonite with plagioclase (pl), orthopyroxene (op) and clinopyroxene (cp) set in large amounts of interstitial alkali feldspar (akf). Note the biotite (bt) with opaque cores interfingering with orthopyroxene similar to Fig. 2.5b. Plane polarized light, width of view 4 mm.
- Figure 2.5f.** Same view as Fig. 2.5e with crossed polars.
- Figure 2.5g.** Pigeonite with distinctive heringbone exsolution texture in alkali feldspar (alk) from a pyroxene monzonite (4-807). Crossed polars, width of view 4 mm.
- Figure 2.5h.** Large euhedral, unzoned zircon from a pyroxene monzonite (4-711). Plane polarized light, width of view 2 mm.



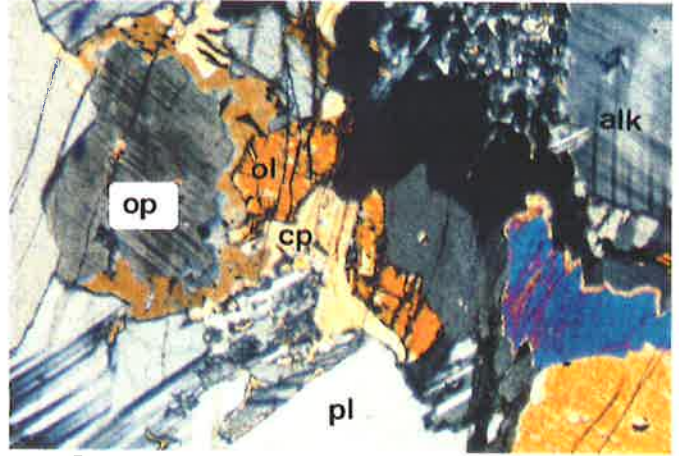
a



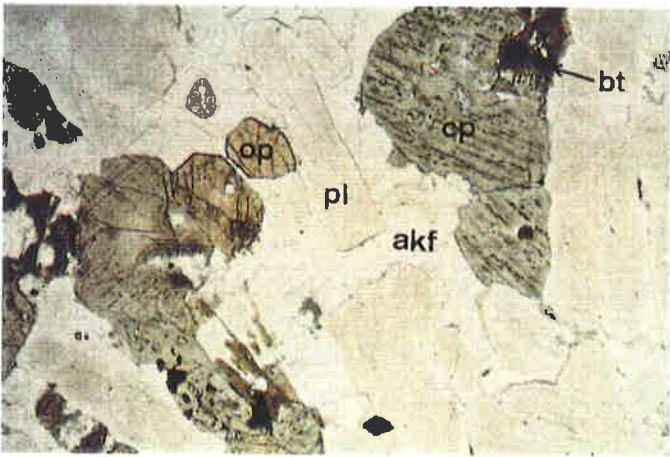
b



c



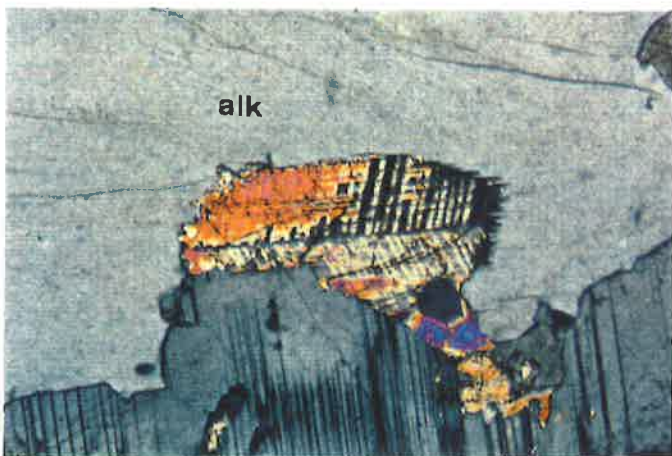
d



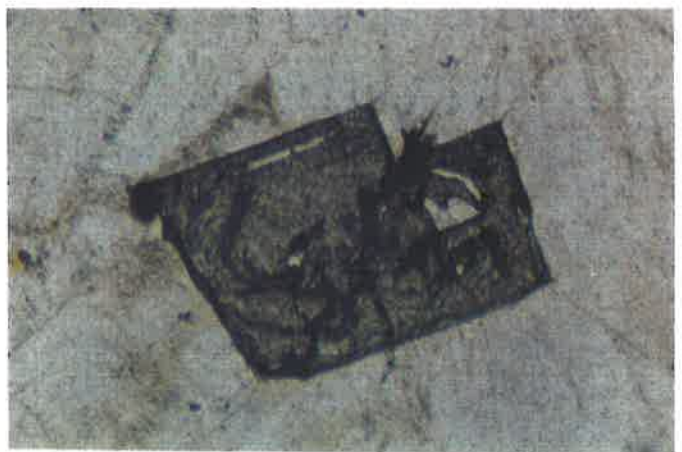
e



f



g



h

these rocks crystallized from highly fractionated liquids. Texturally these monzonites do not appear highly cumulus though plagioclase laths, with large overgrowths, often contain small pyroxene inclusions and apatite may have a cumulate origin. Alkali feldspar occasionally contains microperthitic exsolution and exhibits frequent granophyric intergrowths suggestive of low pressure crystallization. Whilst olivine is not found in the monzonites, early formed pigeonite is abundant often with overgrowths of clinopyroxene. Exsolution and inversion give the pigeonite a broad herringbone texture (Fig. 2.5g) whilst the clinopyroxene overgrowths contain fine pigeonite exsolution lamellae. Orthopyroxene makes up a three pyroxene assemblage, all occurring in roughly equal amounts.

With decreasing pyroxene contents, the pyroxene monzonites grade downwards into anorthosites which typically contain 70% plagioclase and correspondingly reduced amounts of alkali feldspar, quartz, pyroxene, biotite and hornblende with only minor apatite and opaques. Texturally these have a relatively non-cumulate origin and are characterized by large plagioclase laths containing trails of small mafic inclusions and exhibiting complex zoning and overgrowths (Fig. 2.5i). Pyroxene even when not included in plagioclase only forms small subhedral grains. The similar texture and mineralogy with different mode and growth rates suggests that the anorthosites are related to the pyroxene monzonites but that co-precipitation only occurred after an initial period in which the liquid must have been strongly displaced into the plagioclase field.

2.4.3. Troctolites and peridotites

These are the most mafic (magnesian) rocks in the complex and have very distinct cumulate textures. The troctolites have a strong lamination produced by alignment of these plagioclase laths (Fig. 2.5j), however the low density of plagioclase, which makes up 45-60 percent of the troctolites, does not permit an origin by gravitational settling. The plagioclase and olivine can generally be assumed to have co-precipitated although occasionally small plagioclases are found included in olivine. These are mesocumulates to adcumulates often having little intercumulus material (see Table 2.1) and more sodic adcumulus overgrowths on the plagioclases. Intercumulus minerals include amphibole, trace amounts of biotite and opaques which include chrome spinel. Pyroxene, which is predominantly clinopyroxene, forms intercumulus material, coronas around olivine and occasional poikiloblastic plates. These poikiloblasts contain inclusions of plagioclase and olivine which are smaller than those not so included indicating postcumulus growth has occurred on non-included grains.

The olivine content of the troctolites is variable sometimes increasing to 40% and within the lower intersected troctolites are occasional metre-thick layers of coarse grained peridotite. These peridotites contain 40 to 55% olivine with intercumulus pyroxene which

Figures opposite:

Figure 2.5i. Anorthosite (4-926) composed of coarsely intergrown plagioclase containing small pyroxene inclusions. Crossed polars, width of view 4 mm.

Figure 2.5j. Troctolite (5-756) composed of cumulus olivine (ol) and plagioclase (pl) with little intercumulus material. Crossed polars, width of view 4 mm.

Figure 2.5k. Peridotite (5-742) with coarse grained cumulus olivine (ol) set in intercumulus orthopyroxene (op) with green hercynite (sp) and interstitial biotite (bt). Plane polarized light, width of view 4 mm.

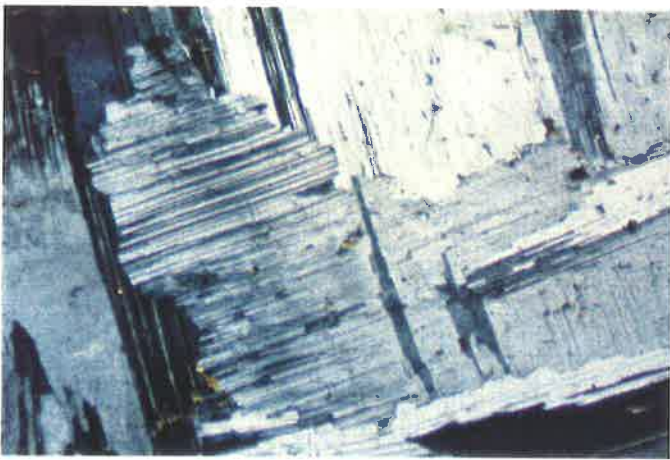
Figure 2.5l. Peridotite (5-742) composed of cumulus olivine (ol) and intercumulus orthopyroxene (op). Crossed polars, width of view 4 mm.

Figure 2.5m. Olivine gabbro (5-590) showing cumulus plagioclase (pl) and olivine (ol) included in clinopyroxene (cp). Crossed polars, width of view 3 mm.

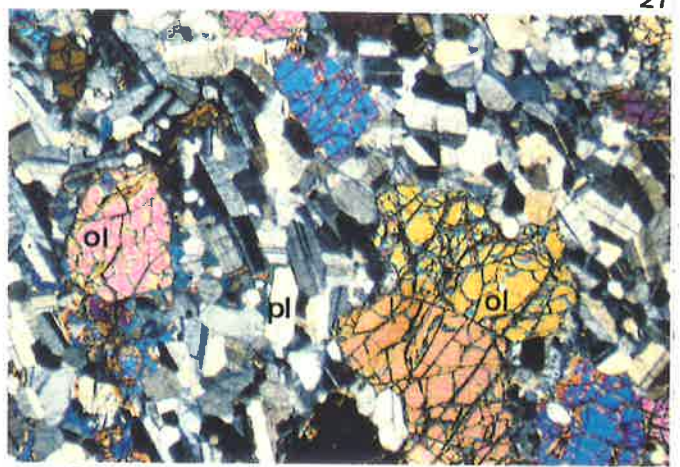
Figure 2.5n. Olivine gabbro (3-834) with biotite (bt) included in olivine (ol) which is rimmed by a vermicular symplectite (sym) in contact with plagioclase (pl). Plane polarized light, width of view 3 mm.

Figure 2.5o. Norite (19-1379) showing fine grained prisms of bronzite orthopyroxene (op) poikilitically included in plagioclase (pl). Crossed polars, width of view 4 mm.

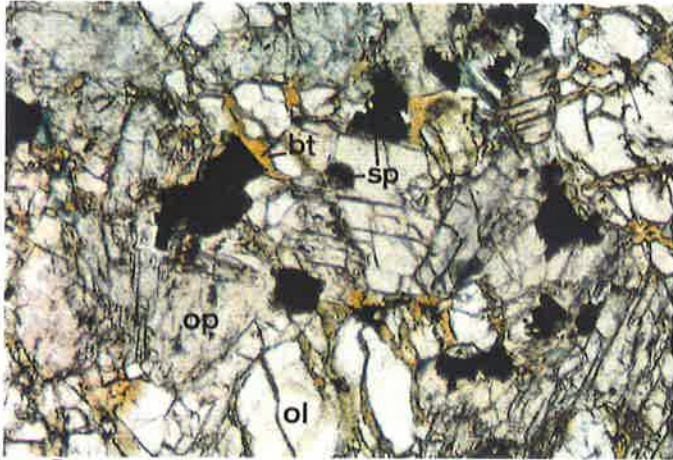
Figure 2.5p. Granophyre (15-301) composed of coarsely perthitic alkali feldspar (alk) and quartz (q) with minor biotite (bt) and plagioclase (pl). Crossed polars, width of view 4 mm.



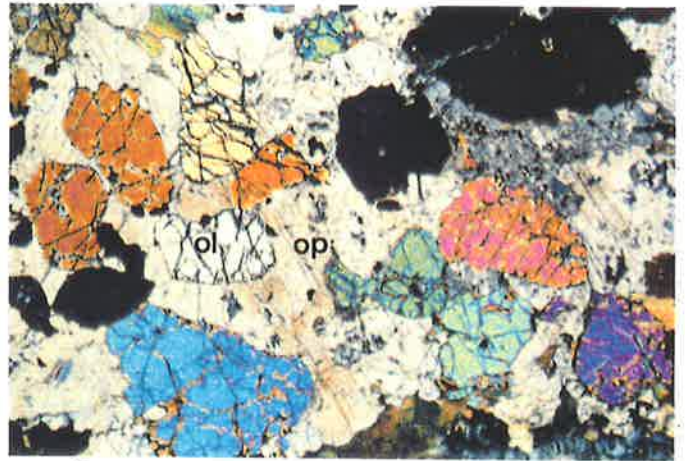
i



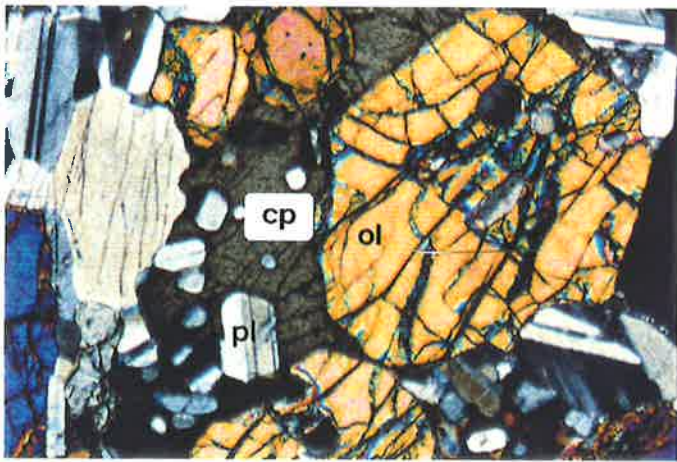
j



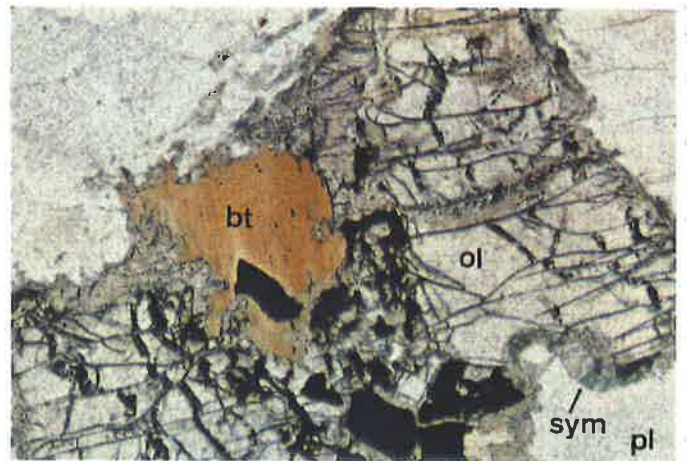
k



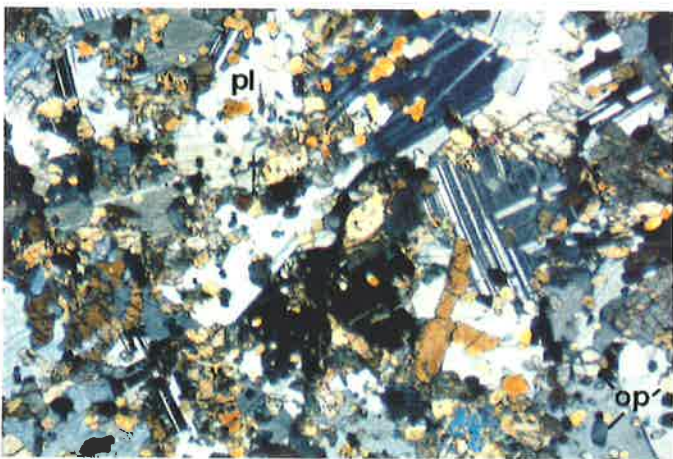
l



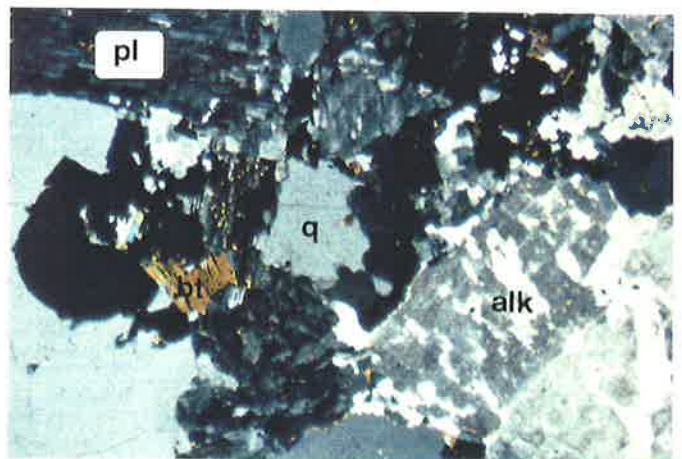
m



n



o



p

is often altered to actinolite (Fig. 2.5k,l). Chromium spinel and hercynite can make up to 5% of these rocks and small amounts of plagioclase are present at the peridotite margins where they grade rapidly into troctolites. The concentration of peridotite layers at the base of the drill holes indicates a likely increased abundance at depth in the hidden zone.

2.4.4. Olivine gabbros

The olivine gabbros are orthocumulates with variable composition such that with decreasing amounts of pyroxene they grade into troctolites and, more commonly, with decreasing olivine content they grade into gabbronorites. The general compositional range is plagioclase 44-69%, clinopyroxene 26-10%, orthopyroxene 16-5%, olivine 10-2%, hornblende 5-11% with biotite ilmenite and magnetite being accessories. Apatite is found in some samples and many contain polymineralic grains of pyrite, chalcopyrite and pyrrhotite. As in the troctolites olivine and plagioclase, which is sometimes found included in olivine, are the cumulus phases whilst both the pyroxenes are intercumulus and often form large plates in which olivine and plagioclase are included (Fig. 2.5m). Again the included olivine and plagioclase grains are smaller than those elsewhere indicating that the enclosing pyroxene has arrested their growth. Biotite and hornblende occur as patchy alteration and rims to pyroxenes though biotite also forms discrete flakes (Fig. 2.5n). Commonly the boundaries between olivine and plagioclase are the site of a vermicular symplectite. This consists of an inner rim of orthopyroxene next to the olivine followed by a rim of amphibole then a zone of anorthite containing vermicular orthopyroxene and amphibole adjacent to the plagioclase (Fig. 2.5n).

2.4.5. Norites

The norites intersected in the Cambrai Pluton consist dominantly of orthopyroxene with lesser plagioclase, clinopyroxene, hornblende and biotite with minor quartz and magnetite. Characteristically textures are heteradcumulate with fine grained, euhedral prisms of orthopyroxene (chromium-bronzite) poikilitically included in anhedral, intercumulus plagioclase (Fig. 2.5o). In crystallization order, nucleation rate and modal content therefore, the norites are strikingly different to the gabbros previously described. Fine grained bronzites sometimes accumulate into layers which define a near horizontal lamination whilst elsewhere plagioclase nucleates more readily to form individual grains which also define a layering (eg. Fig. 2.3c). Clinopyroxene, hornblende and biotite all form interstitial material which often contain inclusions of bronzite and occasionally plagioclase. Weakly pleochroic actinolite and talc often rim bronzite grains. Small amounts of apatite occur along with minor interstitial quartz. Sulphides however, can be abundant and in one zone even replace plagioclase as the intercumulus phase suggesting the formation of an immiscible sulphide liquid.

2.4.6. Coarse zones

Localized areas of altered gabbros at Black Hill have a significantly coarsened grain size and pyroxene becomes replaced by a hydrous assemblage of amphiboles and biotite. Hercynite and sphene are characteristic of the alteration assemblage. Wager and Brown (1968) attribute mineralogically and texturally similar zones, in the Skaergaard intrusion, to reaction with xenoliths of country rock which the zones surround. At Black Hill these zones clearly reflect localized volatile build-up and this is also indicated by zones where gabbro norites become increasingly hornblende rich and pyroxene poor. The quarry and outcrop at Black Hill contain fractures lined with green actinolite. The coarse zones and these actinolite veins may have formed when the hydrothermal system set up upon initial intrusion collapsed inwards into the gabbros during their final and brittle cooling stage. Some coarse zones, forming narrow bands at lithological boundaries, may have formed at the top of the cumulate pile as fractionated, volatile rich, intercumulus liquid was expelled upwards (see Fig. 2.3d).

2.4.7. Granophyres

Dyke or sill like bodies of granophyre, interpreted to be highly fractionated liquids, are common amongst the lower layered cumulates. They are composed primarily of alkali feldspar and quartz with occasional minor plagioclase and very rare biotite. Textures range from consertal seriate to completely granophyric (Fig. 2.5p). Alkali feldspar is frequently perthitic and sometimes rimmed by plagioclase to produce rapakivi textures. Accessory phases include opaques, zircon and fluorite. Quite often the drill core shows mixing and mingling relations between the granophyric liquids and their host mafic magmas. Such zones are characterized by an abundance of sphene and zircon. Similar relationships occur in the nearby Mannum Granite (Fig. 1.1) and have been attributed to diffusive fronts set up upon mingling between similar felsic liquids with mafic magma (see discussion in chapter 5). Biotites from the Black Hill granophyres are surprisingly magnesian ($Mg\# = 65-60$) for such highly fractionated residual liquids and so are biotites from the Mannum Granite. These compositions may pertain to a mafic parentage or mixing with mafic magmas.

2.5. Mineral Chemistry

Mineral compositions were determined on a JEOL 733 microprobe and details of the analytical methods and uncertainties for electron microprobe work are detailed in appendix A.

Table 2.2. Representative feldspar analyses (atomic proportions calculated for 32 oxygens per formula unit)

sample #	876-BHG1	876-BHG1	876-BHG1	876-4-711	876-4-711	876-4-807	876-4-807	876-7-510	876-5-710	876-6-377	876-4-879	876-4-879
lithology	K-gabbronorite	K-gabbronorite	K-gabbronorite	Px-monzonite	Px-monzonite	Px-monzonite	Px-monzonite	Gabbronorite	Gabbronorite	Gabbronorite	Anorthosite	Anorthosite
SiO ₂	65.31	53.67	54.78	59.79	67.71	54.00	67.08	55.19	54.24	60.57	52.34	65.71
Al ₂ O ₃	19.82	29.67	29.77	26.58	18.93	30.13	19.16	29.42	29.83	25.58	31.02	19.59
FeO*		0.21	0.17			0.34		0.17		0.14		
CaO	0.75	11.64	11.53	8.30		12.07		11.05	11.77	6.92	13.10	0.33
Na ₂ O	1.40	5.07	5.28	7.02	1.70	5.06	1.82	5.32	5.06	7.38	4.32	2.10
K ₂ O	14.20	0.21	0.27	0.22	14.18	0.24	14.37	0.18	0.13	0.60	0.22	13.43
Total	101.62	100.44	101.81	101.91	102.52	102.14	102.42	101.46	101.02	101.37	101.00	101.30
Si	11.8008	9.6784	9.7399	10.4883	12.0661	9.5981	11.9947	9.8230	9.7067	10.6670	9.4153	11.8653
Al	4.2200	6.3057	6.2381	5.4962	3.9754	6.3484	4.0379	6.1707	6.2915	5.3099	6.5775	4.1680
Fe		0.0313	0.0253			0.0499		0.0249		0.0212		
Ca	0.1446	2.2431	2.1959	1.5604		2.2989		2.1338	2.2569	1.3051	2.5241	0.0645
Na	0.4891	1.7711	1.8210	2.3870	0.5861	1.7446	0.6295	1.8363	1.7550	2.5205	1.5076	0.7336
K	3.2743	0.0488	0.0620	0.0498	3.2233	0.0547	3.2777	0.0417	0.0294	0.1337	0.0500	3.0932
Sum	19.9503	20.0784	20.0822	19.9818	19.8508	20.1109	19.9398	20.0304	20.0394	20.0050	20.0745	19.9443
An	3.7	55.2	53.8	39.0	0.0	56.1	0.0	53.2	55.8	33.0	61.8	1.7
Ab	12.5	43.6	44.6	59.7	15.4	42.6	16.1	45.8	43.4	63.7	36.9	18.9
Or	83.8	1.2	1.5	1.2	84.6	1.3	83.9	1.0	0.7	3.4	1.2	79.5

sample #	876-2-648	876-2-648	876-11-1081	876-11-1081	876-11-923	876-11-923	876-5-544	876-5-544	876-5-756	876-5-756	876-5-727	876-5-727
lithology	Ol-gabbro	Ol-gabbro	Ol-gabbro	Ol-gabbro	Norite	Norite	Troctolite	Troctolite	Troctolite	Troctolite	Peridotite	Peridotite
SiO ₂	52.74	47.72	52.14	55.38	52.24	56.32	50.91	49.61	49.44	48.93	51.15	46.60
Al ₂ O ₃	31.55	34.25	32.00	29.54	31.63	29.22	32.20	33.02	32.68	33.25	32.17	35.12
FeO*	0.15	0.41					0.16	0.26			0.19	0.26
CaO	13.75	16.99	12.60	10.13	12.33	9.58	13.36	14.25	14.16	14.48	13.12	16.59
Na ₂ O	4.28	2.13	4.48	6.10	4.46	6.17	3.82	3.31	3.47	3.17	4.21	1.90
K ₂ O	0.10		0.08	0.06	0.06	0.13						
Total	102.66	101.69	101.65	101.22	100.73	101.58	100.76	100.46	99.88	99.83	100.04	100.60
Si	9.2514	8.6331	9.2997	9.8568	9.3934	9.9574	9.1761	9.0050	9.0202	8.9358	9.2234	8.5061
Al	6.5944	7.3021	6.7258	6.1968	6.7016	6.0877	6.8410	7.0644	7.0268	7.1556	6.8354	7.5559
Fe	0.0219	0.0623					0.0246	0.0391	0.0387		0.0285	0.0395
Ca	2.6123	3.2937	2.4074	1.9322	2.3754	1.8138	2.5807	2.7708	2.7671	2.8327	2.5347	3.2443
Na	1.4721	0.7469	1.5495	0.0138	1.5564	2.1147	1.3339	1.1664	1.2263	1.1241	1.4732	0.6709
K	0.0255		0.0187	2.1038	0.0139	0.0295						
Sum	20.0983	20.0890	20.0699	20.1034	20.0406	20.0233	20.0098	20.0457	20.0792	20.0482	20.0952	20.0510
An	63.6	81.5	60.6	47.7	60.0	45.8	65.9	70.4	69.3	71.6	63.2	82.9
Ab	35.8	18.5	39.0	51.9	39.4	53.4	34.1	29.6	30.7	28.4	36.8	17.1
Or	0.5	0.0	0.5	0.3	0.4	0.7	0.0	0.0	0.0	0.0	0.0	0.0

2.5.1. Feldspars

Plagioclase is a major component in nearly all lithologies and, in most cumulates except in the norites, it is the earliest crystallizing phase (along with olivine). This suggests that the water contents in the initial magma were relatively low as high water contents would delay the saturation of plagioclase. Compositions are typically labradorite but show a broad and continuous range from bytownite and rare anorthite in the troctolites to andesine in the more differentiated gabbronorites, pyroxene monzonites and anorthosites (Table 2.2; Fig. 2.6). Individual thin sections can show a moderate compositional range which reaches up to 20% An component in the more evolved rocks. It seems likely, however, that cumulates in the hidden zone would contain plagioclase at least as calcic as bytownite. Ternary mixing is minimal and the potassium content of the plagioclases is low ($Or < 3\%$). There appears to be no systematic increase of K_2O with Na_2O and in the more potassic gabbros K_2O is taken up in a separate alkali feldspar (and biotite). This may indicate that water contents were high enough to depress the solidus and close the feldspar solvus-solidus gap so that crystallization took place in the two-feldspar field. Using the relationships from Mathez (1973) and the calculated initial magma composition (see chapter 3) the most calcic plagioclases crystallizing at around 1250 °C (from pyroxene thermometry) indicate low water pressures around 500-1000 bars.

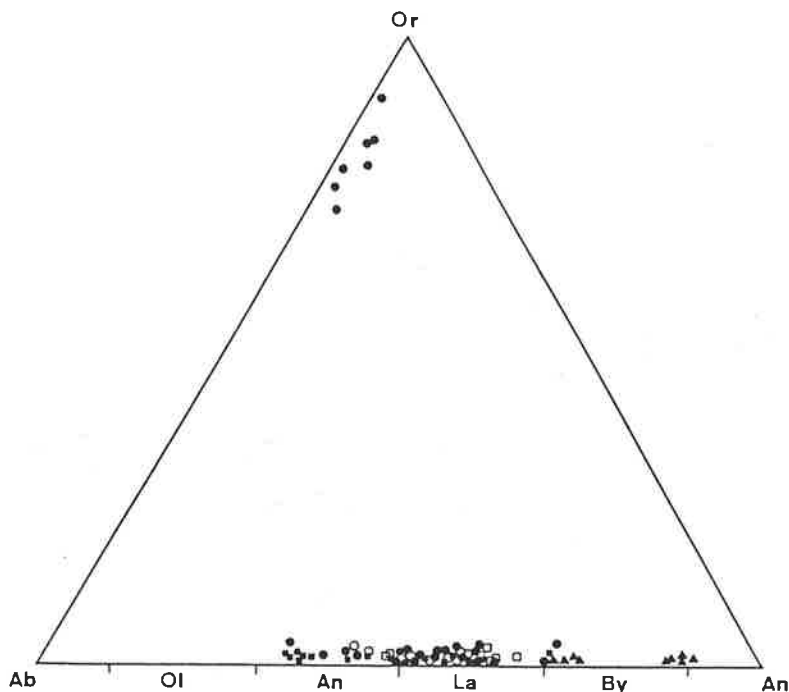


Figure 2.6. Ternary diagram showing the range of feldspar compositions. Symbols: filled circles - gabbronorites, filled triangles - peridotites and troctolites, open squares - norites, filled squares - pyroxene monzonites, potassic gabbronorites and anorthosites, open circles - olivine gabbros.

Normal zoning is common though complex and oscillatory zoning also occurs. Sodic adcumulus overgrowths are common particularly in the anorthosites.

Occasional calcic rims provide further evidence for influxes of more primitive magma into the chambers. In many cases plagioclase is non-zoned but highly corroded indicating resorption. This could be due to a fractionation-induced increase in $p\text{H}_2\text{O}$ depressing the solidus or alternatively could result if a plagioclase laden plume intersected a zone of hotter, convecting magma.

Alkali feldspar is restricted to the border zone pyroxene monzonites, anorthosites and potassic gabbro-norites where it occurs as late interstitial material comprising up to 38 modal percent. XRD analysis indicates a high temperature orthoclase-sanidine structure for this material. In thin section and under the microprobe very fine granophyric exsolution can be seen. Compositions range from 5-25% Ab with 0-5% An. For equilibrium feldspar pairs ternary feldspar modelling (Fuhrman and Lindsley, 1988) on a pair from a roof zone potassic gabbro-norite yielded temperatures around 905 °C ($T_{\text{An}} = 900$ °C; $T_{\text{Ab}} = 907$ °C; $T_{\text{Or}} = 907$ °C), whilst those from a pyroxene monzonite gave 823 °C ($T_{\text{An}} = 825$ °C; $T_{\text{Ab}} = 832$ °C; $T_{\text{Or}} = 814$ °C). Similar feldspar compositions from the pyroxene monzonites and anorthosites is consistent with an origin at the same stage of magmatic evolution. The high plagioclase contents of all the gabbros indicates that whole rock analyses will have lower Si/Al ratios than their contemporary liquids.

2.5.2. Pyroxenes

Crystallization of a two pyroxene assemblage is characteristic of tholeiitic magmas and the occurrence of exsolution features is typical of slowly cooled, continental tholeiitic intrusions. Pyroxene at Black Hill has crystallized later than both olivine and plagioclase and generally appears non-cumulate except in the norites where orthopyroxene is cumulus and preceded plagioclase crystallization.

In the Black Hill gabbros both the calcium-poor and calcium-rich pyroxenes show a continuous iron enrichment trend. Little or no compositional zoning was found in the pyroxenes though overgrowths as previously discussed are quite common. The troctolites, peridotites, norites and olivine gabbros contain bronzite and Mg-rich augite, the gabbro-norites contain hypersthene and augite of intermediate magnesian compositions, while the pyroxene monzonites contain a three pyroxene assemblage of ferro-augite, ferro-hypersthene and pigeonite (Fig. 2.8a). The pigeonites (Figs. 2.5g & 2.9a,b) have cores that have exsolved augite in the basal plane (001), frequently in a herringbone relationship around the (100) twin plane. The remaining less calcic pigeonite is sometimes preserved but more frequently inverted to orthopyroxene. These cores are usually overgrown by augite containing fine lamellae exsolution of pigeonite (001) and occasionally orthopyroxene lamellae (100).

Table 2.3. Representative pyroxene analyses (atomic proportions calculated for 6 oxygens per formula unit)

sample #	876-BHG1	876-BHN	876-BHN	876-7-510	876-7-510	876-19-1084	876-6-377	876-4-879	876-4-711	876-4-711	876-4-807	876-4-807
lithology	K-gabbro	K-gabbro	K-gabbro	Gabbro	Gabbro	Gabbro	Gabbro	Anorthosite	Px-monzonite	Px-monzonite	Px-monzonite	Px-monzonite
SiO2	51.39	53.43	52.22	54.81	54.91	54.76	53.84	53.16	53.32	51.10	52.05	52.27
TiO2	0.37	0.26	0.70	0.16		0.29	0.16	0.40	0.17	0.20	0.18	0.14
Al2O3	1.85	1.18	2.34	1.34	1.47	1.89	0.96	1.69	0.91	0.77	0.65	0.64
FeO*	17.18	24.88	13.10	6.68	14.64	16.52	9.04	14.62	16.47	30.38	28.94	28.66
MnO	0.30	0.49	0.23		0.12	0.40	0.25	0.40	0.32	0.91	0.69	0.62
MgO	13.87	19.97	14.08	15.30	26.79	25.99	14.33	11.88	10.55	12.82	14.65	14.35
CaO	14.61	1.84	18.56	23.17	1.75	1.86	21.91	17.32	20.32	4.89	4.76	5.22
Na2O	0.4		0.37	0.55			0.42	0.35	0.4	0.37	0.29	0.2
Total	99.98	102.06	101.72	102.20	99.68	101.71	100.92	100.10	102.46	101.53	102.26	102.10
Si	1.9522	1.9753	1.9324	1.9786	1.9778	1.9535	1.9860	2.0044	1.9941	1.9813	1.9826	1.9900
Ti	0.0104	0.0073	0.0194	0.0043		0.0077	0.0046	0.0113	0.0048	0.0060	0.0052	0.0040
Al	0.0829	0.0513	0.1020	0.0569	0.0625	0.0795	0.0418	0.0751	0.0401	0.0351	0.0290	0.0290
Fe	0.5459	0.7692	0.4054	0.2016	0.4409	0.4928	0.2788	0.4608	0.5150	0.9852	0.9220	0.9100
Mn	0.0097	0.0154	0.0071		0.0037	0.0121	0.0078	0.0127	0.0102	0.0300	0.0224	0.0200
Mg	0.7854	1.1002	0.7766	0.8235	1.4384	1.3822	0.7882	0.6673	0.5879	0.7407	0.8315	0.8200
Ca	0.5947	0.0729	0.7357	0.8962	0.0675	0.0712	0.8661	0.6997	0.8144	0.2031	0.1943	0.2100
Na	0.0295		0.0262	0.0386			0.0303	0.0257	0.0293	0.0276	0.0214	0.0200
sum	4.0107	3.9917	4.0085	4.0052	3.9909	3.9990	4.0036	3.9739	3.9957	4.0154	4.0116	4.0000
Wo	29.5	3.8	36.5	44.9	3.5	3.7	43.4	34.3	40.7	16.1	14.3	13.5
En	42.6	56.6	42.7	44.8	73.8	71.0	42.2	38.8	31.6	36.6	41.3	40.8
Fs	27.9	39.6	20.8	10.2	22.6	25.3	14.4	26.8	27.7	47.3	44.5	45.7
Mg#	59.0	58.9	65.7	80.3	76.5	73.7	73.9	59.2	53.3	42.9	47.4	47.2
sample #	876-4-807	876-4-807	876-2-648	876-2-648	876-11-1081	876-11-1081	876-11-923	876-11-923	876-11-687	876-11-687	876-5-727	876-5-544
lithology	Px-monzonite	Px-monzonite	Ol-gabbro	Ol-gabbro	Ol-gabbro	Ol-gabbro	Norite	Norite	Norite	Norite	Peridotite	Troctolite
SiO2	52.05	51.61	52.86	56.72	55.47	52.70	54.26	52.10	53.32	56.05	57.60	56.28
TiO2	0.40	0.02	0.73	0.35	0.32	0.43	0.20	0.45	0.11			
Al2O3	1.38	0.60	2.70	1.50	1.42	3.17	2.42	3.26	1.01	1.29	0.65	1.29
FeO*	16.35	29.36	7.93	14.39	14.46	7.56	12.48	6.37	21.05	16.19	9.24	13.00
MnO	0.31	0.69		0.34	0.41				0.45	0.20	0.28	0.37
MgO	11.62	13.26	15.64	28.08	27.44	16.70	27.60	16.85	22.39	26.35	32.63	29.71
CaO	19.13	5.61	21.50	1.31	1.45	18.10	1.78	18.10	0.80	1.48	0.18	0.26
Na2O	0.39	0.34	0.37	0.18		0.24		0.19				
Total	101.62	101.49	102.11	102.86	100.95	99.34	99.16	98.04	99.13	101.56	100.58	100.90
Si	1.9609	1.9900	1.9179	1.9744	1.9715	1.9377	1.9487	1.9355	1.9894	1.9906	1.9961	1.9796
Ti	0.0113	0.0100	0.0200	0.0091	0.0087	0.0119	0.0055	0.0125	0.0032			
Al	0.0612	0.0300	0.1156	0.0616	0.0595	0.1375	0.1025	0.1428	0.0445	0.0539	0.0265	0.0535
Fe	0.5151	0.9500	0.2405	0.4188	0.4297	0.2324	0.3749	0.1977	0.6567	0.4807	0.2679	0.3825
Mn	0.0099	0.0200		0.0099	0.0122				0.0144	0.0060	0.0083	0.0110
Mg	0.6523	0.7600	0.8455	1.4571	1.4535	0.9151	1.4772	0.9330	1.2450	1.3950	1.6852	1.5575
Ca	0.7723	0.2300	0.8356	0.0489	0.0550	0.7129	0.0685	0.7206	0.0320	0.0561	0.0066	0.0096
Na	0.0284	0.0300	0.0259	0.0122		0.0173		0.0140				
sum	4.0114	4.0200	4.0119	3.9919	3.9901	3.9773	3.9888	3.9771	3.9852	3.9824	3.9906	3.9937
Wo	38.8	16.4	40.0	2.6	2.9	33.1	3.7	32.9	1.7	2.9	0.3	0.5
En	35.2	37.8	50.9	75.7	75.0	53.4	76.8	55.4	64.4	72.2	86.0	79.9
Fs	26.0	45.8	9.0	21.8	22.2	13.6	19.5	11.7	34.0	24.9	13.7	19.6
Mg#	55.9	45.7	77.9	77.7	77.2	79.7	79.8	82.5	65.5	74.4	86.3	80.3

Representative pyroxene compositions are given in table 2.3. Mg#s range from 86-41 in both the calcium-poor and -rich varieties. Cr shows a hyperbolic decrease from 7000 ppm at Mg# 82 to less than 1000 ppm by Mg# 75 (Fig. 2.7) consistent with a rapid decrease in the Cr concentration of the magma once pyroxene \pm chromian spinel crystallization commenced. Al decreases with Mg# indicating increasing aSiO₂ whilst Mn is anticorrelated with Mg#. Ti and Al are positively correlated and Ca-Tschermakite (CATS) is generally low (0.1-6.0 mole%) corresponding to low pressures of crystallization (Ellis, 1980). TiO₂ is low consistent with a tholeiitic rather than alkali basaltic origin. Ti-Tschermakite is low (<2) and correlated with acmite substitution which is itself low and indicates low pressures. Jadeite component is very low or absent. Interestingly compositions of pyroxenes from the norites are very similar to those from the other gabbros except for a higher CATS component (higher T).

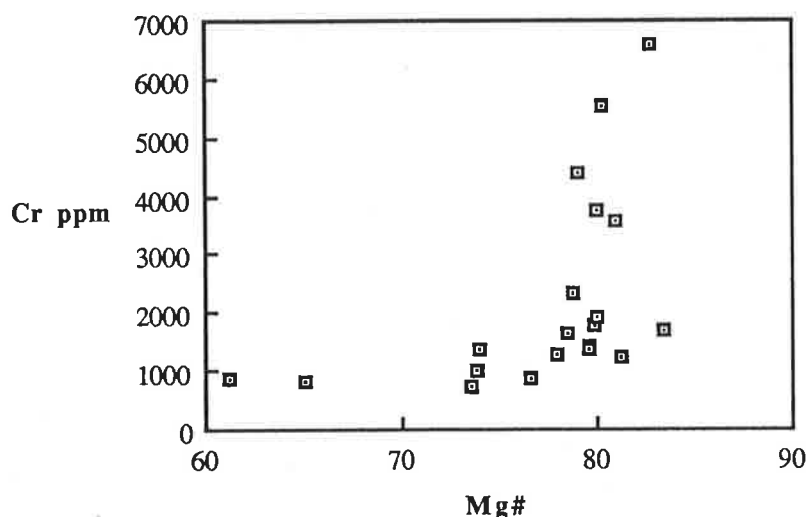


Figure 2.7. Plot of pyroxenes showing a hyperbolic decrease in Cr with decreasing Mg#.

Projecting pyroxene compositions onto Lindsley's (1983) pyroxene quadrilateral for 1 atm. (Fig. 2.8a & b) yields crystallization temperatures decreasing from 1200-1100 °C in the more mafic cumulates to 1050-1000 °C for the gabbro-norites. Area reconstructions for exsolved pigeonite cores from the pyroxene monzonites indicate 1050 °C for initial crystallization, 1000 °C for pigeonite exsolution from cpx, 970-900 °C for cpx exsolution from pigeonite and 700 °C for inversion of pigeonite to opx (Fig. 2.8b). Composition-temperature relationships of Grove and Juster (1989) indicate that a three pyroxene assemblage at 1050 °C will be in equilibrium with a liquid that has a Mg#=30. Subsolidus re-equilibration has resulted in many of the pyroxenes moving down temperature in composition. However the continuous range of pyroxene temperatures in

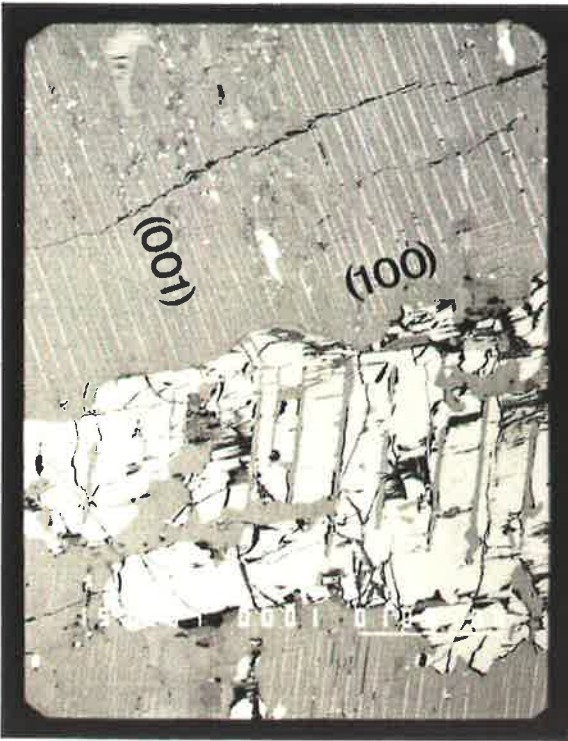
Figures opposite:

Figure 2.9a. Electron microprobe photograph of pigeonite from a pyroxene monzonite (4-807) showing the orientations of the exsolution lamellae and their herringbone relationship to the (100) twin plane. Note the fine lamellae parallel to (100) in the clinopyroxene overgrowth (see text for details). Scale bar is 100 nm.

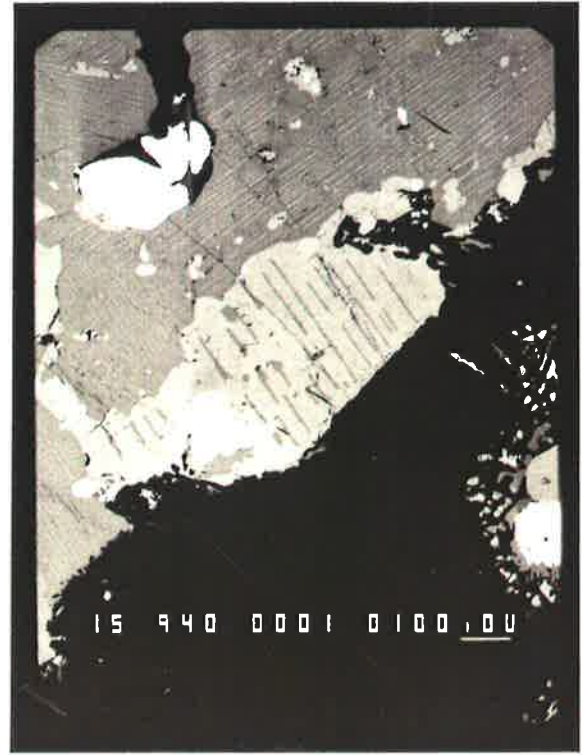
Figure 2.9b. Another electron microprobe photograph of pigeonite from a pyroxene monzonite (4-711) showing similar exsolution relationships to Fig. 2.8a. Scale bar is 100 nm.

Figure 2.9c. Photo of symplectite rim on olivine (ol) from an olivine gabbro (2-648). Plane polarized light, width of view 1 mm.

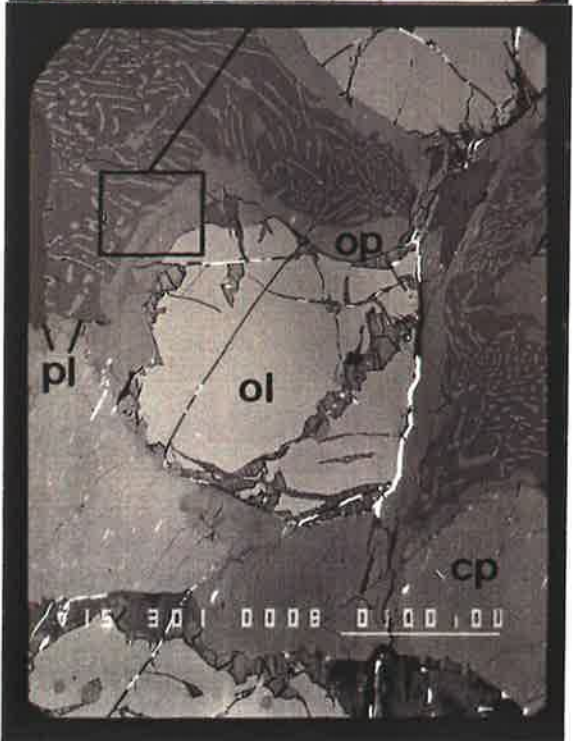
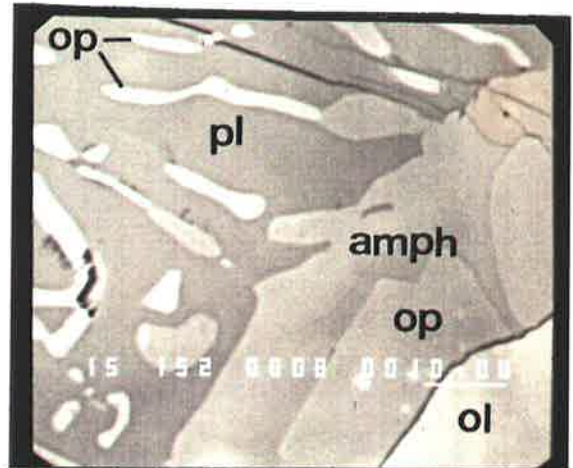
Figure 2.9d. Electron microprobe photographs of symplectite from an olivine gabbro (2-648). Olivine (ol) is rimmed by orthopyroxene (op) and amphibole (amph) which are in turn rimmed by a symplectite of plagioclase containing vermicules of orthopyroxene and occasionally amphibole. Note that the symplectite occurs where olivine is adjacent to plagioclase but not when clinopyroxene (cp) is in contact (see text for discussion). Scale bars are 100 and 10 nm.



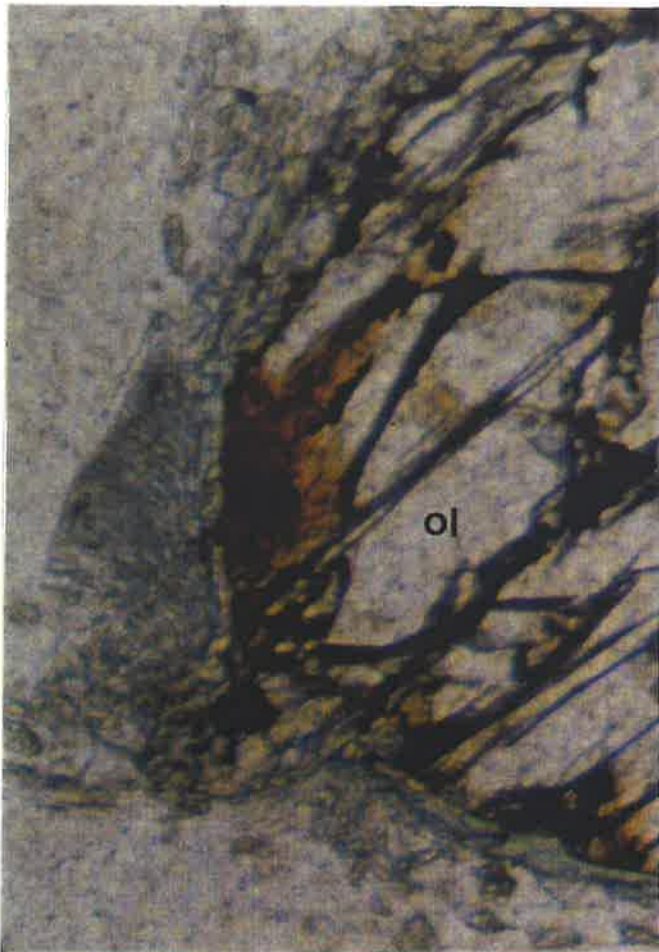
a



b



d



c

most lithologies from >1150 °C down to 900 °C must also, in part, reflect crystallization of pyroxenes over an extended temperature range. It is noteworthy that most of the pyroxenes contain less than 5% non-quadrilateral components. As will be discussed crystallization pressures of 0.5-1 kbar are appropriate for Black Hill however as Lindsley (1983) indicates only a 8.5 degree increase in temperature per kbar the 1 atm diagram is sufficiently accurate.

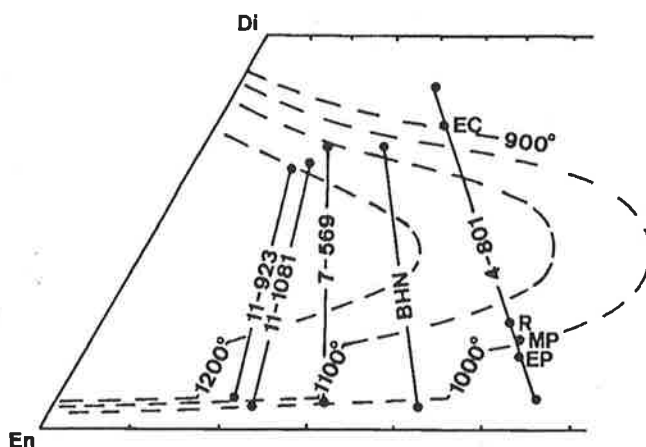
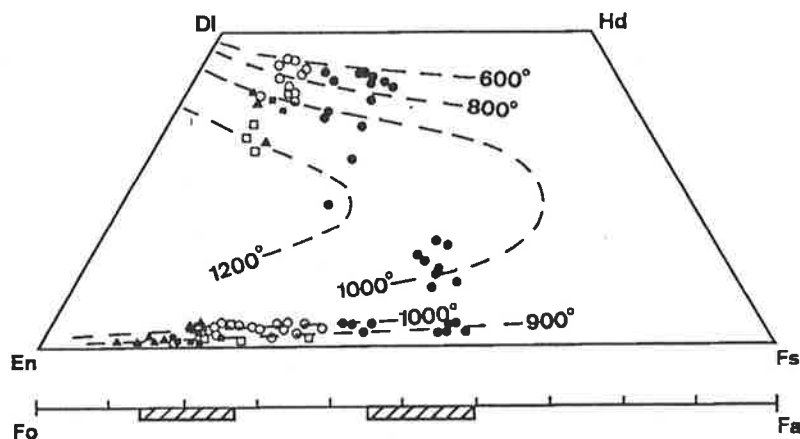


Figure 2.8a. Pyroxene compositions plotted on a quaternary diagram with isotherms from Lindsley (1983). Also shown is the range of olivine compositions and the olivine hiatus. Symbols as for figure 6.

2.8b. Pyroxene pairs and thermometry for a typical norite (11-923), olivine gabbro (11-1081), gabbronorite (7-569), potassic gabbronorite (BHN), and pyroxene monzonite (4-801). For 4-801: R-reconstructed pigeonite, EP-exsolved and uninverted pigeonite, EC-exsolved clinopyroxene, MP-micro exsolved pigeonite from clinopyroxene overgrowth.

2.5.3. Olivines

Olivine is a cumulus phase and the range of compositions is given in table 2.4 and also plotted in figure 2.8a. Olivine occurs in the peridotites (Mg# 86), troctolites (Mg#

Table 2.4. Representative olivine analyses (atomic proportions calculated for 4 oxygens per formula unit)

sample #	876-BHN9	876-BHN9	876-BHN2	876-BHN2	876-BHN	876-5-575	876-5-544	876-5-756	876-11-1081	876-2-648	876-5-727	876-5-727
lithology	K-gabbro	K-gabbro	K-gabbro	K-gabbro	K-gabbro	Troctolite	Troctolite	Troctolite	Ol-gabbro	Ol-gabbro	Peridotite	Peridotite
SiO ₂	34.20	34.47	33.82	34.76	35.67	39.82	38.85	39.12	38.31	39.90	39.72	39.67
Al ₂ O ₃		0.85	0.74	0.64			0.18	0.19	0.11		0.19	0.15
FeO*	47.12	43.03	44.77	40.05	39.33	17.39	20.17	16.48	22.93	21.67	14.06	14.82
MnO	0.69	0.63	0.62	0.50	0.59	0.16	0.31	0.20	0.39	0.24		
MgO	17.44	20.94	19.46	23.98	25.25	43.83	40.01	43.34	38.64	39.63	45.70	44.89
NiO							0.24		0.22		0.23	
Total	100.03	100.13	99.61	100.09	100.84	101.20	99.76	99.34	100.59	101.44	99.90	99.65
Si	1.0148	0.9979	0.9951	0.9910	1.0022	0.9977	1.0026	0.9958	0.9945	1.0153	0.9939	0.9966
Al		0.0290	0.0256	0.0215			0.0056	0.0057	0.0033		0.0057	0.0043
Fe	1.1694	1.0418	1.1017	0.9549	0.9241	0.3643	0.4355	0.3508	0.4977	0.4610	0.2943	0.3114
Mn	0.0173	0.0155	0.0162	0.0121	0.0141	0.0033	0.0067	0.0044	0.0085	0.0053		
Mg	0.0771	0.9034	0.8534	1.0107	1.0574	1.6369	1.5392	1.6445	1.4952	1.5031	1.7047	1.6809
Ni							0.0050		0.0045		0.0046	
sum	2.9728	2.9876	2.9921	2.9902	2.9978	3.0023	2.9946	3.0013	3.0038	2.9847	3.0032	2.9957
Mg#	39.7	46.4	43.6	51.6	53.4	81.8	77.9	82.4	75.0	76.5	85.3	84.4

86-79) and olivine gabbros (Mg# 79-75), is absent in the gabbronorites and norites and reappears in rare samples of the roof zone potassic gabbronorites (Mg# 55-39). The olivines have close to ideal structural compositions with no CaO. Ni decreases from ~2500 ppm at Mg# 85 to below 1000 ppm by Mg# 75 indicating that the magma became increasingly depleted in Ni during olivine fractionation (Fig. 2.10). As in the pyroxenes, no core rim compositional variation was found. This reflects the much quicker equilibration of olivine and pyroxenes (unlike plagioclase) with intercumulus liquids or post cumulus overgrowths.

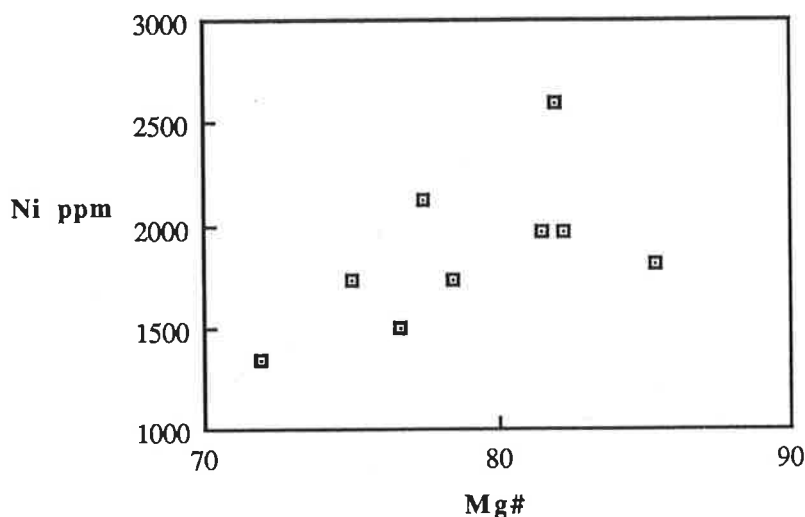


Figure 2.10. Plot showing the depletion of Ni in olivines with decreasing Mg#.

The olivine hiatus, common in layered gabbroic intrusions (Wager and Brown, 1968), places constraints on the crystallization path followed by the liquid in relation to the activity of silica which is shown qualitatively in figure 2.11. Early crystallization of magnesian olivine in the absence of orthopyroxene indicates a low a_{SiO_2} . Fractionation of olivine increased a_{SiO_2} until orthopyroxene joined olivine in the olivine gabbros. Continued fractionation and decreasing Mg# of the liquid resulted in olivine eventually being replaced by orthopyroxene in the gabbronorites and possible in the norites. The transition is a gradual one with textural evidence (e.g. symplectites) suggesting that olivine is reacting with the liquid via the relationship $fa + Sc_2 = 2opx$, and the first appearance of intercumulus quartz in the gabbronorites confirms an increased a_{SiO_2} . Further fractionation and iron enrichment resulted in fayalitic olivine becoming stable with orthopyroxene again (potassic gabbronorites). Following this a pronounced increase in silica activity is indicated by the disappearance of olivine (see Fig. 2.11) in the pyroxene monzonites which also contain considerable free quartz. These rocks contain a three pyroxene assemblage and no olivine despite their high iron contents, indicating that at

least during the late stages of crystallization the Black Hill magmas underwent combined silica and iron enrichment.

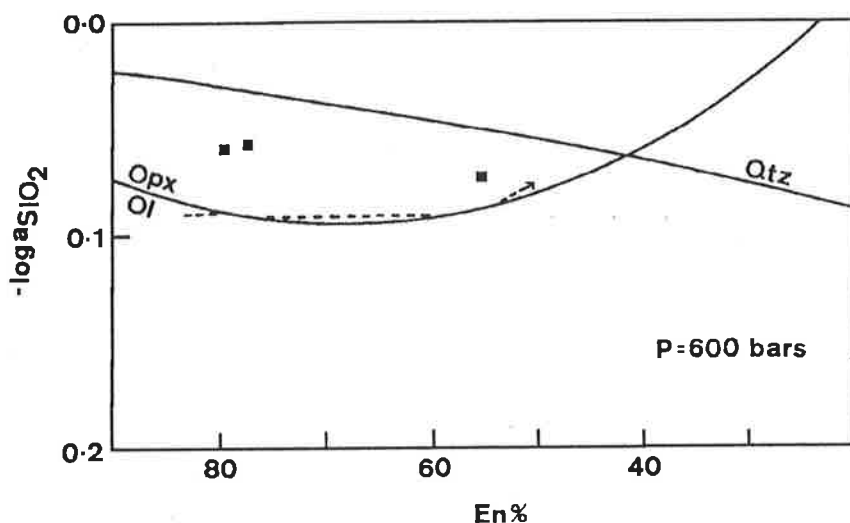


Figure 2.11. Activity of silica against En, for high temperature profile and 600 bars pressure from Campbell and Nolan (1974). Plotted points from Black Hill (see text for details).

Using an average $KD = (X_{\text{Mgl}}/1 - X_{\text{Mgl}})/(X_{\text{Mgol}}/1 - X_{\text{Mgol}}) = 0.32$ (Irvine, 1979) the most magnesian olivines from the peridotites would have been in equilibrium with liquids with $\text{Mg}\# = 63$. This value is quite appropriate for initial tholeiitic magma compositions though the hidden zone likely contains increasingly abundant troctolites and peridotites some of which may contain more magnesian olivines. The unzoned nature of the olivines suggests equilibration with intercumulus liquid which would result in a lowering of their $\text{Mg}\#$'s. Of course many of the rocks, being cumulates, have higher $\text{Mg}\#$'s than their contemporaneous liquids. Using the same relationship and $KD_{\text{Opx}} = 0.28$; $KD_{\text{Cpx}} = 0.23$, the most magnesian orthopyroxenes and clinopyroxenes would have been in equilibrium with liquids with $\text{Mg}\# = 63$ and 59 respectively. The lower value for clinopyroxene could reflect an inappropriate KD or a degree of fractionation occurring prior to the first appearance of clinopyroxene.

2.5.4. Amphibole

Amphiboles are a common phase in most of the gabbros, typically occurring as subsolidus replacement of pyroxene or as postcumulus reaction rims on pyroxene indicating that enough water was present in the magma for this reaction to proceed. Some amphiboles, particularly in the more evolved gabbro-norites appear primary. Microprobe compositions were reprocessed to estimate Fe^{3+} by the method of Spear and Kimball (1986) and this is uniformly low (Table 2.5) though, in the light of the low oxygen fugacity determined for these rocks, this may still be an over estimate. The amphiboles

Table 2.5. Representative amphibole analyses (atomic proportions calculated for 23 oxygens per formula unit)

sample #	876-4-711	876-4-807	876-2-648	876-2-648	876-11-687	876-5-727	876-11-1081	876-11-1081	876-7-510	876-7-510	876-5-575	876-5-575
lithology	Px-monzonite	Px-monzonite	Ol-gabbro	Ol-gabbro	Norite	Peridotite	Ol-gabbro	Ol-gabbro	Gabbronorite	Gabbronorite	Troctolite	Troctolite
SiO ₂	47.04	43.07	43.20	45.25	44.68	44.63	42.15	43.53	50.32	43.19	42.72	44.23
TiO ₂	0.22	1.62	3.76	0.51	2.40	1.42	4.07	3.24	1.21	2.86	0.21	
Al ₂ O ₃	6.61	8.91	11.38	12.13	9.89	12.02	11.74	10.50	5.84	10.73	14.71	13.49
Fe ₂ O ₃	4.70	1.92	0.26	3.12	2.72	3.53	2.15	3.25	3.27	1.37	5.13	4.30
FeO	16.09	19.56	9.39	5.36	9.36	3.18	8.98	9.52	9.06	12.03	3.51	3.60
MnO	0.18	0.23							0.13			
MgO	10.74	8.39	14.69	16.30	13.73	17.28	13.71	13.55	15.90	12.59	16.16	16.73
CaO	11.25	11.67	12.09	12.31	10.79	11.39	10.82	10.57	11.50	11.67	11.81	12.05
Na ₂ O	1.24	1.45	2.23	2.01	1.79	2.29	2.31	2.10	1.02	1.91	2.85	2.65
K ₂ O	0.82	1.51	1.11	0.50	0.63	0.13	0.91	0.71	0.46	0.81	0.21	0.14
Total	98.89	98.33	98.11	97.49	95.99	95.87	96.85	96.97	98.71	97.16	97.30	97.19
Si	6.9890	6.5850	6.2870	6.4850	6.6080	6.4330	6.2160	6.4120	7.1680	6.4130	6.1360	6.3310
Ti	0.0250	0.1860	0.4120	0.0550	0.2670	0.1540	0.4510	0.3590	0.1300	0.3190	0.0230	
Al ^{IV}	1.0110	1.4515	1.7130	1.5150	1.3920	1.5670	1.7840	1.5880	0.8320	1.5870	1.8640	1.6690
Al ^{VI}	0.1470	0.1910	0.2400	0.5350	0.3320	0.4760	0.2570	0.2360	0.1490	0.2910	0.6270	0.6070
Fe ³⁺	0.5260	0.2210	0.0280	0.3370	0.3030	0.3830	0.2390	0.3600	0.3500	0.1530	0.5540	0.4630
Fe ²⁺	1.9990	2.5010	1.1430	0.6420	1.1580	0.3830	1.1080	1.1720	1.0800	1.4940	0.4210	0.4310
Mn	0.0230	0.0300							0.0160			
Mg	2.3780	1.9120	3.1860	3.4820	3.0260	3.7120	3.0130	2.9750	3.3575	2.7860	3.4590	3.5690
Ca	1.7910	1.9120	1.8850	1.8900	1.7100	1.7590	1.7100	1.6680	1.7550	1.8570	1.8180	1.8480
Na	2.3570	0.4300	0.6300	0.5950	0.5130	0.6400	0.6600	0.6000	0.2820	0.5500	0.7940	0.7350
K	0.1550	0.2950	0.2060	0.0910	0.1190	0.0240	0.1710	0.1331	0.0840	0.1530	0.0380	0.0260
sum	15.4010	15.6770	15.7290	15.5910	15.4280	15.5320	15.6090	15.5040	15.2200	15.6040	15.7350	15.6800
Mg#	50.1	41.9	73.3	79.8	68.8	85.0	70.3	67.6	71.8	63.5	80.9	82.4

show a diverse compositional range ($Mg\# = 86-35$) with Al^{IV} and $Na+K$ increasing from actinolite-tremolite to pargasite-hastingsite (Fig. 2.12). This coupled pargasite-

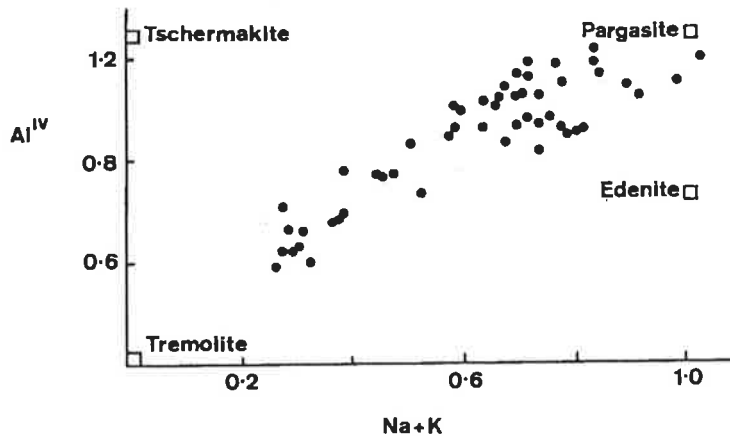


Figure 2.12. Plot of tetrahedral aluminium versus $Na + K$ for Black Hill amphiboles.

tschermakite substitution increases with $Mg\#$ and temperature. The low Al tremolite-actinolite compositions are from subsolidus replacement/hydration of pyroxenes whilst pargasite-hastingsite compositions are likely to be closer to primary magmatic. The presence of magmatic amphibole at the high temperatures and low pressures of intrusion would require that these amphiboles be halogen rich. WDS probe analyses (see appendix A) show amphiboles from a pyroxene monzonite (4-201) contain 1.36% Cl and 0.46% F. Using the most sodic rim compositions of plagioclases (which are likely to be in closest equilibrium with the amphiboles) application of the amphibole-plagioclase

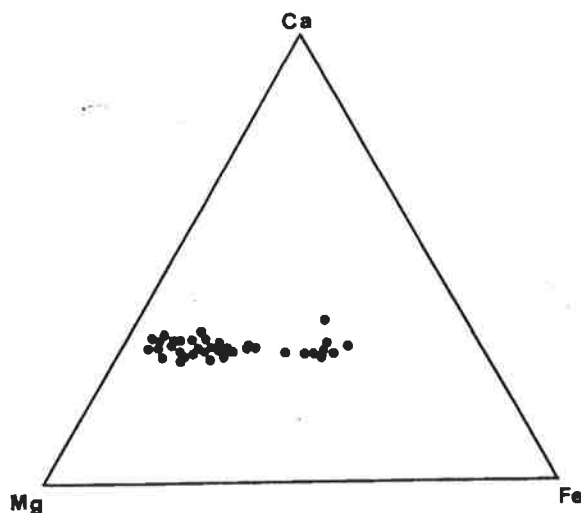


Figure 2.13. Ternary diagram showing the iron enrichment trend of amphibole compositions.

thermometer of Blundy and Holland (1990) gives generally subsolidus temperatures ranging from 900-700 °C (Helz, 1982, places the amphibole-in basalt solidus crossover at 900 °C at 1kbar). At conditions around the solidus fH_2O would be at a maximum, though uralitization of pyroxenes may have also been aided by incursion of ground water at this stage. Titanium and aluminium are positively correlated and Ti contents reach quite high values (4%). Ti and Fe^{3+} increase with tetrahedral Al.

According to the classification of Leake (1978) amphiboles in the gabbronorites have actinolite to Mg-hornblende compositions whilst those in the pyroxene monzonites are ferro-edenite and characterized by low Mg#s. The remaining lithologies contain amphiboles with compositions that range from edenitic-hornblende to pargasite/Mg-hastingsite. Amphibole compositions therefore follow an iron enrichment trend compatible with that shown by the other ferromagnesian phases (Fig. 2.13).

2.5.5. Biotite

Biotite occurs as a non-cumulus phase in minor amounts in most of the gabbros where it is usually of subsolidus origin. However in the more evolved pyroxene monzonites and potassic gabbronorites it is present in considerable quantities and clearly magmatic. These rocks have not, however, developed any amounts of primary hornblende and the preferential stability of biotite reflects the high K_2O contents by this stage of fractionation (& assimilation).

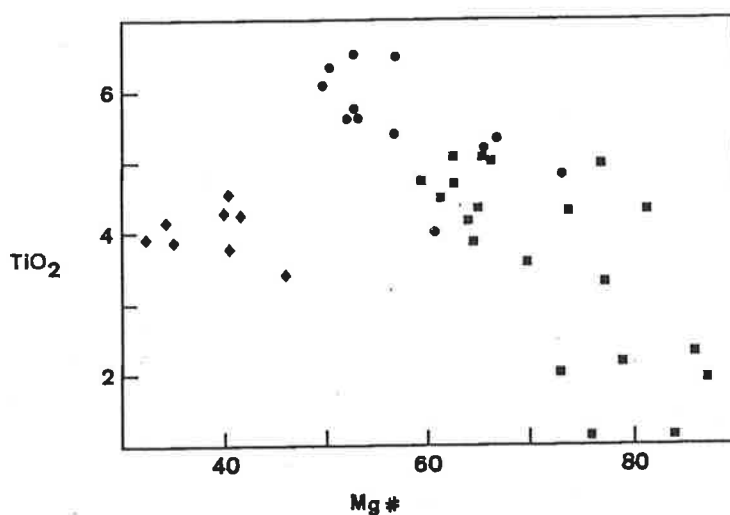


Figure 2.14. TiO_2 vs $Mg\#$ for biotites showing titanium enrichment trend. Note the lower concentration in biotites from the pyroxene monzonites. Filled circles - potassic gabbronorites, filled diamonds - pyroxene monzonites, filled squares - remaining gabbros.

Compositions (Table 2.6) are phlogopite rich and decreasing $Mg\#$, ranging from 90 to 35, corresponds to an increase in annite activity from 0.01 in the olivine gabbros to 0.2 in the pyroxene monzonites. Silica is inversely correlated with whole rock SiO_2

Table 2.6. Representative biotite analyses (atomic proportions calculated for 22 oxygens per formula unit)

sample #	876-BHG1	876-BHG1	876-BHN	876-7-510	876-7-510	876-6-377	876-6-377	876-4-879	876-4-711	876-4-807	876-2-648	876-2-648
lithology	K-gabbronorite	K-gabbronorite	K-gabbronorite	Gabbronorite	Gabbronorite	Gabbronorite	Gabbronorite	Anorthosite	Px-monzonite	Px-monzonite	Ol-gabbro	Ol-gabbro
SiO ₂	36.32	36.02	37.30	36.77	37.27	36.49	36.84	35.42	36.80	36.37	38.90	38.03
TiO ₂	5.64	6.51	5.33	5.05	5.03	4.46	4.69	4.16	3.78	4.56	3.27	4.30
Al ₂ O ₃	14.01	14.02	14.71	13.45	13.88	13.58	13.62	13.20	12.83	12.77	14.72	14.49
FeO*	17.90	17.76	13.58	13.46	13.65	15.92	15.31	24.96	23.99	23.53	9.98	10.96
MgO	11.28	11.01	15.21	14.12	14.75	14.05	14.23	7.28	9.14	8.90	18.66	17.14
Na ₂ O		0.46		0.32	0.44	0.17	0.19	0.19	0.27	0.13	0.46	0.63
K ₂ O	9.81	9.97	10.15	9.28	9.50	9.79	9.77	9.45	9.46	9.76	8.56	8.64
Cl	0.17	0.30	0.21	0.09	0.12	0.12	0.10	0.86	0.59	0.63		
Total	95.29	96.19	96.48	92.54	94.65	94.58	94.89	95.50	96.86	96.66	94.53	94.19
Si	5.5438	5.4703	5.5031	5.6388	5.5955	5.5608	5.5742	5.6316	5.7030	5.6557	5.6751	5.6171
Ti	0.6478	0.7433	0.5914	0.5824	0.5682	0.5114	0.5338	0.4976	0.4401	0.5327	0.3583	0.4771
Al ^{IV}	2.4562	2.5099	2.4969	2.3612	2.4045	2.4393	2.4258	2.3684	2.2970	2.3409	2.3249	2.3829
Al ^{VI}	0.0648	0.0175	0.0602	0.0698	0.0514		0.0032	0.1052	0.0468		0.2061	0.1390
Fe	2.2854	2.2559	1.6754	1.7260	1.7134	2.0290	1.9376	3.3190	3.1096	3.0597	1.2180	1.3531
Mg	2.5670	2.4927	3.3450	3.2287	3.3013	3.1913	3.2092	1.7246	2.1121	2.0636	4.0578	3.7715
Na		0.1347		0.0961	0.1294	0.0492	0.0550	0.0584	0.0814	0.0406	0.1289	0.1812
K ₂ O	1.9099	1.9314	1.9105	1.8416	1.8186	1.9032	1.8856	1.9165	1.8708	1.9360	1.5925	1.6267
Cl	0.0435	0.0763	0.0526	0.0228	0.0297	0.0309	0.0264	0.2311	0.1539	0.1666		
sum	15.5370	15.6319	15.6346	15.5421	15.6119	15.7151	15.6663	15.8523	15.8147	15.7958	15.5616	15.5486
Mg#	52.9	52.5	66.6	65.2	65.8	61.1	62.4	34.2	40.4	40.3	76.9	73.6

whilst the most magnesian biotites from the mafic cumulates are Na-rich and K-poor reflecting primary melt compositions. The majority of biotites show a regular trend of evolution to lower Mg# accompanied by increasing TiO₂ except for biotites from the pyroxene monzonites which have lower TiO₂ (Fig. 2.14). Al₂O₃ increases with decreasing AL^{IV}/AL^{VI} to the extent of entering the field of biotites from metasedimentary rocks (Fig. 2.15).

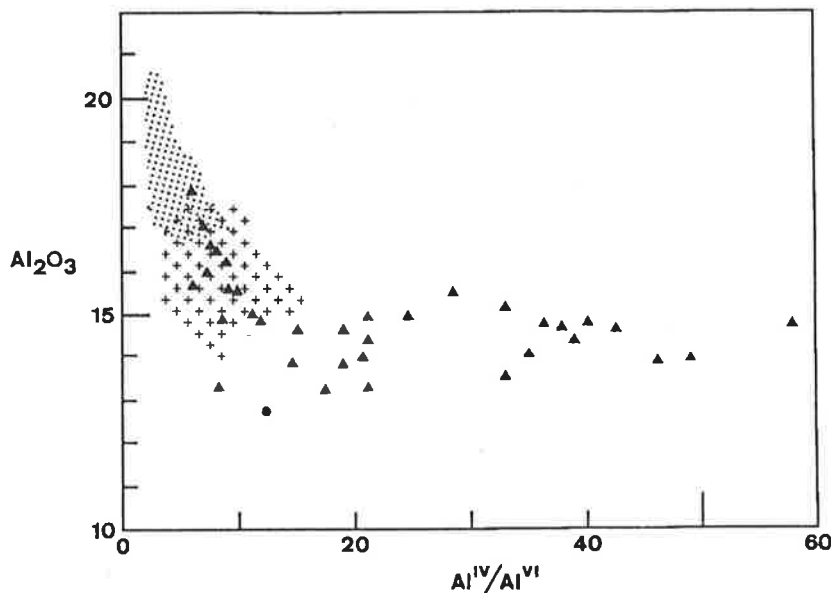


Figure 2.15. Total aluminium against aluminium co-ordination in biotites from Black Hill. Also shown are the fields of biotites from adjacent Kanmantoo metasediments and migmatites (dotted stipple) and from syn-deformational I-type granites nearby (crossed stipple).

The increased biotite content in the evolved rocks, particularly in the roof zone suggests an increased concentration of volatiles through fractionation and or assimilation and their co-existence with clinopyroxene indicates p_{H₂O} of at least several hundred bars (Wones and Gilbert, 1982). These biotites are also enriched in halogens (0.85-1.29% Cl; 0.59-0.70% F; and Fig. 2.16) which in conjunction with the stability of hornblende discussed above indicates that the roof zone magma must have been quite halogen rich. They also have extreme TiO₂ contents (> 0.7 atoms per formula unit). Titanium increases the stability of Mg-biotite; Ti-solubility increases with falling pressure and decreases rapidly with falling temperature (Robert, 1976). Pyroxene thermometry for the roof zone gabbros suggests crystallization temperatures of about 1000 °C. At this temperature phlogopite with a Ti content of 0.7 atoms per formula unit would not be stable at pressures in excess of 1000 bars (Robert, 1976), which constrains the pressures of crystallization to be low. Biotites in the potassic gabbro-norites show a reaction relationship in which they are interfingered with orthopyroxene (Fig. 2.5b). The biotites have magnetite inclusions in their cores indicating the reaction:

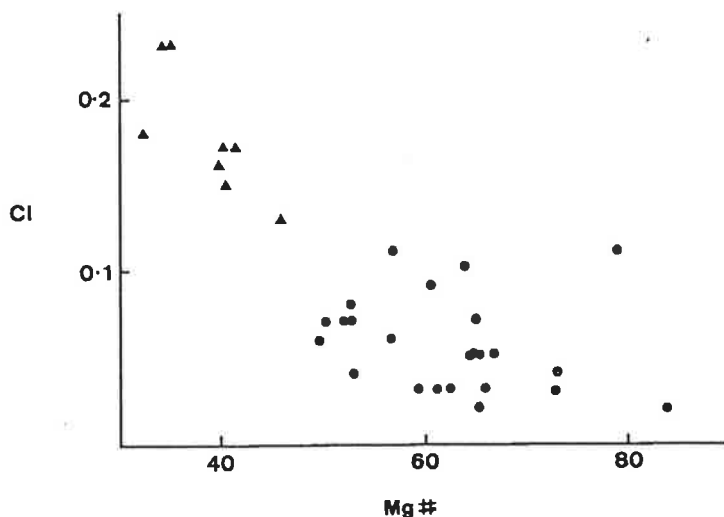
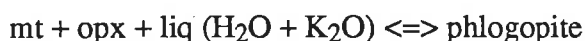
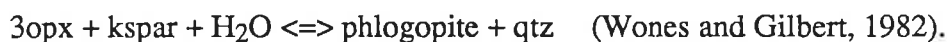


Figure 2.16. Mg# vs Cl in biotites showing the enrichment of halogen contents in the more evolved gabbros, particularly the roof zone gabbros (filled triangles).



and interlocking fingers of biotite and orthopyroxene are separated by quartz suggesting the reaction:



Both these reactions suggest that the increasing amounts of biotite are linked to the development of a hydrous, highly potassic and orthopyroxene rich melt in the roof zone magma. The associated resorption of plagioclase seen in these marginal gabbros may result from the attendant increase in aH₂O depressing the plagioclase liquidus.

2.5.6. Oxides

All lithologies contain oxide phases and representative compositions are given in table 2.7. The peridotites, troctolites and some olivine gabbros contain Mg-spinel, chromium spinel and occasional magnetite with rare ilmenite and hercynite. The gabbro-norites, norites and pyroxene monzonites contain magnetite and ilmenite in roughly equal proportions and by this stage of fractionation iron-enrichment appears to have resulted in magnetite becoming a cumulate phase (total opaques in some gabbro-norites exceeds 5%). In most cases magnetite and ilmenite occur as separate phases.

Ilmenites are Ti-rich and do not appear to have undergone significant subsolidus re-equilibration with X_{Il} remaining relatively constant (0.97-0.99) and correlated with $f\text{O}_2$, whilst magnetites show considerable variation X_{Usp} 0-0.3 indicating subsolidus re-equilibration. Consequently magnetite-ilmenite geothermometry (Buddington and Lindsley, 1964) yields non-magmatic, subsolidus closure temperatures of 400-600 °C. The greater consistency of ilmenite compositions indicates less susceptibility to re-

Table 2.7. Representative oxide analyses (atomic proportions calculated for 3 oxygens per formula unit except ilmenite with 2)

sample #	876-BHG1	876-BHG1	876-6-377	876-6-377	876-4-711	876-4-711	876-5-575	876-5-575	876-5-756	876-5-756	876-5-727	876-5-727
lithology	K-gabbronorite	K-gabbronorite	Gabbronorite	Gabbronorite	Px-monzonite	Px-monzonite	Troctolite	Troctolite	Troctolite	Troctolite	Peridotite	Peridotite
SiO ₂		0.10		0.11	0.10							
TiO ₂	0.63	52.02	0.25	52.10	0.46	52.31			1.44	0.19	1.97	0.36
Al ₂ O ₃	0.43	0.21	0.44	0.13	0.54	0.10	62.98	56.08	9.46	33.27	6.40	29.44
Fe ₂ O ₃	66.45	1.96	67.69	1.64	67.79	3.33	5.16	7.12	33.09	10.48	37.59	13.25
FeO	31.90	44.14	29.92	44.02	31.00	44.64	13.60	16.25	30.35	27.26	30.41	24.94
MnO		1.39		1.31		1.05		0.19	0.42	0.43	0.44	0.36
MgO		0.20	0.15	0.38	0.12	0.30	17.71	14.86	1.88	4.70	2.04	7.52
Na ₂ O		0.19	0.29	0.28	0.22	0.17	0.27	0.41	0.18	0.41	0.18	
V ₂ O ₃	0.94		0.55		0.95				0.42	0.21	0.24	
Cr ₂ O ₃	0.25		0.22		0.14			5.45	22.88	21.90	20.51	23.53
P ₂ O ₅				0.17						0.13	0.18	0.13
Total	100.59	100.29	99.51	100.13	101.32	101.90	99.72	100.36	100.12	99.46	100.43	99.78
Si		0.0025		0.0027	0.0039							
Ti	0.0180	0.9806	0.0097	0.9815	0.0131	0.9718			0.0386	0.0045	0.0533	0.0084
Al	0.0193	0.0063	0.0266	0.0037	0.0242	0.0028	1.9131	1.7631	0.3961	1.2221	0.2711	1.0817
Fe ³⁺	1.9085	0.0370	1.9700	0.0309	1.9252	0.0619	0.1001	0.1429	0.8844	0.2457	1.0165	0.3108
Fe ²⁺	1.0183	0.9251	0.9678	0.9223	0.9782	0.9222	0.2930	0.3625	0.9015	0.7105	0.9141	0.6503
Mn		0.0295		0.0278		0.0220		0.0043	0.0125	0.0113	0.0135	0.0096
Mg		0.0076	0.0111	0.0141	0.0068	0.0110	0.6803	0.5910	0.0996	0.2182	0.1093	0.3497
Na		0.0093	0.0283	0.0135	0.0161	0.0082	0.0135	0.0213	0.0126	0.0246	0.0123	
V	0.0287		0.0226		0.0288				0.0120	0.0052	0.0070	0.5800
Cr	0.0074		0.0087		0.0041			0.1150	0.6426	0.5396	0.5827	0.5800
P				0.0035						0.0034	0.0053	0.0034
sum	3.0002	2.0000	3.0000	2.0000	3.0002	2.0000	3.0000	3.0000	3.0001	3.0000	3.0001	3.0000
Xil		0.99		0.99		0.98						
Xusp	0.02		0.01		0.02							
Cr#								6.10	61.90	30.60	68.20	34.90
Mg#							69.90	62.00	6.10	19.79	6.25	28.62

equilibration and the intersect of X_{il} with pyroxene temperatures indicates oxygen fugacities around 10^{-11} to 10^{-13} for the olivine gabbros and pyroxene monzonites.

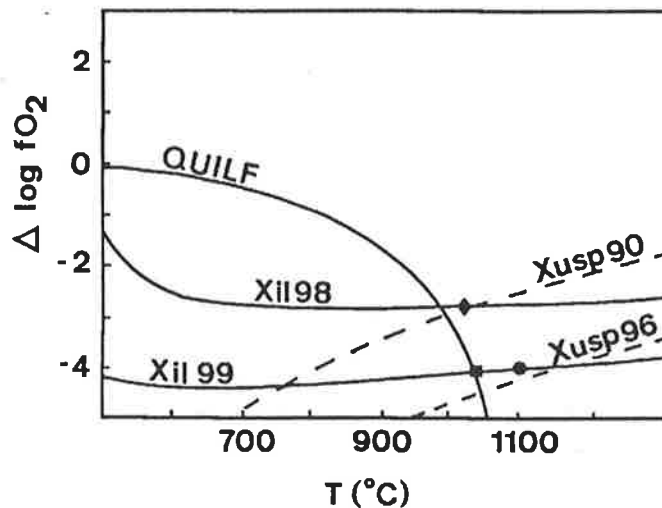


Figure 2.17. Oxygen fugacity vs temperature diagram from Frost *et al.* (1988) with the intersections of ilmenite compositions with pyroxene temperatures for the more evolved gabbros from Black Hill constraining fO_2 .

The assemblage quartz-magnetite-ilmenite-fayalitic olivine (QUILF) which occurs in some of the roof zone potassic gabbronorites and can also be used to constrain crystallization conditions. Using the equilibrium relationship defined by Frost *et al.*, (1988) the intersection of $X_{il}=0.98$ with their QUILF curve corresponds to around 1050 °C (Fig. 2.17) which is in rough agreement with the pyroxene thermometry for this rock and independently confirms the hypothesis that the ilmenites have not undergone substantial re-equilibration. From this intersection the pre-re-equilibration magnetite compositions can be predicted ($X_{usp}=0.90-0.95$) and the oxygen fugacity constrained to a range from $\log fO_2 = -10$ to -12 . Due to the shape of the QUILF curve in this part of the diagram addition of a Mg component to the olivine (actual Black Hill olivines are Fa_{60}) will increase the temperature but have little effect on fO_2 . The oxygen fugacity for the potassic gabbronorites therefore lies close to the QFM buffer.

Including the more magnesian rocks Al_2O_3 shows a negative hyperbolic correlation with total iron (Fig. 2.18) with the most mafic cumulates containing Al-rich Mg-spinel and the evolved gabbros bearing magnetite and ilmenite. A gap in iron composition on this plot occurs between the disappearance of spinel and the maximum Al incorporation in magnetite. Spinel ceases to crystallize when clinopyroxene appears on the liquidus and this spinel gap is predicted by phase relations (Hill and Roeder, 1974) correlating to a period of iron enrichment which is characteristic of tholeiitic magmas. The phase equilibria determined by Hill and Roeder (1974) shows that at low oxygen fugacity

($\log fO_2 < -10$) spinel ceases to crystallize at around 1160 °C when plagioclase and pyroxene join olivine on the liquidus but reappears as magnetite at around 1110 °C.

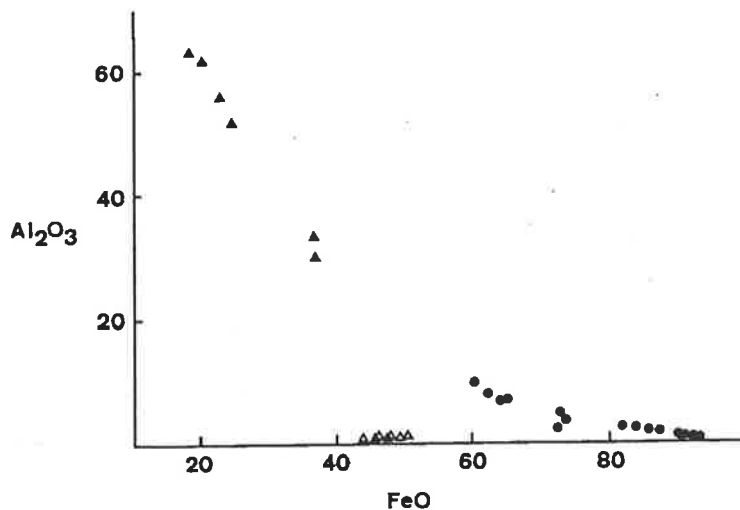


Figure 2.18. Al versus total iron as FeO for spinels from Black Hill showing spinel compositional gap. Filled triangles - spinels from troctolites and peridotites, filled circles and open triangles - magnetites and ilmenites from remaining gabbros.

Chrome spinels occur in the peridotites and in some troctolites showing a wide range of Cr# inversely correlated with Mg#. Chrome spinel compositions tend to be strongly correlated with magma chemistry and as such spinels in near isothermal

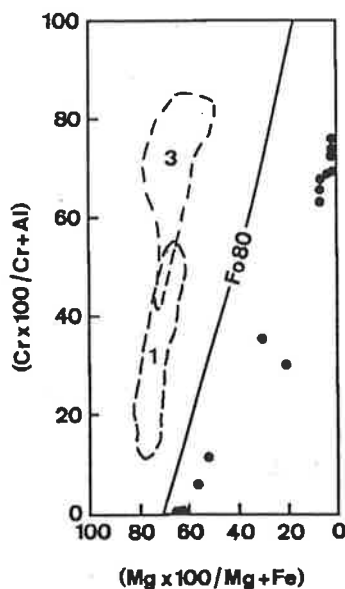


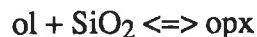
Figure 2.19. Cr# vs Mg# for chromian spinels from peridotites and troctolites. Fields and Fo80 equilibration line from Dick and Bullen (1984), see text for details.

equilibrium with olivine from the peridotites (F_{80}) at 1800 °C would plot along the F_{80} line in figure 2.19. The Black Hill spinels show a coherent trend parallel to this line but with a systematic displacement to the right (lower Mg#) reflecting down temperature re-equilibration in the presence of excess olivine as suggested by Dick and Bullen (1984). The spinels show a compositional range typical of the type II spinels of Dick and Bullen (1984), which they interpret as reflecting a mixture of a depleted, MORB-like source (type I) with an enriched, hydrous island arc type source (type III).

2.5.7. Olivine-plagioclase symplectites

In most of the olivine bearing rocks orthopyroxene forms thin rims to the olivine where it is adjacent to plagioclase. However, in some of the more hydrous (biotite and hornblende rich) olivine gabbros and troctolites, coronitic symplectites rim olivines in contact with plagioclase (Figs. 2.5n & 2.9c,d; compositions in table 2.8). The coronas are cored by olivine which is enclosed in a shell of opx. This is in turn rimmed by amphibole which is itself surrounded by a radial, vermicular symplectite of anorthite which contains elongate vermicules of opx and minor amphibole. The symplectites restricted to boundaries with plagioclase and are not developed at olivine-augite boundaries, they do, however occur projecting into plagioclases included in olivine. Thus olivine and plagioclase are essential components for the development of these symplectites which indicate instability of olivine.

The initial orthopyroxene corona is observed in the troctolites and results from the reaction:



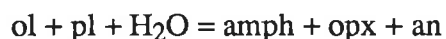
This may occur above the solidus in the presence of more siliceous (fractionated magma). The next corona of amphibole must be related to $a\text{H}_2\text{O}$ and possibly $a\text{Al}_2\text{O}_3$; the tschermakite component of the orthopyroxene strongly increases with distance from olivine. The following change from coronitic to vermicular textures presumably indicates a distance beyond which diffusion became partially restricted. The vermicular part of the symplectites have a radial nature with a diameter up to 150-200 μm in diameter which must represent an upper limit to diffusion under the prevailing conditions. Textural evidence, in which the symplectites impinge on, or grow into plagioclase grains suggests a subsolidus origin (Fig. 2.9d) consistent with the evidence for restricted diffusion distances. Likewise the absence of symplectite at olivine-clinopyroxene boundaries suggests that they grew subsolidus after olivine-plagioclase and olivine-clinopyroxene boundaries had been determined. Local compositional disequilibrium occurs at these boundaries between the anorthitic plagioclase (An_{86}) of the symplectite and the plagioclase it impinges upon which is labradorite (An_{70-63}) typical of these olivine gabbros. These two plagioclases are not in optical continuity.

Table 2.8.

Analyses of symplectite components

analysis #	0.1	0.4	4	1	2	3	0.2	0.3
phase	olivine	plagioclase	opx corona	amph corona (i)	amph corona (e)	opx symp lam	amph symp lam	plag in symp
rel. volume (g)			0.2733	0.3248	0.3248	0.2344	0.0637	1.1949
SiO ₂	38.58	53.21	56.07	45.50	43.59	56.50	45.40	45.87
TiO ₂				0.58	0.34		0.24	
Al ₂ O ₃		31.21	0.89	10.99	15.54	4.60	21.48	35.47
FeO*	24.14	0.38	14.49	8.32	7.68	14.92	5.77	0.27
MnO	0.24		0.37			0.18		
MgO	37.70	0.24	28.00	17.23	14.56	25.50	10.08	0.12
CaO		13.27	0.24	11.86	12.50	1.44	14.81	18.12
Na ₂ O		4.31		1.90	2.22	0.19	1.56	1.56
K ₂ O		0.07		0.31	0.37		0.25	0.10
Total	102.48	102.68	100.06	96.69	96.84	103.32	99.60	101.53
Si	0.9768	9.4225	2.0008	6.5950	6.3029	1.9541	6.2708	8.3473
Ti				0.0631	0.0365		0.0252	
Al		6.5134	0.0375	1.8772	2.6481	0.1874	3.4957	7.6058
Fe	0.5110	0.0563	0.4325	1.0085	0.9284	0.4314	0.6667	0.0418
Mn	0.0051		0.0112			0.0053		0.0330
Mg	1.4224	0.0631	1.4893	3.7214	3.1390	1.3143	2.0748	0.0330
Ca		2.5175	0.0092	1.8421	1.9358	0.0533	2.1920	3.5336
Na		1.4796		0.5349	0.6226	0.0129	0.4172	0.5519
K		0.0162		0.0566	0.0690		0.0441	0.0238
sum	2.9477	20.0685	3.9804	15.6989	15.6943	3.9586	15.1865	20.1372

A generalized reaction for the symplectites can be written:



The critical factor must be $a\text{H}_2\text{O}$ ($\pm a\text{Al}_2\text{O}_3$) which results in the stabilization of amphibole. Na, Ca and Al must be extracted from plagioclase to produce amphibole from olivine whilst Si is likewise used in the formation of orthopyroxene. The net effect appears to be a residual host plagioclase which is more Ca and Al rich than the reactant one. The relative volume of each reaction product component in this reaction has been calculated by integrating the area of each phase in a probe photograph. Mass balance calculations can then be made by multiplying the abundance of each component in each product phase by the relative volume for each phase. The results show that the products can be accounted for by reacting equal proportions of the reactants giving the stoichiometry:



This indicates that the symplectites have formed under closed system conditions (with the exception of water).

Although olivine-plagioclase symplectites are common, most reported in the literature (see Nishiyama, 1983 for review) have evidently formed at high pressures with garnet and or spinel with cpx as typical reaction products. Furthermore many apparently have a metamorphic origin which is not tenable at Black Hill. The Black Hill gabbros have similar whole rock compositions to many of these examples however pressures were lower. The following estimates of symplectite formation conditions should be treated with suspicion yet do nonetheless seem reasonable given their agreement with conditions determined for the plutons as a whole. Temperature from amphibole-plagioclase thermometry (Blundy and Holland, 1990): 980 °C. Pressure from CATS geobarometer (Ellis, 1980): 0.5-0.8 kbars. Activity of silica from ol-opx equilibria: $-\log a\text{SiO}_2 = 0.13-0.16$.

2.6. Discussion of crystallization conditions

The foregoing discussion shows that crystallization temperatures are well documented by pyroxene thermometry to range from 1100-1250 °C for the olivine gabbros and cumulates and ~1000 °C for the more evolved rocks. Quantitative estimates of pressure are harder to make even though the crystallization sequence is characteristic of low pressures. By spatial association with high level granites and rhyolites at the same structural level (chapter 4) pressures can be presumed to be low. The occurrence of granophyric intergrowths and high-Ti biotite in the more evolved monzonites also indicates low pressures.

In order to try and more quantitatively constrain pressure the program "THERMOCALC" devised by Powell and Holland (1988) was run for one of the pyroxene monzonites whose mineral assemblage allows some calculations to be made. The results are listed in table 2.8 indicating pressures around 500 bars (equivalent to 2km depth) though the error range is large. In summary pressures are likely to be no greater than 1 kbar, at which the basalt solidus occurs around 900 °C.

Given the approximate pressure the solubility of water in the magmas is low. The experiments of Burnham (1975), show that basalt at 1100 °C cannot contain more than 1.9 wt% dissolved H₂O at 500 bars and no more than 3% at 1kbar. Clearly enough volatiles were present for the stabilization of biotite and amphibole, though the crystallization of plagioclase at temperatures in excess of 1100 °C restricts the total water pressure possible (Tuttle and Bowen, 1958).

Silica activity is qualitatively detailed in figure 2.11 which uses the high temperature gradient of Campbell and Nolan (1974) and a pressure of 600 bars. These conditions seem quite appropriate for Black Hill and produce an olivine gap over the right magnesian interval. A fundamental implication of this diagram is that silica activity remained low with only minor increases until the very late stages of crystallization. It seems most likely that this late change in the rate of increase of a_{SiO_2} reflects the onset of magnetite fractionation (possibly enhanced by assimilation) driving the liquid towards rapid silica enrichment. As an attempt at quantitative estimates, a_{SiO_2} was calculated for several Black Hill gabbros using olivine-orthopyroxene equilibria. As can be seen these points lie above the curves of Campbell and Nolan (1974) indicating either lower pressures or higher temperatures or both.

The low oxygen fugacities determined are in accordance with those found for other layered gabbroic intrusives. This is also consistent with the ubiquitous presence of sulphides and the spinel compositional gap. In the later stages of fractionation the assemblage fa-qtz-opx-mt buffered oxygen fugacities to near QFM.

The late stage subsolidus evolution of the Black Hill plutons involved the growth of symplectites between olivine and plagioclase and some development of amphibole and biotite. In particular the formation of the coarse zones and late actinolite veins may be related to inward collapse of a hydrothermal system set up around the cooling magma body.

2.7. Conclusions and the problematic lithologies

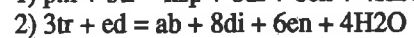
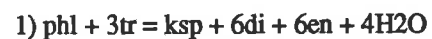
The available mineralogical and textural data demonstrates that the Black Hill gabbros formed from a continental tholeiitic magma undergoing slow crystallization at low pressures. Layering developed primarily as a result of in situ crystallization though

Table 2.9. Pressure estimates using "THERMOCALC" (Powell and Holland, 1988)

Sample 876-4-807

Temperature = 1050 C Activity quartz = 1, Activity of H2O = 1

reactions:



Pressure estimates (kbar):

Temp	1050	1075	1100	1125	1150	1175
ave. P	-	-	0.50	0.60	0.70	0.90
std. dev.	-	0.43	0.56	0.70	0.86	1.03

convective processes were operative, at least in the early stages, producing scour and trough structures. A marked compositional break between the roof/border zone gabbros and the layered cumulates beneath may indicate a separate, upper convective cell in which assimilation was most marked.

The ferromagnesian minerals show an evolution involving decreasing Mg# paralleled by feldspar evolution recording calcium depletion. The peridotites indicate early olivine crystallization. This was soon joined by plagioclase with the liquid evolving along the olivine-plagioclase cotectic producing the voluminous olivine plagioclase cumulates intersected in drill core. From the modal analyses intercumulus material typically constitutes around 10-20% in the olivine gabbros and troctolites though some troctolites may contain as little as 2%. Pyroxene may have joined the cumulus assemblage later but for the most part appears to be post-cumulus. As soon as plagioclase joined olivine the liquid must have embarked upon a trend of iron enrichment accompanied by minor silica enrichment. Low oxygen fugacity delayed magnetite fractionation further aiding this iron enrichment. In the late stages (gabbronorites) magnetite fractionation caused the liquid to undergo iron depletion and the sudden increase in modal quartz in these differentiated rocks indicates that this was accompanied by rapid silica enrichment. Silica enrichment resulted in olivine being replaced by orthopyroxene in rocks with Mg# <75. At high iron contents (Mg#60) fayalitic olivine reappeared but with increasing SiO₂ at the lowest Mg#'s and around 1050 °C this was replaced by pigeonite to form a three pyroxene assemblage. The olivine gap and the earliest pigeonites at Black Hill have the same Mg#'s as those from the Bushveld and Kiglapait intrusions. Skaergaard however has the olivine hiatus at lower (ol) Mg#'s and the first pigeonites are more magnesian. Incompatible elements were concentrated throughout fractionation and the most evolved gabbros contain free quartz, abundant alkali feldspar and rare zircon.

The norites as mentioned represent a significant change in crystallization order, nucleation rate and mode. A perturbation in silica activity, perhaps due to interaction with more fractionated magma or due to assimilation, would result in displacement of the magma into the opx field (see Fig. 2.11). One possible explanation for these rocks is that they were initiated by fresh injections of primary magma into the chamber. If the residual magma in the chamber is cooler the injected magma may become supercooled effecting rapid nucleation. Additionally the resident magma is likely to be more fractionated and SiO₂-rich than the fresh influx. Rapid and turbulent mixing, likely on injection of a hot magma into a colder one, would result in an increased SiO₂ and silica activity in the injected magma which as described above would result in orthopyroxene precipitation. The effect of cooling on the injected magma is to lower the aSiO₂ of the opx/ol curve above En₅₀ in figure 2.11 (Campbell and Nolan, 1974) which will also promote opx crystallization. Cyclical occurrences of norite horizons, as in the Cambrai Pluton, may

indicate repetition of such a process as influxes of silica-rich liquid cause opx crystallization which itself returns the magma to its original crystallization path. The fact that the norites appear to be restricted to the Cambrai Pluton may reflect a coincidence of recharge events with the stage of evolution of the resident magma that did not occur in the Black Hill Pluton which is considerably larger and may have evolved more slowly. The occurrence of greatly increased proportions of sulphides in the norites may reflect saturation effected by mixing and has interesting implications for platinoid mineralization. A major sulphide rich horizon occurring at the base of a norite layer in the Cambrai Pluton contains 135ppb Pd and 45ppb Pt, and according to Keays *et al.*, (1990) the zones just beneath these would be likely locations for Merensky Reef type mineralization. Recharge mechanisms have been invoked by Campbell *et al.*, (1983) to explain the platinum horizons in the Bushveld complex.

Finally there is no observable gradation, through intermediate rocks, from the most evolved gabbro-norites and monzonites to the granophyres. This favours their evolution by some other process such as immiscibility or liquid fractionation processes at areas of sidewall crystallization. At such zones of possibly rapid crystallization, highly fractionated, light liquids would be capable of efficient gravitational separation and removal (McBirney *et al.*, 1985). Further interaction with the mafic magma could produce the observed mixing and mingling textures. These possibilities are further considered in the next chapter along with the geochemical and isotopic data.

Chapter 3. Petrogenesis of late-orogenic layered gabbros at Black Hill, South Australia: Part 2. Geochemical and isotopic constraints on fractionation, assimilation and the source

3.1. Introduction

Continental layered gabbroic bodies have been extensively studied for over 60 years because of their potential to elucidate fractionation processes. More recently open system processes such as assimilation and chamber recharge have received increasing attention. Intrusion of basaltic magma to form these layered bodies occurs during active continental rifting (eg Skaergaard), and in late-orogenic (post deformation; eg this study) and non-orogenic settings (eg Bushveld). A fundamental question in the study of these continental tholeiites and their extrusive counterparts, the continental flood basalts, is the nature of the source. Additionally the source of heat for melting to produce late orogenic and non-orogenic magmas, which are not obviously associated with crustal tension, is not well understood (cf. chapter 1). This becomes even more problematic if the magma was derived by melting of predominantly lithospheric mantle and it is therefore important to try and distinguish asthenospheric and lithospheric derived magmas.

In a continental setting it is likely that mafic magmatic rocks can tell us something about the composition of the subcontinental mantle lithosphere which is likely to be an important component in continental tholeiites. Some authors have proposed that it is the principle source region for continental tholeiites (eg Allegre *et al.*, 1981; 1982; Ellam and Cox, 1989). Frequently continental flood basalts and layered gabbroic intrusions show some isotopic and incompatible element enrichment and much debate centres around whether this results from crustal contamination of asthenospheric melts or instead reflects an enriched lithospheric mantle source. Independent evidence from mantle xenoliths (e.g. Menzies, 1983; Hawkesworth, *et al.*, 1983) demonstrates that at least some parts of the continental mantle lithosphere are enriched in incompatible elements and that this enrichment has often existed long enough for the evolution of Sr and Nd isotopes. Therefore it should be possible to distinguish asthenospheric and lithospheric mantle derived magmas though it is also probable that both sources may contribute (e.g. Menzies *et al.*, 1984).

This chapter attempts to constrain the source of the continental tholeiitic Black Hill magma. As chapter 2 has shown these plutons represent the mafic members of a bimodal igneous suite that intruded to high crustal levels just after the end of convergent

deformation in the Cambro-Ordovician Delamerian Orogeny. The exposed and intersected parts of the plutons consist of layered cumulates (olivine + plagioclase \pm pyroxene) and gabbronorites (plagioclase + two pyroxenes) with roof and marginal wall rocks which are composed of much more potassic gabbronorites and pyroxene monzonites. These unusually potassic, biotite-bearing gabbros at the pluton margins are in contact with mid to upper crustal amphibolite grade (quartz-alkali feldspar-biotite-plagioclase) metasediments which suggests the potassium enrichment reflects contamination. The gabbronorites that accompany the cumulates appear to have been more insulated from the effects of contamination. Mineral chemistry and petrographic investigations (chapter 2) suggest that chamber recharge may have been an important process in producing norites in which fine grained bronzite crystallized prior to plagioclase. In light of recent investigations of assimilation and recharge in the Skaergaard Intrusion (Stewart and DePaolo, 1990) and the debate over the late evolution of the Skaergaard liquid (Hunter and Sparks, 1987; McBirney and Naslund, 1990; Morse, 1990; Brooks and Nielsen, 1990; Hunter and Sparks, 1990) this chapter attempts to use geochemical and isotopic data to constrain fractionation, recharge and assimilation at Black Hill.

3.2. Geochemistry

3.2.1. Analytical techniques

Whole rock geochemical analyses were performed on 108 gabbros by conventional XRF methods except for Na₂O which was analysed by atomic absorption. In addition selected samples were chosen for rare earth element (by isotope dilution) and Rb-Sr, Nd-Sm isotope analyses which were performed on a Finnigan Mat 261 solid source thermal ion mass spectrometer. Representative geochemical analyses are presented in table 3.1 and isotope analyses in table 3.2. A more detailed discussion of techniques and errors as well as a complete listing of analyses can be found in appendix A. The hyphenated sample numbers refer to samples taken from drill core, the first number being the drill hole number and the second the depth of the sample (in feet).

3.2.2. Major and trace element geochemistry

The Black Hill gabbros are plagioclase, diopside and either olivine or hypersthene normative. The evolved monzonitic gabbros contain increased normative orthoclase and quartz. Many of the cumulates and some olivine gabbros are slightly nepheline normative however these do not represent liquids. The estimated parental magma compositions (see section 3.3.2.) are olivine normative and typical of continental tholeiitic magmas rather than alkali basalts. In contrast alkali basalts typically follow a different crystallization path to that shown by the Black Hill magmas, in which orthopyroxene and pigeonite are absent

Table 3.1. Representative geochemical analyses for Black hill gabbros

Sample #	876-5-742	876-5-756	876-5-544	876-5-514	876-11-1081	876-7-510	876-19-1278	876-11-941	876-19-635	876-4-926
Rock Type	peridotite	troctollite	troctollite	ol-gabbro	ol-gabbro	gabbro-norite	gabbro-norite	norite	norite	anorthosite
SiO ₂	40.51	43.76	45.49	46.02	49.09	49.91	52.76	54.96	52.28	52.98
TiO ₂	0.43	0.14	0.29	0.41	0.84	0.94	1.07	1.13	0.67	1.08
Al ₂ O ₃	7.29	18.99	22.35	17.47	16.41	16.14	14.91	10.91	15.50	20.51
Fe ₂ O ₃ *	13.33	7.25	6.59	8.22	9.45	10.25	9.13	10.26	7.73	7.34
MnO	0.20	0.11	0.09	0.13	0.15	0.17	0.17	0.18	0.16	0.12
MgO	29.35	15.98	9.84	12.71	10.42	8.40	8.77	10.67	9.25	2.17
CaO	4.38	9.34	10.65	11.57	8.99	9.34	8.73	4.57	10.44	8.46
Na ₂ O	0.93	1.68	2.22	1.80	2.75	2.88	2.57	2.57	2.47	3.22
K ₂ O	0.16	0.06	0.16	0.12	0.53	0.65	0.79	1.29	0.45	3.04
P ₂ O ₅	0.10	0.02	0.04	0.07	0.09	0.14	0.13	0.28	0.08	0.49
LOI	2.84	1.70	1.78	1.00	0.72	0.44	0.85	2.25	0.20	0.12
Total	99.52	99.03	99.50	99.52	99.44	99.26	99.88	99.07	99.23	99.53
Mg#	81.44	81.46	74.85	75.50	68.73	62.03	65.69	67.46	70.46	37.08
Cr	1738	510	11	396	194	136	296	336	280	11
Ni	1176	635	291	347	228	151	163	246	107	12
Sc	12.5	8.1	7.3	21	24	29	34	28	40	15.8
V	80	25	41	67	145	163	176	108	148	108
Pb	4	nd	2	1	1	3	2	6	2	16
Rb	5.9	1.8	4.6	1.7	17.3	19.9	30	59	14.7	182
Sr	90	288	411	311	273	337	253	202	266	676
Ba	26	23	49	49	104	169	153	194	105	558
Ga	6	11	15	14	15	17	18	16	16	23
Nb	2.9	0.5	1.8	2.5	6	8.3	8.9	15	5.6	12.4
Zr	58	11.1	26	33	84	115	129	165	64	279
Y	9.3	2.1	3.4	7.8	17.9	24.4	24	34	18.5	23.5
Th	0.6	nd	nd	1.6	3.2	4	4.4	7.3	3.1	21
U	nd	2.4	2	2.7	2.3	2	3	2.4	0.9	5.7
La	2.600	1.989	4.603	4.652	8.668	13.962	13.939	32.760	8.049	30.622
Ce	6.006	4.287	9.383	9.731	22.595	30.462	30.792	54.392	16.935	67.613
Nd	3.309	2.678	4.320	5.192	9.324	14.343	14.377	33.565	8.547	31.650
Sm	0.817	0.606	0.921	1.249	2.257	3.262	3.255	6.774	2.071	5.998
Eu	0.239	0.369	0.615	0.593	0.858	1.182	1.048	1.705	0.781	1.689
Gd	0.932	0.580	0.984	1.450	2.222	3.626	3.548	5.235	2.409	7.382
Dy	0.832	0.529	0.962	1.488	2.769	3.758	3.785	5.752	2.618	3.870
Er	0.463	0.303	0.550	0.823	1.600	2.129	2.272	3.253	1.529	2.029
Yb	0.443	0.309	0.520	0.767	1.601	2.004	2.243	3.122	1.455	1.897

Sample #	BHG-1	BHN-II	876-4-201	876-4-726	876-15-597	876-11-750	876-5-625	876-15-301	876-1-376	779-50
Rock Type	K-gabbronorite	K-gabbronorite	px-monzonite	px-monzonite	tonalite	diorite	granophyre	granophyre	metasediment	leucosome
SiO ₂	47.30	52.26	54.92	56.41	57.53	60.52	73.75	73.80	60.85	71.70
TiO ₂	1.20	1.29	1.29	1.22	0.69	0.64	0.19	0.31	1.03	0.70
Al ₂ O ₃	15.64	16.77	17.28	17.06	13.45	15.19	13.60	13.07	16.33	12.50
Fe ₂ O ₃ *	10.81	10.10	8.66	8.12	6.71	5.58	1.67	1.64	7.40	4.74
MnO	0.18	0.17	0.15	0.13	0.23	0.09	0.05	0.05	0.16	0.06
MgO	6.14	4.55	3.01	2.40	6.33	4.45	0.40	0.01	3.39	1.71
CaO	10.15	8.69	7.06	6.08	6.60	6.11	1.40	0.51	3.35	0.64
Na ₂ O	2.18	2.60	3.07	3.15	3.41	3.81	3.73	3.52	3.33	3.07
K ₂ O	1.37	2.51	3.90	4.44	1.92	1.14	3.81	6.20	2.44	4.25
P ₂ O ₅	0.34	0.43	0.56	0.52	0.28	0.11	0.04	0.02	0.19	0.21
LOI	4.07	0.00	0.26	0.20	1.44	1.67	0.49	0.30	0.82	0.80
Total	99.38	99.39	100.16	99.73	98.59	99.31	99.14	99.42	99.29	100.00
Mg#	53.10	48.49	40.93	37.08	65.20	61.39	32.40	1.20	47.73	41.80
Cr	103	117	21	20	298	251	5	5	101	59
Ni	41	37	12	20	92	66	4	3	46	26
Sc	30	28	23	19	22	19	4	4.7	23	10
V	328	143	184	147	183	97	13	7	170	70
Pb	6	23	19	19	6	3	16	9	5	6
Rb	75	148	238	298	77	45	167	163	145	135
Sr	596	564	535	477	992	236	132	24	143	116
Ba	338	635	982	837	543	245	586	116	378	893
Ga	19	23	22	20	17	18	17	19	23	17
Nb	5.9	10	14.5	20	13.9	21	23	30	16.3	13
Zr	81	127	170	231	127	168	146	236	190	411
Y	22	24	31	28	23.2	51	38	142	35	42
Th	8.6	13	22	29	6.3	17	28	18	17	25
U	4.1	5.9	9.1	8.5	4.6	6.7	9.6	6.9	5.9	4
La	23.000	27.881	39.375	45.395	33.005	31.496	24.814	61.316	36.374	53.780
Ce	55.000	59.776	84.121	97.734	80.541	61.191	47.336	154.156	78.724	88.628
Nd	31.870	29.776	36.608	45.556	36.642	25.441	15.394	91.461	29.994	39.614
Sm	7.047	6.005	7.631	8.623	6.091	5.937	3.042	25.630	5.352	6.376
Eu	2.160	1.673	1.882	1.851	1.668	1.271	0.784	3.231	1.296	1.367
Gd	6.216	5.310	5.828	6.346	4.662	6.786	3.652	25.900	7.511	4.403
Dy	5.525	4.285	4.768	5.615	3.592	7.625	4.117	24.562	4.969	3.147
Er	3.621	2.263	2.689	2.980	1.893	4.675	2.762	10.720	2.891	1.283
Yb	2.663	2.113	2.504	2.841	1.813	5.072	3.356	7.587	3.005	1.069

and clinopyroxene, which tends to be titaniferous, often precedes plagioclase crystallization. The mineralogy of the gabbros records iron enrichment followed by iron depletion accompanied by silica enrichment and the appearance of quartz in the late stages (chapter 2). On a conventional alkalis-FeO+MnO-MgO triangular plot (Fig. 3.1) the Black Hill gabbros initially show little iron enrichment however, as plagioclase becomes a major cumulus phase the trend follows a moderate iron enrichment path. Notably this iron enrichment trend is not as extreme as that interpreted for the Skaergaard intrusion. The most evolved gabbros lie on a trend of alkali enrichment and iron depletion directed towards the granophyres.

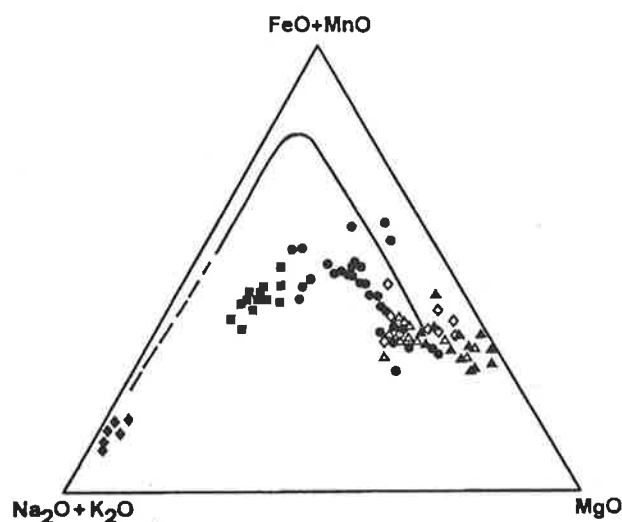
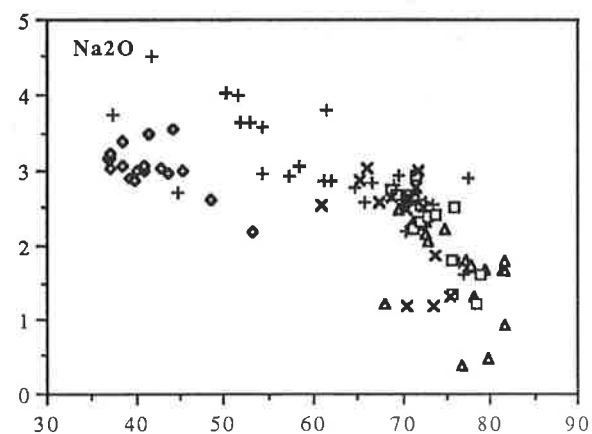
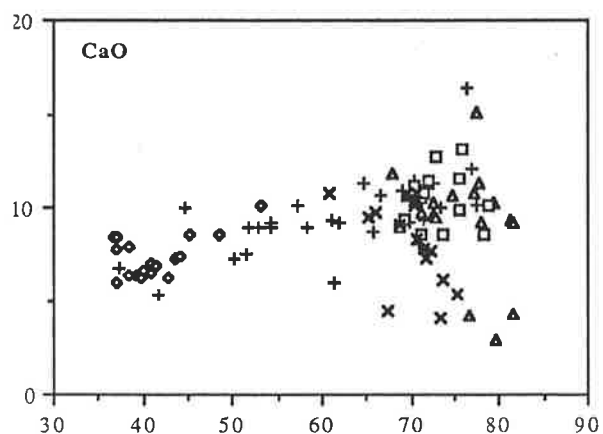
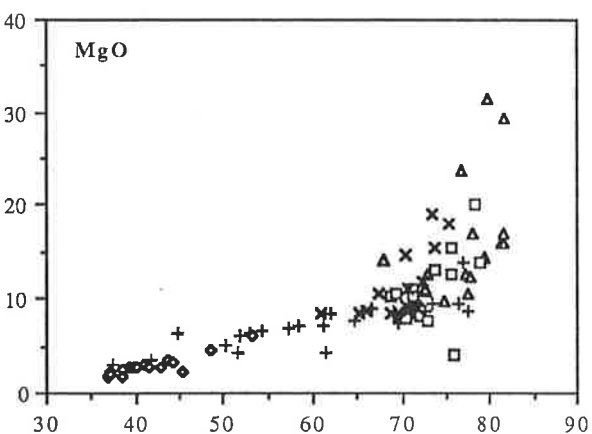
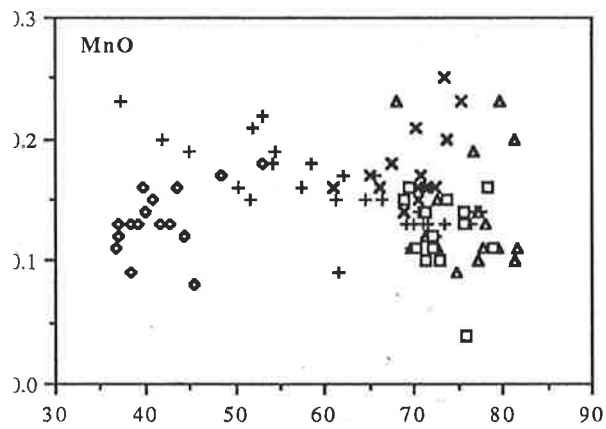
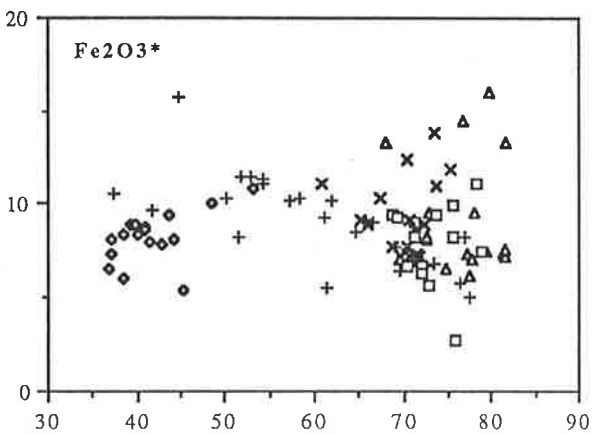
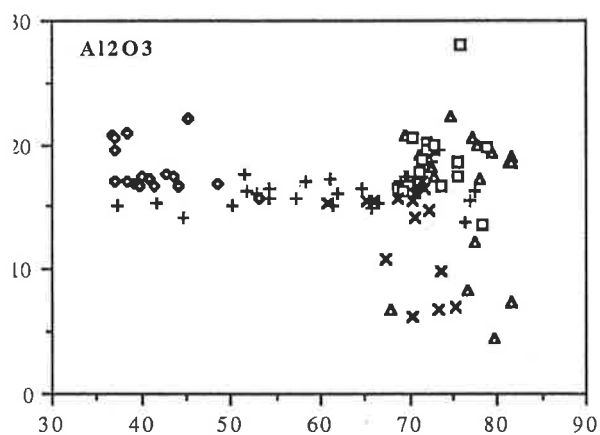
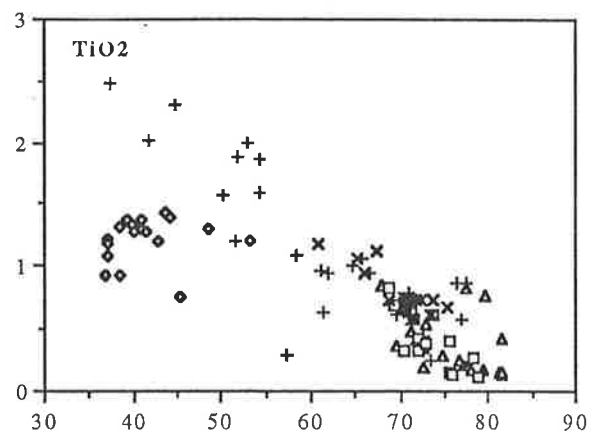
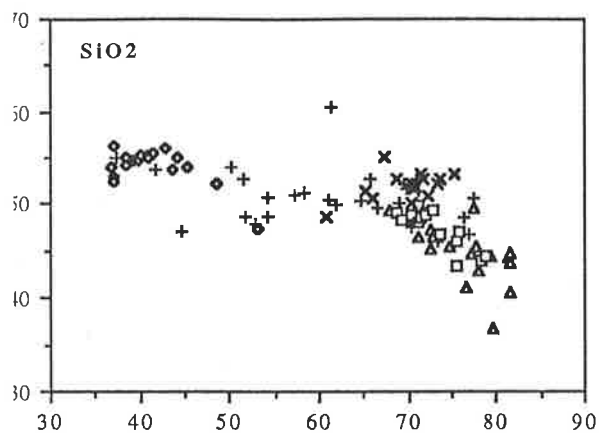


Figure 3.1. AFM ternary plot for the Black Hill gabbros showing a less pronounced iron enrichment trend than the Skaergaard trend (drawn curve) Filled triangles - peridotites and troctolites, filled circles - gabbronorites, open triangles - olivine gabbros, open diamonds - norites, filled squares - pyroxene monzonites and potassic gabbronorites, closed diamonds - granophyres).

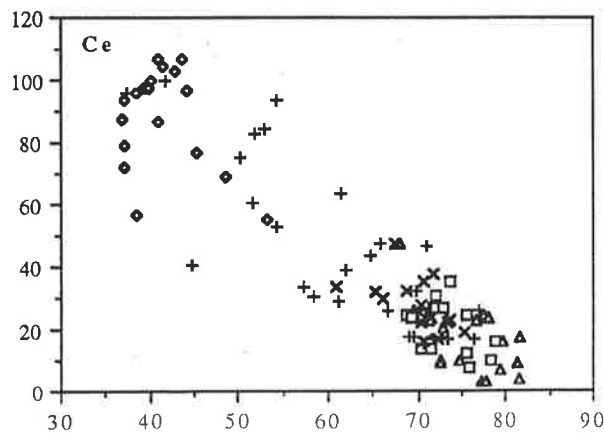
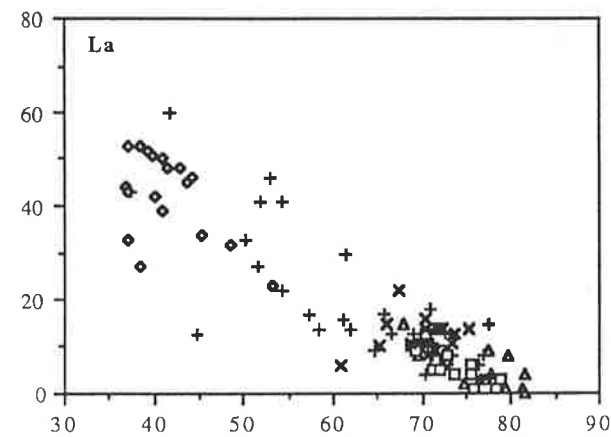
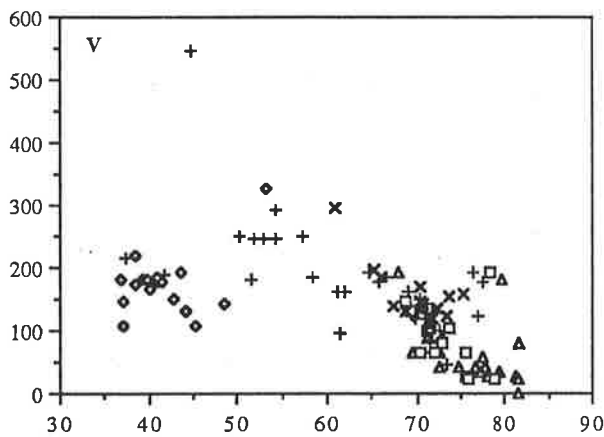
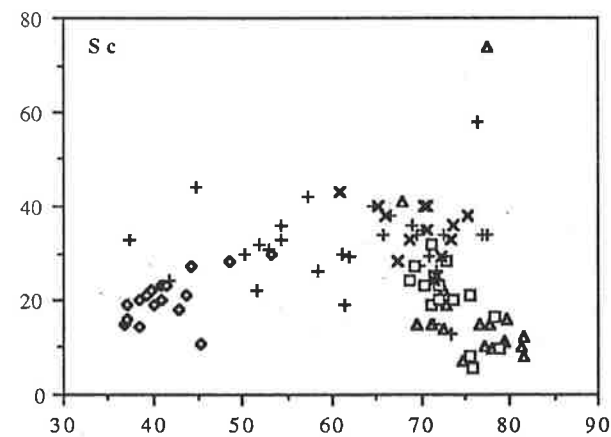
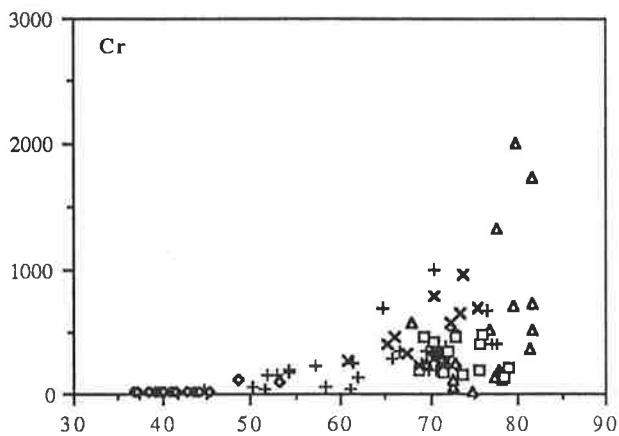
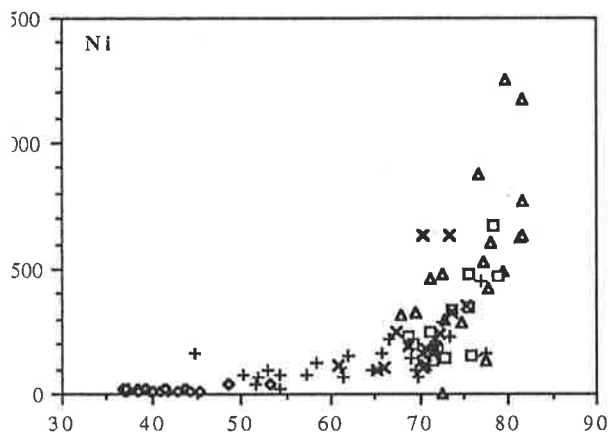
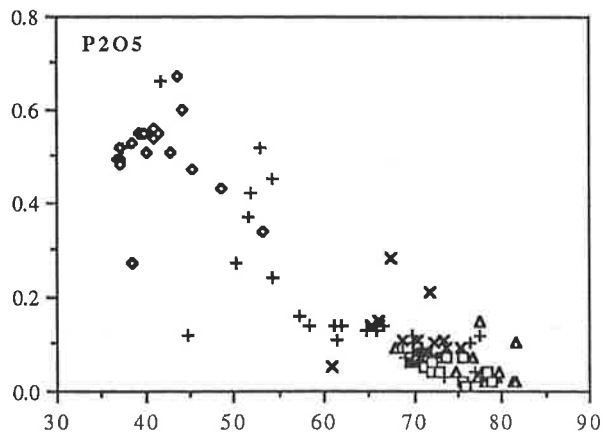
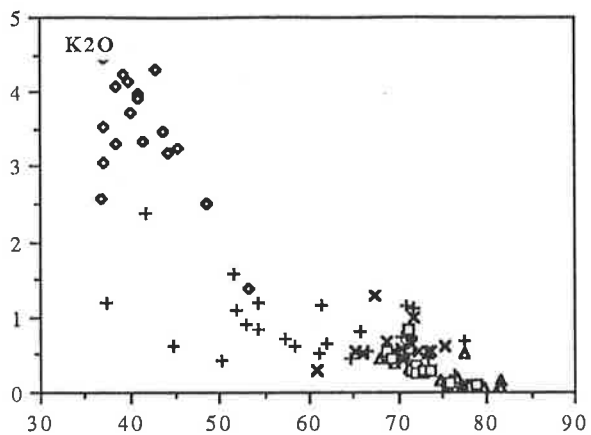
In order to show the complete compositional range of the gabbros and cumulates variation diagrams in which oxides and trace elements are plotted vs Mg# are shown in figure 3.2. Magnesium number was chosen as the most appropriate abscissa because it has a greater range than either SiO₂ or MgO and it should decrease continuously with fractionation even when magnetite becomes a fractionating phase. Compositional variation relative to silica shows considerable complexity due to the fact that silica has remained relatively constant or even decreased until the later stages of fractionation, therefore SiO₂ is an inappropriate differentiation index.

Overleaf Figure 3.2. Mg# variation diagrams for Black Hill gabbros (triangles - peridotites and troctolites, squares - olivine gabbros, x's - norites, crosses - gabbronorites, diamonds - pyroxene monzonites and potassic gabbronorites).



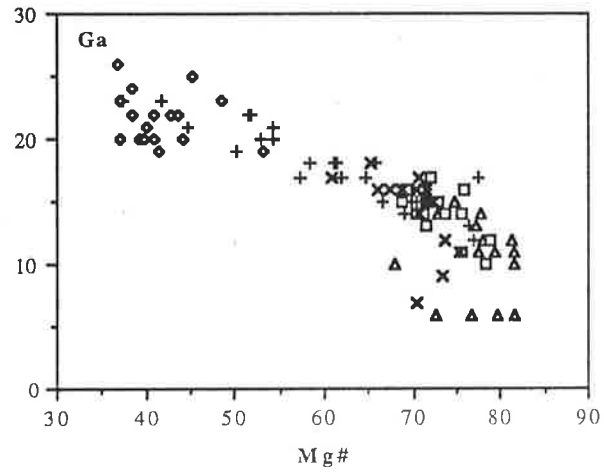
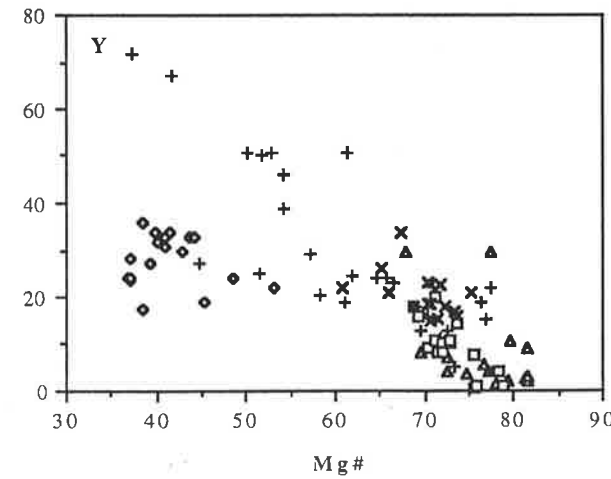
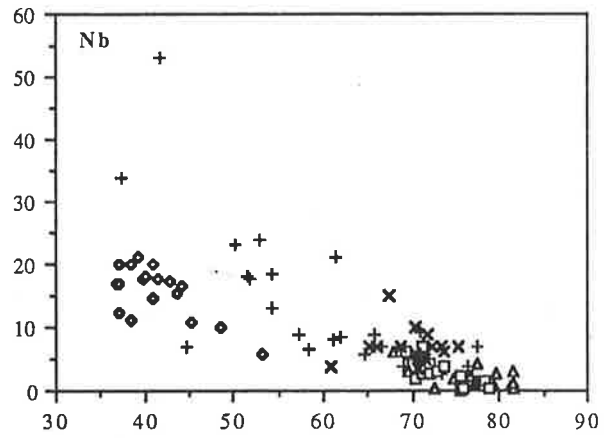
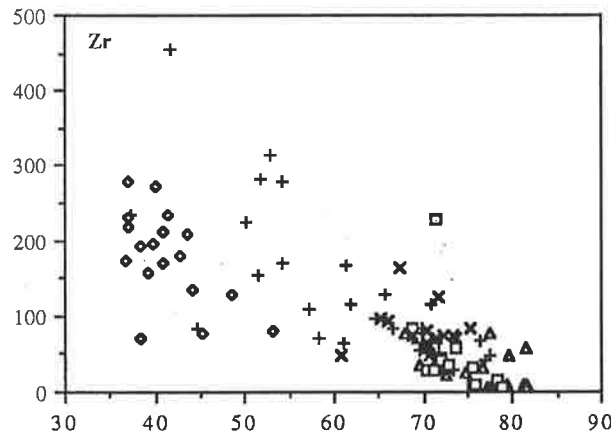
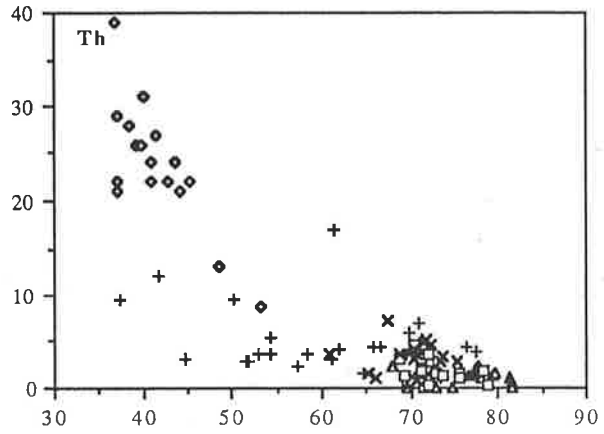
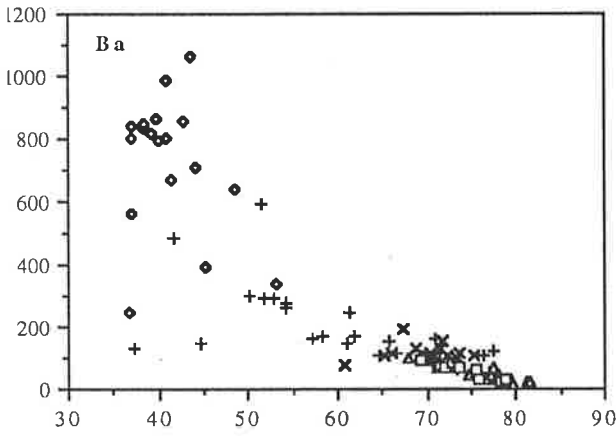
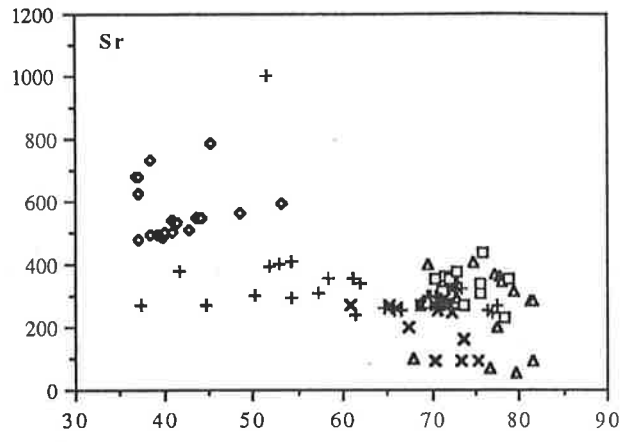
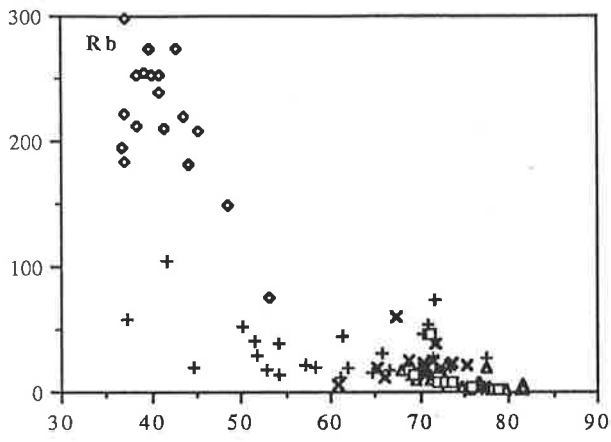
MG#

MG#



Mg#

Mg#



Mg#

Mg#

It has been argued that multiply-saturated liquids are much like their cumulates and that liquid and cumulate compositions converge with increasing fractionation (McBirney and Naslund, 1990; Morse, 1990). In keeping with this the gabbro-norites and pyroxene monzonites ($Mg\# < 70$), which have relatively non-cumulate textures appear to approximate the liquid line of descent whilst the peridotites, troctolites, olivine gabbros and norites are cumulates ($Mg\# > 70$). In many of the plots the potassic gabbro-norites (roof rocks) and pyroxene monzonites (upper wall margin rocks) diverge from the apparent trend of the gabbro-norites indicating increased involvement of another component interpreted to be assimilated country rock.

Silica shows a limited increase from 48 to 55% with decreasing $Mg\#$, there is some reversal in the trend just before $Mg\# 55$ after which SiO_2 increases more rapidly. Titanium rises from 1 to 2% until $Mg\# 55$ after which it decreases in the pyroxene monzonites. Vanadium which is partitioned into magnetite, displays a curvilinear trend increasing until $Mg\# 55$ followed by depletion. This inflection in TiO_2 and V therefore marks the onset of magnetite fractionation and corresponds to the point after which SiO_2 begins to increase more rapidly. Total iron is shown as $Fe_2O_3^*$ (though the low oxygen fugacities determined in chapter 2 mean that nearly all iron would have been in the ferrous state) and displays an enrichment trend in the gabbro-norites from 6 to 10% after which magnetite fractionation produces a steep decline to 3.5%. The plot for manganese suggests similar behaviour to that of titanium and iron.

Magnesium decreases from 10-2% with the removal initially of olivine and in the later stages, pyroxene. Some of the cumulates contain as much as 30% MgO and these also contain the highest iron concentrations. Nickel exhibits strong depletion, like MgO, and is enriched in the cumulates (up to 1400 ppm) then displaying a steady decrease in the gabbro-norites corresponding with fractionation of olivine. Chromium shows like depletion and the maximum solubility of chromium in basaltic liquids at 1200 °C and $\log fO_2$ of -11 is 800ppm whereas at 1150 °C it is only 400ppm (Hill and Roeder, 1974). The occurrence of chromium spinel in peridotites with 2000 ppm Cr, whose pyroxenes indicate temperatures around 1200 °C suggests that the parental magma may have had up to 800ppm Cr. Chromium would have entered chromian spinel, pyroxene and subsequently magnetite during the later stages of fractionation. Textural evidence suggests that pyroxene only crystallized from intercumulus liquid in the more primitive gabbros and did not become a fractionating phase until later. Therefore the early decrease in Cr is likely to reflect spinel fractionation rather than removal of pyroxene. Scandium, which enters pyroxene, constrains the onset of pyroxene fractionation, initially increasing from 25 to 45ppm and subsequently decreasing after about $Mg\# 62$. Therefore pyroxene crystallization commenced well after that of olivine but when it did appear Sc and Cr

concentrations were quickly depleted so that the more evolved gabbros with high pyroxene contents have low Sc (& Cr) contents.

CaO decreases continuously from 11 to 5% after an early increase when olivine was the only fractionating mineral. Plagioclase must have been the next liquidus phase after olivine and spinel because CaO contents start to decrease prior to Mg# 62 when the inflection in Sc concentrations marks the onset of pyroxene fractionation. Thereafter the fractionating assemblage always contained a Ca-bearing phase. Al₂O₃ generally remains relatively constant around 15-17%, except in the extremely plagioclase enriched or depleted cumulates. Na₂O on the other hand shows enrichment from 2.8 to 3.2%. Gallium which apparently substitutes for aluminium (Taylor, 1965) increases regularly throughout the series from 15 to 25ppm.

K₂O is clearly incompatible and increases from 0.4% to at least 1.5% in the gabbronorites whilst the pyroxene monzonites and potassic gabbronorites show extreme enrichment of K₂O indicative of contamination. Nevertheless the fractionated intercumulus liquids were still K₂O-rich enough to crystallize small amounts of biotite even in the primitive cumulates (cf. chapter 2). The implied K₂O (~0.8%) and Na₂O (~2.6%) contents of the parental magma are quite high for a tholeiite though not as high as in alkali basalts. P₂O₅ likewise shows incompatible behaviour except in the pyroxene monzonites which first show enrichment then an inflection at Mg# 42 after which the crystallization of apatite reduces the concentration.

Rubidium mirrors the behaviour of K₂O and is particularly instructive in showing the divergence of the pyroxene monzonites and potassic gabbronorites to extremely enriched values (>300ppm) whilst the trend of the gabbronorites increases regularly from 10ppm to around 75ppm. K₂O/Rb consequently decreases with fractionation. Barium behaves like rubidium and the pyroxene monzonites and potassic gabbronorites display extreme enrichment up to 1000ppm. Thorium, and also uranium and lead (not plotted), all display trends of enrichment similar to potassium and rubidium with highest concentration in the monzonites where zircon and sphene first appear.

Strontium remains relatively constant throughout the gabbronorite trend suggesting a distribution coefficient close to 1 and an parental magma concentration around 300 ppm. The plagioclase-rich cumulates particularly the troctolites have somewhat higher Sr concentrations. The pyroxene monzonites, potassic gabbronorites and anorthosites are Sr-enriched with respect to the gabbronorite trend with values up to 800 ppm. These gabbros are chemically evolved and this suggests their high Sr concentration is partly due to fractionation (combined with assimilation ?) at the pluton margins. Rb/Sr increases continuously with decreasing magnesium number and Ba/Sr has a sharp inflection at Mg#=49 in the monzonites corresponding to the increased Sr in the evolved gabbros.

The highly charged incompatible elements (Zr, Y, Nb) and Th, U and Pb all behave in a similar incompatible manner. The cumulates, not surprisingly, are depleted in these elements whilst the gabbronorite trend shows continuous enrichment with decreasing Mg#. The potassic gabbronorites and pyroxene monzonites from the pluton roof and margins often contain the highest concentrations of these elements but themselves display a trend of depletion indicating the onset of minor phase fractionation. Yttrium for example, which behaves similarly to the heavy rare earths, shows continuous enrichment with fractionation from the gabbronorites to the potassic gabbronorites and pyroxene monzonites which then show declining concentrations. This curvilinear trend in the marginal rocks, also observed for phosphorus, suggests apatite fractionation. A similar pattern of behaviour is shown by Zr and one of the pyroxene monzonites contains zircon which is large, euhedral and unzoned indicating a magmatic origin. Zircon saturation in basaltic liquids only occurs after concentration by high degrees of fractionation (Dickinson and Hess, 1982), confirming that these crystallized from highly fractionated magmas.

The discussion so far has concentrated on fractionation trends for the gabbros which are more likely to approximate liquid compositions. The cumulate compositions are complementary to these trends (see Fig. 3.2). The most primitive gabbros, with high MgO, Ni and Cr contents are cumulate peridotites containing olivine \pm chrome spinel. Early fractionation of these phases produced trends involving decreasing MgO, Cr and increasing CaO. Plagioclase then commenced crystallization producing troctolite cumulates with high Al₂O₃, CaO, MgO and Sr. Plagioclase and olivine are likely to have had a combined SiO₂ content similar to the of the magma resulting in fractionation that had little effect or even decreased SiO₂ concentrations. Subsequently pyroxene (clinopyroxene > orthopyroxene) and later magnetite joined the fractionating assemblage resulting respectively in olivine gabbro cumulates and some opaque-rich gabbronorites which have high TiO₂. Fractionation producing these cumulates pushed the liquid towards SiO₂ enrichment. In the late stages minor phases, particularly apatite became important in controlling trace element evolution.

The norites which are composed principally of small grains of orthopyroxene (bronzite) set in plagioclase oikocrysts form a unique group of cumulates. On the variation diagrams these plot as a group which is often divergent from the other gabbros and cumulates. In particular the norites show trends of decreasing SiO₂, Fe₂O₃, Ni, Cr, increasing Al₂O₃, CaO, Na₂O, Ga whilst incompatible element abundances would seem to remain relatively constant. The composition of the norites is clearly dominated by their degree of accumulation of orthopyroxene. Thus the trends essentially converge on the composition of bronzite and move to lower Mg# and higher Al₂O₃ with increasing amounts of intercumulus plagioclase.

3.2.3. Rare earth elements

Rare earth patterns for representative gabbros covering a broad range of whole rock compositions are shown in figure 3.3 and the analyses are listed in table 3.1. The more primitive cumulates contain 1 to 5x chondritic abundances of HREE and up to 15x chondritic La. The troctolites have positive europium anomalies indicating plagioclase accumulation whilst the peridotite has a slight negative europium anomaly. Total REE contents increase through the olivine gabbros and gabbronorites and this is accompanied by increasingly smaller positive, and eventually, negative Eu anomalies. The more evolved gabbros (the pyroxene monzonites and potassic gabbronorites) contain very high total rare earth contents, over 100x chondrite for La, consistent with high degrees of fractionation. These also have slight negative Eu anomalies indicating plagioclase removal. Interestingly the anorthosite, with a similar pattern to these pyroxene monzonites, has no positive Eu anomaly. Plots of the light rare earths lanthanum and cerium against Mg# for the whole suite of gabbros (Fig. 3.2) show REE enrichment throughout the suite.

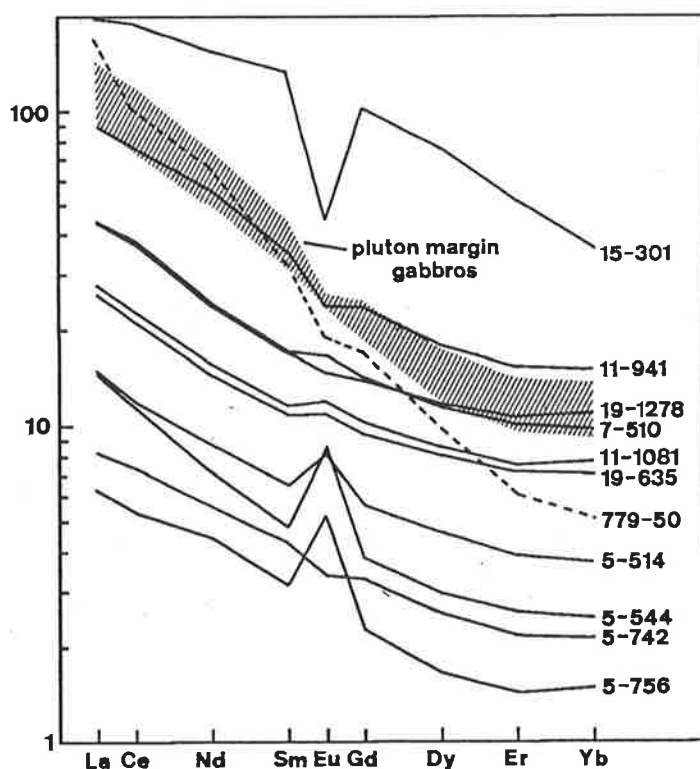


Figure 3.3. Chondrite normalized rare earth patterns for Black Hill gabbros (5-742 - peridotite, 5-756 & 5-544 - troctolites, 11-1081 & 5-514 - olivine gabbros, 7-510 & 19-1278 - gabbronorites, 11-941 & 19-635 - norites, 15-301 - granophyre, 779-50 - migmatite leucosome, shaded region - pyroxene monzonites, potassic gabbronorites and anorthosite).

The relative LREE enrichment through the gabbros is of interest. Of the fractionating phases involved (ol, pl, px) plagioclase is likely to preferentially incorporate Eu, and the pyroxenes have slightly higher distribution coefficients for the HREE. In general, however, distribution coefficients are similar for all the rare earths. Consequently fractionation will increase the total REE concentrations but have little effect on the slope of the patterns particularly when pyroxene is not a major fractionating phase as seems to be the case for the early history of the Black Hill magmas. Excluding the marginal rocks there is minor LREE enrichment from the troctolites and peridotites through the olivine gabbros to the gabbronorites with La/Yb_N increasing from 3.5 to ~5. Because crustal rocks are LREE-enriched, processes which involve assimilation, however, might be expected to produce increasingly LREE enriched patterns. The La/Yb_N ratios for the pyroxene monzonites, potassic gabbronorites and anorthosites are considerably higher than the other gabbros at around 9-11. This may also reflect the increasing role of pyroxene, which preferentially incorporates the HREE, in the later stages of fractionation to produce these rocks.

On the other hand all of the gabbros, including the most primitive cumulates with minimal intercumulus material, have LREE enriched patterns with La/Yb_N of at least 3.5. LREE enrichment in mantle derived melts is largely controlled by the degree of melting and residual garnet, which preferentially incorporates the HREE. Moderate degrees of partial melting (10-20%) of a depleted mantle source produce magmas (eg MORB) with flat or LREE depleted patterns. Smaller degree partial melts will have LREE enrichment however they also tend towards alkali-basalt compositions (eg Gast, 1968). The Black Hill gabbros did not follow an alkali basaltic crystallization path nor is the inferred parental magma composition highly alkalic and is consequently unlikely to have resulted from small degree partial melting. The cumulates are unlikely to have higher La/Yb_N than the liquid they crystallized from so it seems that the parental magma already had this LREE enriched signature prior to injection into the present magma chambers. This signature must therefore either derive from contamination during ascent through the crust (eg. Huppert and Sparks, 1985) or be a reflection of the source characteristics.

3.2.4. Radiogenic isotopes and geochronology

Previous age determinations for Black Hill were carried out by Milnes *et al.* (1977) giving a Rb-Sr whole rock age of 487 ± 5 Ma and a K-Ar biotite age of 486 Ma. As part of the present investigation a whole rock-seven mineral isochron was determined for a potassic gabbronorite outcropping beneath the trigonometric station at Black Hill. This yielded a 489 ± 10 Ma Nd-Sm isochron with an initial $^{143}\text{Nd}/^{144}\text{Nd}$ ratio of 0.51179 (Fig. 3.4). Alkali feldspar lies just below this isochron however, as will be discussed in the following sections, these gabbros from the roof zones of the pluton owe their K-rich

Table 3.2. Isotope analyses for Black Hill samples

Sample	Lithology	Rb	Sr	87Rb/86Sr	87Sr/86Sr	87Sr/86Sr(t)	Nd	Sm	147Sm/144Nd	143Nd/144Nd	134Nd/144Nd(t)	eps Nd (t)	Tmod (dep)
5-742	peridotite	5.5	93.1	0.172288	0.705039 +/-26	0.703843	3.31	0.82	0.149278	0.512665 +/-21	0.512189	3.35	0.94
5-756	troctolite	0.8	292.3	0.007829	0.703986 +/-30	0.703932	2.68	0.61	0.136769	0.512579 +/-23	0.512143	2.45	0.96
5-544	troctolite	5.3	468.4	0.032371	0.704298 +/-27	0.704073	4.32	0.92	0.919212	0.512553 +/-31	0.512142	2.43	0.92
11-1081	ol-gabbro	18.0	279.4	0.186470	0.705662 +/-23	0.704368	9.32	2.26	0.146424	0.512495 +/-20	0.512028	0.21	1.25
5-514	ol-gabbro	2.9	378.6	0.015810	0.704229 +/-31	0.704119	5.19	1.25	0.145516	0.512627 +/-24	0.512163	2.84	0.97
7-510	gabbro	19.8	344.2	0.166043	0.706719 +/-28	0.705567	14.34	3.26	0.137578	0.512432 +/-20	0.511993	-0.47	1.23
19-1278	gabbro	32.9	257.7	0.343045	0.706890 +/-35	0.704510	14.38	3.26	0.136951	0.512459 +/-30	0.512022	0.09	1.17
11-941	norite	59.1	207.0	0.825553	0.712001 +/-27	0.706272	33.57	6.77	0.122082	0.512318 +/-21	0.511929	-1.74	1.21
19-635	norite	15.2	269.6	0.159862	0.705949 +/-28	0.704840	8.55	2.07	0.146572	0.512507 +/-28	0.512039	0.43	1.23
4-926	anorthosite	182.4	683.4	0.772475	0.711805 +/-18	0.706445	31.65	6.00	0.114641	0.512148 +/-22	0.511782	-4.59	1.37
BHG-1	K-gabbro	74.9	595.6	0.364184	0.708504 +/-28	0.705977	31.87	7.05	0.133754	0.512262 +/-39	0.511835	-3.56	1.47
BHN-II	K-gabbro	148.5	528.9	0.759496	0.711422 +/-19	0.706152	29.78	6.01	0.121992	0.512194 +/-22	0.511805	-4.15	1.40
4-201	px-monzonite	241.8	548.6	1.276154	0.715385 +/-22	0.706529	36.61	7.63	0.126091	0.512191 +/-20	0.511789	-4.47	1.47
4-726	px-monzonite	299.4	445.6	1.809607	0.719520 +/-28	0.705513	45.56	8.62	0.114498	0.512171 +/-26	0.511764	-3.56	1.34
11-750	diorite	46.7	232.5	0.141068	0.708747 +/-26	0.707764	25.44	5.94	0.126569	0.512453 +/-30	0.512045	0.58	1.06
15-597	tonalite	76.9	1003.0	0.221847	0.705497 +/-21	0.703958	36.64	6.09	0.100547	0.512372 +/-25	0.512051	0.66	0.93
15-301	granophyre	158.7	24.2	19.213340	0.836737 +/-41	0.703409	91.46	25.63	0.169514	0.512462 +/-20	0.511921	-1.88	1.89
5-625	granophyre	169.4	128.0	3.668366	0.729981 +/-99	0.704525	15.39	3.04	0.119534	0.512420 +/-34	0.512039	0.42	1.03
1-376	metasediment	145.5	144.1	2.931438	0.747210 +/-44	0.726868	29.99	5.35	0.107939	0.511781 +/-33	0.511437	-11.34	1.78
779-50	leucosome	139.7	111.0	3.652989	0.747864 +/-74	0.722515	39.61	6.38	0.097361	0.511684 +/-55	0.511373	-12.58	1.74

character in a large part to contamination by the local country rocks. It appears that alkali feldspar, which on textural grounds is interstitial and clearly late crystallized (chapter 2), suffered the most contamination and was unable to equilibrate isotopically with the earlier formed phases.

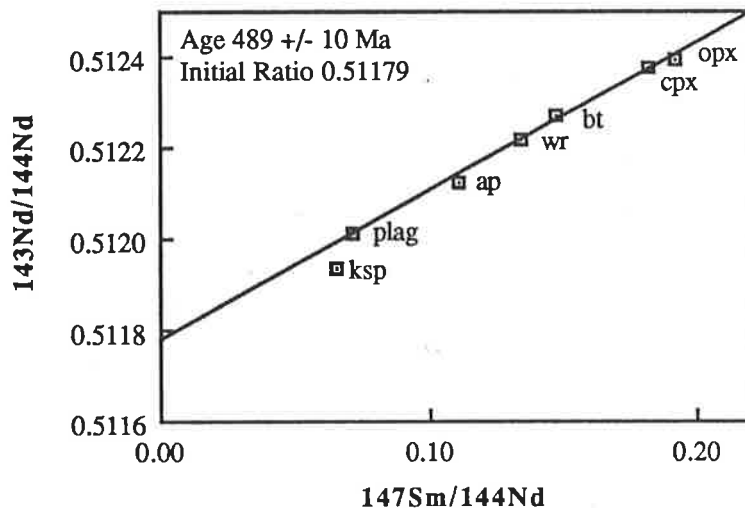


Figure 3.4. Whole rock-mineral isochron determined on a roof zone potassic gabbro-norite BHG-1 (see text for discussion).

The samples selected for REE determinations were also analysed for their rubidium-strontium and neodymium-samarium isotopic ratios (Table 3.2; Appendix A) which were then age corrected to 487 Ma consistent with the age data on the Black Hill gabbros and other intrusives of the late-orogenic suite by Foden *et al.* (1990b). The troctolites, peridotite and a primitive olivine gabbro have high epsilon Nd values around +2.4 to +3.4 and low initial $^{87}\text{Sr}/^{86}\text{Sr}$ from 0.7038 to 0.7041 suggesting dominance of a mantle component. The measured Rb and Sr isotopic concentrations for the most primitive troctolite and peridotite lie on a 487 Ma isochron indicating that these samples crystallized from isotopically similar magma potentially unaffected by in-situ contamination. These samples have near identical initial $^{87}\text{Sr}/^{86}\text{Sr}$ around 0.7038 which may reflect that of the parental magma. Progressing to the more evolved olivine gabbros, gabbro-norites and norites, ϵNd is lower (0 to -2) and initial $^{87}\text{Sr}/^{86}\text{Sr}$ higher (0.7044 to 0.7055) suggesting contamination relative to the cumulates. Overall these gabbros and cumulates have an ϵNd range from +3.4 to -1.8 and initial $^{87}\text{Sr}/^{86}\text{Sr}$ range from 0.7038 to 0.7055 making a trend towards more radiogenic values.

The potassic gabbro-norites and pyroxene monzonites which come from the pluton margins have considerably lower ϵNd (around -4) and higher initial $^{87}\text{Sr}/^{86}\text{Sr}$ (around 0.7066) consistent with increased crustal contamination by the (?metasedimentary) wall rocks which were displaced during intrusion of the mafic magma. Unless the parental

magma entrained considerable volumes of xenolithic material it should have been isotopically homogeneous, especially as its ascent through the crust is likely to have taken place in narrow dykes and the subsequent injection into the magma chambers was probably turbulent. Consequently the observed within pluton variation and particularly the increased radiogenic isotopes of the most evolved gabbros from the pluton margins strongly argues for in-situ contamination by the wall rocks which are likely to have been stopped or melted into the magma.

On a ϵ_{Nd} -Sr initial ratio diagram (Fig. 3.5) all of the gabbros lie on the mantle array and define a trend that extends from the region of time integrated depletion of Rb/Sr and Nd/Sm relative to bulk earth as represented by MORB, into the region which represents time integrated enrichment relative to bulk earth. The best known mafic rocks of similar isotopic composition and range that lie on the mantle array extending into this

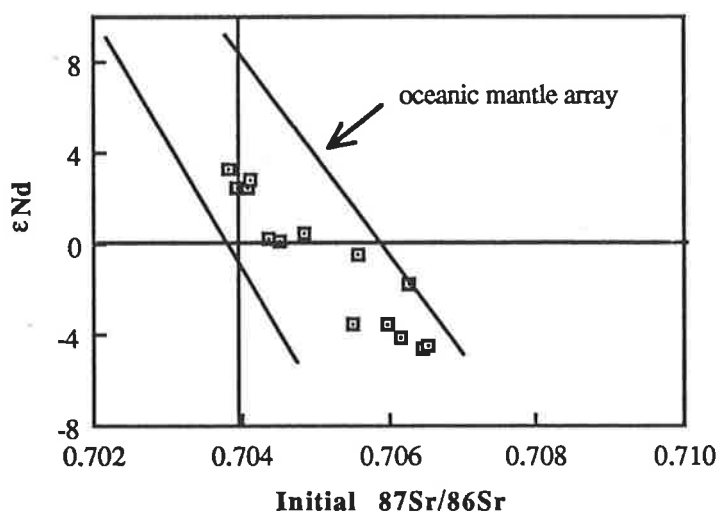


Figure 3.5. ϵ_{Nd} vs initial Sr ratio diagram for the Black Hill gabbros. Mantle array from White (1985).

region of time integrated enrichment are the ocean island basalts (OIB). These islands do not overlie continental crust and must rely on their "enrichment" from some other source or be derived from enriched mantle, for example McKenzie and O'Nions (1983) suggest that this source may be enriched lithospheric mantle that has become detached from continental crust and incorporated in convective flow in the asthenosphere. In the case of the Black Hill gabbros however this trend suggests contamination of mantle derived magma with a component which has low ϵ_{Nd} and high $^{87}Sr/^{86}Sr$. This end member is most likely to be continental crust and one interpretation is that the trend is simply one of "enrichment" of melts from the contemporary depleted mantle by contamination with a crustal component. However, the positive ϵ_{Nd} and low initial Sr ratios of the cumulates must limit contamination with the possibility that the isotopic characteristics and LREE

enriched patterns of these cumulates may actually be a feature of their source. An alternative then is that the parental magma was derived from enriched subcontinental lithospheric mantle. The tonalite sample (11-750) has a much higher $^{87}\text{Sr}/^{86}\text{Sr}$ than the gabbros and may be a xenolith of one of the preceding syn-orogenic granites (cf. chapter 1).

The two granophyres analysed have surprisingly primitive isotopic ratios considering their composition. For example they have very high SiO_2 and incompatible element contents (see Table 3.1) yet are isotopically more primitive than most granitic rocks such as the I- and S-type granites from the Lachlan Fold Belt (McCulloch and Chappell, 1982). With ϵNd 0.5 to -2, and initial $^{87}\text{Sr}/^{86}\text{Sr}$ 0.7034-0.7045 they compare isotopically with the olivine gabbros and more primitive gabbro-norites. This precludes their origin by crustal anatexis and allows the possibility that they are genetically related to the gabbros.

3.3. Petrogenesis

3.3.1. Phase equilibria constraints

Following Irvine (1970), Walker et al., (1979) and Grove and Baker (1984) the Black Hill gabbros are shown as quartz, clinopyroxene and plagioclase projections onto the olivine-plagioclase-clinopyroxene, olivine-plagioclase-quartz and olivine-clinopyroxene-quartz planes of the olivine-plagioclase-clinopyroxene-quartz tetrahedron for low pressures (Figs. 3.6a, b, c). Although most of the rocks are at least partial cumulates their alignment still indicates, and often parallels or projects towards, the path the liquid must have taken. This allows analysis of the liquid evolution path without a prior knowledge of the parental magma composition.

Referring to figures 3.6a-c the dispersion of data towards the olivine apex in all three diagrams indicates that this parental magma lay in the ol+liq volume and underwent early olivine crystallization consistent with the chemical trends and the presence of peridotite cumulates. This allows that the parental magma may have undergone some olivine fractionation during ascent prior to injection into the magma chambers. Additionally the primary pyroxene fields expand at the expense of olivine with increasing pressure (Stolper, 1980). Therefore at higher pressures it is possible that pyroxene (opx) would have been on the liquidus instead of, or in addition to, olivine. Decompression then leads to displacement of the magma into the expanding olivine primary phase volume.

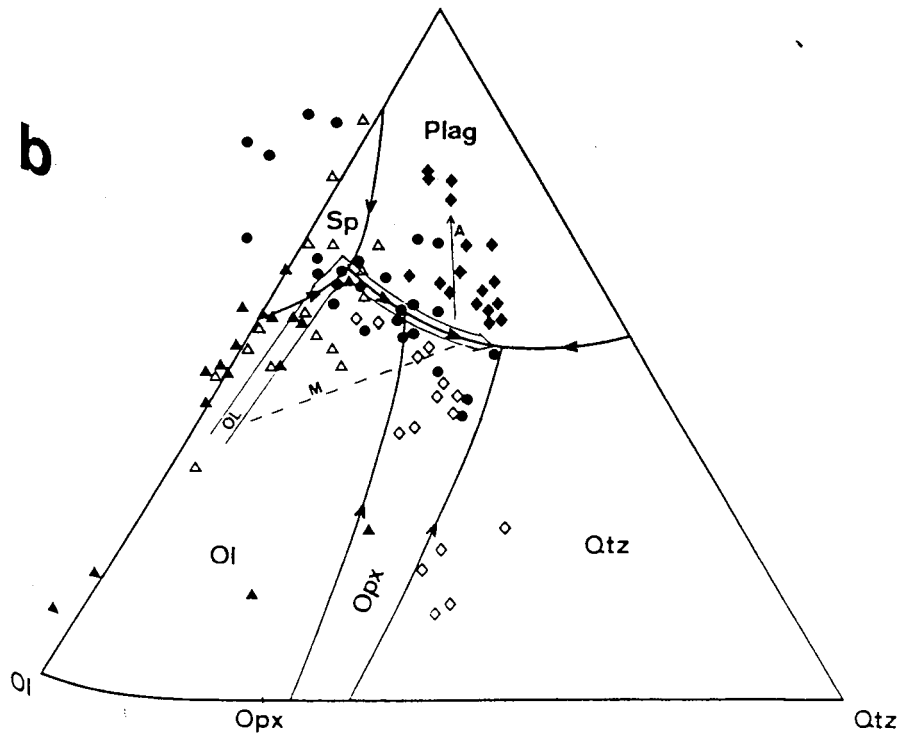
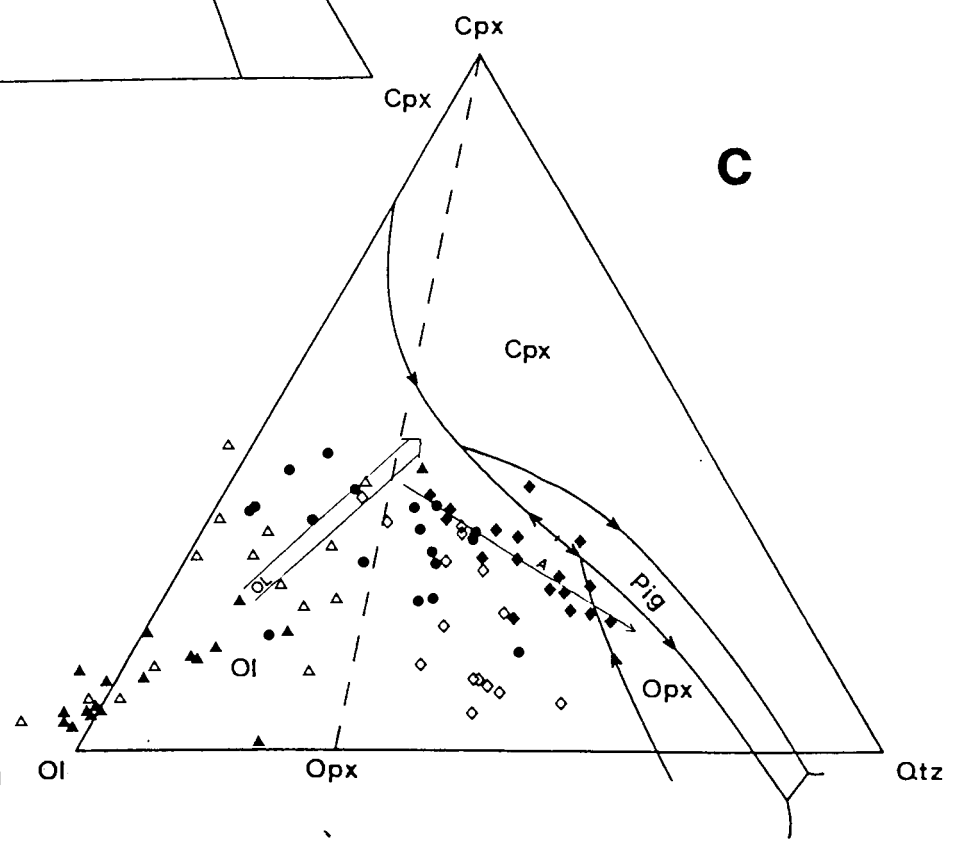
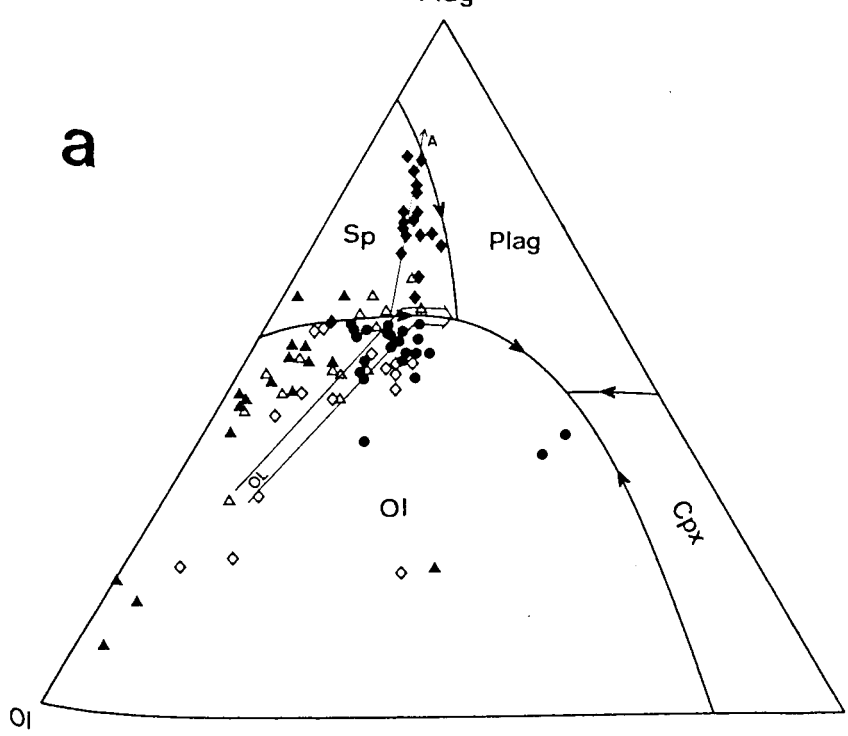
By the time the parental magma had reached its upper crustal chambers it lay in the primary olivine volume. In the ol-pl-qtz and ol-pl-cpx diagrams this liquid must have lain on a line projected from olivine and the data indicate that this evolved until it intersected

Figure 3.6a. Projection* from quartz showing a likely evolution path for the Black Hill magma involving early olivine crystallization. The effect of assimilation (A) is also shown displacing the magma into the plagioclase field (filled triangles - peridotites and troctolites, filled circles - gabbro-norites, open triangles - olivine gabbros, open diamonds - norites, filled diamonds - pyroxene monzonites, potassic gabbro-norites, and anorthosites).

Figure 3.6b. Projection* from clinopyroxene illustrating possible evolution paths for the Black Hill magma with mixing lines showing the effects of assimilation (A) and recharge with fresh magma (M) (symbols as before).

Figure 3.6c. Projection* from plagioclase showing how the effect of silica enrichment due to assimilation is to move the liquid towards the fields of pigeonite and orthopyroxene (symbols as before).

*All projections were performed using NORM's calculated for $Fe^{2+}/Fe_{total} = 0.9$ and the phase boundaries are drawn for 1 atm pressure (references in text).



the ol-sp boundary curve. Olivine and spinel crystallized until the ol-plag cotectic was reached where spinel ceased to crystallize. Plagioclase and olivine then crystallized until they were subsequently joined by pyroxene shortly after which olivine ceased to crystallize. From this point continued cooling caused the liquid to evolve towards the quartz apex stopping at the quaternary minimum where the remaining liquid crystallized plagioclase, pyroxene and minor quartz. The reappearance of spinel as magnetite (not shown) occurred after pyroxene commenced crystallization. Given that this typical tholeiitic evolution is consistent with petrographic evidence (chapter 2) specific details regarding recharge and contamination may now be assessed.

Assimilation of upper crustal metasediments such as those that the Black Hill plutons intruded will produce an increase in SiO_2 . Such peraluminous contaminants and partial melts of these metasediments will also induce an increase in normative plagioclase (Nielsen, 1989; Ellis *pers. comm.*). With this in mind the potassic gabbros from the pluton margins, the pyroxene monzonites and potassic gabbro-norites are displaced upwards from the cotectic into the plagioclase + liquid fields on the cpx and qtz projections. Contamination has displaced the liquid into the plagioclase field necessarily causing increased plagioclase crystallization which provides an explanation for the anorthosites which are spatially, chemically and isotopically associated with the pyroxene monzonites. The similar chemistry of the anorthosites to the pyroxene monzonites and the unusual lack of a positive Eu anomaly are consistent ^{with} this plagioclase rich unit being formed by displacement of the evolved magma into the plagioclase field rather than an origin involving plagioclase accumulation.

In the projection from plagioclase (Fig. 3.6c) the potassic gabbros form a linear dispersion towards the quartz apex which leads towards the orthopyroxene and pigeonite fields. The potassic gabbros contain increased modal abundances of orthopyroxene and it is the pyroxene monzonites which have developed pigeonite. This is partly due to their iron-rich nature but also partly due to their lower temperatures and enriched SiO_2 content which can be seen to be consistent with a contamination hypothesis. Under conditions of pure equilibrium crystallization an olivine normative liquid would crystallize completely at the reaction point cpx-pig-ol in the plagioclase projection in figure 3.6c (Grove and Baker, 1984). However, the dispersion of data indicates that the liquid evolved beyond this point suggesting fractional crystallization and deflection of the liquid path towards the quartz apex by contamination.

Fine grained norites, in which orthopyroxene crystallized prior to plagioclase, occur frequently in at least one of the Black Hill plutons. On the basis of mineralogical and thermodynamic data these are interpreted to have resulted from fresh influxes of parental magma that mixed with cooler, more evolved magma resident in the chamber (chapter 2). The recharge hypothesis for the origin of the norites can be examined using

the cpx projection in figure 3.6b. Mixing the partially evolved magma with a fresh influx of olivine normative magma, as shown in the cpx projection, will displace the liquid into the opx+liq volume resulting in a period of opx crystallization until the liquid returns to the plag-px boundary. Such a course could account for the abrupt change in crystallization sequence demonstrated by the norites.

3.3.2. Composition of the parental magma

A central problem in all studies of layered gabbroic intrusions is the identification of the composition of the parental magma injected into the chambers. Unfortunately chilled margins, which have so often been used as parental magma compositions, have not been found at Black Hill due to the lack of outcrop of the margins of the intrusions. The mineralogy and chemical trends show the parental magma was an olivine normative, continental tholeiite. A primary magma in equilibrium with an olivine-orthopyroxene-clinopyroxene-garnet upper mantle should have high Mg# (~70), Ni (~400 ppm), Cr (~1000 ppm) and olivine of around Fo₈₈₋₉₀. Olivines in equilibrium with primitive tholeiites such as Kilauea, for example, would have compositions around Fo₈₈ (Irvine, 1979). The apparently high Cr and Ni contents of some of the most mafic cumulates at Black Hill argues for a quite primitive parental magma, probably relatively undiluted by crustal contamination, and must restrict the amount of olivine fractionation en-route to the near-surface plutons. At Black Hill magma the most magnesian olivines with Fo₈₆ would have been in equilibrium with a liquid that had Mg# ~63-65 (chapter 2). This calculation represents a minimum estimate because the olivines are unzoned, indicating equilibration with more iron-rich intercumulus liquid, and more magnesian olivines may exist in deeper zones of the pluton (chapter 2). Microprobe data from these mafic cumulates show the olivines and pyroxenes contain 2500 ppm Ni and 6500 ppm Cr respectively. Using a distribution coefficient of 10 in each case (Cox et al, 1979) this indicates the parental magma had 250 ppm Ni and 650 ppm Cr. Therefore the parental magma was not a primary depleted mantle magma and had undergone some fractionation during its passage through the crust. Solving the Rayleigh fractionation equation to obtain the implied Ni and Cr contents from a primary magma with 400 ppm Ni and 1000 ppm Cr restricts this fractionation to < 5%.

There is also evidence that the parental magma was somewhat enriched in incompatible elements. The foregoing discussion on the REE data suggests that the parental magma is likely to be LREE enriched with a La/Yb_N ratio of about 3 and this may reflect an enriched source. This is quite similar to the mildly LREE enriched patterns observed for ocean island basalts and continental flood basalts. For most of the gabbros Zr/Nb ratios (10-12) and Y/Nb ratios (2-4), which are not altered by most basaltic fractionation processes, are relatively low and similar to continental flood basalts such as

those from the Parana basin (Fodor, *et al.*, 1985). Such values lie between the values typical of more enriched P-type MORB and those of ocean island basalts (OIB) from enriched mantle sources (Wilson, 1989).

If the gabbronorite trend is taken to approximate the liquid trend then the concentration of any element in the parental magma can be approximated from the variation diagrams by reading the value, for that element, that corresponds to the parental magma Mg# value (~65 from olivine equilibria). This composition (Table 3.3) is more enriched than typical MORB but similar to the parental magma compositions interpreted for many other continental tholeiites. Figure 3.7 is a MORB-normalized spidergram showing the incompatible trace element pattern for the approximated parental magma and a continental flood basalt from the Deccan Traps for comparison. The two patterns are very similar and both are enriched in the lithophile elements and LREE's compared to MORB which would plot as a straight line at around 1 on this diagram.

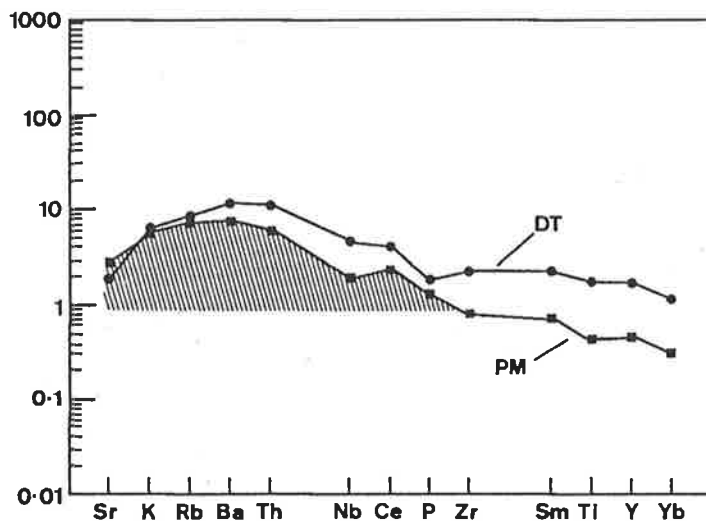


Figure 3.7. MORB normalized spidergram showing the parental Black Hill magma composition and a basalt from the Deccan Traps (data from Thompson *et al.*, 1983). Shaded area shows enrichment relative to typical MORB which would plot as a straight line at 1. Normalization factors and order of elements after Pearce (1983).

Whether this is a valid approximation of the true parental magma can be tested, in part, by modelling fractionation and comparing the resultant compositions with those observed through the plutons. Using least squares mixing (eg Wright and Doherty, 1970), to model from one specific composition to another, is hampered by the problem that many of the gabbros are partially adcumulative and therefore the true liquid composition is not known for any particular stage of fractionation. A more appropriate approach, in this situation, is that of Nathan and Van Kirk (1978) whereby phase equilibria are used to determine the mineral assemblage on the liquidus for a given magma

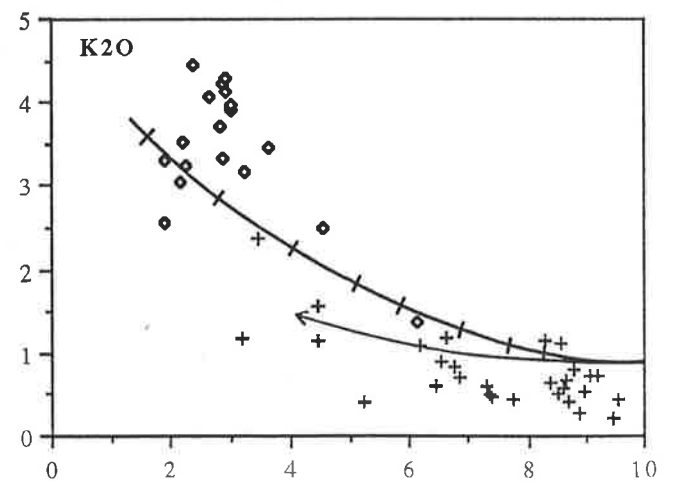
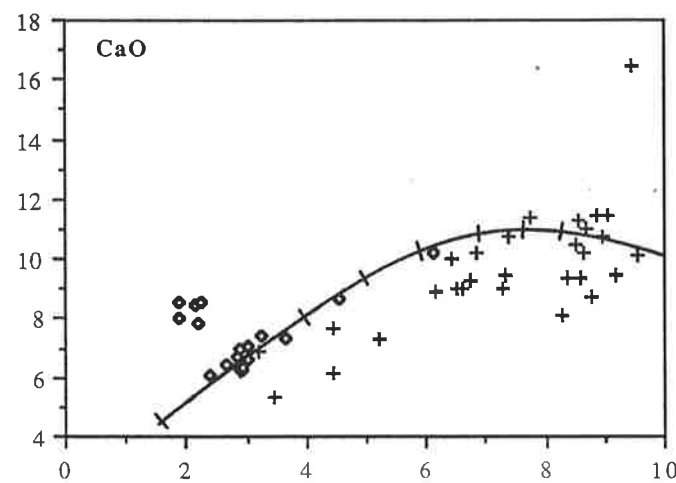
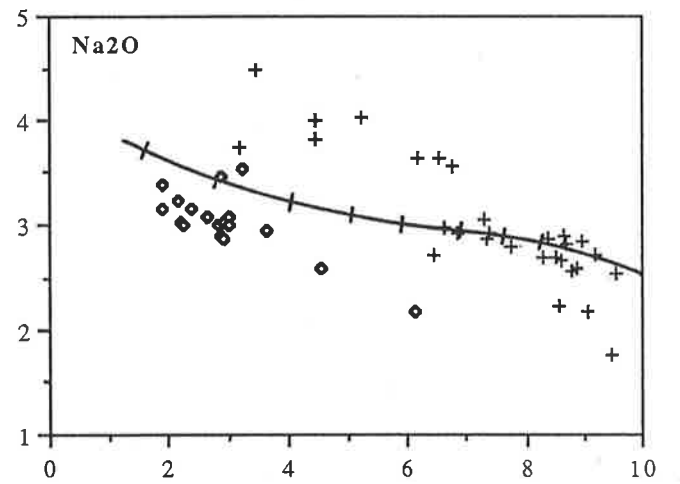
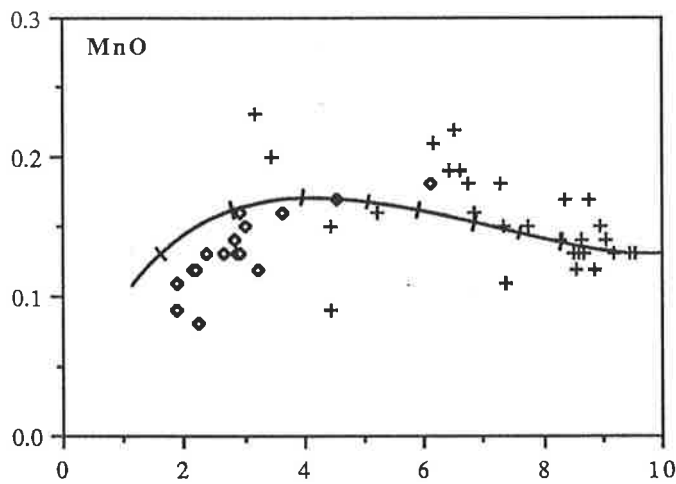
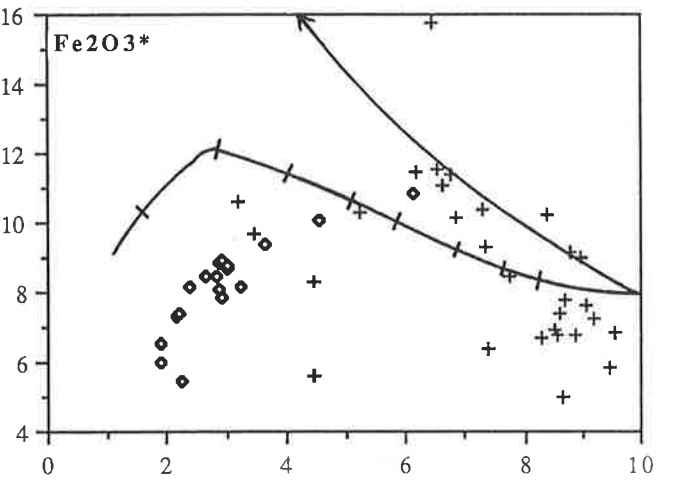
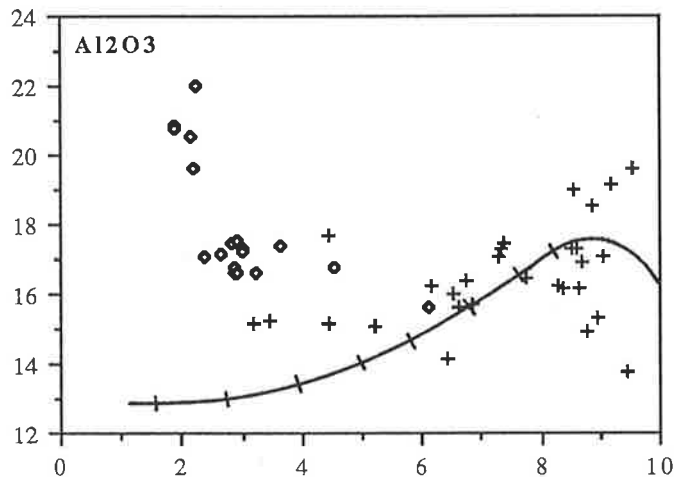
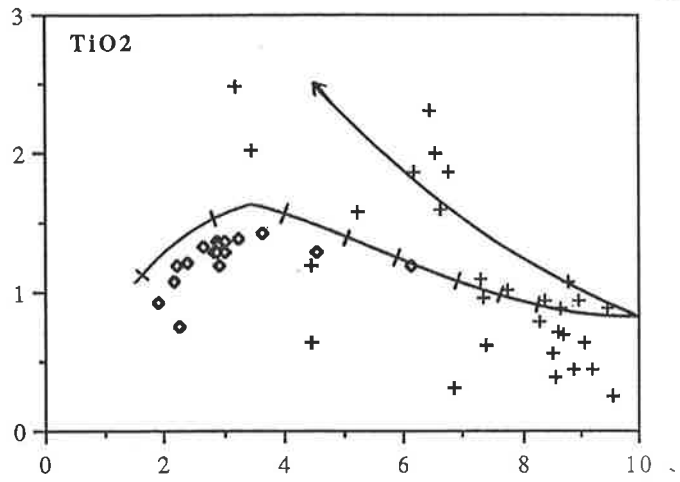
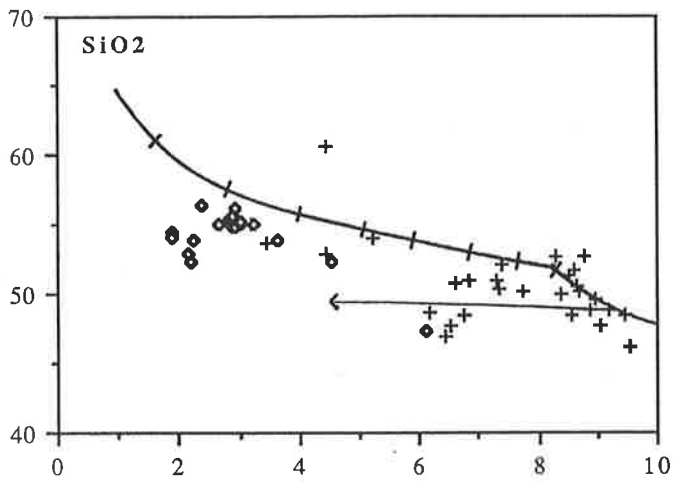
composition and temperature (which is itself calculated from the composition). The equilibrium compositions and proportions of these minerals are then calculated and their total composition subtracted from the magma. The mineral assemblage appropriate to the new magma composition and temperature is then calculated and the process repeated iteratively as a model of fractionation. The geochemical trends produced can then be compared with the gabbro data bearing in mind that the more adcumulative samples will lie off the trends. This approach also has the advantage that the fractionating assemblage is constrained by phase diagram information to be realistic for a given composition and increasingly sophisticated computer simulation programs have been developed over the last 10 years. The modelling reported here was performed using a 1990 version of the low pressure basaltic fractionation simulation program of Nielsen (1988b). This program (TRACE5) uses partition coefficient data to calculate the trace element concentrations simultaneously with the major element liquid lines of descent. The mathematical rationale is described in detail in Nielsen (1988a, b) and Defant and Nielsen (1990). For all program runs fO_2 was set at QFM and $Fe^{2+}/Fe_{total} = 0.9$ in accordance with the findings in chapter 2.

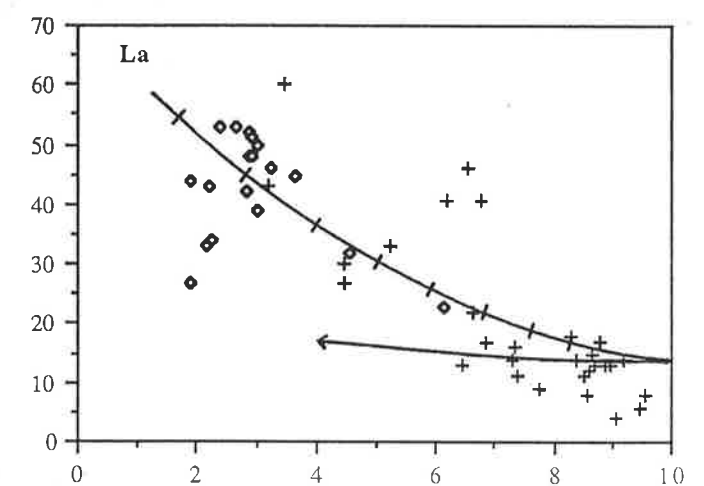
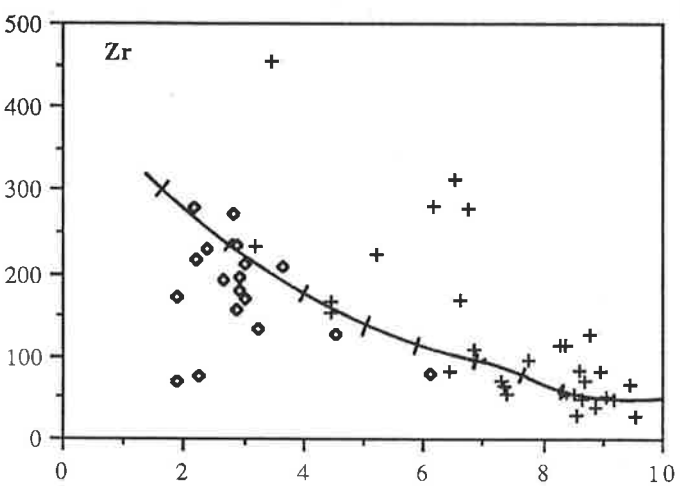
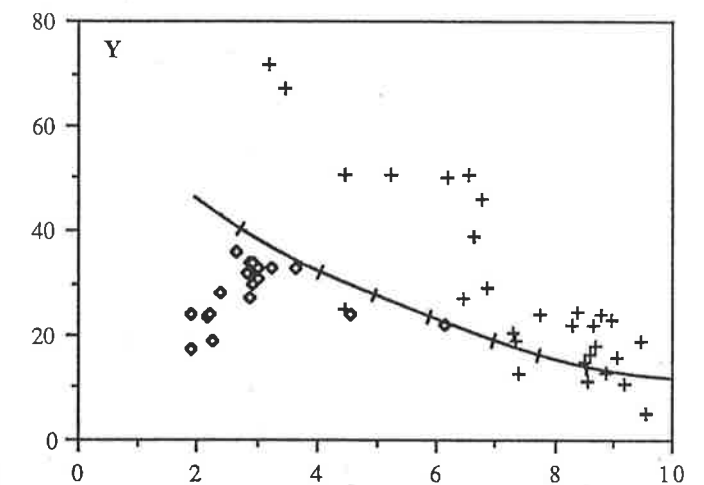
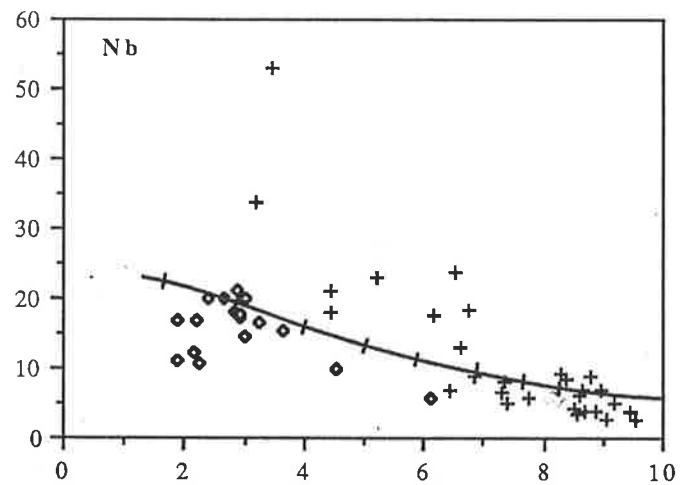
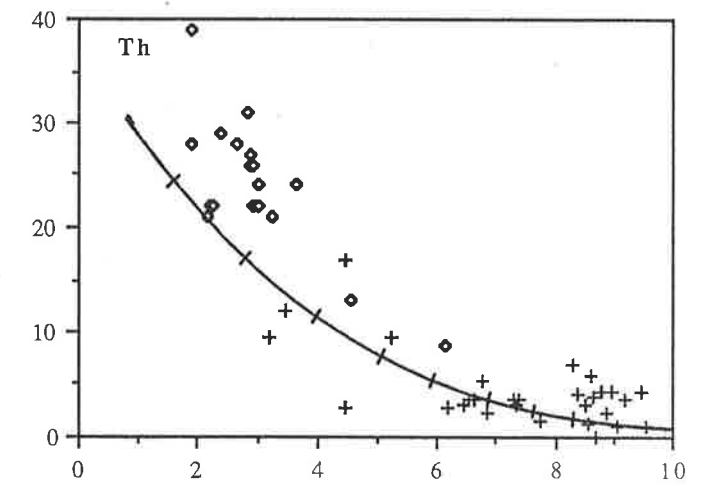
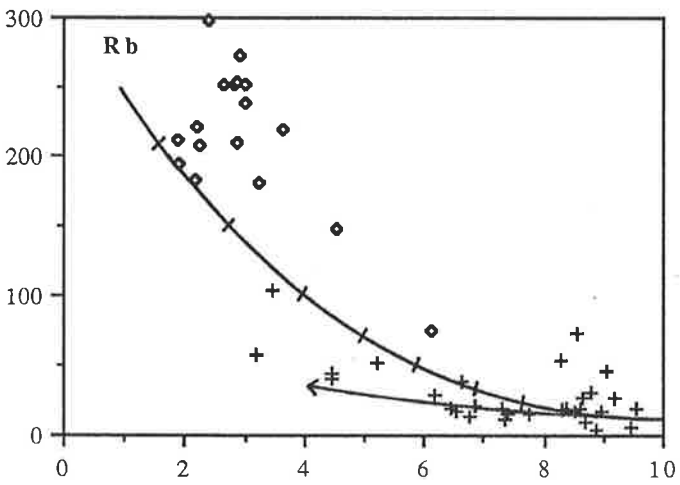
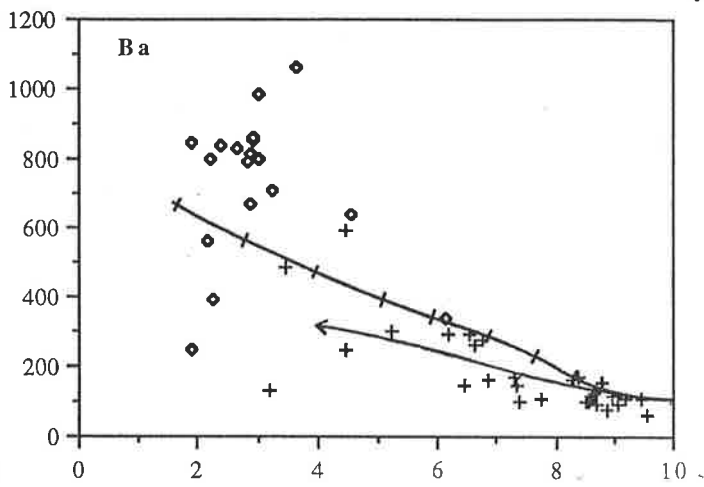
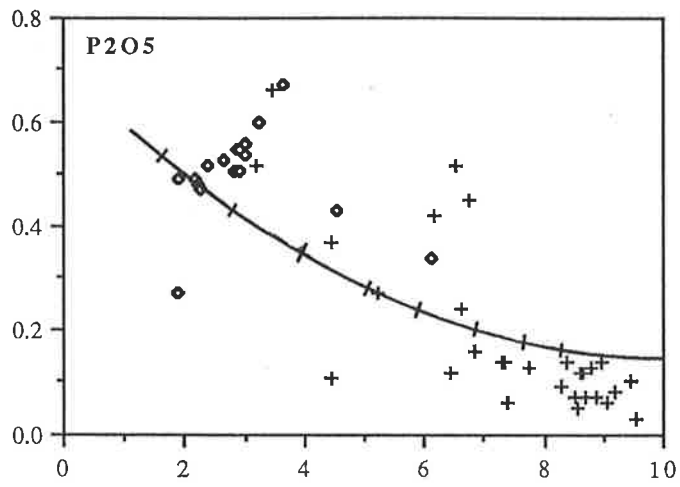
The results of modelling the approximated parental magma are shown on MgO variation diagrams (Fig. 3.8) on which the gabbros with Mg# < 65 that are thought to approximate the liquid line of descent are plotted for comparison. It is apparent that simple fractionation of olivine subsequently joined by plagioclase and then pyroxene from this composition will not satisfactorily reproduce the observed chemical variation. In particular the enrichment factors for incompatible components (SiO_2 , K_2O , Rb, Ba, LREE) seen in the pyroxene monzonites and potassic gabbro data would require such extreme degrees of fractionation that the corresponding major element compositions would be too low in MgO and CaO. Early plagioclase fractionation produced a trend of rapidly increasing iron contents with little increase in SiO_2 . The decreases in TiO_2 , Fe_2O_3 and V seen in the gabbro data which evolved to silica enrichment with only moderate iron enrichment (indicating magnetite fractionation), are not reproduced. These observations indicate that this pure fractionation model is inappropriate, however this need not be due to an incorrect choice of parental magma composition. Indeed it is clear from the isotope data that more complex open system models involving assimilation are applicable.

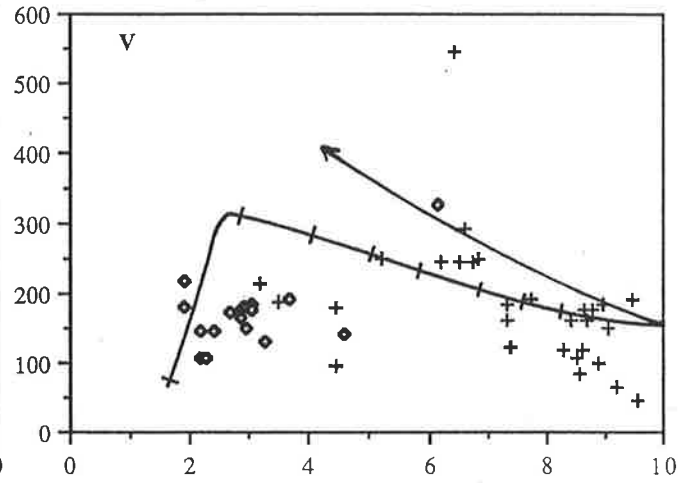
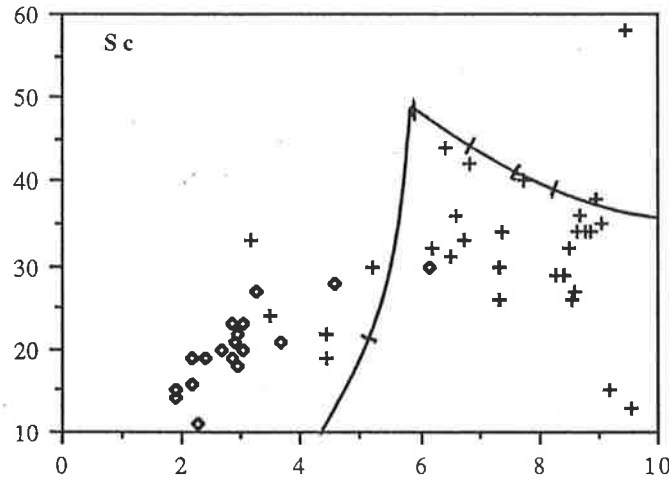
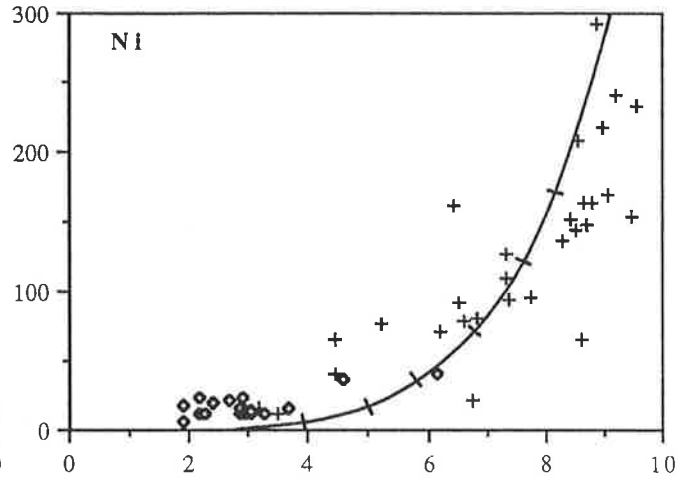
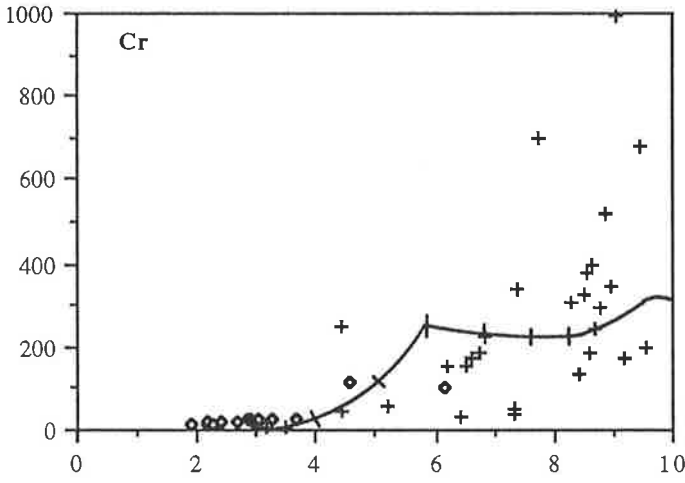
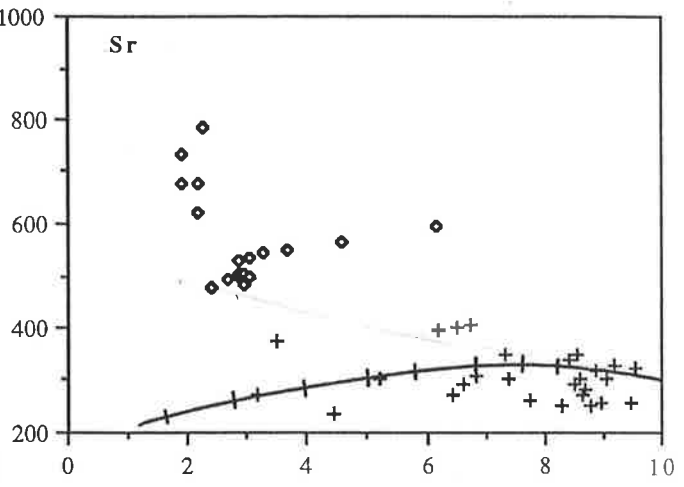
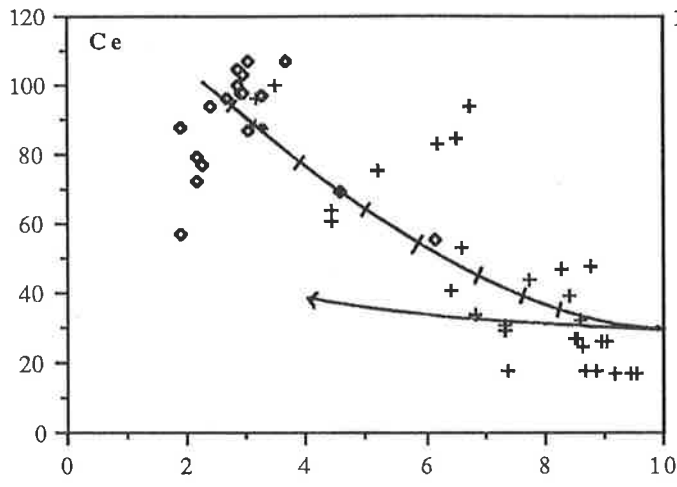
3.3.3. Combined assimilation and fractionation (AFC)

Convection in sizable basaltic intrusions efficiently transfers heat to the roof zone

Overleaf Figure 3.8. MgO variation diagrams with the trends modelled by TRACE5 for fractionation with 15% assimilation, the curves are marked in increments of 10% crystallization (crosses - gabbro data, diamonds - pyroxene monzonites and potassic gabbro data). Also plotted are some curves for straight fractionation with no assimilation. The end of these curves marked, with an arrow, is the composition after 70% fractionation for comparison with the last tick (70%) on the AFC curves.







enabling fusion of the roof rocks. Isotopic work on layered intrusions such as Skaergaard (Stewart and DePaolo, 1990) and laboratory experiments (e.g. Turner and Campbell, 1986) further indicate that assimilation occurs principally in-situ at the roof and margins of such intrusions. Accordingly the most likely assimilants for Black Hill are the local Late Precambrian to Cambrian Kanmantoo metasediments which the magma had to push upwards or stope in order to make room for itself. Table 3.1 contains an analysis of a typical metasediment from a drill hole near the intrusions as well as a migmatite leucosome from nearby metasedimentary outcrops which may approximate a partial melt of such metasediments. Between them this metasediment and leucosome broadly encompass the range of compositions displayed by the local metasediments (data from

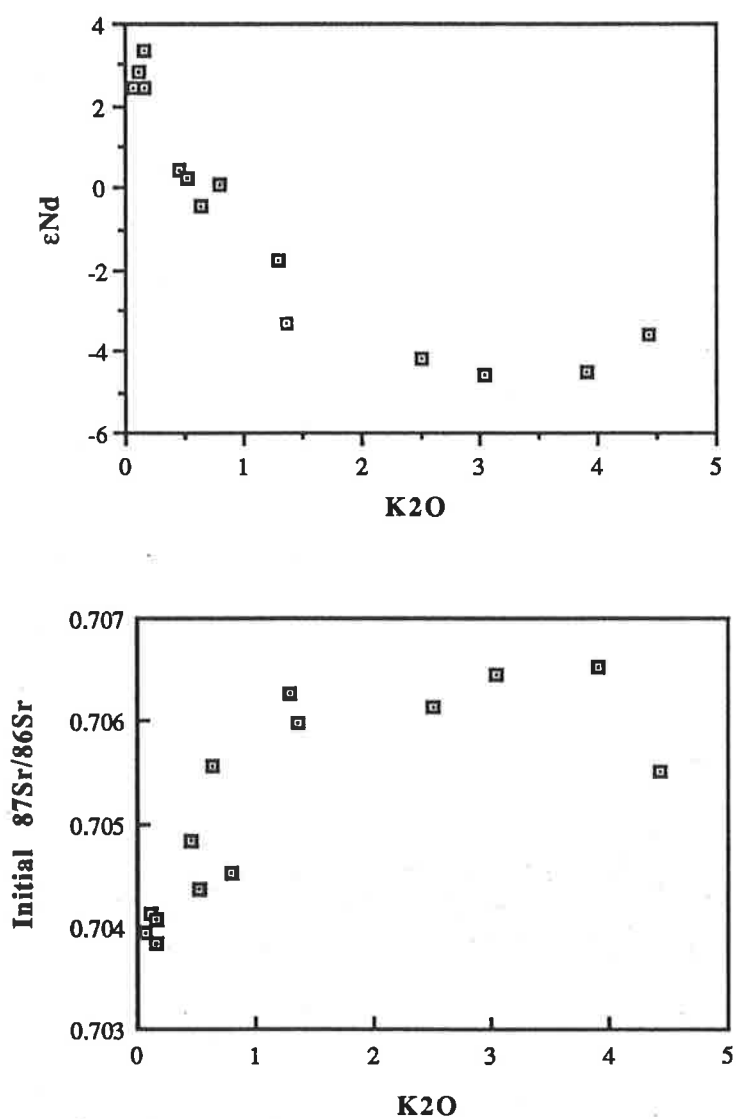


Figure 3.9. Plot of ϵ_{Nd} and initial Sr ratio vs K_2O showing the contamination trend of the Black Hill gabbros.

Mancktelow, 1979) and leucosomes which tend to be incompatible element enriched (data from Moeller, 1980). It has been argued that assimilation is likely to be wholesale rather than just a partial melt of the wall rock (eg. Turner and Campbell, 1986). For example the matrix of a partially molten wall rock may not be able to support itself and therefore the entire rock will founder into the magma. On the other hand the assimilant may be the composition of the first melt extractable from the country rock. Watson (1982) suggests that kinetic controls result in selective assimilation of some components such as SiO_2 and K_2O . The LREE enriched patterns and high K_2O concentrations (Fig. 3.9) of the monzonites from the margins of the Black Hill plutons suggests that the leucosome(s) may be the best approximation of the assimilant.

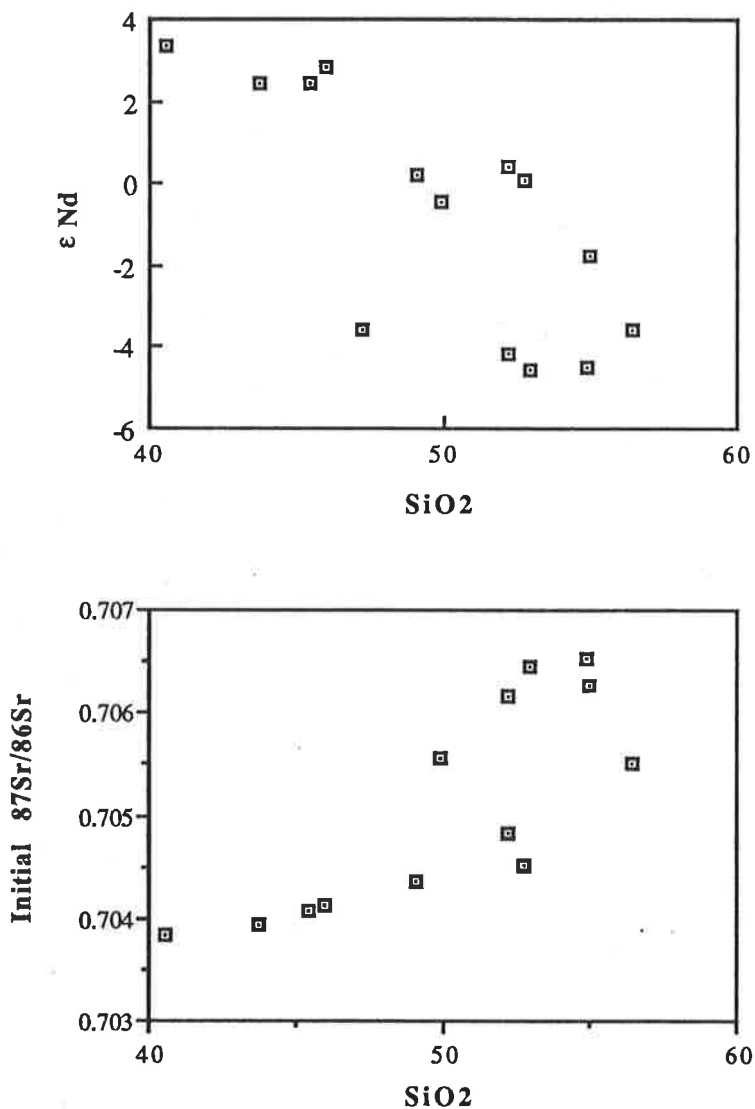


Figure 3.10. Plot showing the positive correlation between ϵNd and initial Sr ratio vs SiO_2 suggesting combined fractionation and assimilation for the Black Hill gabbros.

Contamination throughout the series of gabbros is indicated by the correlation between K_2O and both ϵNd and initial $^{87}Sr/^{86}Sr$ (Fig. 3.9). However, simple mixing between mantle derived magma with $<1\%$ K_2O and the Kanmantoo samples with 3-5% K_2O would require that the marginal gabbros, containing up to 4.4% K_2O , be near 100% crustal melts. Such a hypothesis is clearly untenable and combined assimilation and fractionation is more probable. In figure 3.10 initial $^{87}Sr/^{86}Sr$ shows a curvilinear increase with increasing silica whilst ϵNd displays a curvilinear decrease. Although the most SiO_2 -poor samples are cumulates, such correlations between an index of differentiation and isotopic values are evidence for combined assimilation and fractionation (AFC).

The program used to assess pure fractionation, TRACE5, is designed to also model AFC processes following the equations of DePaolo (1981). Modelling the same parental magma as before, this time with varying degrees of contamination was tried and a reasonable fit to the data was achieved for fractionation combined with 20% assimilation of the migmatite leucosome (assimilation rate/fractionation rate = $r = 0.2$). In the MgO variation diagrams (Fig. 3.8) it can be seen that the modelling comes quite close to approximating the Black Hill compositional array which straddles the calculated trends for most elements. Importantly the sequence of incoming fractionating phases and their proportions (see table 3.3) are appropriate to those expected from the phase diagrams (section 3.3.1) and correspond well to the cumulates found at Black Hill (chapter 2). The compositions of these phases (table 3.3) generally correspond to those found in the cumulates with the exception that the olivine hiatus in which orthopyroxene replaced olivine is not reproduced.

Looking in more detail it is not surprising that some discrepancies remain, particularly as the gabbros are not representative of pure liquids. In the plots for TiO_2 , V and $Fe_2O_3^*$ these elements become too enriched because magnetite commences fractionation too late so that the inflection marking magnetite fractionation is displaced to low MgO values. Some evolved gabbronorites lie below the modelled trend for SiO_2 and well above the TiO_2 and Y trends suggesting they contain cumulus magnetite and apatite and are not properly representative of liquids. These samples are themselves complimentary to pyroxene monzonites which on textural grounds are likely to be the closest approximation of liquids. The pyroxene monzonites are displaced below the trends for TiO_2 and Y suggesting a cumulate-liquid relationship with the TiO_2 and Y enriched gabbronorites. These contaminated monzonites from the pluton margins are displaced to slightly higher Rb, K_2O , Ba and Th than the calculated trends.

The Cr and Ni values used for the parental magma are typical of MORB and the Ni trend is closely matched. This is not true for Cr however the mineralogical data suggest Cr (and Ni) should be higher in the parental magma. The modelled trend for Sc

Table 3.3. Modelling results from TRACES for fractionation with 20% assimilation (see text for details)

% Crystallized	Parental Magma	Assimilant	5%	10%	20%	30%	40%	50%	60%	70%	80%	90%
SiO2	48.18	71.70	50.82	51.07	51.85	52.77	53.91	55.06	56.34	58.04	62.62	71.68
TiO2	0.80	0.72	0.65	0.91	1.01	1.13	1.27	1.42	1.57	1.69	1.12	0.06
Al2O3	16.10	12.50	17.52	17.17	16.41	15.56	14.63	13.90	13.51	13.13	12.93	13.19
Fe2O3*	7.98	4.74	8.15	8.38	8.89	9.43	9.97	10.66	11.41	12.10	9.90	3.33
MnO	0.13	0.06	0.13	0.14	0.14	0.15	0.16	0.17	0.17	0.16	0.13	0.05
MgO	10.00	1.71	8.55	8.23	7.63	6.91	5.95	5.04	4.02	2.83	1.67	0.33
CaO	10.01	0.64	10.82	10.67	10.43	10.18	9.95	9.19	7.85	6.08	4.23	1.25
Na2O	2.60	3.07	2.84	2.85	2.89	2.93	2.98	3.07	3.23	3.41	3.69	4.22
K2O	0.82	4.25	0.92	1.00	1.18	1.38	1.63	1.95	2.37	2.95	3.81	5.24
P2O5	0.15	0.21	0.16	0.17	0.19	0.22	0.25	0.29	0.34	0.41	0.52	0.70
Cr	300	59	219	213	226	225	221	153	51	3	0	0
Ni	400	26	225	185	121	71	34	14	4	1	0	0
Sc	35	10	37	38	41	44	48	30	10	2	0.4	0.1
V	150	70	160	166	183	201	224	249	279	313	73	0.5
Pb	5	6	5.5	5.7	6.2	6.8	7.5	8.5	9.7	11.2	13.5	16
Rb	14	135	18	21	30	41	56	76	106	156	254	538
Sr	300	116	326	323	318	310	300	290	278	254	209	85
Ba	160	893	180	199	236	280	332	397	480	588	739	913
Nb	6.4	13	7	7.5	8.4	9.6	11	13	15	18	22	26
Zr	50	411	57	65	80	99	121	149	186	234	302	392
Y	13.5	42	15	16	18	21	25	29	33	39	47	52
Th	1.2	25	1.7	2	3	4.3	6	8.5	12	17.8	29	63
U	2.25	4	2.6	2.6	2.9	3.3	3.8	4.4	5	6.3	7.9	10
La	14	53.8	15.6	16.8	19.4	22.5	26.2	30.9	36.9	44.9	56.4	72.4
Ce	30.5	88.6	33.7	36	41.2	47.3	54.7	64	75.8	91.5	114.5	147
Nd	14	39.6	15.5	16.5	18.9	21.6	25	29.1	34.3	40.9	50.6	62.5
Sm	3.3	6.4	3.6	3.8	4.3	4.9	5.6	6.5	7.5	8.8	10.5	12
Eu	1.2	1.4	1.3	1.3	1.5	1.7	1.8	2	2.2	2.4	2.7	2.8
Gd	3.6	4.4	3.9	4.1	4.6	5.2	5.8	6.6	7.6	8.7	10.2	11.3
Dy	3.8	3.2	4.1	4.3	4.8	5.3	6	6.8	7.6	8.6	10	10.9
Er	2.1	1.3	2.3	2.4	2.6	2.9	3.3	3.7	4.1	4.6	5.3	5.7
Yb	2	1.1	2.2	2.3	2.5	2.8	3.1	3.5	4	4.8	5	2.9
Liquidus Temperature (C)			1205	1196	1195	1184	1168	1152	1133	1103	1079	1042
Fractionating Assemblage:												
Ol, %; Fo			99:89	64:88	27:87	28:85	30:83	18:79	9:75	6:69	6:62	
Plag, %; An				35:69	73:68	72:67	70:65	60:63	51:60	50:55	46:51	40:44
Px, %; En:Fs:Wo								22:46:43:11	40:44:42:14	44:40:40:20	38:36:41:23	42:32:43:25
Sp, %			1	1							10	18
Cumulate			peridotite	troctolite	troctolite	troctolite	troctolite	ol gabbro	ol gabbro	ol gabbro	ol gabbro	gabbro
Epsilon Nd	3.35	-12.6	2.25	1.3	-0.3	-1.5	-2.5	-3.4	-4.1	-4.75	-5.3	-5.8
87Sr/86Sr	0.7038	0.7225	0.7039	0.7041	0.7045	0.7048	0.7052	0.7057	0.7062	0.7067	0.7075	0.7085

becomes depleted too quickly once pyroxene crystallization commences indicating that the assigned partition coefficient is too high.

The enrichment of Sr and Al_2O_3 in many of the pyroxene monzonites is not reproduced. Sr and Al_2O_3 would be contained in alkali-feldspar which occurs in high abundance in these rocks though it is not cumulative in origin. The only cumulates that are complimentary to the Sr and Al_2O_3 trends for these monzonites are the norites (see Fig. 3.2) which are not spatially associated with the monzonites. The enrichment of Sr and Al_2O_3 remains an unsolved problem.

TRACE5 does not simulate minor phase fractionation and in the case of P_2O_5 , for example, enrichment should probably be reached earlier and then be followed by a decrease in the pyroxene monzonites due to apatite fractionation. Minor phase separation or accumulation is probably important in explaining much of the variation seen in the LREE and incompatible elements of the evolved gabbros.

Nevertheless without trying to exactly reproduce the trends of the gabbros, which are not perfectly representative of liquids anyway, this modelling shows that compositions like those of the more evolved gabbros can be obtained by approximately 70% fractionation of a tholeiitic parent accompanied by some 20% assimilation (Table 3.3). Figure 3.11 shows the close match between the calculated composition and a typical pyroxene monzonite.

To further assess in-situ contamination the Kanmantoo metasediment and the migmatite leucosome were analysed for their isotopic characteristics (Table 3.2). For the purposes of the following modelling the leucosome and metasediment are roughly

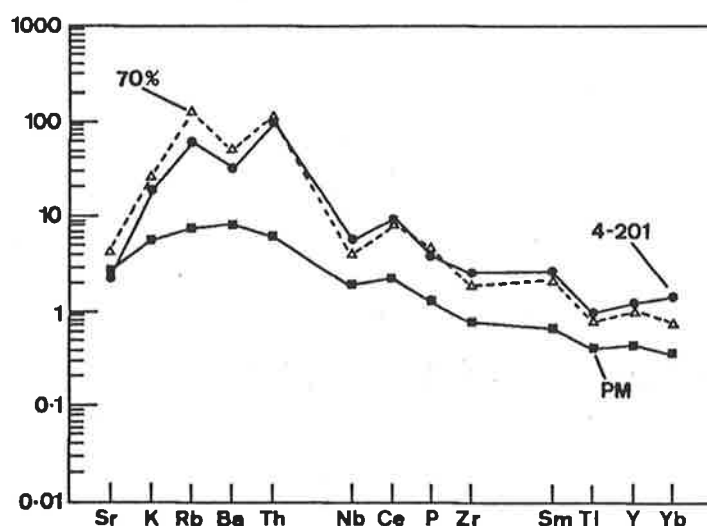


Figure 3.11. Spidergram as in Fig. 3.7. with the parental Black Hill magma composition and the product of 70% crystallization calculated by TRACE5 compared with a pyroxene monzonite from Black Hill.

interchangeable due to their similar Sr and Nd concentrations and isotopic ratios (Table 3.2). The Nd and Sr concentrations chosen as a starting composition were the same as those for the parental magma used in the modelling above, and the isotopic composition the same as the most mafic cumulate. Using KD's from Jacobsen and Wasserburg (1979) bulk distribution coefficients of D_{Sr} 0.65 and D_{Nd} 0.035 appropriate for 60% plagioclase and 40% olivine fractionation were calculated. The incoming of clinopyroxene has little effect on D_{Sr} whilst increasing D_{Nd} , however changing the D's within reasonable limits has only minor effect on the modelling compared with varying the parental magma concentrations and isotopic compositions. Figure 3.12 shows an AFC curve, calculated using the AFC equations of DePaolo (1981), involving 20% assimilation of the leucosome ($r = 0.2$). The curve reproduces the isotopic array of the gabbros quite well and importantly the pyroxene monzonite compositions are matched at about 70% crystallization which agrees with the results from the preceding modelling.

This then provides a self consistent model which appears broadly able to account for the origin of the gabbros after intrusion into their upper crustal chambers. However, although the parental magma composition cannot be rigidly defined, the implied parental magma isotopic ($\epsilon_{Nd} +3.4$, $^{87}Sr/^{86}Sr$ 0.7038) and elemental compositions are not appropriate for a primary melt from the contemporary depleted mantle. Modelling of

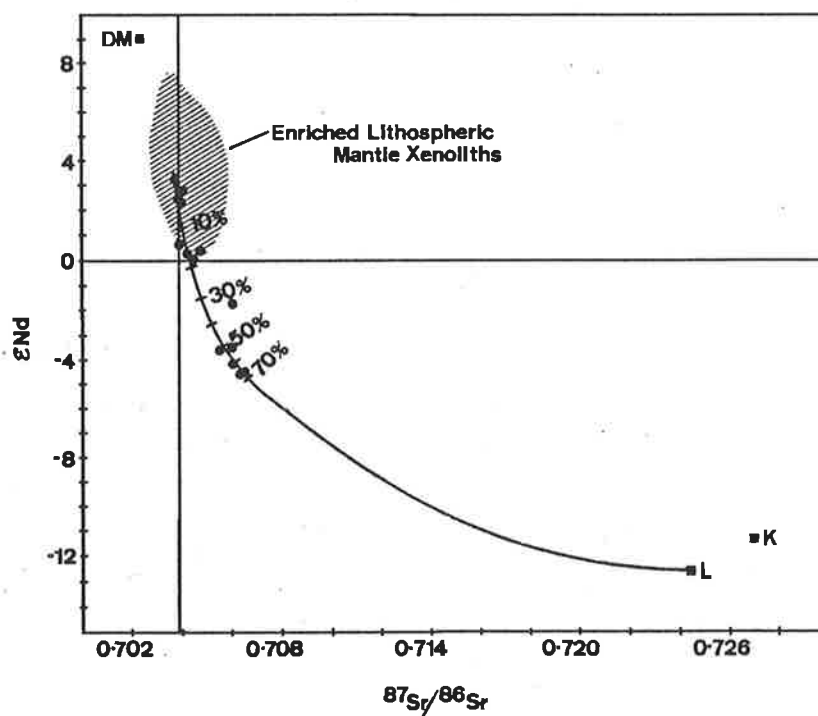


Figure 3.12. Plot of ϵ_{Nd} vs Sr initial ratio for the Black Hill gabbros with the calculated AFC curve for 20% assimilation of the migmatite leucosome (L). Diagram also shows the positions (at 487 Ma) for the depleted mantle (DM), the Kanmantoo metasediment (K) and the field of lithospheric mantle xenoliths (stippled). Xenolith data from McDonough and McCulloch (1987), Griffin *et al.* (1988).

combined assimilation and fractionation starting with a MORB-type end-member, with depleted mantle isotope ratios, requires more than 45% assimilation to produce the isotopic ratios of the pyroxene monzonites by ~70% crystallization. This degree of assimilation results in a modelled composition that is far more siliceous than the observed monzonites and has double the observed incompatible element composition. Modelling the monzonites to result from less crystallization does not reproduce their chemistry either and is in conflict with the presence of phases like zircon that indicate these are highly fractionated rocks (cf chapter 2).

3.3.4. Source implications

An important result from both the data on the peridotites and the modelling above, is that their parental magma was both isotopically and incompatible element (Rb, Ba, K₂O, LREE) enriched relative to depleted mantle. Furthermore the isotopic enrichment indicates that the incompatible element enrichment is not simply a function of small degree partial melting of a depleted mantle source. The olivine and pyroxene data suggest that the parental magma did not undergo more than 5% fractionation prior to filling the upper crustal magma chambers, therefore contamination can be assessed using mixing calculations instead of AFC.

Three possible origins of the enrichment include: 1) increased assimilation of local Kanmantoo material; 2) lower crustal contamination during magma ascent; 3) an enriched lithospheric mantle contaminant or source. These scenarios will be considered in conjunction with mixing calculations in table 3.4. These calculations mix a MORB-like depleted mantle magma (at 487 Ma ⁸⁷Sr/⁸⁶Sr = 0.70248, ¹⁴³Nd/¹⁴⁴Nd = 0.512480 and for a ~10% mantle partial melt Sr = 185 ppm, Nd = 7.3 ppm, La = 2.8 ppm, Rb = 2 ppm, K₂O = 0.15%) with possible contaminants to achieve the La, Rb and K₂O contents of the parental magma in table 3.3. The isotopic characteristics of the resultant mix are then compared with the isotopic character of the parental magma which taken to be no more evolved than the most primitive peridotite at Black Hill (εNd 3.35, ⁸⁷Sr/⁸⁶Sr 0.7038).

1) If the parental magma resulted simply from mixing with mid to upper crustal Kanmantoo-like metasediment then 9% assimilation is required to produce the Rb content of the parental Black Hill magma, 29% for K₂O and 30% for La. As shown in table 3.4 this results in εNd too low and ⁸⁷Sr/⁸⁶Sr too high when compared with the Black Hill peridotite data above. The results are similar for a model involving the leucosome as a partial melt approximation (9-20% required). Additionally, high amounts of assimilation of the leucosome would produce a resultant magma with Mg# <65 which would therefore not crystallize olivines of Fo₈₆. The resultant increase in SiO₂ may also force the magma to follow a more calc-alkaline trend (Grove and Baker, 1984) and cause orthopyroxene to

Table 3.4. Selected analyses of potential contaminants of the parental Black Hill magma including outcropping Late Proterozoic/Cambrian Kanmantoo metasediments and leucosome (1-376, 779-50), Early Proterozoic rocks from Eyre Peninsula FGG-1, QGNG & EAGG (Mortimer, 1984), lithospheric mantle xenoliths DR 11308 & DR 9735 (Griffin *et al.*, 1988; O'Reilly and Griffin, 1988) and a lower crustal xenolith (815). Also listed is the range of isotopic values applicable to these samples at 487 Ma. The lower part of the table gives the % assimilation of each of these, required to contaminate a hypothetical MORB magma (Sr 185 ppm, $^{87}\text{Sr}/^{86}\text{Sr}$ 0.70248, Nd 7 ppm, $^{143}\text{Nd}/^{144}\text{Nd}$ 0.512480) in order to achieve the La, Rb and K₂O contents estimated in the parental Black Hill magma, and the calculated $^{87}\text{Sr}/^{86}\text{Sr}$ ratio and ϵNd that would result from this contamination.

Rock type Sample #	Metased 1-376	Leucosome 779-50	Opx-granitoid FGG-1	Gabbro-norite QGNG	Granite EAGG	Gt-cpx granulite 815	Lherzolite Xen DR 11308	Pyroxenite Xen DR 9735
SiO ₂	60.85	71.70	68.33	56.45	76.96	48.33	43.61	43.92
TiO ₂	1.03	0.70	0.65	0.80	0.07	0.45	0.05	2.60
Al ₂ O ₃	16.33	12.50	14.67	14.64	11.91	14.40	2.17	12.11
Fe ₂ O ₃ *	7.40	4.74	4.58	9.85	1.04	9.55	10.65	10.40
MnO	0.16	0.06	0.07	0.15	0.03	0.16	0.18	0.11
MgO	3.39	1.71	0.97	5.74	0.14	10.74	39.36	14.30
CaO	3.35	0.64	2.82	6.71	0.75	13.54	2.66	15.20
Na ₂ O	3.33	3.07	2.83	2.44	3.00	1.60	0.40	1.85
K ₂ O	2.44	4.25	5.07	2.38	5.20	0.40	0.11	0.35
P ₂ O ₅	0.19	0.21	0.16	0.21	0.00	0.02	0.33	0.05
Cr	101	59	12			725	23	402
Ni	46	26	21	105	11	143	1953	188
Sc	23	10	13	28	1	46	9.9	34
V	170	70	41	159		223	52	397
Rb	145	135	229	109	405	4	0.85	4
Sr	143	116	147	227	12	161	80.2	175
Ba	378	893	915	558	5	500	9	80
Nb	16.3	13	16	11	5	10	8	5
Zr	190	411	305	206	109	18	21	48
Y	35	42	41	34	52	9	6	18
La	36	54	59	33		1	6.2	3.4
Ce	79	89	120	67		2	14.5	14.1
Nd	30	40	49	29	34	3	6.79	15
At 487 Ma:								
epsilon Nd	-11.3	-12.6	-16 to -30	-16 to -30	-16 to -30	-12 to -32	4.6	4.3
$^{87}\text{Sr}/^{86}\text{Sr}$	0.7269	0.7225	0.787	0.729	>1	>0.712	0.7049	0.7032
For La=14								
% assim	30	20	19	33	28	>100%	>100%	>100%
$^{87}\text{Sr}/^{86}\text{Sr}$	0.7086	0.7052	0.7158	0.7125	0.7098			
epsilon Nd	-4	-3.5	-6.3	-7.6	-7.1			
For Rb=14								
% assim	9	9	5	11	3	>100%	>100%	>100%
$^{87}\text{Sr}/^{86}\text{Sr}$	0.7042	0.7037	0.7059	0.706	0.7031			
epsilon Nd	3.1	1.4	2.5	0.7	5.8			
For K₂O=0.85								
% assim	29	17	14	29	14	>100%	>100%	>100%
$^{87}\text{Sr}/^{86}\text{Sr}$	0.7083	0.7048	0.7122	0.7113	0.7056			
epsilon Nd	-3.7	-2.4	-4.1	-6.5	-1.8			

replace olivine as the liquidus phase which also contradicts the observations. Scenarios of major assimilation seem unlikely on thermal grounds as well.

2) An alternative is that the parental magma injected into the magma chambers suffered contamination at lower crustal levels. Potential lower crustal material in this terrain is preserved in Archaean and Proterozoic felsic and mafic gneisses that outcrop to the west on Eyre Peninsula. These were potentially once near the base of the crust and preserve evidence of 800-1000 °C, 8-10 kbar granulite facies metamorphism (Fanning, 1975). Isotopically, at 490 Ma, these would have had $\epsilon_{Nd} \sim -16$ to -30 and $^{87}Sr/^{86}Sr > 0.76$ (Webb *et al.*, 1986; McCulloch, 1987; Daly and Fanning, 1990). Geochemical data on these basement gneisses (Fanning, 1975; Mortimer, 1984) are similar to other lower crustal rocks (eg Weaver and Tarney, 1980, 1981) in having moderate K_2O contents but Zr/Nb ratios (~ 20) considerably higher than the likely parental Black Hill magma (10-12). Thus on the one hand the isotopes and Zr/Nb ratios only permit small amounts of assimilation by the parental Black Hill magma and on the other quite large amounts are required if these are the source of incompatible element enrichment. The calculations in table 3.4 show that, for a range of felsic, intermediate and moderately mafic potential contaminants, to achieve the incompatible element enrichment in the parental magma results in a magma with $^{87}Sr/^{86}Sr > 0.7066$ which is higher than the most contaminated pyroxene monzonites.

Estimates of lower crustal mafic granulite compositions have very low Rb, LREE, K_2O and highly radiogenic isotopic characteristics (Weaver and Tarney, 1980, 1981; Taylor and McLennan, 1985) which does not allow them to contribute significantly to incompatible element enrichment without producing severe isotopic shifts. Mafic granulite and eclogite xenoliths from the lowermost crust (10-16 kbars) found in kimberlites in the Adelaide Foldbelt have isotopic compositions (McCulloch *et al.*, 1982; Table 3.4) which make them suitable contaminants (at 490 Ma $\epsilon_{Nd} -12$ to -21 , $^{87}Sr/^{86}Sr$ 0.7066 to 0.71196). However their incompatible element abundances (Arculus *et al.*, 1990) are less than the inferred parental Black Hill magma which therefore cannot be a depleted mantle magma contaminated by these granulites (see Table 3.4).

3) A further alternative is that the Black Hill magma was contaminated by enriched subcontinental lithospheric mantle such as the K-rich layer of McKenzie (1989). The data of Griffin *et al.*, 1988; O'Reilly and Griffin, 1988; McDonough and McCulloch, 1987) on spinel lherzolite and Al-augite pyroxenite xenoliths from Mt Gambier and western Victoria provide ample evidence that parts of the local lithospheric mantle are enriched in incompatible elements. However, similar arguments to those above suggest the incompatible element enrichment in these xenoliths (Table 3.4) are too low to produce the parental Black Hill magma by contamination of a MORB-like magma, given the isotopic constraints.

Another possibility is that this enriched lithospheric mantle was itself the source of the parental Black Hill magma. The low KD's for incompatible elements in mantle phases result in partial melting producing considerably incompatible element enriched magmas. That a partial melt of such a source would be enriched in incompatible elements is demonstrated by the enriched nature of the basalts that host the xenoliths (eg McDonough *et al.*, 1985). At 487 Ma these xenoliths have ϵ_{Nd} which ranges from +6 to -1 and $^{87}Sr/^{86}Sr$ around 0.7035-0.7069 which can be seen in figure 3.12 to be quite appropriate for the Black Hill parental magma. Depleted mantle T_{DM} model ages for the lithospheric mantle xenoliths extend from 600 Ma to 1200 Ma (McDonough and McCulloch, 1987) reflecting the (protracted) time over which enrichment occurred. T_{DM} model ages for the Black Hill gabbros fall similarly around 0.9 - 1.2 Ga.

The foregoing arguments show that the combined isotopic and incompatible element enrichment of the parental Black Hill magma (Fig. 3.7) is not easily explicable in terms of a model involving crustal contamination. This is because the evolved isotope data of the Proterozoic and Archean country rock and crustal basement do not permit enough contamination to produce the concentrations of incompatible elements inferred for this parental magma. In contrast, partial melting only requires moderate enrichment of the source provided that it has the right isotopic characteristics. Although it may not be possible to conclusively reject the crustal contamination hypothesis, because the parental magma composition is only an estimate, the preferred model is one involving partial melting of an enriched lithospheric mantle -for which there is some evidence. No magmatic rocks from the late-orogenic suite in South Australia have isotopic values more primitive than $\epsilon_{Nd} +5$ and $^{87}Sr/^{86}Sr$ 0.70341 (Turner and Foden, 1990b) and the limiting factor may be the nature of the source.

3.3.5. Chamber recharge and the norites

Any proposed origin for the norites has to explain the crystallization of orthopyroxene prior to plagioclase unlike all the other gabbros. This is not generally expected from basaltic magmas at low pressures where the typical crystallization sequence is ol \rightarrow ol + plag \rightarrow plag + px. At high pressures the crystallization sequence becomes ol \rightarrow opx \rightarrow opx + plag and the cross-over from ol + liq to opx + liq occurs between 3 and 5 kbars at 1200 °C even for high MgO, high SiO₂ rocks like boninites (Van Der Laan *et al.*, 1989). For tholeiites this cross-over is likely to be at higher pressures and so this cannot be the origin of the norites at Black Hill which demonstrably crystallized at low pressures along with other gabbros that display a typical low pressure, tholeiitic crystallization sequence. In chapter 2 it was suggested that the norites could result from fresh influxes of parental magma that mixed with more evolved (SiO₂-rich) magma resident in the chambers. Phase equilibria diagrams (Fig. 3.6b) indicate this is consistent with the

increase in SiO₂ pulling the resultant magma into the orthopyroxene volume.

Unfortunately the chemistry of the norites is strongly dominated by the modal content of opx making recharge difficult to assess. However recharge possibly accompanied by eruption, seems likely in such chambers and may be critical in producing the repetition of cyclical units. Interestingly some of the gabbros which most closely approximate the composition of the parental Black Hill magma composition are norites (eg 19-635 in particular the relatively fine grained (chilled) base of a norite layer; sample 19-877, Appendix B). This may reflect their partial origin in fresh injections of parental magma. A more detailed isotopic study than has been attempted here, comparing norite layers with the gabbros above and below seems the best way to test the recharge hypothesis. If this hypothesis is correct then each norite layer should show a reversal to more chemically and isotopically primitive values than the layers above or below it. Some isotopic and chemical data do support this, for example, norite 19-635 has a more primitive chemical and isotopic composition than the gabbro-norite 19-1287 below it consistent with mixing with isotopically more primitive magma. Likewise norite 11-941 has SiO₂ and REE concentrations similar to many of the evolved pyroxene monzonites yet much higher Cr and Ni and this sample lies off the isotope AFC trend at a higher εNd (Fig. 3.12) again suggesting mixing with isotopically more primitive magma.

3.3.6. Origin of the granophyric sills

Granophyre composed of quartz and alkali feldspar with occasional plagioclase and rare splinters of subsolidus biotite occurs as dyke or sill like bodies up to 6m thick both in outcrop and within the gabbros intersected in drill core. The relative timing of the generation of these granophyres, relative to their host gabbros, is difficult to establish though typically there is evidence for mixing with mafic magma at their margins to produce a mesocratic rock (chapter 2). This suggests contemporaneity and interstitial granophyric material, which could be the source of these sills, occurs in many of the gabbro-norites (cf Fig. 2.5c). Chemically the granophyre is rhyolitic with >70% SiO₂ and rich in alkalis and incompatible elements (Zr, Nb, Y, Ga, Rb). CaO, Al₂O₃ and compatible trace elements (Ni, Cr, Sc, V, Sr) are depleted. Rb/Sr and Ga/Al ratios are typically high whilst Ba/Rb is low. Rare earth patterns of several granophyres have very high overall REE concentrations (up to 200 x chondrite for La), show considerable LREE enrichment, similar to the gabbros (La/Yb >5) and have large negative europium anomalies (see Fig. 3.3). These are all characteristics of A-type granite (Collins *et al.*, 1982). Incompatible element ratios, that might be indicative of their parental magma, such as Zr/Nb, Y/Nb and La/Yb are often indistinguishable from the gabbros. Furthermore the isotopic characteristics of the granophyres are primitive like the olivine gabbros and gabbro-norites indicating that they too owe little of their origin to evolved crustal material.

Similar observations have been made by Stewart and DePaolo (1990) on granophyric pods in the Skaergaard Intrusion and the data seems consistent with evolution of the granophyre from the same source/parental magma as the gabbros.

McBirney (1975) postulated a mechanism of origin for some Skaergaard granophyres involving liquid immiscibility. However experimental data (eg. Ryerson and Hess, 1978) which shows that incompatible elements such as Zr, Nb, Y, LREE should be strongly partitioned in to the mafic liquid is inconsistent with the data from the Black Hill granophyres where the opposite is true. It seems more likely that they are the end products of extreme fractionation. Figure 3.13 shows a comparison between a Black Hill granophyre and the modelled TRACE5 composition resulting from 90% fractionation. The two patterns are very similar except for Ba and P which are too high in the modelled composition because the program does not fractionate apatite or

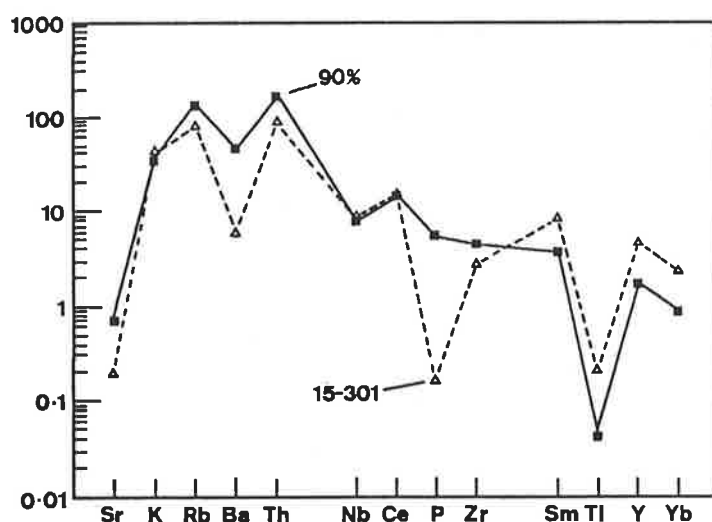


Figure 3.13. Spidergram comparing the result modelled by TRACE5 for 90% crystallization of the parental Black Hill magma and a granophyre from Black Hill (15-301). Normalization factors and order of elements after Pearce (1983).

alkali feldspar. There are still a few problems with this hypothesis because few rocks of intermediate composition (58-68% SiO₂) are observed and also the isotope data shows granophyric sills are less contaminated than the pyroxene monzonites. This means they do not form a continuation of the AFC processes that produced the pyroxene monzonites though the increased contamination in the pyroxene monzonites seems to be due to their location at the upper pluton margins and the granophyres may be have been derived from inner regions.

Possible mechanisms for the origin of the granophyric liquid include formation during an early stage when convection was strong and low density, fractionated liquids were gravitationally separated from crystals at areas of sidewall crystallization. Laboratory

experiments using aqueous solutions (see Turner and Campbell, 1986 for review) have suggested such mechanisms to be highly effective in removing fractionated liquids to an upper zone of a magma chamber.

A preferred mechanism, discussed further in the next chapter, involves coalescing of interstitial granophyric magma. Interstitial liquid in cumulates becomes enriched in components incompatible with the cumulus matrix of olivine, pyroxene and plagioclase. Intermediate compositions are not produced because the components for intermediate compositions are removed by diffusion to become incorporated in overgrowths on the cumulus phases. Alkalis and incompatible elements will not readily become incorporated in these overgrowths and become enriched in the rhyolitic residua that forms interstitial granophyric material (eg Fig. 2.5c). This liquid will have a solidus like the granite minimum, much lower than the surrounding matrix material, and will remain liquid for considerable periods. It seems likely that such interstitial liquid, which is also seen in other layered gabbroic plutons, could be capable of coalescing and/or gravitational separation. Compaction of the cumulate pile is probable (Sparks *et al.*, 1985) and would force expulsion of this granophyre to form sills at the top of the pile or even to leave the pluton as a separate felsic diapir.

As observed in the next chapter, geophysical evidence indicates the presence of a major mafic lopolith beneath the Black Hill plutons to which they are most likely connected. A silicic cap on such a pluton produced by either of the above mechanisms may become gravitationally unstable and separate intruding the mafic plutons above alternatively injection of mafic magma into the outcropping plutons could entrain rhyolitic liquid from the roof zone.

3.4. Discussion

There has been considerable debate over contamination and the origin of incompatible element enrichment in continental tholeiites, particularly continental flood basalts. Although the parental magma composition for Black Hill can only be estimated, the modelling serves to illustrate that fractionation was accompanied by about 20% in-situ assimilation of upper crustal metasediments this being most pronounced at the pluton margins. Not all of the ubiquitous incompatible element enrichment and isotopic signature can be fully accounted for by this in-situ contamination and must therefore have been partly a feature of the parental magma implying either lower crustal contamination or an enriched mantle source. Whilst it may not be possible to conclusively reject hypotheses involving some lower crustal contamination a significant component from an enriched source seems necessary. This coincides with numerous studies of continental flood basalts (eg. Menzies *et al.*, 1984) which indicate that incompatible element enrichment is

due to both upper crustal contamination and source region enrichment. It is suggested that this source was subcontinental lithospheric mantle that had been enriched by infiltration of small partial melts from the asthenosphere between 700 and 1200 Ma.

Both theoretical studies (eg. O'Nions and McKenzie, 1988) and direct observations on mantle xenoliths (eg. Menzies and Murthy, 1980; McDonough and McCulloch, 1987) indicate that much of the subcontinental mantle lithosphere is likely to be enriched in incompatible elements including the LREE. This enrichment seems likely to result from infiltration of small (<1%) partial melts from the asthenosphere (O'Nions and McKenzie, 1988; McKenzie, 1989) which will cause parts of the lithospheric mantle to have a lowered solidus. Such small partial melts will be strongly fractionated so that the increased Rb/Sr and Nd/Sm will over time develop isotopic anomalies. Nd model ages for the Black Hill gabbros (Table 3.2) and local mantle xenoliths (McDonough and McCulloch, 1987) are clustered around 0.7-1.2 Ga suggesting that LREE enrichment of the source occurred around this time when the lithosphere was undergoing extension forming the sedimentary troughs of the Adelaide Geosyncline (eg Foden *et al.*, 1989, appendix E3).

Fractionation of the tholeiitic Black Hill magma resulted in early iron enrichment with only mild silica enrichment during the removal of olivine and plagioclase and later pyroxene. With the onset of magnetite fractionation at about 60% crystallization this trend was followed by iron depletion and silica enrichment. Continued fractionation produced rapid silica enrichment and ultimately rhyolitic liquids after about 90% crystallization. At Black Hill granophyres testify to the development of such liquids though the mechanism may be complexly related to compaction of the cumulate piles and attendant expulsion of interstitial liquids. This fractionation of a mafic tholeiitic magma through a period of moderate iron enrichment and ultimately to rhyolite is similar to the evolution of tholeiites in Iceland (Macdonald *et al.*, 1990). It is also similar to the controversial proposal by Hunter and Sparks (1987) for the late evolution of the Skaergaard magma though it is important that no rocks as iron-rich as the Skaergaard ferrogabbros have been found at Black Hill.

In the case of the Black Hill magma there is some indication that this evolution is partly a consequence of assimilation which forced silica enrichment earlier than would occur under closed system fractionation. Running TRACE5 with the same starting magma composition and no assimilation results in a magma which after 70% fractionation has 16% Fe₂O₃* and only 51% SiO₂ (Rb 94 ppm, La 25 ppm). This is much like the evolutionary trend traditionally interpreted for Skaergaard. It appears that one consequence of assimilation, other than incompatible element enrichment, is to cause the magma to follow a fractionation path of SiO₂ enrichment. This can be seen in the ol-cpx-qtz ternary (Fig. 3.6c) where the parental liquid starting in the ol field evolves to intersect

the ol-cpx cotectic (note that all fields, cotectics and reaction points are + plag, because the diagram is plagioclase saturated). After this a liquid undergoing equilibrium crystallization will crystallize completely at the point ol-cpx-pig. With fractional crystallization liquids can proceed along the cpx-pig cotectic towards the pig-cpx-qtz point however the effect of assimilation of siliceous country rocks is to pull the path of the liquid towards the quartz apex much more quickly. Therefore assimilation effectively forces the liquid to follow a more calc-alkaline trend (see the extended discussion in Grove and Baker, 1984), reducing the degree of iron enrichment experienced relative to SiO_2 . This assimilation also seems to induce magnetite fractionation at an earlier stage assisting in SiO_2 enrichment and iron depletion. One point argued by McBirney and Naslund (1990) against the Hunter and Sparks (1987) interpretation for Skaergaard is that there is no evidence for the volumes of rhyolite predicted. In the South Australian example there is considerable evidence for such magma which may be the origin of the plutons and volcanics discussed in the next chapter.

Chapter 4. Source and evolution of A-type granites and volcanics from the Padthaway Ridge, South Australia: implications for A-type genesis

4.1. Introduction

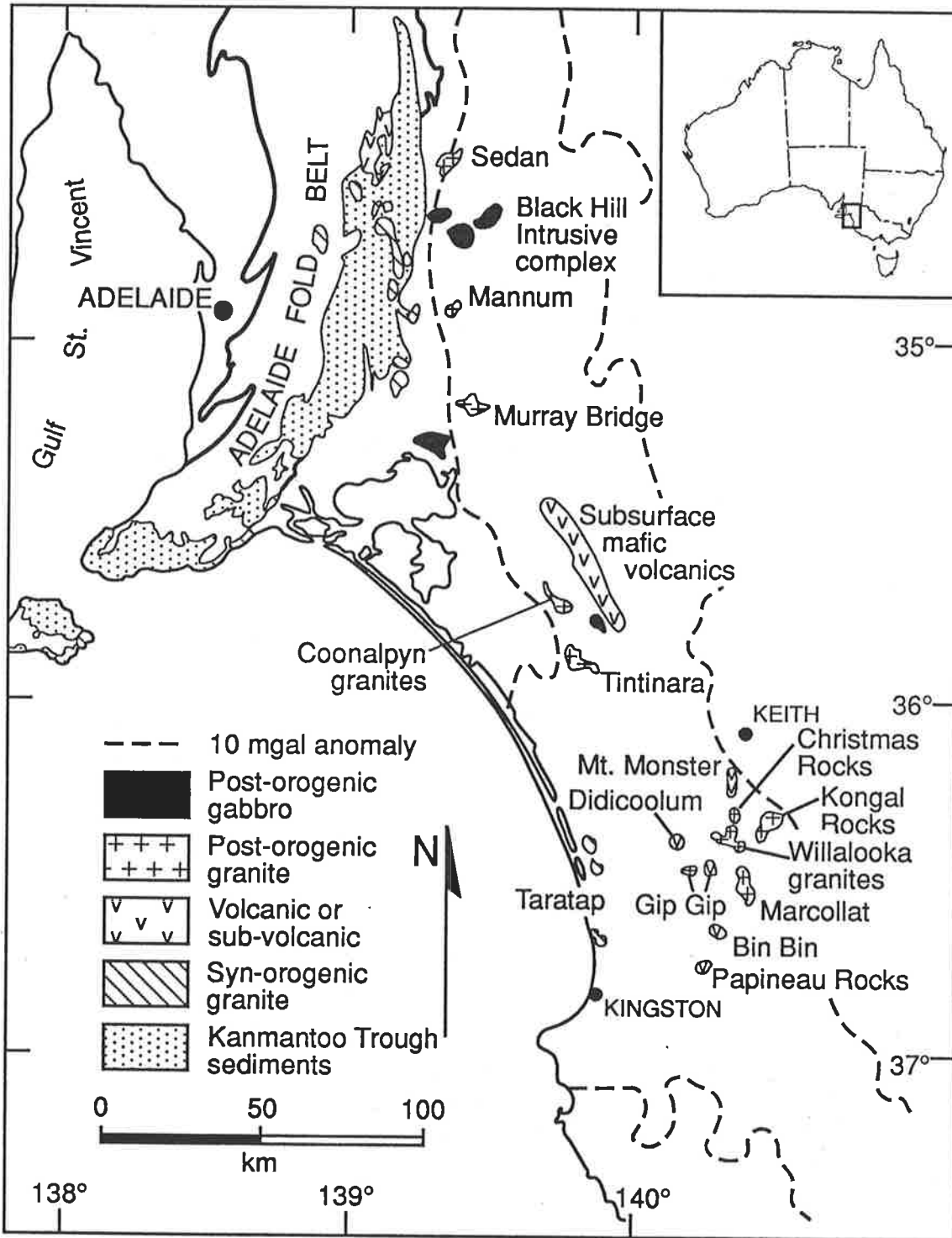
A series of shallow granite and acid volcanic outcrops, occurring as isolated exposures surrounded by Tertiary sediments, in southeastern South Australia form a roughly linear basement trend known as the Padthaway Ridge (Fig. 4.1). They were first described by Mawson and Parkin (1943), Mawson and Dallwitz (1945), Mawson and Segnit (1945) and later by Henstridge (1970) and Mancktelow (1979). In more recent studies (Turner, 1986; Turner *et al.*, 1989; Foden *et al.*, 1990a), the granites have been recognized to belong to the group of late-Delamerian granites with A-type characteristics that extend from the eastern Mt. Lofty Ranges through into western Victoria.

In chapter 3 it was noted that granophyric sills from the Black Hill plutons also have A-type compositions and that they appear genetically related to their host gabbros. This chapter investigates this possible relationship further by providing detailed petrology, geochemistry and isotope data for the Padthaway granites and volcanics. In so doing, the characteristics of A-type rocks are reviewed along with possible petrogenetic schemes for their origin. Through various lines of evidence it is suggested that these A-type magmas are not products of partial melting of lower crustal, melt depleted granulites. Rather, they formed by fractionation of mantle derived melts which obviates the need for an external heat source in their genesis.

4.2. Geological Setting

Although contacts are not exposed, drill core data indicate that the Padthaway granites intrude amphibolite grade metasediments analogous to the nearby Cambrian Kanmantoo Group (Rochow, 1971) which was deformed by the Cambro-Ordovician Delamerian Orogeny. The granites and volcanics display no metamorphic fabric, indicating that they post-date the deformation of this orogeny. Whole rock Rb-Sr isotope analyses Webb (1976) yield early Ordovician ages and low initial $^{87}\text{Sr}/^{86}\text{Sr}$ ratios between 0.704 and 0.708. More recent data constrain the age of this late-orogenic

Overleaf Figures 4.1. Map showing the localities of the Padthaway Suite granites and volcanics with the outline of the +10 milligal gravity anomaly of which the Padthaway Ridge forms part. (interpretation of subsurface mafic volcanics by Dredge, 1979).



activity to 485-490 Ma and includes a U/Pb zircon age of $490 \pm 6/-15$ Ma for the Marcollat Granite from the Padthaway Ridge (Foden *et al.*, 1990b).

Subsurface drilling (Dredge, 1979) on the Padthaway Ridge near Coonalpyn has revealed mafic rocks as well as extensions of the granites. Of particular interest here are unmetamorphosed basaltic volcanics and biotite-bearing, two pyroxene tholeiitic gabbros which further substantiate evidence elsewhere (eg Chapters 1, 2 & 5) that the post-Delamerian magmatism was bimodal. Nearer the Mt. Lofty Ranges the Black Hill intrusive complex (Chapters 2 & 3) is evidence of extensive contemporaneous mafic magmatism.

In a recent study of the nature of the basement beneath the Murray Basin, Brown *et al.* (1988) show that the southeast of South Australia is in magnetic continuity with the Adelaidean and Cambrian sequences outcropping to the west in the Mt. Lofty Ranges (Fig. 4.1). The Padthaway Ridge itself forms part of an extensive gravity and magnetic high which extends from western Victoria towards the Mt. Lofty Ranges and then curves up northwards (Fig. 4.1). The outcropping granites along this trend have low magnetic susceptibility, low density and thus cannot be responsible for the geophysical anomaly, though mafic rocks like those at Black Hill could be. Geophysical modelling (Kennedy, 1989) shows that this anomaly is consistent with an extensive, predominantly subsurface, tract of mafic plutonism co-extensive with the granites and acid volcanics at the surface.

4.3. Field relations

4.3.1. Granitic Rocks

The granitic rocks of the Padthaway Ridge form isolated whalebacks and inselbergs that extend from Coonalpyn to Naracoorte (Fig. 4.1). Predominantly they are coarse grained, pink and homogeneous, though fresh samples from drill core of the Marcollat Granite are bright green. A characteristic feature is the presence of large smoky quartz grains and purple fluorite. Alkali feldspar, often rimmed by plagioclase, and quartz are the dominant phases and mafic minerals, usually amphibole \pm biotite, constitute less than 5% of most samples.

The outcrops around Willalooka and Kongal rocks contain a finer grained but mineralogically identical, porphyritic microgranite. At Christmas Rocks the outcrop is solely comprised of a similar microgranite. These finer grained rocks are frequently granophyric, with alkali feldspar and quartz phenocrysts often enclosed by a graphically intergrown groundmass. Cross-cutting field relations show these shallow porphyritic microgranites to be intruded by the coarser-grained granites.

The Coonalpyn, Tintinara and Christmas Rocks outcrops contain miarolitic cavities indicative of late fluid saturation and high level emplacement (consistent with the occurrence of extrusive equivalents at the same structural level, see below). Small, rare

inclusions of the microgranitic and porphyritic material are interpreted as early, chilled border zones broken up by the intrusion of the main granite phase. Pegmatites are scarce, except as thin discontinuous veins healing late stage brittle fractures, and this indicates that the magmas were relatively dry. Few non-cognate xenoliths have been observed; rare fine grained mafic xenoliths occur in the Marcollat and Tintinara Granites and the Gip Gip exposure contains some dioritic xenoliths.

4.3.2. Volcanic rocks

At Mount Monster a 2km² exposure of a red-brown, quartz-feldspar, porphyry forms a low ridge. Mawson and Dallwitz (1945) interpreted this porphyry to be a shallow sub-surface intrusive, while others (eg Rochow, 1971) have postulated it to be extrusive. Tabular phenocrysts of quartz and feldspar have an orientation indicative of flowage and fine grained, angular, cognate inclusions show flow banding, both suggesting an extrusive origin. Four km to the south of Mount Monster occurs a coarser-grained, pale green porphyry with subhedral, smoky quartz and feldspar phenocrysts up to 8mm in diameter in an aphanitic felsic groundmass. Some feldspar phenocrysts show development of rapakivi textures. Veins and fractures in the porphyry are lined with epidote and fluorite.

Pyroclastic and auto brecciated rhyolites outcrop at Bin Bin, 10km south-southwest from the main Marcollat Granite body. These siliceous volcanics show extremely well developed flow banding defined by alignment of quartz and rarer feldspar phenocrysts.

Similar but smaller outcrops of volcanics are found between the Marcollat Granite and Gip Gip Rocks which contain pyroxene and feldspar phenocrysts and consist in places of a welded breccia of rhyolite fragments.

At Papineau rocks, thirty-six km east of Kingston, outcrops of acid volcanic breccia are composed of rhyodacite clasts within rhyodacite, both containing feldspar phenocrysts up to 3mm in size. Here the volcanics are undeformed and contain a sub-horizontal banding.

In contrast, brecciated acid volcanics at Didicoolum contain a steeply dipping banding which Mawson and Dallwitz (1945) considered to be due to local shearing. The data presented here shows these volcanics are chemically and mineralogically related to the other undeformed volcanics and granites. They contain numerous feldspar phenocrysts and are also cross-cut by dolerite dykes which represent the only surface expression of mafic activity in the area.

4.3.3. Taratap Adamellite

The Taratap Adamellite forms a distinctly different, grey-blue, megacrystic granite characterized by alkali feldspar phenocrysts up to 5cm in diameter. It outcrops to the west of the Padthaway Ridge, along and immediately inland from the Coorong as well as at

some small exposures to the north near Meningie. This granite often displays flow-lined megacrysts and cumulate texture and is characterized by the abundance of xenoliths composed of planar slates, schists and porphyritic diorite. Mawson and Parkin (1943) equated the Taratap Adamellite with the Encounter Bay Granites (Fig. 1.1) and, on the grounds of its chemistry, the presence of a weak biotite defined foliation and its high initial $^{87}\text{Sr}/^{86}\text{Sr}$ ratio (0.7160; Webb 1976) Foden *et al.* (1990a) have also assigned it to this separate, syn-deformational group of I-type granites.

4.4. Petrography

The Padthaway Suite granites tend towards a one feldspar mineralogy and can therefore be divided into hypersolvus and subsolvus varieties. The volcanics have a similar mineralogy (and chemistry) indicating they represent extrusive equivalents of the granites. Modal analyses for both the granites and the volcanics are listed in table 4.1.

4.4.1. Hypersolvus granites

These include the Marcollat Granite, several of the outcrops at Kongal Rocks and the Christmas Rocks microgranite. These granites are generally homogeneous with hypidiomorphic to xenomorphic-granular textures and plagioclase is rare or absent. The dominant mineral in these rocks is microcline which forms large subhedral to anhedral grains with tartan and occasional simple twinning and coarsely exsolved albite. In some cases albite exsolution has reached grain boundaries producing rapakivi rims whilst remaining in optical continuity with perthite exsolution in the source grain. In other places the exsolution has formed a thin mantle of albite around the alkali feldspar. Rare grains of plagioclase are found included within alkali feldspar. Quartz^{which} crystallized early and is often included in alkali feldspar, is the next most abundant mineral, occurring as slightly undulose grains. This tendency to form beta-quartz indicates low pressures of crystallization, as do granophyric intergrowths seen in the Christmas Rocks granite and the porphyries.

Mafic phases are scarce (see Table 4.1) and most tend to be interstitial to alkali feldspar (Figs. 4.2a,b). Biotite is the main mafic phase in the Christmas Rocks and Kongal Rocks granites and tends to be small and patchy with brownish-green to golden yellow pleochroism. Minor phases in these granites include euhedral, unzoned zircon with pleochroic haloes, fluorite, titanomagnetite, ilmenite, apatite and rare allanite; all of which can be found as inclusions in the major phases.

In the Marcollat Granite, amphibole is predominant and biotite only occurs as rare flakes or as a replacement of amphibole. The amphibole shows olive-green to green-brown pleochroism and is often host to inclusions of clinopyroxene (Fig. 4.2a). In places these clinopyroxenes themselves contain relicts of orthopyroxene (orthoferrosilite) and

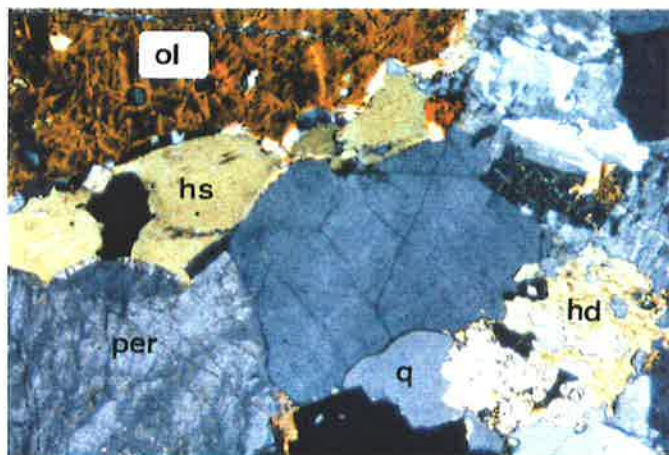
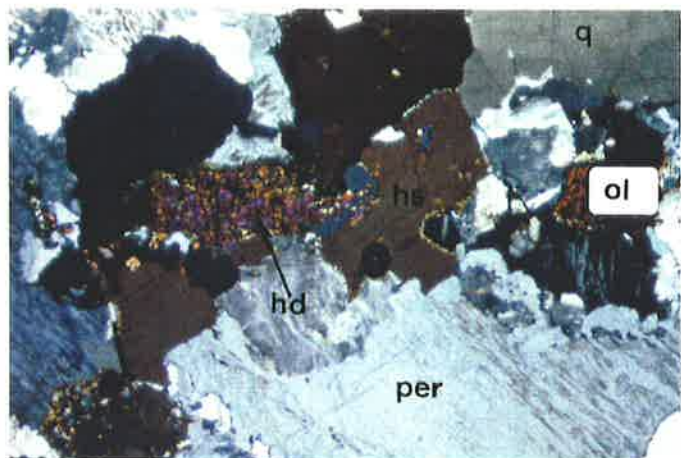
Table 4.1. Approximate modal analyses for the Padthaway Ridge samples

Locality Lithology	Marcollat granite	Christmas microgranite	Coonalpyn granite	Tintinara granite	Mt Monster porphyry	Kongal granite	Kongal granite	Willalooka granite	Gip Gip granite	Gip Gip rhyodacite	Papineau rhyolite	Bin Bin rhyolite	Didicoolum rhyolite
Quartz	35	25	37	25	17	34	40	30	30	-	-	-	-
Plagioclase	tr	tr	11	28	8	tr	15	10	30	11	7	-	2
Perthite	58	70	48	40	20	65	40	50	30	-	-	-	-
Biotite	tr	5	3	4	-	tr	5	10	tr	-	-	-	tr
Amphibole	5	-	1	2	-	-	-	tr	10	-	-	-	-
Clinoxene	2	-	-	-	tr	-	-	-	-	tr	-	-	tr
Orthopyroxene	tr	-	-	-	-	-	-	-	-	-	-	-	-
Apatite	tr	-	tr	tr	tr	-	-	-	-	-	-	-	-
Sphene	-	-	tr	tr	tr	-	-	-	tr	tr	-	tr	-
Ilmenite	tr	-	tr	tr	tr	tr	tr	tr	tr	tr	tr	-	tr
Magnetite	-	-	tr	tr	tr	-	-	tr	tr	tr	tr	-	tr
Allanite	tr	-	-	tr	tr	-	-	tr	-	tr	-	-	-
Zircon	tr	-	tr	tr	tr	tr	tr	tr	tr	-	tr	tr	tr
Carbonate	-	-	-	tr	tr	-	-	-	-	tr	-	tr	-
Epidote	-	-	tr	-	tr	-	-	tr	-	tr	-	-	-
Olivine	tr	-	-	-	-	-	-	-	-	-	-	-	-
Fluorite	tr	-	tr	-	tr	-	-	-	-	-	-	-	-
Groundmass	-	-	-	-	55	-	-	-	-	89	93	100	98



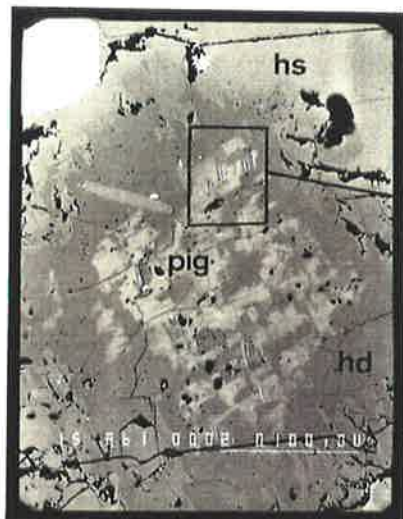
Figures opposite:

- Figure 4.2a.** Photomicrograph from the Marcollat Granite (A861-08) composed of perthite (per) and quartz (q) with interstitial fayalitic olivine (ol), now altered to iddingsite, and hastingsite (hs), with inclusions of hedenbergite (hd). Crossed polars, width of view 4 mm.
- Figure 4.2b.** The one feldspar Marcollat (PG11 - 2725) granite showing quartz (q), perthite (per), hastingsite (hs), relict olivine (ol) and hedenbergite (hd). Crossed polars, width of view 4 mm.
- Figure 4.2c.** Electron microprobe photograph from the Marcollat Granite (PG11 - 2727) of relict pigeonite (pig) within hedenbergite (hd) included in hastingsite (hs). Scale bar is 100 mm.
- Figure 4.2d.** Enlargement from Fig. 4.2c. showing the exsolution lamellae in the pigeonite and their interpreted orientations. Scale bar is 10 mm.
- Figure 4.2e.** The ignimbritic Mount Monster Porphyry (2722) containing quartz and relict sanidine phenocrysts and a fine grained, flow banded volcanic fragment. Plane polarized light, width of view is 4 cm.
- Figure 4.2f.** Embayed beta-quartz phenocryst set in a microcrystalline groundmass in the Mount Monster Porphyry (2323). Crossed polars, width of view 4 mm.
- Figure 4.2g.** Papineau Rocks rhyolite (2340) containing plagioclase and elongate opaque phenocrysts within a microcrystalline groundmass. Crossed polars, width of view 4 mm.
- Figure 4.2h.** Fine grained Gip Gip rhyodacite (2341) containing numerous angular volcanic breccia and deformed pumice fragments. Crossed polars, width of view 4 mm.

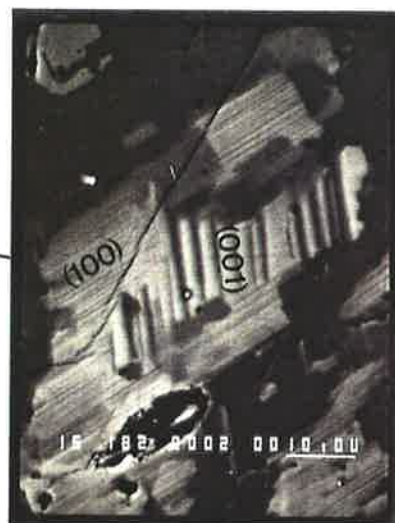


a

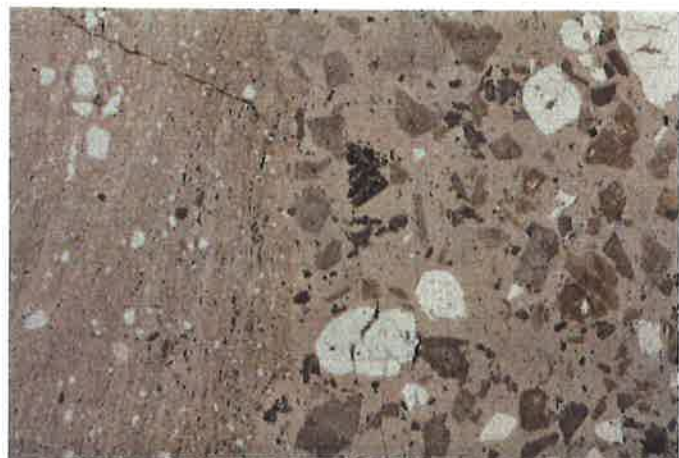
b



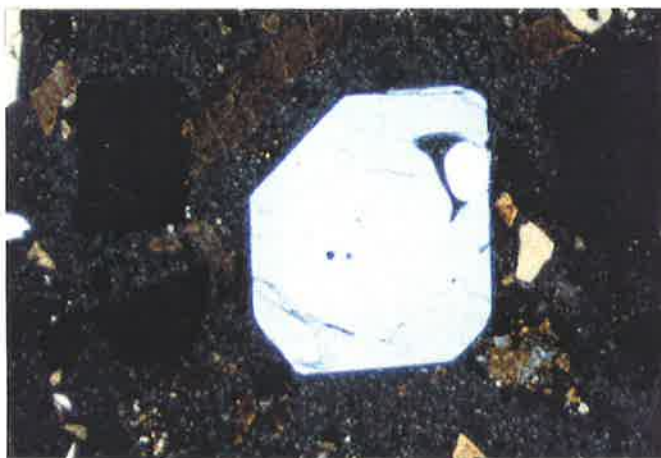
c



d



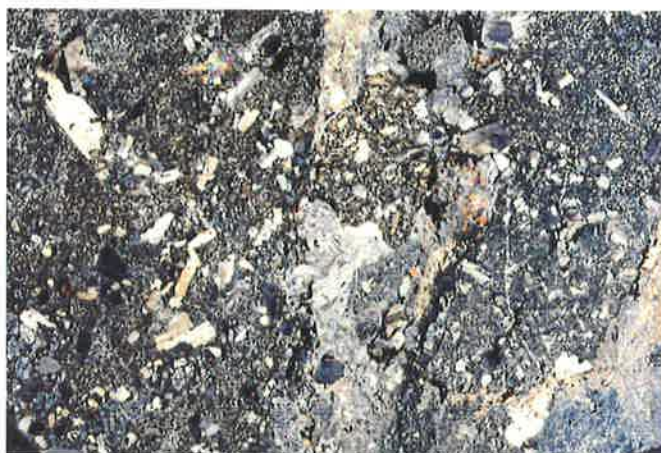
e



f



g



h

pigeonite which has inverted to opx with cpx lamellae (Figs. 4.2c,d). Fayalite, now hydrated to orange-brown pleochroic minerals such as iddingsite (Fig. 4.2a,b) still retains the fracture morphology typical of olivines and contains inclusions of zircon and titanomagnetite. The occurrence of fayalite and clinopyroxene is rare in granitic rocks and may be characteristic of anorogenic melts (eg Ike *et al.*, 1984). The deduced crystallization sequence is given in figure 4.3.

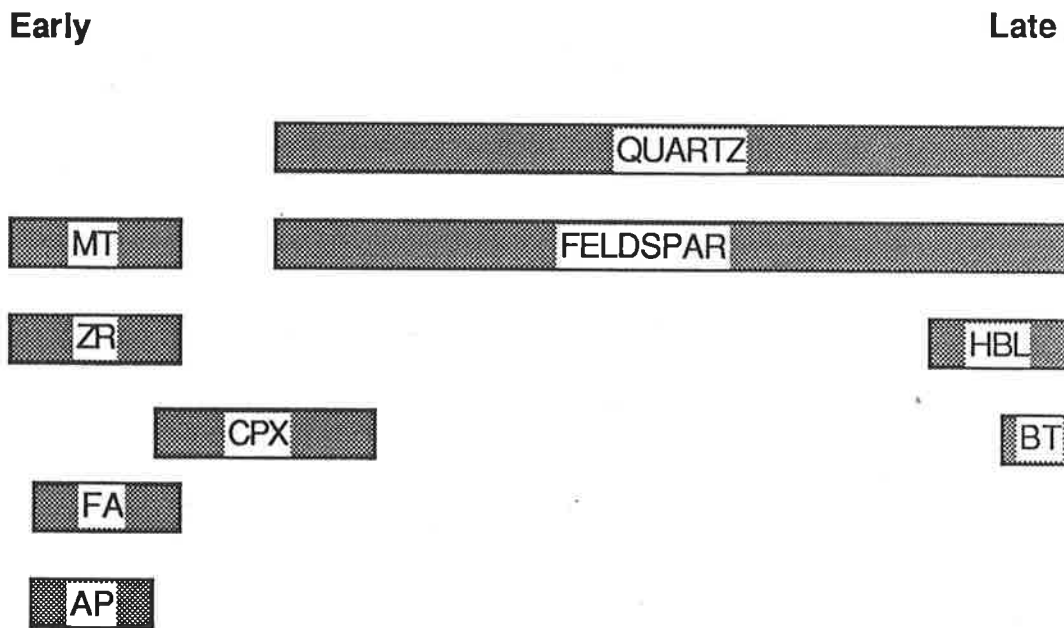


Figure 4.3. Deduced crystallization sequence for the Marcollat Granite.

4.4.2. Subsolvus granites

The remaining granites contain a primary two feldspar assemblage with varying plagioclase contents. These granites show hypidiomorphic textures and grains are subhedral to anhedral varying in size from 1 to 10mm in diameter. They are distinguishable from the hypersolvus ones by the presence of subhedral to euhedral, plagioclase laths reaching 8mm in length. These grains are weakly zoned with more calcic cores and two generations are found: an early group occurring as inclusions in alkali feldspar; and a second, later group that appears to have co-precipitated with the alkali feldspar. The alkali feldspar generally contains albite exsolution, and is often rimmed by albite to produce rapakivi textures. Quartz occurs as large non-undulose grains that tend to be equant.

Mafic constituents are present in greater amounts than in the hypersolvus granites and consist of biotite and/or hornblende. Hornblende when present is green and commonly well formed whilst biotite tends to be interstitial with greenish-brown (sometimes reddish-brown) to straw yellow pleochroism and contains inclusions of fluorite, apatite and opaques. Pyroxene and olivine are not found in these more hydrous

granites. Accessory phases include zircon, fluorite, apatite, calcite, ilmenite, titanomagnetite and zoned allanite whilst secondary alteration involves minor scapolite, leucoxene, epidote and chloritization of biotite.

4.4.3. Volcanics

The outcrop at Mt. Monster is a phenocryst-rich (40-45%), quartz-feldspar porphyry composed of 3-4mm (up to 8mm in the coarser southern outcrop) feldspar and quartz phenocrysts in an aphanitic, felsic groundmass (Fig. 4.2e). The groundmass was welded ash but is now recrystallized to microgranular quartz (15%) and alkali feldspar (85% ; Ab₃₀:Or₇₀). It shows few features but contains rare granitic fragments and plagioclase-hornblende rich inclusions which have a trachytic texture. These later inclusions may represent co-mingled mafic magma. Phenocrysts of sanidine and lesser plagioclase are subhedral to euhedral, the alkali feldspar being perthitic and often surrounded by a rim of albite. Quartz phenocrysts have bipyramidal (β -) form though many have undergone subsequent partial resorption due to depressurization leaving somewhat embayed and rounded grains (Fig. 4.2f). Additionally, many quartz phenocrysts are fractured and broken providing further evidence of an ignimbritic origin. Mafic phases are a minor constituent with ilmenite and biotite (which is usually altered to chlorite) being the most common although some minor pyroxene (CPX and ?OPX) cores occur with hornblende coronas. Accessory phases are zircon, apatite, sphene, titanomagnetite, fluorite and allanite. Alteration includes epidote after clinopyroxene; chlorite and calcite. Rare mafic xenoliths from Mount Monster are composed of plagioclase and hornblende with a trachytic texture.

The remaining volcanics are, for the main part, hypocrystalline rhyolites with a low phenocryst content (eg Papineau Rocks <7%) set in a felsic microcrystalline groundmass (Fig. 4.2g). This has recrystallized from glassy ash, contains some pumiceous fragments and sometimes shows perlitic textures indicative of expansion caused by hydration on interaction with ground waters. Flow banding is well defined and volcanic xenoliths, that may be incorporated chilled fragments, have irregular, fractured edges (eg Gip Gip rhyodacite Fig. 4.2h). Some of the rhyolites contain calc-silicate xenoliths and the Papineau Rocks rhyolite contains numerous rhyolite clasts. Phenocrysts consist largely of plagioclase, which often occurs in glomeroporphyritic aggregates, with subordinate sanidine and little or no quartz. Mafic phases are rare but can include clinopyroxene (sometimes found as embayed inclusions in plagioclase phenocrysts) and Fe-Ti oxides whilst accessories include allanite, sphene, fluorite and secondary epidote. The Gip Gip volcanic is a rhyodacite which contains dacitic to rhyodacitic fragments, shows extensive viscous flow banding and contains Mg-augite as well as possible relict olivine phenocrysts.

4.5. Mineral chemistry and crystallization conditions

Miarolitic cavities and granophyric intergrowths in the granites along with comagmatic volcanics at the same structural level containing beta-quartz indicates that the Padthaway magmas were intruded to very high levels in the crust. Emplacement occurred in pulses with earlier porphyries being intruded by the granites. The general lack of inclusions or xenoliths along with the homogeneous interlocking quartz-feldspar textures and the presence of nearly aphyric rhyolites suggests the magmas were emplaced in a wholly molten state. The accessory phases olivine and pyroxene crystallized early followed by quartz and plagioclase then finally alkali feldspar, hornblende and biotite. Further constraints on the crystallization conditions have been obtained from mineral chemistry and selected microprobe analyses are given in Table 4.2.

4.5.1. Pyroxene

Pyroxene occurs in some of the hypersolvus granites, the Mt. Monster Porphyry and in several of the rhyolites. Compositions range from Mg-augite in the rhyolites to hedenbergite and ferrohedenbergite accompanied by rare iron-rich orthopyroxenes in the granites. Characteristically the pyroxenes have high Mn and low Na, Al and Ti contents. According to the geothermometer of Lindsley (1983) single pyroxenes yield minimum crystallization temperatures and single ferro-hedenbergites from the granites indicate temperatures of 500-600 °C (Fig. 4.4), suggesting extensive sub-solidus re-equilibration. In the Marcollat Granite ferro-hedenbergites are accompanied by iron-rich orthopyroxenes and relict fayalite indicating the reaction:



which occurs at low pressures and low Mg#.

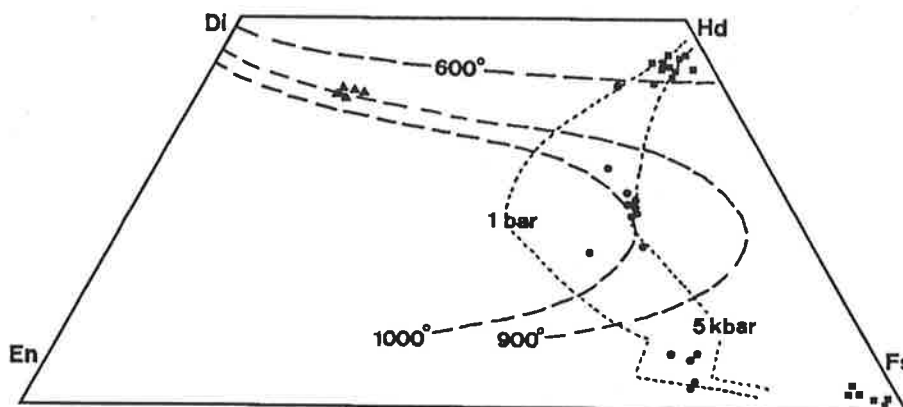


Figure 4.4. Padthaway pyroxenes plotted on Lindsley's (1983) pyroxene projection showing a tholeiitic style iron enrichment trend and relevant temperature contours (filled triangles are Mg-augites from the Gip Gip rhyodacite). Pressure contours define the limit of the "prohibited zone" and samples that plot to the right of these contours are metastable with respect the pressure indicated (see text for details).

Table 4.2. Selected microprobe analyses from the Padthaway samples

Location Mineral	Marcollat plagioclase	Didicoolum plagioclase	Marcollat perthite	Mt. Monster sanidine	Mt. Monster groundmass	Marcollat hastingsite	Marcollat hastingsite	Seismograph hastingsite	Marcollat biotite	Seismograph biotite	Coonalpyn biotite
SiO2	69.98	69.09	66.07	67.10	77.80	39.84	39.41	41.74	36.49	34.12	33.69
TiO2					0.12	1.69	1.82	1.69	1.26	3.28	3.46
Al2O3	20.47	20.63	19.13	19.25	11.05	7.03	6.6	7.14	10.89	11.72	11.03
FeO					1.34	30.63	32.7	29.49	29.35	31.11	31.93
Fe2O3											
MnO						1.01	0.97	0.79	0.31	0.28	0.71
MgO					0.29	1.29	0.76	2.74	6.57	3.65	3.38
CaO	0.20	0.72	0.16	0.23		9.76	10.01	10.14	0.64		0.00
Na2O	12.23	10.85	5.83	4.81	2.18	5.11	4.85	2.33	0.31	0.21	0.18
K2O	0.24	0.09	8.50	9.75	6.18	1.15	1.17	1.09	9.16	8.09	8.96
Cl						0.63	0.63	na	na	na	0.71
F						0.51	0.60	na	na	na	0.94
Total	103.12	101.38	99.69	101.14	98.96	98.64	99.54	97.14	94.97	92.47	95.02
Si	11.8886	11.8868	11.9308	11.9719	13.6098	6.5363	6.4822	6.7674	6.4365	5.7325	5.6186
Ti					0.0163	0.2089	0.2246	0.2056	0.1665	0.4140	0.4343
Al	4.0981	4.1823	4.0717	4.0468	2.2783	1.3596	1.28	1.3634	2.2637	2.3199	2.1685
Fe2+					0.1953	4.2028	4.4981	3.9986	4.3296	4.3712	4.4536
Fe3+											
Mn						0.1397	0.135	0.1079	0.0461	0.0398	0.0997
Mg					0.0748	0.3151	0.1861	0.6632	1.7268	0.9150	0.8400
Ca	0.0363	0.1325	0.0312	0.0445		1.7151	1.7642	1.7605	0.1205		
Na	4.0266	3.6197	2.0419	1.6645	0.7410	1.6239	1.5462	0.7316	0.1077	0.0693	0.0573
K	0.0523	0.0208	1.9573	2.3184	1.3797	0.2414	0.2454	0.2252	2.0623	1.7327	1.9068
Cl						0.1423	0.1442	na	na	na	0.1639
F						0.1874	0.2192	na	na	na	0.3498
Sum	20.1017	19.8422	20.0329	19.9462	18.2953	16.6725	16.7252	15.8235	17.2958	15.5943	16.0961
Mg#						7.0	4.0	14.2	28.5	17.3	15.900
An:Ab:Or	0.9:97.8:1.3	3.5:95.9:0.6	0.8:50.7:48.6	1.1:42.4:56.5	0.0:34.9:65.1						
Wo:En:Fs						26.4:2.4:71.2	27.5:10.5:62				
Xil											

Location Mineral	Marcollat ilmenite	Marcollat ilmenite	Marcollat fayalite	Marcollat pigeonite	Marcollat pigeonite	Marcollat Fe-opx	Marcollat Mg-opx	Marcollat Mg-cpx	Marcollat Fe-cpx	Gip Mg-augite	Gip Mg-augite
SiO2		0.18	37.44	51.05	51.26	48.65	50.04	50.21	49.24	52.90	53.49
TiO2	51.27	51.94		0.11	0.14			0.19		0.30	
Al2O3	0.21	0.32	1.94	0.73	0.61	0.16	0.41	0.55	0.35	1.08	0.19
FeO	42.19	43.43	39.4	31.39	34.18	45.13	35.95	25.23	28.71	10.67	11.38
Fe2O3	0.68	1.37									
MnO	5.67	3.04	2.32	1.59	2.09	3.55	2.38	1.00	1.34	0.84	1.6
MgO		0.12	1.05	6.36	5.94	0.45	5.51	3.48	1.04	14.37	9.97
CaO			0.60	6.12	4.18	0.34	2.70	18.97	20.12	20.28	24.47
Na2O		0.21	0.40	0.92	0.76	0.58	0.67	0.75	0.90	0.47	0.17
K2O				0.06					0.06		
Cl											
F											
Total	100.66	100.86	83.15	98.28	99.17	98.85	97.66	100.52	101.76	100.90	101.28
Si		0.0045	1.2930	2.0675	2.0747	2.0862	2.0759	2.0058	1.9928	1.9667	2.0128
Ti	1.9310	0.9729		0.0033	0.0044			0.0057		0.0083	
Al	0.0127	0.0094	0.0789	0.0350	0.0293	0.0082	0.0199	0.0260	0.0169	0.0473	0.0086
Fe2+	1.7670	0.9047	1.1380	1.0639	1.1567	1.6183	1.2472	0.8428	0.9716	0.3317	0.3582
Fe3+	0.0255	0.0641									
Mn	0.2405	0.0044	0.0679	0.0547	0.0715	0.1288	0.0838	0.0338	0.0459	0.0263	0.0509
Mg			0.0541	0.3840	0.3585	0.0289	0.3406	0.2069	0.0627	0.7961	0.5595
Ca			0.0223	0.2658	0.1811	0.0154	0.1201	0.8118	0.8722	0.8080	0.99865
Na		0.0099	0.0268	0.0721	0.0599	0.0479	0.0535	0.0583	0.0704	0.0342	0.0126
K				0.003					0.0031		
Cl											
F											
Sum	4.0000	2.0000	2.6809	3.9494	3.9362	3.9336	3.9409	3.9951	4.0355	4.0185	3.9892
Mg#			4.5	26.5	23.7	1.8	21.4	19.7	6.1	70.6	
An:Ab:Or											
Wo:En:Fs			15.5:22.4:62.1	10.7:21.1:68.2	0.9:1.7:97.3	7:119.9:73	43.6:11.1:45.3	45.8:3.3:51.0	41.7:41.1:17.1		
Xil	0.97	0.983									

Also in the Marcollat Granite are pyroxene relicts which occur within more magnesian clinopyroxene inclusions in hastingsite (Figs. 4.2a,c,d). Some are ferrohypersthene whilst others may represent ferropigeonite and contain two sets of lamellae (Fig. 4.2d) suggesting exsolution of cpx (001) and inversion of the host pigeonite to an orthopyroxene which exsolved a calcic pyroxene (100). These form a more magnesian group of pyroxenes with the pigeonites indicating temperatures of 1000 °C (Fig. 4.4). On the pyroxene projection of Lindsley (1983) these low-Ca pyroxenes lie within the 1 bar prohibited zone (Fig. 4.4) at which pressures they would be metastable with respect to quartz and iron-rich olivine according to equation 1. This necessitates that they crystallized at higher pressures (allowing them to lie to the right of the prohibited zone) and their clustering around the 5 kbar limit to the prohibited zone indicates minimum crystallization pressures of 5 kbars.

The most magnesian augites are from the Gip Gip rhyodacite and these indicate temperatures around 900 °C (Fig. 4.4). These compositions are very magnesian and suggest derivation from basaltic magma. Using $K_d \text{Mg\#}_{\text{liq}}/\text{Mg\#}_{\text{cpx}} = 0.23$ (Grove and Bryan, 1983) these augites would have crystallized from magma with $\text{Mg\#} = >40$ which is more typical of a monzo-gabbro than the Padthaway suite which typically has $\text{Mg\#} = 2-12$. Even the pigeonite relicts from the Marcollat Granite are rather magnesian for a high-silica granite and pigeonites of the same composition, for example, occur in the Sybille Monzonite, Wyoming which has a $\text{Mg\#} = 20$ (Fuhrman *et al.*, 1989).

In summary these rocks contain a complex pyroxene population some of which seem rather too magnesian to have crystallized from magmas with the composition of their host rocks. Additionally, miarolitic cavities, extrusive equivalents and textural evidence all suggest the granites were intruded to very shallow levels (< 1 kbar) yet some of the pyroxenes would be metastable at less than 5 kbars. Therefore these pyroxenes are out of equilibrium with both the composition and crystallization conditions of their present host rocks suggesting inheritance from hotter more mafic parental magmas at depth.

4.5.2. Amphibole

The amphiboles are pleochroic (X= greenish-brown, Y=Z= very dark greenish-brown) and tend to have low total Al contents, mostly in tetrahedral coordination. MgO contents are low and Fe is high (Fig. 4.5) with low Mg#'s corresponding to ferrohastingsite compositions ($\text{Ca}_{26}\text{Mg}_2\text{Fe}_{72}$). The amphiboles typically contain 65-83% ferrohastingsite with Al^{IV} and Na+K contents that range from hornblende towards edenite (Fig. 4.6). MnO contents are high and tschermakite substitution shows little variation ($\text{Al}^{\text{IV}}=1.3$). None of these granites shows any compositional range extending to sodic varieties as seen in some anorogenic suites (eg Collerson, 1982). Rather, the range

of Mg# for the pyroxenes (70-2) and amphiboles (14-4) indicates crystallization followed an iron enrichment trend.

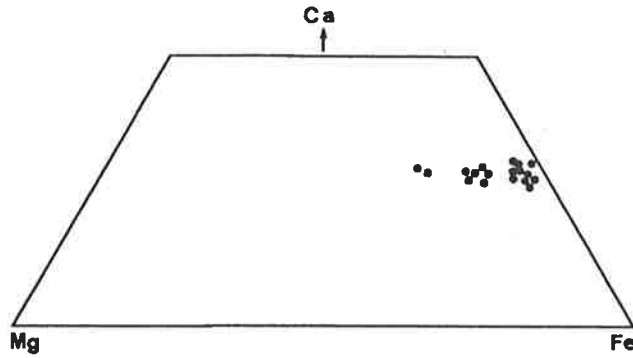


Figure 4.5. Padthaway amphiboles showing iron enrichment trend similar to the pyroxenes.

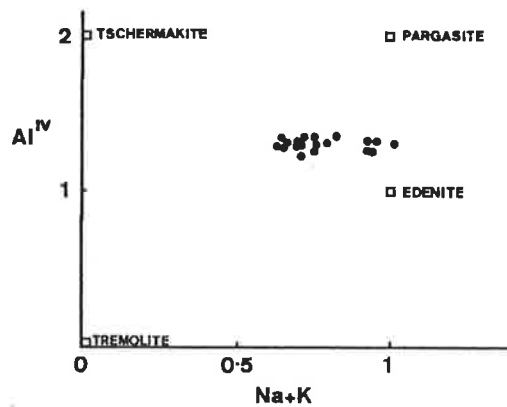


Figure 4.6. Compositional variation of the Padthaway amphiboles on an alkali's vs Al^{IV} diagram.

The Al content of the amphiboles implies pressures around 2-2.5 kbar (Fig. 4.7), according to the geobarometer of Johnson and Rutherford (1989). In the Marcollat Granite these amphiboles are host to the pyroxene inclusions interpreted to have crystallized at around 5 kbar. As the magmas were finally emplaced at or near the surface

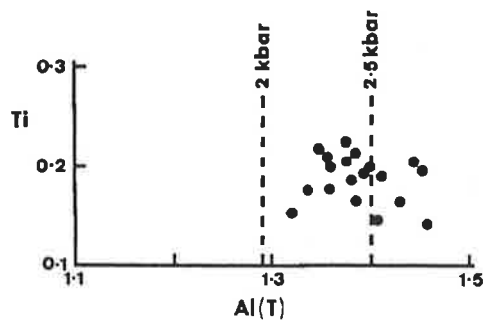


Figure 4.7. Diagram of Ti vs Al_{total} for the Padthaway amphiboles with pressure contours determined according to Johnson and Rutherford (1989).

these data record polybaric crystallization during ascent through the crust. The amphiboles have elevated fluorine and chlorine contents (Table 4.3) and their stability at the high temperatures and low pressures of emplacement reflects overall high fluorine contents of the magmas (see later discussion).

4.5.3. Biotite

In these rocks biotite, which shows show greenish-brown (sometimes greenish-red or almost opaque) to straw yellow pleochroism, is interstitial, late formed and may have a subsolidus origin. Its chemistry is particularly characteristic and low Al_2O_3 distinguishes them from metasediments, migmatites and other granites in the foldbelt (Fig. 4.8). This reflects the late stage formation of biotite when the magmas were strongly depleted in Al_2O_3 . The biotites are Fe-rich, reflected in their very dark pleochroism and most Al is in tetrahedral co-ordination, which places them in the annite rich portion of the annite-phlogopite series. Consequently $\text{Al}^{\text{IV}}/\text{Al}^{\text{VI}}$ extends to quite high values (see Fig. 4.8) whilst fluorine and chlorine contents are high (Table 4.3). TiO_2 levels are around 3% whilst Mg#'s are often below 5. Many biotites show partial alteration to chlorite, as evidenced by low SiO_2 , K_2O and totals.

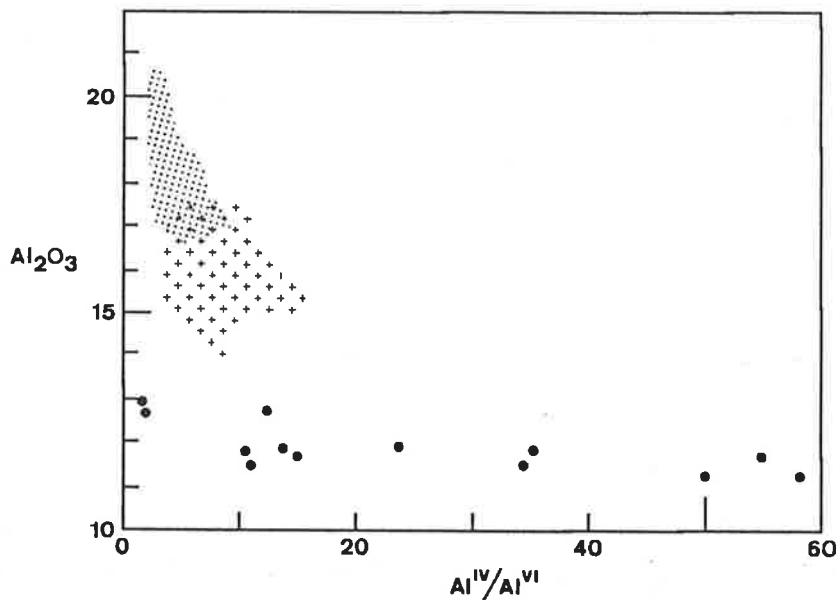


Figure 4.8. Plot of aluminium co-ordination vs Al_2O_3 for the Padthaway suite biotites with fields marked for biotites from metasediments and migmatites (dotted stipple) and syn-deformational, I-type granites from the Kanmantoo Group.

The assemblage annite-sanidine-magnetite would allow water fugacity to be estimated according to the method of Wones (1972) unfortunately the chloritic alteration shown by most of the biotites does not permit conclusive results. Nevertheless the general scarcity of pegmatites and hydrous phases along with the occurrence of

hornblende or pyroxene in preference to biotite indicates relatively anhydrous magmas. Further assessment of water contents can be made by comparison with experimental work on very similar A-type granite compositions (Clemens *et al.*, 1986). These experiments produced a crystallization sequence and temperatures much in keeping with that deduced for the Marcollat Granite. Closest analogies with their work are achieved when water contents are in the range 2-3 wt% H₂O.

4.5.4. Quartz-fayalite-oxide assemblage

The development of fayalite along with quartz occurs due to the metastability of low-Ca pyroxene at low pressures (equation 1). This assemblage combined with an oxide phase in the Marcollat Granite can be used to constrain the conditions of crystallization. Manganian ilmenite, which is common in peralkaline suites, is the predominant oxide and indicates low oxygen fugacity. Magnetite-ilmenite pairs with the lowest MnO contents (1-2 wt%) have been analysed using the data of Buddington and Lindsley (1964). Those from the volcanics give temperature estimates of 800-1000 °C whilst those from the granites yield 500-800 °C, clearly indicating subsolidus re-equilibration. This re-equilibration appears to have principally affected the magnetites which show highly variable ulvospinel contents. However, the ilmenites do not seem to have altered and show relatively consistent $X_{il} = 0.976$.

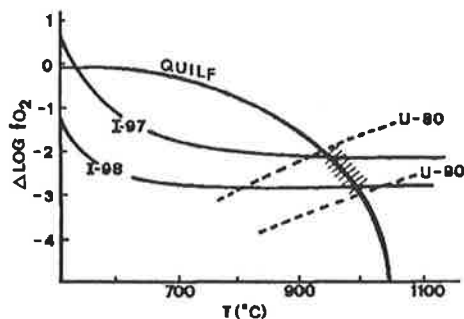


Figure 4.9. Diagram from Frost *et al.* (1988) showing the temperature and oxygen fugacity indicated by the intersection of the Marcollat Granite ilmenites (stippled area) with the QUILF (quartz-ilmenite-fayalite stable assemblage) curve. Also shown are the compositional contours for magnetite that would be in equilibrium with this assemblage.

Analyses of the relict olivine in the Marcollat Granite suggest low Mg#s (Table 4.3) and, as noted above, in highly evolved igneous rocks there is an equilibrium relationship between Fe-rich olivine, quartz and Fe-Ti oxides (equation 1). Using the recent work of Frost *et al.* (1988) ilmenites from the Marcollat Granite can be intersected with the curve on which this four phase assemblage co-exists (Fig. 4.9). This coincides with pigeonite crystallization temperatures at around 960-1000 °C and indicates a low

oxygen fugacity several units below the QFM buffer ($\log f_{\text{O}_2} = -14.4$), from which pre-equilibration magnetite compositions can be inferred to have had $X_{\text{usp}} = 0.87$ (see Fig. 4.9).

4.5.5. Feldspars

The range of feldspar compositions is shown in figure 4.10. The Padthaway suite contains two feldspar rocks and the A-type phase diagram of Clemens *et al.* (1986) shows a considerable crystallization interval (>100 °C) between the plagioclase saturation surface and the solidus. These authors note that plagioclase is likely to be replaced at lower temperatures by a single feldspar and many of the Padthaway suite rocks are one-feldspar rocks in which the alkali feldspars are usually perthitic, the perthite being composed of near equal amounts of orthoclase and albite. Electron microprobe area scans show the pre-exsolved compositions were about $\text{Ab}_{50}:\text{Or}_{50}$, the same as sanidines analysed from the volcanics. This suggests that the crystallizing feldspars in the hypersolvus rocks were sanidine, which subsequently exsolved in the granites.

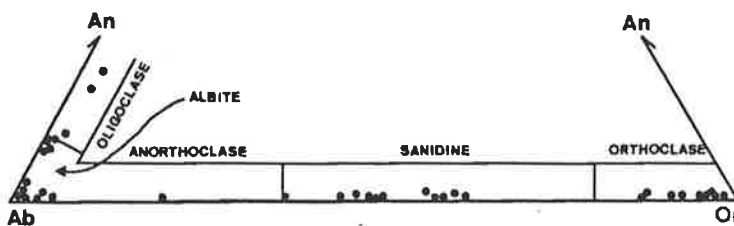


Figure 4.10. Ternary feldspar diagram for the Padthaway suite with reconstructed perthites plotting with sanidines from the rhyolites.

Ternary feldspar modelling for plagioclase and reconstructed perthite from the Marcollat Granite has been approached using the program of Fuhrman and Lindsley (1988) yielding: $T_{\text{Ab}}=827$ °C; $T_{\text{An}}=832$ °C; $T_{\text{Or}}=1058$ °C. Following Fuhrman and Lindsley (1988) this indicates a "close to equilibrium" feldspar pair with crystallization temperatures of at least 830 °C, considerable discrepancy in T_{Or} suggesting higher temperatures probably prevailed. In the volcanics plagioclase-groundmass compositions give temperatures (according to the method of Kudo and Weill 1971; Mathez 1973) consistent with the other thermometry at around 1000 °C if $p_{\text{H}_2\text{O}}$ is assumed to be 100 bars which provides some additional estimate of $p_{\text{H}_2\text{O}}$.

4.6. Geochemistry and isotopes

Major and trace element data for the Padthaway Ridge intrusives are presented in table 4.3, and selected Harker diagrams are shown in figure 4.11. It should be noted that,

Overleaf Figure 4.11. SiO_2 variation diagrams for the Padthaway Suite volcanics and granites (filled squares - Marcollat Granite sample).

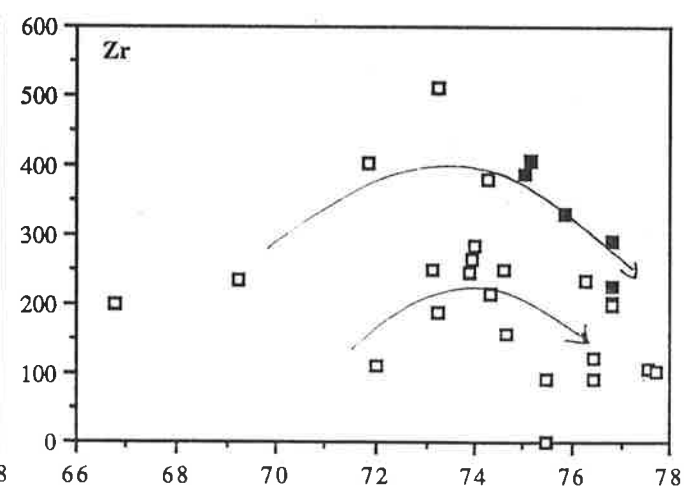
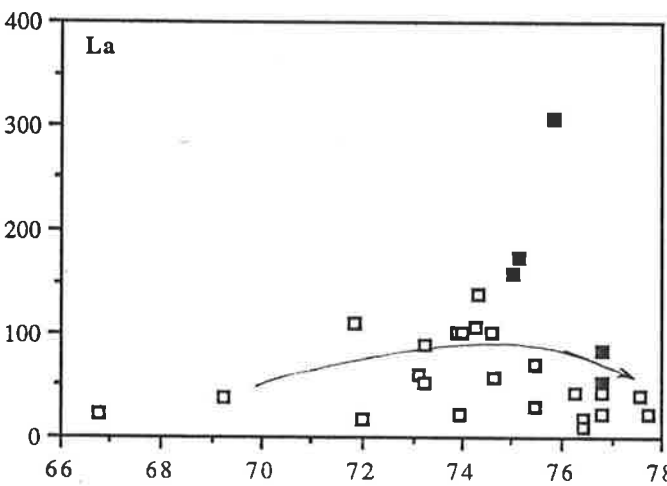
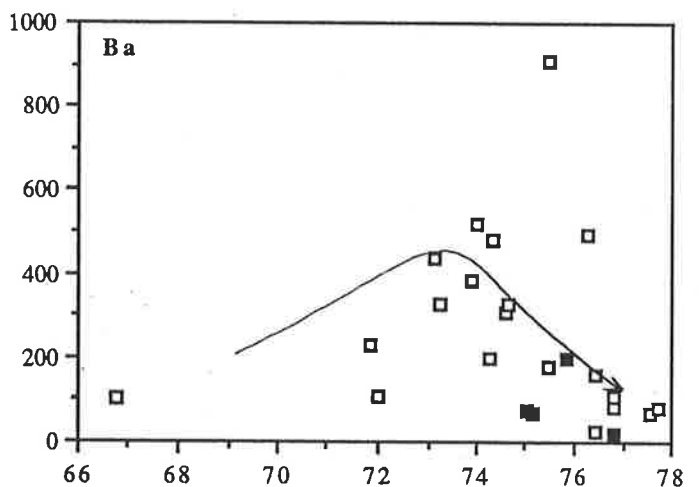
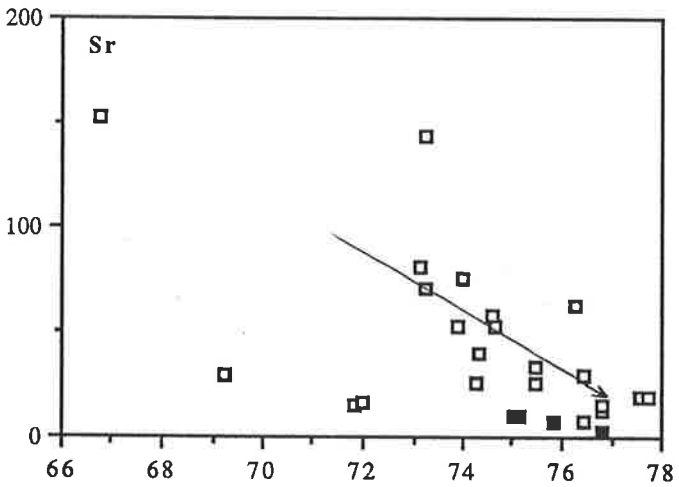
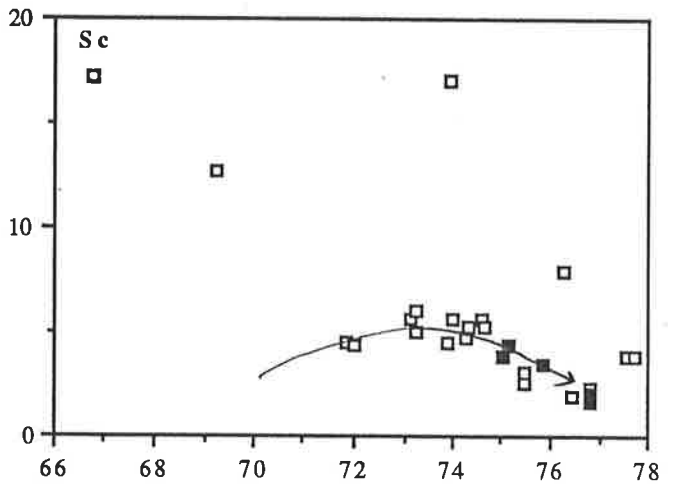
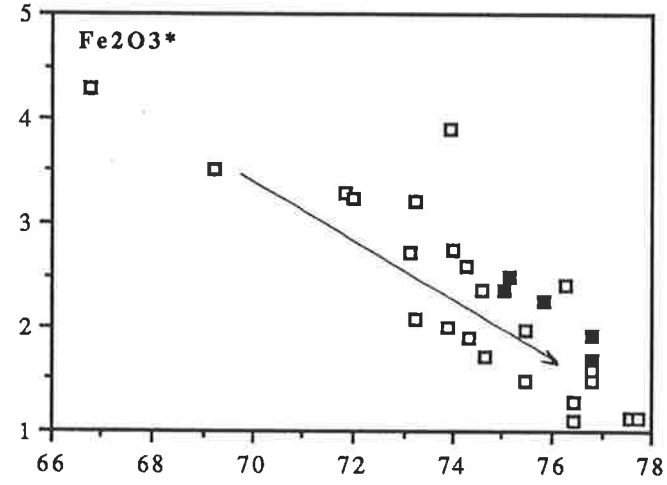
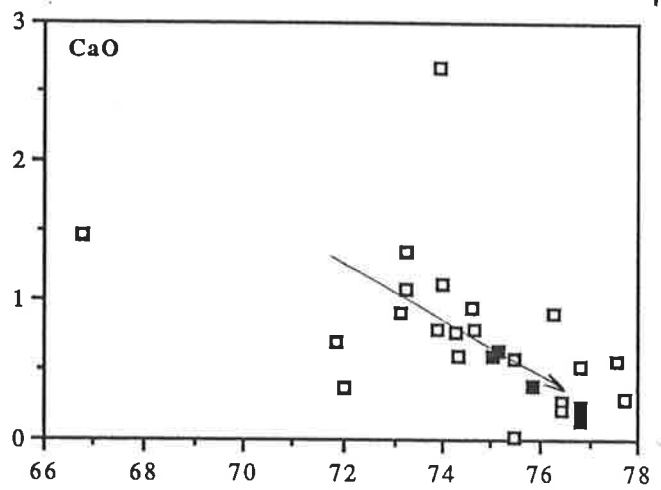
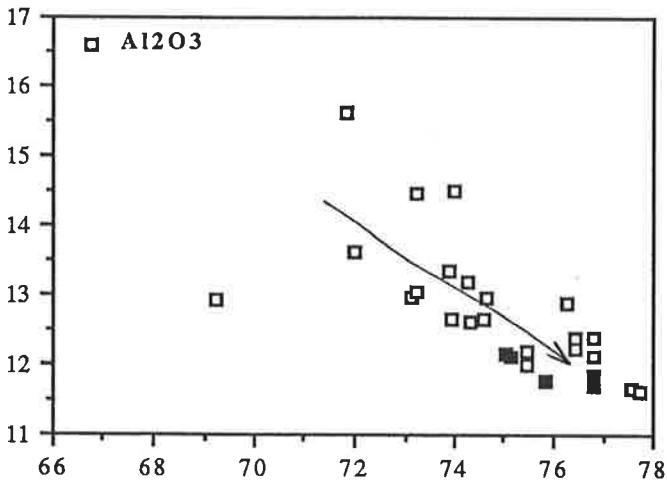


Table 4.3. Geochemistry of samples from the Padthaway Ridge

Sample Location Lithology	876-C1 CSR-SS gabbro	2003 Marcollat granite	PG11 Marcollat granite	339-LA Marcollat granite	339-E Marcollat granite	339-A Marcollat granite	339-GB Gip Gip rhyodacite	339-B Bin Bin rhyolite	339-DA Diddicoolum rhyolite	339-P Papineau rhyolite	2001 Mt. Monster porphyry	339-MC Mt. Monster porphyry	2009 Basins microgranite	2011 Basins microgranite	339-CA Christmas microgranite
SiO ₂	45.08	75.05	75.14	75.82	76.80	76.83	66.75	69.24	73.26	73.93	73.89	74.01	76.43	76.45	76.81
TiO ₂	4.09	0.19	0.21	0.20	0.14	0.12	0.84	0.28	0.21	0.35	0.19	0.29	0.07	0.07	0.12
Al ₂ O ₃	14.28	12.14	12.11	11.77	11.70	11.84	16.56	12.92	14.46	12.67	13.34	14.51	12.25	12.39	12.37
Fe ₂ O ₃ *	15.85	2.36	2.48	2.25	1.69	1.93	4.29	3.50	3.21	3.91	1.99	2.74	1.10	1.29	1.49
MnO	0.24	0.07	0.09	0.10	0.06	0.05	0.14	0.16	0.08	0.23	0.05	0.07	nd	0.02	0.05
MgO	5.84	0.08	0.19	nd	nd	0.08	0.66	0.97	0.40	0.71	0.23	0.25	0.34	0.09	nd
CaO	10.57	0.59	0.64	0.39	0.13	0.23	1.47	nd	1.34	2.67	0.78	1.12	0.27	0.22	0.51
Na ₂ O	2.90	3.74	3.51	3.29	3.83	3.80	7.72	0.37	4.71	1.99	3.75	3.26	3.67	3.47	3.69
K ₂ O	0.50	5.32	5.21	5.21	4.44	4.37	0.30	9.84	2.85	3.22	5.47	5.10	4.84	4.77	4.32
P ₂ O ₅	0.39	0.02	0.01	nd	nd	nd	nd	nd	nd	nd	0.03	nd	0.01	nd	nd
LOI	0.37	0.29	0.18	0.30	0.46	0.22	1.07	1.34	0.48	1.22	0.70	1.16	0.42	0.55	1.10
Total	100.15	99.56	99.77	99.03	98.79	99.25	98.73	97.28	100.52	99.68	99.72	101.35	99.40	99.32	99.36
F	nd	550	na	na	na	na	na	na	na	na	780	na	na	na	na
Cr	5	5	nd	5	5	5	5	5	5	5	5	5	nd	nd	5
Ni	5	3	nd	5	2	2	2	3	nd	1	6	2	nd	2	2
Sc	45	3.8	4.3	3.5	1.7	2	17.2	12.7	5	17	4.5	5.7	1.9	1.9	2
V	490	2	2	4	2	2	30	3	2	6	5	15	2	2	3
Pb	4	14	26	14	13	16	13	8	6	6	20	15	19	20	24
Rb	9	109	101	120	177	152	5.6	237	46	92	187	195	261	289	375
Sr	401	10.5	10.5	8.3	2.2	2.2	153	30	144	528	52	76	29	8.2	12.8
Ba	182	76	68	200	15	21	100	1082	2046	1039	386	520	163	27	84
Ga	22	19	19	19	21	20	18	16	25	22	20	20	23	24	29
Nb	9.8	19.4	19.9	24	25	21.8	12.3	23.9	27	17.5	20	22.1	23	29	75
Zr	124	390	409	331	227	294	199	235	511	267	247	285	125	94	204
Y	36	38	36	64	38	71	52	39	192	82	51	53	43	35	125
Th	1.4	24	26	22	19	20	12	17	28	14	28	27	38	43	55
U	2.6	2.2	3.5	3	2.3	3.6	2	3.9	5.6	3.4	5.3	5.1	8.6	8.9	16
La	21	159	175	308	53	85	24	38	89	24	103	102	17	9	43
Ce	65	250	330	353	142	136	57	81	204	64	167	181	36	84	101
Nd	26	119	138	239	54	84	31	34	126	36	71	77	13	10	59

Sample Location	861-17 Christmas microgranite	339-DC Willalooka granite	339-BC Willalooka granite	339-DB Willalooka granite	2000 Seismograph granite	339-BA Willalooka granite	339-GA Gip Gip granite	339-KE Kongal granite	339-KG Kongal granite	2002 Kongal granite	339-KF Kongal granite	2006 Tolmer's granite	2007 Cold & Wet granite	876-C4B CSR-SS granite
SiO2	76.83	71.84	73.15	74.29	74.61	75.48	76.25	72.02	75.45	77.59	77.71	73.23	74.31	74.63
TiO2	0.08	0.21	0.28	0.20	0.20	0.17	0.91	0.14	0.21	0.09	0.13	0.28	0.18	0.20
Al2O3	12.11	15.62	12.95	13.19	12.67	12.20	12.90	13.63	12.01	11.64	11.63	13.03	12.62	12.95
Fe2O3*	1.59	3.29	2.73	2.60	2.37	1.98	2.40	3.24	1.48	1.13	1.14	2.08	1.89	1.71
MnO	nd	0.08	0.10	0.05	0.05	0.08	0.06	0.12	0.08	0.05	0.06	0.04	0.09	0.10
MgO	0.01	nd	0.15	0.22	0.11	0.06	nd	0.52	0.52	0.10	nd	0.27	0.13	0.34
CaO	0.15	0.69	0.90	0.76	0.95	0.57	0.90	0.37	0.01	0.56	0.29	1.07	0.60	0.78
Na2O	4.00	3.70	3.20	3.65	3.89	3.64	4.74	1.45	1.12	3.31	3.06	3.65	3.68	3.22
K2O	4.66	5.17	5.02	4.96	4.79	4.67	2.85	6.20	7.28	4.71	4.36	5.11	5.22	5.13
P2O5	0.02	nd	nd	nd	0.03	nd	nd	nd	nd	0.01	nd	0.06	0.03	0.05
LOI	0.71	0.58	0.52	0.55	0.42	0.49	0.30	1.14	0.93	0.49	0.78	0.29	0.34	0.34
Total	99.45	100.60	98.48	99.92	99.67	98.85	101.01	97.69	98.16	99.19	98.38	98.82	98.75	99.45
F	520	na	na	na	1130	na	na	na	na	1360	na	na	na	na
Cr	5	5	5	5	5	5	5	5	5	5	5	5	5	nd
Ni	7	3	2	1	2	3	5	3	2	2	2	nd	3	2
Sc	2.3	4.5	5.6	4.8	5.7	2.6	8	4.3	3.1	3.9	3.8	6	5.3	5.2
V	1	3	6	5	6	5	6	6	14	3	5	18	5	6
Pb	23	30	18	23	17	18	6	23	17	23	20	22	22	16
Rb	376	163	220	174	190	255	98	530	208	346	323	277	262	258
Sr	14.9	15.7	81	25	58	33	63	16.7	26	19.7	18.8	70	40	53
Ba	110	233	439	199	305	182	493	111	913	69	84	328	481	326
Ga	29	19	22	22	22	23	20	19	10	17	16	19	19	22
Nb	55	25	28	27	25.9	29	15.9	36	26	28.7	27	17	16.6	10.9
Zr	201	403	251	380	251	1.76	234	111	94	109	102	189	215	157
Y	81	46	66	52	74	92	84	58	13	70	46	56	125	42
Th	42	29	30	34	36	38	14	52	18	52	47	45	44	54
U	10	4.5	4.5	3.3	7.3	8	3.1	9.1	3.2	8.6	6.4	16	23	14
La	22	110	62	107	102	71	43	19	32	41	22	55	139	60
Ce	40	226	129	202	168	145	95	62	50	80	67	112	214	119
Nd	20	84	56	84	80	69	52	20	16	41	27	42	127	47

due to various degrees of alteration the diagrams show some scatter. This is particularly the case with the volcanics, alkali-rich rocks being particularly prone to gain or loss of alkali elements during crystallization and/or secondary hydration (Noble, 1970). Fresh samples from drill core of the Marcollat Granite serve to elucidate the general trends described.

All of the rocks analysed have high SiO_2 contents, usually between 70 and 80% and they are metaluminous to mildly peraluminous but not peralkaline ($\text{Al}_2\text{O}_3/\text{Na}_2\text{O}+\text{K}_2\text{O} = 1.3-1.6$) and consequently sodic amphiboles and pyroxenes have not developed. TiO_2 ranges from 0.4 to 0.1% showing a curvilinear decrease with increasing silica. Al_2O_3 exhibits a strong negative linear relationship with silica, decreasing to 11% in the most evolved samples. Fe_2O_3^* displays a similar trend decreasing from 4 to 1% whilst MgO shows a rapid curvilinear decrease and MnO contents are very low (less than 0.1%). CaO , like Al_2O_3 , is quite depleted in these rocks (<1.5%) and steeply decreases with increasing silica. Over the silica range 71-80% Na_2O has a relatively constant abundance of 4% whilst K_2O decreases from 6 to 4%. P_2O_5 displays a marked decrease after 73% SiO_2 .

The trace element chemistry of these rocks is quite distinctive. The presence of olivine and relicts of high temperature, magnesian pyroxenes implies a mafic parent and the low values and decreasing concentrations of MgO , iron and Cr, Ni, Sc, V are consistent with fractionation of these ferromagnesian phases. The lithophile elements K, Rb, Ga display high or enriched values. Strontium is highly depleted with values dropping rapidly from 200 to less than 10ppm as SiO_2 increases. In contrast, Rb shows typical incompatible behaviour with enrichment from 100 to 400ppm. Consequently, Rb/Sr shows a steep increase with silica whilst K/Rb decreases. Barium values, like Sr display an inflected trend with a decrease against silica from 500 to <100ppm. Gallium varies from 16 to 29ppm and, due to the low Al_2O_3 in these rocks Ga/Al, is characteristically high.

The highly charged incompatible elements (Nb, Zr, Ti, Y, Th) are, with the exception of Ti, enriched but show an inflection at around 75% SiO_2 indicating the onset of accessory phase fractionation. Niobium is more or less constant around 30ppm, showing little variation against SiO_2 . Zirconium is extremely enriched (up to 400ppm) and displays a transition from enrichment to depletion at 75% SiO_2 . Yttrium has a mean value of about 65ppm but shows considerable variation after 73% SiO_2 . Thorium concentrations average around 30ppm whilst fluorine measured on representative samples was high (500 to >2000ppm). The light rare earths are enriched but also decrease after 75% SiO_2 . Incompatible element diagrams for these rocks (Fig. 4.12) are highly fractionated with high Rb, Nb, La, Ce, Zr, Y and low Ba, K, Sr, Ti.

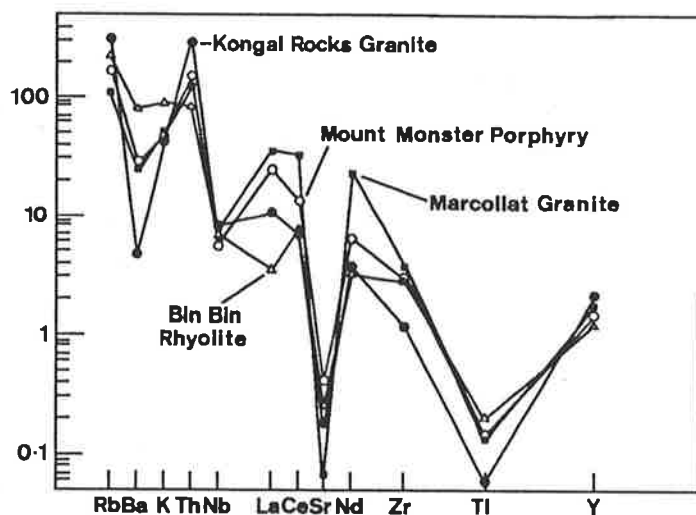


Figure 4.12. MORB normalized spidergram for several members of the Padthaway suite. The Bin Bin rhyolite with 69% SiO_2 shows the least fractionated pattern, whilst the Marcollat Granite and a granite from Kongal Rocks are the most fractionated with the Mount Monster Porphyry in between.

Rare earth patterns for a subsurface gabbro at Coonalpyn ($\text{SiO}_2 = 45\%$), the Gip Gip rhyodacite ($\text{SiO}_2 = 67\%$), Mt Monster porphyry ($\text{SiO}_2 = 73\%$), Seismograph granite ($\text{SiO}_2 = 74\%$) and Marcollat Granite ($\text{SiO}_2 = 75\%$) are given in table 4.4. Considering the silica range of these samples there is a remarkable consistency of shape of the patterns (Fig. 4.13). The gabbro has quite high REE contents ($\text{La} = 55 \times \text{chondrite}$) and by the time the granites are reached REE contents are extremely high ($\text{La} = 420 \times \text{chondrite}$).

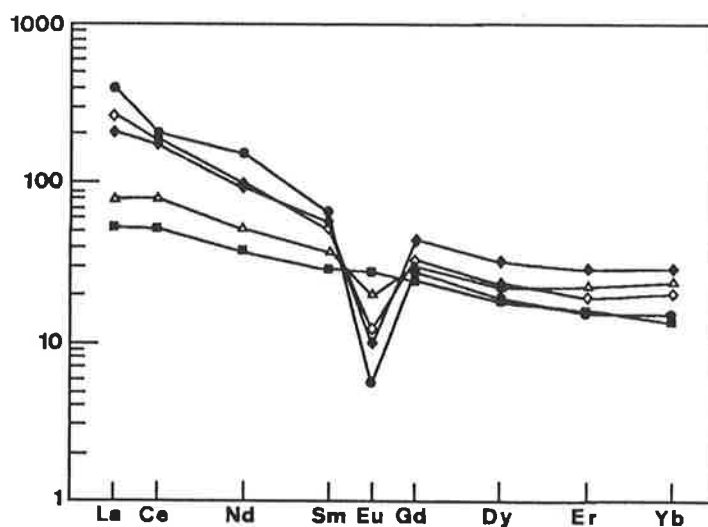


Figure 4.13. Chondrite normalized rare earth diagram for a subsurface gabbro (squares), the Gip Gip rhyodacite (triangles), the Seismograph granite (filled diamonds), the Mount Monster Porphyry (open diamonds), and the Marcollat Granite (circles) all showing considerable light rare earth enrichment and the progressive development of a negative europium anomaly with increasing fractionation.

Table 4.4. Rare earth and isotopic analyses of selected samples

Sample Locality Lithology	876-C1 Drill Core gabbro	339-GB Gip Gip rhyodacite	2000 Seismograph granite	2001 Mt Monster porphyry	PG11 Marcollat granite
La	17.37	25.41	72.50	86.61	132.80
Ce	45.45	67.98	152.91	165.50	253.67
Nd	24.12	32.12	60.60	61.33	96.08
Sm	5.75	7.13	11.69	9.81	13.52
Eu	2.09	1.52	0.76	0.93	0.43
Gd	6.42	7.64	12.23	8.70	7.52
Dy	6.47	7.70	11.13	7.90	6.48
Er	3.51	4.76	6.38	4.40	3.43
Yb	3.20	5.02	6.36	4.34	3.36
147Sm/144Nd	0.1443	0.1343	0.1167	0.0968	0.0838
143Nd/144Nd	0.512599 +/-19	0.512481 +/-32	0.512171 +/-30	0.512240 +/-19	0.512145 +/-23
143Nd/144Nd (487Ma)	0.512139	0.512053	0.511899	0.511931	0.511878
eps Nd	2.4	0.7	-2.3	-1.7	-2.7
Tmod(dep)	1.0	1.1	1.2	1.1	1.1
Rb	2.5	5.4	201.4	193.1	104.1
Sr	405.0	150.1	56.9	50.3	11.2
87Rb/86Sr	0.0649	0.1059	9.5379	10.4748	26.0609
87Sr/86Sr	0.704516 +/-32	0.705679 +/-22	0.772482 +/-33	0.776709 +/-26	0.880510 +/-30
87Sr/86Sr (487Ma)	0.704066	0.704944	0.706295	0.704021	0.702569

Analyses performed at the University of Adelaide on a Finnigan Mat261 thermal ion solid source mass spectrometer
Errors quoted are two standard errors of the mean

The PG11 sample analysed for isotopes has Nd 118.85 ppm, Sm 16.47 ppm.

This increase is accompanied by LREE enrichment with La/Yb increasing from 3 to 26 as might be expected to result from fractionation of pyroxene. In addition, as the REE contents and SiO₂ increase, negative Eu anomalies develop and become progressively larger which taken with the decreasing trends of Sr, CaO and Al₂O₃ confirm extensive feldspar fractionation.

These same five samples were also analysed for their Nd and Sr isotopic composition (Table 4.4). Both the gabbro and the silicic rocks have high initial ¹⁴³Nd/¹⁴⁴Nd ratios with εNd values (at 487 Ma) from +2.4 to -2.7 and low initial ⁸⁷Sr/⁸⁶Sr ratios in the range 0.7026 - 0.7063 indicating a major mantle component in their genesis. However, before trying to assess the origin of the Padthaway Suite it is instructive to look at their characteristics in general and some current ideas on their petrogenesis. In particular the evidence from Black Hill for an origin involving basalt fractionation requires closer scrutiny.

4.7. Characteristics of A-type rocks and a comparison with the Padthaway Suite

A-type granitic and volcanic rocks are widely distributed in space and time, they have been extensively reviewed in the recent literature (Collins *et al.*, 1982; Whalen *et al.*, 1987; Sylvester, 1989; Eby, 1990) and a compilation of their occurrences and features is presented in table 4.5. The following discussion presents a brief summary of their distinctive features. A-types occur in bimodal association with mafic rocks (basalt and/or gabbro) and the presence of miarolitic cavities along with the frequent association with volcanic equivalents demonstrates that they are emplaced at high crustal levels. Petrographic examination indicates that they crystallized from relatively anhydrous magma that was close to wholly molten; xenoliths and restitic material being typically absent. Mineralogically they tend towards one feldspar (hypersolvus) rocks composed of quartz and alkali feldspar with perthitic exsolution and granophyric intergrowths being common. Mafic phases are generally scarce and typically consist of annite which is late and interstitial, less common are hastingsite-, hedenbergite- and fayalite-bearing examples. Peralkaline examples may contain riebeckite or sodic pyroxene. Accessory phases include fluorite, euhedral magmatic apatite and zircon, and occasional allanite.

Chemical analyses of average A-types are shown in Table 4.6. Their major element characteristics (enrichment in SiO₂, Na₂O, K₂O and depletion in Al₂O₃, MgO, CaO, P₂O₅) are dictated by the quartz-feldspar-liquid eutectic (eg Tuttle and Bowen, 1958) which can be achieved either by small degrees of partial melting of a quartz-bearing mafic source or extreme fractionation of basaltic magma. Low Sr, Eu, Sc, V, Ni, Cr and high Rb, Zr, Y, Nb, LREE, Ga, F are characteristic of A-types. Many trace elements show a large range of absolute values from one A-type to another (eg Ba 2-1530 ppm), however,

Table 4.5. Summary of occurrences of A-types and some of their reported features

Abbreviations: p, plutons; v, volcanics; g, gabbro; b, basalt; h, hypersolvus; s, subsolvus; r, rapakivi; f, fluorite; c, cpx; o, opx; a, amphibole; m, mirolitic cavity.

Location	Age	Tectonic setting	Bimodal	Mineralogy	Rb/Sr	Zr ppm	Eu/Eu*	initial 87Sr/86Sr	References
Hizaz, Arabian Shield	Pre-Cambr	post-orogenic (29Ma)	p,v,g	h,s,r,f	2 - 5	231-823	0.5	0.702 - 0.710	Jackson et al (1984)
Evisa, Corsica	246 Ma	post-orogenic (4Ma)	p,g	h,s,f,c	6 - 102			0.7034	Bonin et al (1978)
Seward Peninsula, Alaska	70-80 Ma	post-orogenic (30 Ma)		s,f	6 - 90	low	negative	0.708 - 0.72	Hudson and Arth (1983)
New England Batholith, Aust	Triassic	post-orogenic (30Ma)			2 - 10		negative		Shaw and Flood (1981)
Topsails terrane, Newfoundland	429 Ma	post-orogenic (10Ma)	p,v,b,g	h,a,m	7			0.704	Whalen et al (1987)
Adrar des Iforas, Mali	543-591 Ma	post-orogenic (10Ma)	p,v,b	h,s,c,f,a	1.7 - 17		negative	0.703 - 0.707	Liegeois and Black (1987)
Lachlan Fold Belt	Devonian	post-orogenic (<50Ma)	p,v,b,g	h,s,f,m	0.7 - 8	163-589	negative		Collins et al (1982)
Gawler Range Volcanics, Aust	1592 Ma	post-orogenic (12Ma)	p,v,g,b	h,s,c,f,a	1 - 2.6	240-654	negative	0.703 - 0.707	Stewart and Foden (1990)
Padthaway Suite, South Aust	490 Ma	post-orogenic (<10Ma)	p,v,g	h,s,c,o,f,a,m	0.1 - 80	100-500	0-0.1	0.702 - 0.706	this study
Southern Tibet, Himalaya	15-10 Ma	post-orogenic (40 Ma)	v,b		1.54	187			Coulon et al (1986)
Basin and Range W USA	Cenozoic	post-orogenic extension	v,b		2 - 33	900	negative	0.713	Burt et al (1982); Gans et al (1989)
Sabaloka Complex, Sudan	383 Ma	post-orogenic/rifting	p,v,b	s,o,c	14	138-490	0.3-0.4	0.711	Harris et al (1983)
North America	Proterozoic	anorogenic/incipient rift	p,g	h,s,a,c,o,r	2 - 18		negative	0.705	Anderson (1983)
Trans-Pecos, Texas	37-26 Ma	late-orogenic	p,v,b	h,c,a	> 20	41-2200	negative	0.707 - 0.709	Barker (1987)
SE Queensland	Tertiary	anorogenic	v,b	h,s,c,o,f,a	5.6 - 471	137-1228		0.705 - 0.709	Ewart (1981)
Bushveld, South Africa	Proterozoic	anorogenic	p,g	h,s,a,f,m	1 - 101	180-607			Kleeman and Twist (1989)
Peralkaline granites, Labrador	1260 Ma	anorogenic/uplift	p,g	h,s,c,o,f	4.5 - 161	188-4378		0.708	Collerson (1982)
Yemen Plateau	Tertiary	continental extension	p,b	h,s,a	0.56 - 22	80-2090	0.06-0.6	0.704 - 0.705	Capaldi et al (1987)
Gardar province, Greenland	Proterozoic	continental extension	p,b	h,c,o,f,a	1 - 28	2440-5736		0.702 - 0.704	Upton and Ernieleus (1987)
Velasco, Bolivia	134-142 Ma	? continental rift	p,v	s,c	2.3 - 3.5	348-574		0.704 - 0.709	Fletcher and Beddoe-Stephens (1987)
Chilwa province, Malawi	135-105 Ma	continental rift	p,g,b	h,c,f	6 - 20	100-2200			Woolley and Jones (1987)
Kenya	< 2 Ma	continental rift	v,b,g		208 - 318	> 1600	0.04-0.27	0.703 - 0.706	Macdonald (1987)
Fantale, Ethiopia	Quaternary	continental rift	v,b	h,c,o	4.2 - 27	930-1450		0.704	Gibson (1974)
Pantellaria	Recent	extensional	v,b	h,c	2.6 - 12	>2000	negative	0.702 - 0.707	Villari (1974)
Mull	58 Ma	continental rift	p,g	f	3 - 5	271-366	negative	0.706 - 0.710	Walsh et al (1979)
Nigeria	307-150 Ma	extension/mantle plume	p,g		15 - 139	37-399		0.700 - 0.717	Rahaman et al; Bowden et al (1987)
Oslo rift, Norway	Permian	continental rift	p,v,b,g	h,f	2 - 50	500-1000	0.5	0.705 - 0.707	Rasmussen et al (1983)
Iceland	Recent	mid ocean ridge	v,b	s,c	0.9 - 10	504-1103	negative	0.703	Macdonald et al (1990)
Ascension Island	Recent	oceanic island	p,v,g,b	h,c	62 - 109	871-1516	negative		Harris (1983)

the enrichment of incompatible elements relative to compatible ones leads to diagnostically high ratios of Rb/Sr, K/Rb, Ga/Al, Zr/Ni, Y/Sc, Fe₂O₃/MgO, K₂O/MgO, K₂O+Na₂O/CaO and Zr+Nb+Y+Ce which distinguishes them from the more common I- and S-types (see tables 4.5 and 4.6 and Whalen *et al.*, 1987).

The presence of pyroxenes and olivine, the hypersolvus mineralogy and the shallow emplacement levels of A-types indicates that they were relatively anhydrous magmas. Experimental work conducted at 1 kbar on the Watergums A-type granite from the Lachlan Foldbelt demonstrates that A-type magmas were very hot, possibly in excess of 900 °C, and that they were water undersaturated with H₂O <4% (Clemens *et al.*, 1986). Likewise 1 kbar experiments on similar composition Hebridean granites also demonstrated liquidus temperatures in excess of 900 °C (Thompson, 1983). Such evidence is in marked contrast to I- and S-types which typically contain more hydrous two feldspar, hornblende/biotite-rich assemblages and whose temperatures are dictated by the breakdown of biotite (White *et al.*, 1982) and typically lie in the range 750-850 °C (eg Hildreth, 1981; Wyborn *et al.*, 1981; White *et al.*, 1982).

A further distinction is that, unlike many I- and S-type granites, A-types rarely contain deformational fabrics. Instead they occur in anorogenic (ie unrelated to orogenesis in space or time) and continental rift settings, or else in the orogenic cycle, they post-date the development of convergent strain (usually by less than 30 Ma; Table 4.5). There is no apparent chemical, or other, distinction between A-types in these different tectonic settings the common link between settings seems to be a lack of convergent strain or a developing tensional regime which is consistent with the high level emplacement of A-types.

All of the mineralogical and chemical features of the Padthaway suite are consistent with the definition of A-types outlined above. They are highly fractionated with high Rb, Nb, La, Ce, Zr, Y and low Ba, K, Sr, Ti values quite comparable with the average A-type compositions in table 4.5. Their Ga/Al ratios are high classifying them as A-types according to Collins *et al.* (1982) and their high Rb, Y, Nb puts them in the within-plate granite field of Pearce *et al.* (1984). In figure 4.14 they plot in the A-type field defined by Whalen *et al.* (1987). The high level emplacement and relatively anhydrous, hypersolvus mineralogy is similar to most described A-types though the diverse pyroxene mineralogy of the Padthaway Suite is not preserved in many A-type suites. An example with similar mineralogy are A-type volcanics, from a bimodal suite in Queensland, described by Ewart (1981). Geochemically, the Padthaway Suite compositions span from the Ba and Sr-rich "post-orogenic" to the Ba and Sr-poor "early anorogenic" A-type subdivisions of Bonin (1990). The data presented here, including the decreasing trends of Sr, K₂O and the curvilinear trend for Ba, suggest that this compositional range is related by fractional crystallization in particular the onset of alkali

Table 4.6. Comparison of average I-, S-, and A-type granites with silicic rocks from large mafic intrusions

Data: 1- Whalen et al (1987); 2- White and Chappell (1983); 3- Kleeman and Twist (1989); 4- Nasund (1989); 5- Macdonald et al (1990); 6- Hergt (1987); 7- Ewart (1981); 9- Harris (1983).

	1 Average I-type (532)	1 Average S-type (316)	1 Average A-type (148)	2 Average A-type (31)	3 Bushveld Granite	4 Skaergaard granophyre	5 Iceland rhyolite	6 Tasmanian granophyre	8 Black Hill granophyre	9 Ascension Is comendite
SiO ₂	67.89	69.08	73.81	73.60	74.38	71.00	73.48	67.29	73.80	74.05
TiO ₂	0.45	0.55	0.26	0.33	0.21	0.45	0.21	0.83	0.31	0.13
Al ₂ O ₃	14.49	14.30	12.40	12.69	11.77	11.60	12.58	11.09	13.07	12.44
Fe ₂ O ₃ *	4.13	4.32	2.70	2.90	3.32	5.49	3.32	9.42	1.64	2.81
MnO	0.08	0.06	0.06	0.06	0.05	0.09	0.08	0.14	0.05	0.06
MgO	1.75	1.82	0.20	0.33	0.00	0.11	0.03	0.20	0.01	0.04
CaO	3.78	2.49	0.75	1.09	0.96	1.72	0.38	3.60	0.51	0.22
Na ₂ O	2.95	2.20	4.07	3.34	3.76	4.44	5.23	2.89	3.52	5.53
K ₂ O	3.05	3.63	4.65	4.51	5.00	3.43	4.16	3.08	6.20	4.60
P ₂ O ₅	0.11	0.13	0.04	0.09	0.02	0.05	0.01	0.19	0.02	0.02
Cr	27	46	-	3	-	25	-	1	5	-
Ni	9	17	1	2	12	8	-	1	3	-
Sc	15	14	4	14	2	3.5	0.7	17.8	4.7	-
V	74	72	6	10	-	9	-	1	7	-
Rb	132	180	169	199	180	75	125	121	163	147
Sr	253	139	48	105	54	130	15	101	24	1.34
Ba	520	480	352	605	737	840	180	635	116	-
Ga	16	17	24.6	21	20	-	-	18	19	-
Nb	9	11	37	22	24	90	173	16	30	205
Zr	143	170	528	342	355	1080	1045	334	236	871
Y	27	32	75	76	68	170	128	59	142	113
La	29	31	-	55	85	103	127	39	59	83.7
Ce	63	69	137	134	170	222	249	88	148	189.3
Nd	23	25	-	56	-	107	110	42.5	99	85.8
Rb/Sr	0.52	1.29	3.52	1.90	3.33	0.58	8.33	1.20	6.79	109.70
Zr/Ni	15.89	10.00	528.00	171.00	29.58	135.00		334.00	78.67	
Zr+Nb+Ce+Y	242.00	282.00	777.00	574.00	617.00	1562.00	1595.00	497.00	556.00	1378.30

feldspar fractionation. In terms of tectonic setting the Padthaway Suite intruded after orogenic deformation similar to many A-type suites (cf Table 4.5).

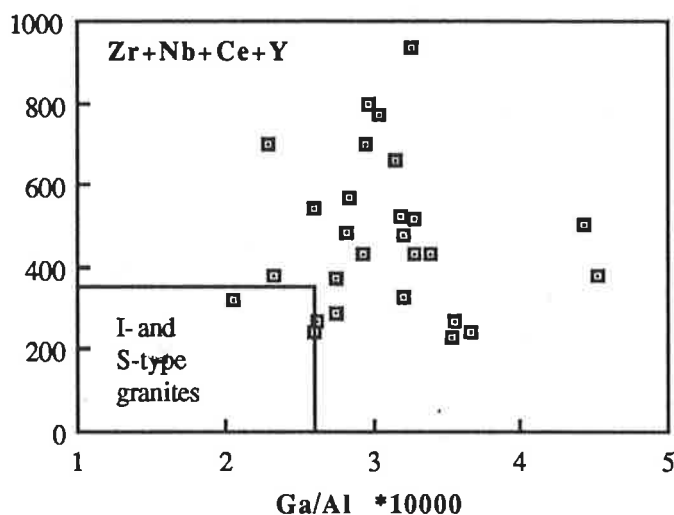


Figure 4.14. Plot of $10\,000 \cdot \text{Ga}/\text{Al}$ vs $\text{Zr}+\text{Nb}+\text{Ce}+\text{Y}$ showing that the Padthaway Suite rocks lie in the field of A-types as defined by Whalen *et al.* (1987).

4.8. Models for A-type magma genesis

Any model for A-type genesis must explain the features outlined above, for example Collins *et al.* (1982), Whalen *et al.* (1987) and Clemens *et al.* (1986) noted that derivation by differentiation of I- or S-types can be ruled out by the hotter and more anhydrous nature of A-types. Similar arguments suggest partial melting of a tonalitic source (eg Anderson, 1983; Sylvester, 1989) with a two *feldspar*-hornblende dominated mineralogy, which may have the appropriate chemistry to yield an A-type magma (Sylvester, 1989), is unlikely to produce the F-rich, hypersolvus and pyroxene-bearing mineralogy typical of A-type rocks. A model involving CO_2 and halogen metasomatism has been assessed and discounted by Whalen *et al.* (1987).

In the original definition of A-type granites, Loiselle and Wones (1979) outlined two alternative genetic histories for such rocks: one in which basalt interacts with a granulite facies lower crust (which has already undergone a previous partial melting episode) to generate magmas with high initial $^{87}\text{Sr}/^{86}\text{Sr}$ ratios; and one whereby enriched basalt fractionates directly to yield magmas with low initial $^{87}\text{Sr}/^{86}\text{Sr}$ ratios. Low initial $^{87}\text{Sr}/^{86}\text{Sr}$ ratios characterise the available isotope data (Table 4.5) and despite the fact that crustal contamination could be responsible for some suites ranging to higher values a currently popular model is melting of a granulitic residue remaining after generation and segregation of a previous granitic melt (Collins *et al.*, 1982; Clemens *et al.*, 1986; Whalen *et al.*, 1987).

4.8.1. The melt depleted granulite model

In this model the chemical characteristics of A-types result from small degree partial melting of a source which has already had an I-type granitic partial melt extracted (Collins *et al.*, 1982; Whalen *et al.*, 1987). The advantage of this model is that it explains the higher temperatures and relatively anhydrous, fluorine-rich nature of the magmas compared with earlier I- and S-type granites. Where initially proposed for the Lachlan Foldbelt (Collins *et al.*, 1982) this model has the additional advantage of explaining that the A-types were post-orogenic because their source region was only created by extraction of the earlier magmas during orogenesis, though it would be incorrect to pre-suppose this tectonic setting for all A-types (eg Whalen *et al.*, 1987).

It is necessary in accessing this model, to establish that such a source has the appropriate composition to produce an A-type. Fluid absent melting reactions of the type that will produce I-type melts produce residual plagioclase, pyroxenes and sometimes hornblende, sphene and ilmenite (Clemens and Vielzeuf, 1987; Vielzeuf *et al.*, 1990; Rushmer, 1989). According to White and Chappell (1977) and Chappell *et al.* (1987) calcic plagioclase, pyroxenes, apatite and zircon all occur as restite phases in granitic melts. These along with some quartz and possibly alkali feldspar would form a relatively anhydrous residue which would be termed a granulite (eg Nesbitt, 1980) and would require much higher temperatures to produce a second melt. In order to contain the K, F and incompatible elements (Zr, Nb, Y, LREE) found enriched in A-types this granulite is required to contain the more refractory fluorine-rich amphibole and biotite end members as well as apatite, zircon and possibly sphene (Collins *et al.*, 1982). However, unlike I- and S-type granites, the low TiO₂ and P₂O₅ contents and lack of inherited zircon in A-types seem inconsistent with apatite, zircon or sphene being significant phases in their sources.

Exposed granulites have highly variable composition (eg Vielzeuf and Vidal, 1990) and it is not easy to exactly constrain the composition of granulitic residues from melting events as these might be expected to be quite variable in composition from province to province. Nevertheless some constraints can be made. I-type granites are thought to be derived from basaltic to dioritic source rocks (Chappell and Stephens, 1988). The residues left after this melt extraction will be more mafic than the melt removed (Nesbitt, 1980; Vielzeuf *et al.*, 1990), ie a mafic granulite enriched in MgO, CaO and transition elements and depleted in incompatible elements, alkalis and Rb. Whilst the major element chemistry of A-types is dictated by the quartz-feldspar-liquid eutectic, trace elements can be used to constrain petrogenetic models. A characteristic often taken to indicate that a granulite has lost a partial melt is depletion in incompatible trace elements leaving very low incompatible to compatible element ratios (*i/c* ratios) such as Rb/Sr, K₂O/MgO, Zr/Ni (eg Rudnick and Presper, 1990). The residue therefore becomes *less* like an A-type when

a first partial melt is extracted. Partial melts of such residues are unlikely to obtain the high *i/c* ratios of A-types and migmatites in mafic granulites have quite low Rb/Sr, K_2O/MgO , Zr/Ni etc (eg Tait and Harley, 1988).

The difficulty of producing high *i/c* compositions from mafic residues is illustrated in table 4.7 which shows the trace element modelling results for melting of two mafic I-types from the Lachlan Foldbelt. According to Compston and Chappell (1979), Chappell (1984) and Chappell *et al.* (1987) these most mafic samples from I-type suites should be close approximations of residues because they lie closest to the restite end of restite-melt mixing lines. Assuming the optimum case where all accessory phases are completely consumed the trace element composition of small degree batch melts in equilibrium with a residue of 60% plagioclase, 25% clinopyroxene and 15% orthopyroxene have been calculated using the equation $C_L = C_0/(F+D-FD)$ from Cox *et al.* (1979). Figure 4.15 shows the partial melt compositions normalized to the average A-type of White and Chappell (1983). The elements are ordered so that those on the left (Rb-Y) are elements found enriched in A-types and those on the right (Ba-Sr) are typically depleted. Many A-types having more extreme compositions than the White and Chappell (1983) average

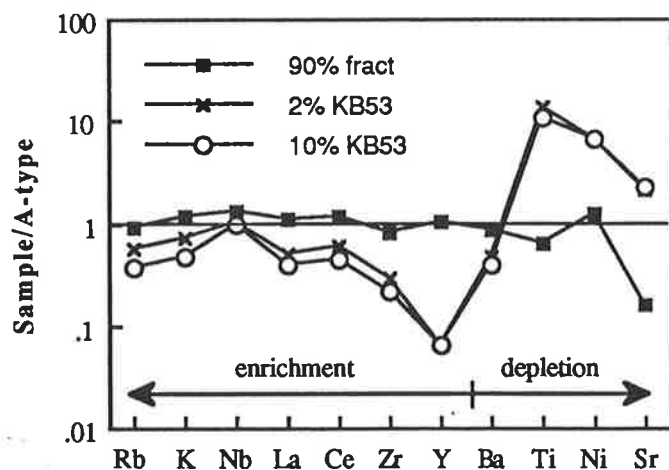


Figure 4.15. Spidergram, normalized to the average A-type granite of White and Chappell (1983) given in table 4.6, comparing small degree partial melts of a mafic I-type (taken to approximate a melt depleted source) with the composition resulting from 90% fractionation of a typical tholeiitic basalt (see text for details).

therefore plot above 1 for Rb-Y and below for Ba-Sr. It is clear from figure 4.15 that the modelled partial melts show quite the opposite trend. Compared with the average A-type composition these have compatible element concentrations which are too high and incompatible element concentrations which are too low so that their *i/c* ratios (Table 4.7) are much lower than those of A-type rocks (Table 4.6). It is possible that the chosen mafic I-types contain some melt and do not represent true restite, however this would

Table 4.7. Modelling of partial melts from mafic I-type granites.

Sample#	KB53	Bulk D	2% Melt	10% Melt	KB139	10% Melt
SiO ₂	47.25				55.50	
TiO ₂	0.77	0.200	3.60	2.75	0.70	2.50
Al ₂ O ₃	19.86				18.63	
FeO	9.47				6.81	
MnO	0.17				0.12	
MgO	6.42				4.81	
CaO	11.41				8.10	
Na ₂ O	1.48				2.22	
K ₂ O	0.40	0.104	3.28	2.07	0.95	4.91
P ₂ O ₅	0.05				0.10	
Cr	34	2.830	12	13	37	14
Ni	14.5	1.112	13	13	15	14
Sc		9.774		0	32	4
V	348	0.024	303	306	169	149
Pb		0.000		0	6	60
Rb	15	0.118	110	73	39	190
Sr	438	1.958	226	235	256	138
Ba	90	0.298	288	245	215	585
Nb	5*	0.198	23	22	5	18
Zr	19	0.180	97	73	68	260
Y	8	1.680	5	5	18	11
Th	1.8	0.086	17	10	4	23
U	0.2	0.000		2	4	40
La	6	0.198	28	22	13	47
Ce	14	0.158	80	58	30	124
Rb/Sr	0.03		0.49	0.31	0.15	1.38
Zr/Ni	1.31		7.46	1.69	4.53	18.57
Zr+Nb+Ce+Y	46		205.00	158	121	413

KD's from Cox et al (1979), Tait and Harley (1988)

Sample KB53 from Hine et al (1978) *Nb estimated, KB139 from Chappell (1984).

only make the match worse because their incompatible element concentrations (and therefore those of the modelled melts) would be higher than for true restite. In fact calculated restite compositions for some I-types in the Lachlan Foldbelt (Compston and Chappell, 1979) have lower Rb (2-5ppm), K₂O (0.5%) and higher Sr (400-1200ppm) than the examples used here. Irrespective of their exact composition depleted sources are unlikely to yield A-type magmas. Independent modelling by Sylvester (1989) has shown that the melt depleted sources proposed for the Lachlan Foldbelt and even the average lower crustal composition of Taylor and McLennan (1985) would have Rb, Ba, Sc, Y and probably LREE contents too low to allow them to yield the observed A-types.

A further problem lies in the ability of the melt to leave its source. The trace element match can be partially improved by very small degrees of partial melting where enrichment of an incompatible element approaches $1/F$ with a limit of $1/D$ (where F is the fraction of melt and D is the bulk distribution coefficient) however McKenzie (1985) has shown that it is unlikely that granitic partial melts less than 10% can separate from their sources. Even though high temperatures and elevated fluorine contents would lower A-type viscosities it is not clear that melt fractions much less than 10% could separate from their matrix.

Collins *et al.* (1982) and Whalen *et al.* (1987) argue that A-type magmas have not undergone significant fractionation subsequent to partial melting. However it seems clear from the enrichment of incompatible elements and the low Rb/Sr ratios typical of A-types that they have indeed undergone considerable fractionation. Furthermore residues from 1st cycle melt extraction, which will contain residual calcic plagioclase, would not be expected to have negative Eu anomalies and may even have positive Eu anomalies. Analyses suggested to be typical of the lower crust and melt depleted granulites have very low Rb/Sr and positive Eu anomalies (Taylor and McLennan, 1985). Consequently the large negative Eu anomalies characteristic of A-types and must indicate protracted feldspar fractionation. The question is how much fractionation and what was the parental magma?

4.8.2. A basalt fractionation model

In light of the bimodal association of A-types with gabbros and basalts it seems surprising that a model involving fractionation from basaltic magma has not been more closely scrutinized. This model can equally well explain the high temperature, relatively anhydrous nature of A-types, with mantle magmas being readily accessed in tensional environments. High F contents may well develop, since mantle derived tholeiitic melts contain 200-500 ppm F (Schilling *et al.*, 1980) and these will be increased by fractionation.

Basaltic magma typically undergoes plagioclase, pyroxene and olivine dominated fractionation in layered sills or intrusions. A least squares mixing approach to assess production of an A-type composition by such fractionation. The modelling (Table 4.8)

Table 4.8. Results of two stage modelling of fractionation of a tholeiitic basalt to produce an A-type granite.
Trace element results for Rayleigh fractionation, KD's as for table 4.7

Step 1: tholeiitic basalt to quartz dolerite			Step 2: quartz dolerite to A-type granite		
Parent observed (Tholeiitic basalt)	Parent estimated (sum residuals squared = 1.54)		Parent observed (= quartz dolerite and daughter from step 1)	Parent estimated (sum residuals squared = 0.22)	Daughter (A-type)
F (fraction of quartz dolerite magma produced) = 31.9% Assemblage fractionated: plag 53%; cpx 34%; ol 13%			F (fraction of A-type magma produced) = 33.5% Assemblage fractionated: plag 56%; cpx 34%; mt 10%; ap 0.4% (total fractionation from tholeiite to A-type = 90%)		
SiO ₂	53.62	53.28	55.68	55.67	75.14
TiO ₂	0.57	0.56	1.54	1.55	0.21
Al ₂ O ₃	15.86	16.12	15.53	15.46	12.11
Fe ₂ O ₃	8.10	8.86	12.18	12.18	2.48
MnO	0.19	0.29	0.15	0.17	0.09
MgO	7.41	7.26	1.84	1.83	0.19
CaO	11.31	11.88	7.72	7.76	0.64
Na ₂ O	1.75	2.40	2.31	2.77	3.51
K ₂ O	0.58	0.64	1.86	1.81	5.21
P ₂ O ₅	0.13	0.13	0.19	0.14	0.01
	Cl	bulk D	Cl	bulk D	Cl
Ni	74	2.063	22	3.046	2.4
Sc	42	1.034	40	1.226	32
V	236	0.383	477	3.380	36
Rb	33	0.044	68	0.115	179
Sr	135	1.004	131	2.875	17
Ba	217	0.129	488	0.961	514
Nb	4.5	0.099	13	0.199	28
Zr	95	0.091	245	0.131	279
Y	20	0.300	49	0.529	77
La	11	0.122	33	0.450	59
Ce	24	0.184	86	0.474	153
Nd	12	0.214	32	0.591	50

was done in two stages via an intermediate quartz dolerite starting with a typical continental tholeiite composition similar to the quenched margins from the Tasmanian Dolerites (Hergt *et al.*, 1989). Mineral compositions used in the first stage were from the Tasmanian Dolerites and in the second stage compositions from the Padthaway Suite (see subsequent sections). The expected trace element composition of the fractionated melt was calculated assuming simple Rayleigh fractionation ($C_L = C_0 F^{(D-1)}$). The end product of 90% crystallization is plotted on figure 4.15 and is clearly a good approximation of an A-type magma with high i/c ratios comparable to the averages in table 4.6. Further fractionation will continue to enrich Rb-Y, and deplete Ba-Sr (see Fig 4.15).

Evidence for extreme fractionation (usually combined with some crustal assimilation) of mafic magma is well documented, resulting in high concentrations of silica, alkalis and incompatible trace elements and low concentrations of MgO, CaO, Al₂O₃ and compatible trace element contents. Examples include the Loch Ba ring-dyke (Sparks, 1988), the Woods Mountains volcanic centre (Musselwhite *et al.*, 1989), Mount Ascutney (Foland *et al.*, 1988) and La Primavera (Mahood and Haliday, 1988). That A-type compositions specifically are produced from basaltic magma is demonstrated by the occurrence of granophyres with A-type compositions in layered mafic complexes such as Skaergaard and the Tasmanian Dolerites, A-type rocks on oceanic volcanic islands like Ascension, Reunion, Easter and Kergulean (Baker, 1974) and by A-type rhyolites from bimodal volcanos in Iceland and Queensland. Compositions of some of these rocks including the Bushveld granites are compared with the average A-type compositions in Table 4.6. The intimate association of A-type compositions and mafic magmas is further demonstrated by mingling between the two magma types as in the Topsails terrane (Whalen and Currie, 1984) and both the plutonic (Sparks and Marshall, 1986) and volcanic (McGarvie *et al.*, 1990) environments of the British Tertiary Province.

The general lack of intermediate compositions has been raised in objection to the fractionation model for A-types however this does not in itself disprove the hypothesis. Lavas with $57\% < \text{SiO}_2 < 63\%$ have not been found on Ascension Island where continental crust and earlier I-type granites are clearly absent yet magmatic rocks span 50-77% SiO₂ at Velasco, Bolivia (Fletcher and Beddoe-Stephens, 1984) and A-type magmas have developed in both localities. The mechanisms of production of A-type liquids in large mafic intrusions without voluminous intermediates, such as those described above, are not well understood. Possible scenarios involve liquid fractionation processes (eg McBirney, 1980) or coalescing and gravity segregation of the late interstitial granophyric liquids seen in many layered mafic complexes. For example, during cooling (from 1200-1000 °C) of a tholeiitic melt, olivine, pyroxenes, plagioclase and magnetite sequentially crystallize. Once convection has stopped these minerals will form a grain-supported matrix containing a residual interstitial liquid depleted in MgO, CaO, Al₂O₃, Cr, Ni, Sc,

V, Sr. Continued cooling (1000-900 °C) allows adcumulus growth ultimately leaving the liquid enriched in components incompatible with these minerals (ie SiO₂, Na₂O, K₂O, Rb, Ba, Zr, Nb, Y, LREE). The pods and sills granophyric material in the Skaergaard Intrusion are evidence that such liquids develop and have A-type compositions (see Table 4.5). Isotopic data on granophyric pods from the upper zones of the Skaergaard Intrusion confirms their derivation from the gabbroic liquids though some have clearly been contaminated by the country rock gneisses (Stewart and DePaolo, 1990). Likewise the upper sections of the Tasmanian Dolerites contain granophyres resulting from fractionation of the mafic magma (McDougall, 1962). These have A-type compositions (see Table 4.5) and probably formed by coalescing of interstitial granophyric material which can be seen in many of the Dolerites. Continued cooling and movement of such interstitial liquid through the crystal matrix would further slow diffusive exchange with the cumulus minerals. Compaction of the cumulate pile is probable and will expel the interstitial liquid (Sparks *et al.*, 1985) which may then separate from the pluton as a diapir. Importantly A-type liquids produced by such a process would be at temperatures well above their solidus (800-725 °C for 1.5 to 3% H₂O, Clemens *et al.*, 1986) explaining why A-types have such high temperatures and are emplaced in a near wholly molten state.

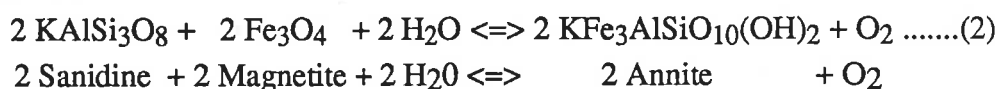
4.9. Petrogenesis of the Padthaway Suite

The data presented above show that the Padthaway Ridge A-type granites and volcanics were derived from highly fractionated, high temperature and relatively anhydrous magma. Their mineralogy implies an extended history of polybaric crystallization from more mafic magma. They differ from the slightly earlier (516-~500 Ma, Foden *et al.*, 1990b) Delamerian I- and S-type "syn-tectonic" granites of this same terrain in that these older granite series are all two-feldspar granites with more moderate enrichments of K₂O and lithophile trace elements and all contain biotite even those of relatively mafic granodiorite compositions (Foden *et al.*, 1990a). The earlier granites appear to have been F-poor and relatively hydrous, consistent with their apparent emplacement and crystallization at greater crustal depths (10-15 Km).

4.9.1. Implied quaternary quartz-feldspar relationships

Relative to the two feldspar (sub-solvus) types, the Padthaway one feldspar (hypersolvus) granites have mineral assemblages consistent with development at either higher temperatures or at lower aH₂O (or lower PH₂O). Granites from Marcollat for instance are biotite-free, fluoro-ferrohastingsite (with ferro-augite cores) -bearing, with no plagioclase and with relicts of fayalite. The single alkali feldspar in these is now very coarse perthite composed of almost pure albite and potassic microcline and has a

reconstructed primary sodic sanidine composition of Ab₅₀:Or₅₀, the same as sanidines analysed from the volcanics. This is very close to the minimum melt composition on this join. The subsolvus Padthaway volcanics and granites crystallized from plagioclase-poor two-feldspar magmas. In these plagioclase is sodic oligoclase (An₁₀₋₂₀) and the alkali feldspar is again coarsely perthitic. Biotite is much more common in this two feldspar group implying that the reaction:



is displaced to the right. Such a reaction is favoured either by falling temperature or by increased aH₂O.

The one feldspar mineralogy of the hyper-solvus granites implies that crystallisation took place at low pressures (eg Martin and Bonin, 1976) under conditions where there is an interval of one feldspar crystallisation between the solidus and the solvus in the quaternary Q-Ab-Or-An system (eg Tuttle and Bowen, 1958; Carmichael *et al.*, 1974; Clemens *et al.*, 1986). At 1 kbar this gap is about 150 °C under water saturated conditions and this will expand by migration of the solidus to increasing temperatures with aH₂O values decreasing <1. Similarly at 1 kbar, the ternary eutectic temperature increases from about 710 to 950 °C as aH₂O decreases from 1 to 0. In the quaternary Q-Ab-An-Or (+H₂O) system fractional crystallisation of more mafic magmas will result in the precipitation and removal of first plagioclase and then plagioclase together with a potassic alkali feldspar followed finally by a single ternary alkali feldspar.

The high temperatures and low water contents of the Padthaway suite favour a liquid evolution path which intersects the water undersaturated granite minimum and permits ongoing fractionation of ternary alkali feldspar and quartz until the fluid-saturated minimum is reached. At 1 kbar, such a process could involve crystallisation through a temperature interval as large as 200 °C with very little change in the major element chemistry of the magma. Trace element compositions however would be highly modified during this stage. Depletion of Eu, Sr and Ba due to their partition to the feldspar, and complimentary enrichments of trace elements which continue to remain incompatible (e.g. LREE, Zr, Nb, Y) would be expected to develop at this stage.

4.9.2. The role of fluorine

Fluorine has important effects in modifying relations in the granite minimum melt system and fluorine measured on representative samples of the Padthaway granites was high (500 to >2000ppm) exemplified by the fluorine-rich character of the amphiboles and biotites (Table 4.2). In the water-saturated Q-Ab-Or system Manning and Pichavant (1983) demonstrate that the addition of F shifts the ternary eutectic towards more albite-rich compositions (expands the primary phase field of quartz). In this sense the effects are

equivalent to F-free increase in PH_2O . The addition of 2% F has the same effects in shifting the water saturated eutectic as does the increase in PH_2O from 1 to 10 kbars. At the same time F markedly reduces the temperature of this minimum. 2% F decreases the 1 kbar water-saturated liquidus minimum from 730 to 670 °C and depresses the solidus to 650 °C or less. The normative Q-Ab-Or compositions of the Padthaway granites fall between the F-free 1 kbar and the 1% F cotectics in direct accord with their F concentrations showing the displacement of these compositions away from the 0.5 and 1kbar F-free minima (Fig 4.16).

Differentiation at high temperatures and relatively anhydrous, F-rich conditions means the magmas evolved to high F^-/OH^- ratios. Under these conditions, accessory phases such as zircon, sphene, apatite and allanite which buffer the concentrations of the above elements in "normal" I-type granites, precipitate late in the crystallisation sequence. White *et al.* (1982) have suggested that in fluorine rich magmas, such as these, Zr, Nb and Ga form alkali-fluoro complexes delaying the saturation of phases such as zircon which would result in depletion of these elements. Recent experimental work shows that

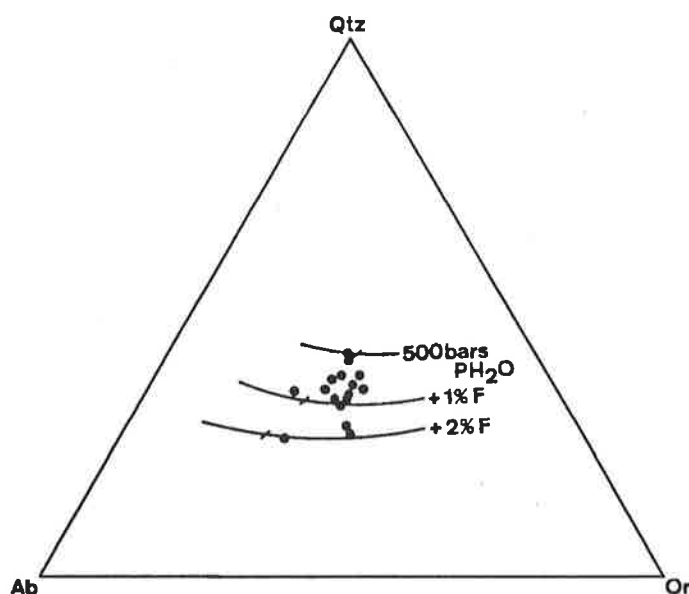


Figure 4.16. CIPW normative plot for selected Padthaway granites showing their displacement from the water saturated ternary minimum ($\text{PH}_2\text{O} = 500$ bars) towards the same minimum with added fluorine. The position of the minima is marked by dashes on the curves which are taken from Manning and Pichavant (1983).

the rare earths become similarly co-ordinated by fluorine (Ponader and Brown, 1989). The trace element (and P_2O_5) data indicates that minor phase fractionation involving zircon, apatite and possibly allanite became significant but only commenced when the magma had reached 75% SiO_2 .

4.9.3. Isotopes and source compositions

As discussed, in detail above, the development of one feldspar assemblages implies fractionation from more mafic parental magmas in the primary plagioclase phase volume. Features such as curvilinear trends for many elements the very low Mg and Fe contents and high Fe/Mg ratios, low CaO, low Al₂O₃, low K/Rb, very low Sr, low Ba, large negative Eu anomalies ($Eu/Eu^*=0.12$) very high LREE contents, high La/Yb ratios and high Rb/Sr ratios all show that the Padthaway granites experienced an extended history of fractional crystallisation of ferromagnesian phases, plagioclase and potassium feldspar.

Initial $^{87}Sr/^{86}Sr$ and $^{143}Nd/^{144}Nd$ isotopic ratios allow definition of possible source compositional characteristics and the high ϵNd and low initial $^{87}Sr/^{86}Sr$ ratios of the Padthaway Suite demonstrate a major mantle component though the trend towards lower ϵNd and higher $^{87}Sr/^{86}Sr$ with increasing SiO₂ and K₂O indicates some crustal contamination. At 487 Ma the local country rock (Kanmantoo Group metasediments) have ϵNd around -11 and $^{87}Sr/^{86}Sr$ around 0.7245. Clearly the Padthaway magmas were not derived by partial melting of these sediments or the older basement beneath which has even more evolved values. Granites and their restite should, by definition, be in isotopic equilibrium. If the Padthaway A-types were derived from residues left by the earlier I-type granites they should have isotopic values indicative of the same source. However data on these I-types such as the Taratap Adamellite adjacent to the Padthaway Ridge (ϵNd -8.55;

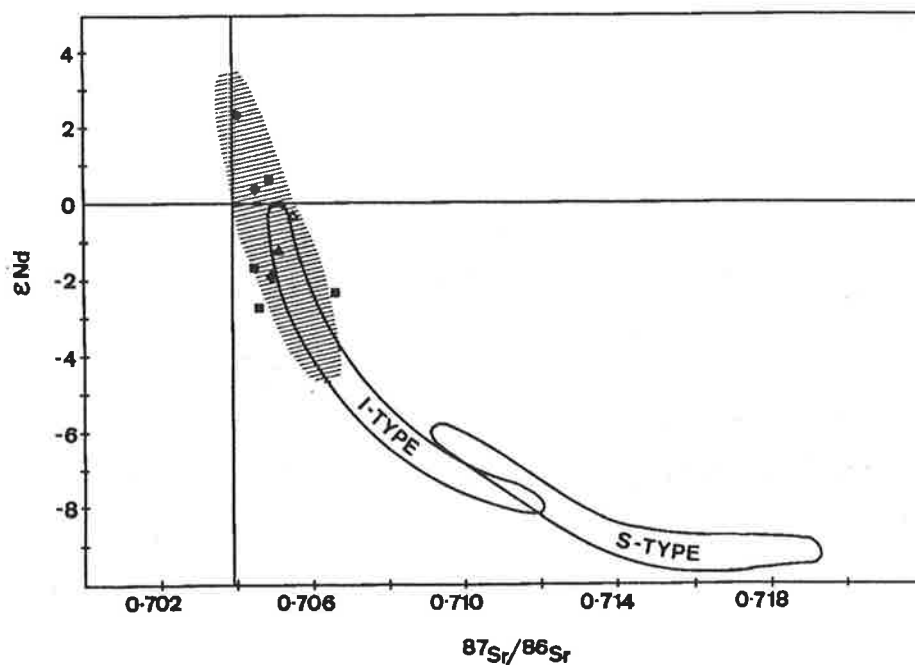


Figure 4.17. ϵNd vs initial Sr ratio diagram showing the overlap of the Padthaway samples (squares) with the range of the Black Hill granophyres (diamonds) and gabbros (shaded region). Also shown are the subsurface gabbro from the Padthaway Ridge (circle), a dioritic enclave and granite from Mannum Quarry (open and closed triangles respectively; see chapter 5 for details) and the range of values for I- and S-type granites from the Lachlan Foldbelt (data from McCulloch and Chappell, 1982).

$^{87}\text{Sr}/^{86}\text{Sr}$ 0.714657 Turner and Foden unpublished data) does not favour such an origin. Furthermore the high Rb (207 ppm) and Zr (234 ppm) concentrations of the Taratap Adamellite indicate its depleted source region would be an unlikely source for subsequent A-type magma generation.

In summary all the available data indicate that the Padthaway A-types were derived by fractionation from contemporaneous tholeiitic magmas like those at Black Hill or Coonalpyn. This is strongly supported by the presence of late stage granophyres in the Black Hill complex which have compositions identical to the Padthaway Ridge and other A-types (cf chapter 3). Isotopically these granophyres are indistinguishable from the Padthaway A-types ($\epsilon\text{Nd} +0.42$ to -1.88 and initial $^{87}\text{Sr}/^{86}\text{Sr}$ 0.7034-0.7045) and figure 4.17 shows that the range of isotopic data from Black Hill overlaps that of the granophyres and the A-type granites and volcanics. Also shown in the range of I- and S-type granites from the Lachlan Foldbelt most of which are isotopically much more evolved than the Padthaway suite A-types.

In the previous chapter fractionation at Black Hill was modelled using the program TRACE5 and the final magma composition resulting from 90% fractionation was a close approximation of the granophyric sills found at Black Hill. Figure 4.18 shows this, the primary magma and a granophyre from Black Hill all normalized to the average A-type of White and Chappell (1983). The granophyre and the modelled 90% fractionate are almost indistinguishable from each other or average A-type compositions. Note that extended fractionation has resulted in even lower Ba, Ti, Ni and Sr than the average A-type (cf Fig. 4.15 and discussion).

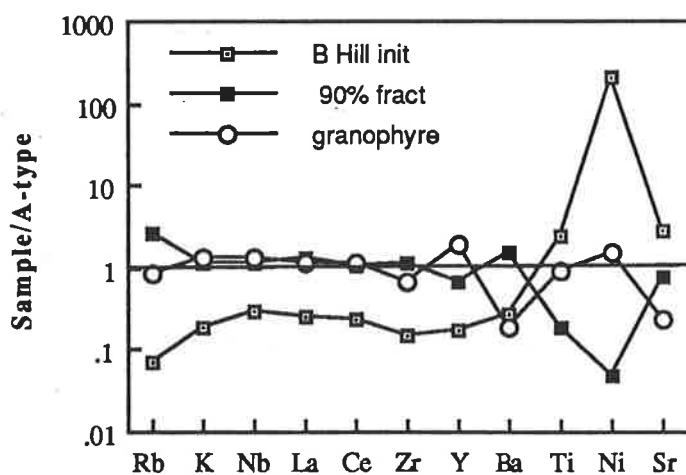


Figure 4.18. Spidergram, as in figure 4.15, showing the composition of the parental Black Hill magma from chapter 3, a granophyre from Black Hill and the modelled composition resulting from 90% fractionation taken from table 3.3.

4.10. Concluding remarks

The distinctive characteristics of A-type magmas clearly demand a petrogenetic origin different to that of I- and S-types. Features such as high i/c ratios and large negative Eu anomalies are hard to reconcile with derivation from a melt depleted source. However they are explicable by a model involving fractionation from mafic magma. The bimodal association, high magma temperatures and relatively anhydrous mineralogy of A-types are also readily understood in such a model. Where these features can be established the additional evidence from high ϵNd and low $^{87}\text{Sr}/^{86}\text{Sr}$ ratios seems unequivocal evidence of a mantle origin. Modelling seems to require some enrichment of the basaltic magma starting composition which could imply crustal contamination or derivation from enriched lithospheric mantle such as the K-rich layer of McKenzie (1989) (cf chapter 3).

There may be subdivisions of A-types with varying origins such as suites with more evolved isotopic signatures that have a significant crustal contribution. Flat REE patterns (excepting Eu) may indicate a pyroxene rich residual source contribution whilst LREE enriched patterns result from fractionation. Bonin (1990), for example, has suggested a breakdown into high Ba, post-orogenic suites which have a crustal contribution and low Ba, anorogenic suites that lack crustal contamination. However, A-types show a broad range in Ba content and fractionation of alkali feldspar at the granite minimum will lead to low Ba, low Sr magmas whose $^{87}\text{Sr}/^{86}\text{Sr}$ ratios will be very susceptible to contamination (samples of the Marcollat granite show a range of Ba 200-15, Sr 10-2 ppm).

Finally, if the model for A-type genesis presented here is accepted, the high degree of fractionation (~90%) required to produce A-type magmas necessitates that large volumes of mafic magma be intruded into the crust even though A-type rocks are generally volumetrically minor compared to I- and S-types (eg Collins *et al.*, 1982; Clemens *et al.*, 1986). In the case of the Padthaway Ridge, for example, the gravity anomaly indicates the presence of voluminous subsurface mafic rock. The A-type examples from Mull, Oslo and the Gawler Ranges are also underlain by large gravity anomalies (see references listed in table 4.5). Therefore A-type suites, in both rifting and post-orogenic environments, may represent episodes of crustal growth in which considerable volumes of mantle material are added to the crust. The intimate association between the mafic and felsic magmas resulting from such a process is frequently demonstrated by evidence for mingling between mafic and silicic magmas. In the case of the southern Adelaide Foldbelt such a situation is exemplified to the south of Black Hill at Mannum and this is the topic of Chapter 5.

Chapter 5. The Mannum Granite: magma mingling, diffusion and implications for the origin of A-type magmas

5.1. Introduction

The Mannum Granite is an Early Ordovician intrusive exposed in a quarry on the eastern side of the Murray River near the town of Mannum 70km east of Adelaide. It occurs to the east of the prominent range of Late Proterozoic to Cambrian sedimentary rocks of the Adelaide Fold Belt (Figs. 1.1 & 2.1). In the sub-division of Delamerian granitic rocks into syn- and post-tectonic suites (Foden *et.al.*, 1990a) the Mannum Granite belongs to the latter group. Well defined by a marginal magnetic anomaly, it is a roughly circular pluton about 11 km in diameter. Although its contacts are obscured by Tertiary rocks, it is thought to intrude the same Cambrian metasedimentary sequences as the syn-tectonic granites further to the west. Nearby, granite bodies of similar age and composition also occur at Sedan and Murray Bridge (Fig. 2.1).

As already discussed the late-orogenic suite comprises A-type granites and volcanics and these may be associated with a period of crustal relaxation or extension just after the close of the Delamerian Orogeny. Mafic dykes and plutons which accompany the silicic suite, making the late-orogenic magmatism bimodal. Evidence presented in chapters 3 and 4 suggest that the mafic and silicic magmas were at least thermally related. Their similar initial $^{87}\text{Sr}/^{86}\text{Sr}$ and $^{143}\text{Nd}/^{144}\text{Nd}$ isotopic compositions and geochemical modelling suggest that they have common parental magmas (chapter 4). This chapter further investigates the interaction between these contemporary mafic and silicic magmas through apparent evidence for magma mingling in the Mannum pluton.

5.2. Age constraints

One aim of this chapter is to show that during the late-orogenic phase in question, mafic and silicic magmatism were contemporaneous. This is already indicated by the available geochronological data. Gabbros from the Black Hill intrusive complex yielded a Rb-Sr total-rock - biotite age of 487 ± 5 Ma and a K-Ar Bt age of 486 Ma (Milnes *et al.*, 1977) whilst a seven point Nd-Sm mineral isochron gave 489 ± 10 Ma (chapter 3). U-Pb zircon data (Foden *et al* in prep) on an undeformed diorite at Reedy Creek (490 Ma) and the undeformed A-type Marcollat Granite (490 Ma) from further to the south east further constrains this Delamerian late-orogenic igneous activity to 487-490 Ma.

At the Mannum Quarry, the granite and a series of six samples taken from core to rim of a 25 cm mafic enclave were selected for Sr isotopic analysis and yielded a model 1 isochron with an age of 488 ± 10 Ma and an initial $^{87}\text{Sr}/^{86}\text{Sr}$ value of 0.70565 (Foden *et al.*, 1990b). A meter-wide dolerite dyke that cross-cuts the granite falls just below this isochron and at 488 Ma would have a slightly lower $^{87}\text{Sr}/^{86}\text{Sr}$ ratio of 0.70485. These data either indicate that the mafic enclaves and the granite were of separate origin but that their Sr isotopic compositions were homogenised at the time of intrusion, or that they were differentiates of a common parent magma. If the common initial ratio results from homogenization then it is probably very close to that of the granite as the mafic enclaves only constitute a minority of the pluton whose composition shows little evidence for whole-sale mafic contamination. Either way the granite's initial ratio is low suggesting a mafic and/or young source. As the mid-Proterozoic crystalline basement that underlies the Adelaide Fold Belt would have had an $^{87}\text{Sr}/^{86}\text{Sr}$ range of about 0.7110 - 0.7450 at that time it is clear that the origin of these A-type granites owes little to underlying sialic crystalline basement.

Although Sr isotopic homogeneity occurred at the age of the intrusion this cannot be used as unequivocal evidence for magma mingling as diffusion rates may be fast enough for equilibration between a magma and solid xenoliths at magmatic temperatures over about ten centimetres in timespans < 1 Ma (Margaritz and Hofmann, 1978).

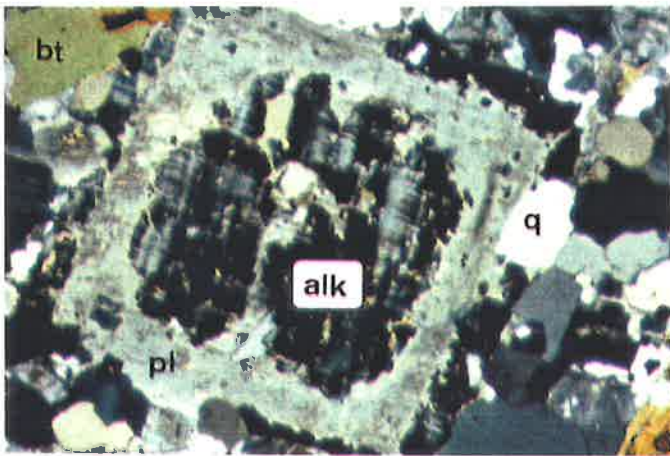
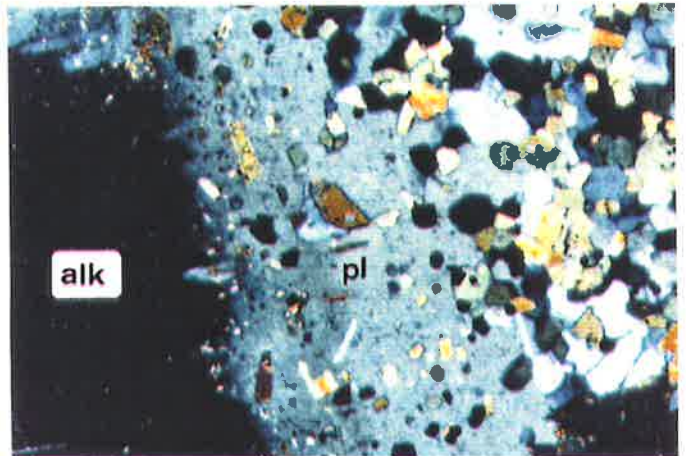
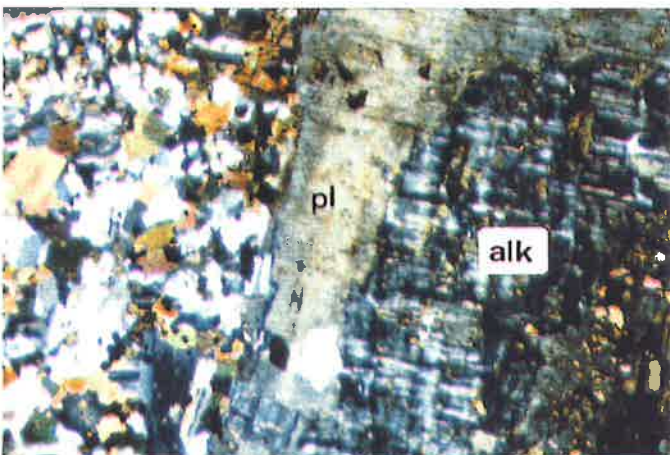
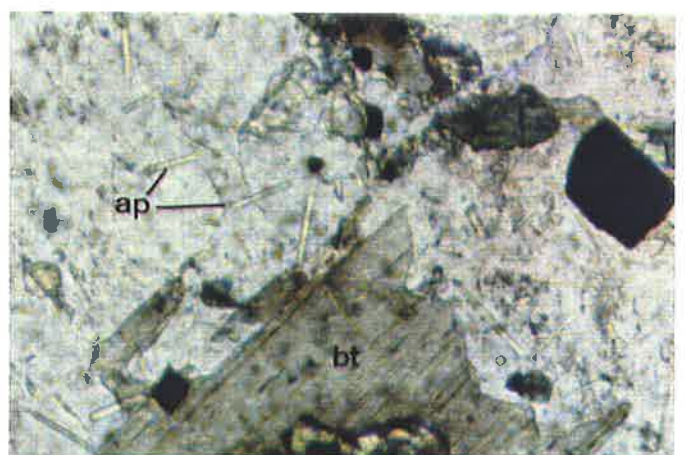
5.3. Field relationships

At the Mannum Quarry the granite is cut by a mafic dyke (Fig. 5.1a) and is host to numerous dioritic enclaves which constitute about 5% of the outcrop (Figs. 5.1a-d). In the quarry the main constituent rock type, is a medium-coarse grained alkali feldspar-rich granite with a pink-buff colour. It is composed of large grains of alkali feldspar, which are frequently mantled by plagioclase to produce rapakivi textures, quartz, plagioclase, biotite and euhedral sphene. Richness in sphene appears to be a regional characteristic of the Delamerian granites of the Southern Adelaide Fold Belt and those in the Mannum Granite often reach 1cm in length. The granite also contains minor magnetite, fluorite and quite abundant carbonate whose euhedral textural relations make it appear contemporary with magmatic crystallization.

The coarse granite hosts numerous sizable (up to 4m across) blocks of a much finer and more even grained, but mineralogically and chemically similar microgranite (both coarse and fine phases plot close to the Ab-Or-Q ternary eutectic). These are concentrated towards the top of the quarry and contacts between the two phases are very sharp (Fig. 5.1b). Mirolitic cavities are common particularly in the fine grained granite their presence implying high level intrusion. In thin section the projection of euhedral,

Figures opposite:

- Figure 5.1a.** Dolerite dyke cutting the coarse grained Mannum Granite. Note the mafic enclaves to one side of the dyke.
- Figure 5.1b.** Large chilled block of fine grained granite stopped into the coarser host granite at Mannum Quarry. Note the sharp edges to the chilled block.
- Figure 5.1c.** Dioritic enclaves in the granite containing numerous rapakivi feldspar inclusions. Note the more diffuse grey areas of hybrid rock.
- Figure 5.1d.** "Double enclave" containing amoeboid patches of darker enclave within a more hybridized grey enclave zone. Note the rapakivi phenocrysts in both phases.
- Figure 5.1e.** Photomicrograph of rapakivi texture from the coarse Mannum Granite (A861-94). Bt = biotite, pl = plagioclase, alk = alkali feldspar, q = quartz. Crossed polars, width of view 4 mm.
- Figure 5.1f.** Rapakivi feldspar from within an enclave (A779-60) showing how the plagioclase (pl) rim on the alkali feldspar core (alk) overgrew and trapped nuclei growing in the enclave. Note the corroded outline of the alkali feldspar core. Crossed polars, width of view 4 mm.
- Figure 5.1g.** Similar photomicrograph to Fig. 5.1f. showing a large rapakivi feldspar from the granite included in a dioritic enclave (A861-96). Note again the corroded outline of the alkali feldspar core. Crossed polars, width of view 4 mm.
- Figure 5.1h.** Dioritic enclave (A779-64) containing biotite (bt) and numerous needles of apatite (ap). Plane polarized light, width of view 1.5 mm.

**a****b****c****d****e****f****g****h**

needles of feldspar into patches of carbonate suggests that the carbonate may be a filling to these cavities.

Swarms of fine- to medium-grained, dioritic enclaves are distributed abundantly through the coarse-grained granite (Figs. 5.1a-d). The enclaves show a diverse spectrum of relationships to the host granite. Some are dark and homogeneous with well defined, sharp, irregular, brittle looking edges. Much more commonly however, they have globular, rounded shapes with smooth cusped or lobate outlines and appear to have been able to undergo plastic deformation. Some show comet-like or tear-drop forms with elongate tails. In the latter case, the enclaves show disaggregation into droplets in the tail, where there is also a high proportion of completely hybridized mafic material. These shapes argue strongly for a liquid origin of the enclaves.

Many of the enclaves show varying degrees of reaction with the host granite to produce a mesocratic rock which contains the most abundant development of rapakivi feldspars (Figs. 5.1c & d). This hybridization effect commonly results in prominent zonation of the enclaves, with pale grey outer zones and darker inner zones (Figs. 5.1c & d) similar to the "double microgranular enclaves" of Didier (1973). The presence of some enclaves is indicated in outcrop solely by pale grey hybrid patches.

Large, pink, rapakivi feldspars are common within and particularly in the outer zones of some enclaves (Figs. 5.1c & d) and these exhibit much broader albite rims than do the feldspars in the host granite away from the enclaves. Most of the mafic enclaves are between 5 and 50cm, though one large enclave is at least 5m in diameter and shows complex net veining by the granite. The enclaves do not have visible chilled margins, though the metre-wide, vertical, fine-grained dolerite dyke that cuts all phases of the granite does show marginal quenching. This dyke has straight parallel margins and evidence for chilling is provided by the very fine-grained contacts. There is no evidence for metamorphism or re-melting of the granite. The exact age of the dyke is not known though it clearly intruded the granite after it had cooled enough to undergo brittle fracture.

The mafic xenoliths are not found in any of the microgranite blocks and it appears granite intrusion occurred in a number of pulses with magma mingling occurring during a later pulse that involved major block-stopping of an earlier, chilled (marginal) phase. The absence of any indication of fusion of the marginal granite by the latter in spite of its minimum melt composition, speaks strongly against any suggestion that the mafic enclaves were themselves melts formed from originally solid xenoliths.

5.4. Petrography and microtextures

Selected electron microprobe analyses are given in table 5.1. The host granite has a bimodal grain size distribution in which large (4-15 mm) phenocrysts of quartz and

Table 5.1. Selected mineral analyses from Mannum

Sample Lithology Mineral	861-94 granite biotite	861-94 granite hornblende	861-94 granite plagioclase	861-94 granite k-spar	MG6-F granite perthite	779-60 enclave biotite	779-60 enclave hornblende	779-60 enclave plagioclase	779-60 enclave k-spar	MG6-B enclave biotite	MG6-B enclave plagioclase
SiO2	38.52	47.07	66.80	67.59	67.10	39.61	48.10	67.86	66.25	39.25	66.88
TiO2	1.13	0.93				0.95	0.37			0.86	
Al2O3	11.30	6.17	22.37	19.20	19.14	11.67	6.09	22.11	18.79	12.20	22.47
FeO	15.99	16.81				15.33	17.64			14.48	0.13
MnO	0.98	1.37				0.53	0.97			0.73	
MgO	15.15	11.61				16.39	11.38			16.06	0.09
CaO		11.34	2.70				11.95	2.35			2.88
Na2O		2.12	10.21	1.18	3.53	0.18	1.37	10.65	0.35	0.23	10.26
K2O	10.11	0.96	0.12	15.75	11.72	9.82	1.07	0.10	16.36	9.99	0.38
Cl	nd	0.06				na					
F	1.49					na					
Total	94.68	98.44	102.19	103.73	101.48	94.48	98.94	103.07	101.75	93.79	103.10
Si	5.9699	7.0393	11.4921	11.9952	12.0006	5.9919	7.1433	11.5684	12.0118	5.9709	11.4439
Ti	0.1317	0.1042				0.1085	0.0413			0.0988	
Al	2.0640	1.0882	4.5350	4.0156	4.0333	2.0811	1.0653	4.4417	4.0157	2.1881	4.5320
Fe2+	2.0724	2.1029				1.9389	2.1907			1.8416	0.0189
Mn	0.1286	0.1732				0.0681	0.1222			0.0939	
Mg	3.5003	2.5890				3.6962	2.5191			3.6406	0.0222
Ca		1.8171	0.4979				1.9019	0.4287			0.5285
Na		0.6144	3.4042	0.4071	1.2235	0.0523	0.3955	3.5209	0.1213	0.0669	3.4050
K	1.9989	0.1824	0.0262	3.5651	2.6740	1.8959	0.2020	0.0228	3.7844	1.9376	0.0837
Cl		0.0150									
F	2.4498										
Sum	22.0000	15.7257	19.9555	19.9830	19.9314	15.8330	15.5814	19.9824	19.9332	15.8383	20.0342
Mg#	62.800	55.2				65.6	53.5			66.4	
An:Ab:Or			12.7:86.7:0.7	0:10.2:89.8	0:31.4:68.6			10.8:88.6:0.6	0:3.1:96.9		13.2:84.8:2.1

alkali feldspar are contained in a finer grained (0.5-1 mm) matrix of interlocking quartz, feldspar and mafic phases. Alkali feldspar (50%) in the matrix is microcline whilst the phenocrysts are coarsely perthitic with ribbon-like albite exsolution, show simple twins and contain frequent quartz and plagioclase inclusions. Reconstructed phenocrysts have anorthoclase-sanidine compositions ($Ab_{31}:Or_{69} - Ab_{50}:Or_{50}$). Rapakivi textures are formed in the phenocrysts by albite rims that are often optically contiguous with the plagioclase component of the perthite exsolution (Fig. 5.1e). In places these rims are formed by composites of plagioclase grains. Quartz (20%) forms anhedral grains with frequent mosaic textures and subgrain development. Plagioclase (20%) is largely restricted to the matrix where it occurs as variably sized (0.5-3 mm), subhedral, tabular prisms. These are moderately zoned to more calcic cores (Ab_{99-84}) and myrmekite is often developed as lobate protrusions where these grains are in contact with quartz. Biotite (4%) forms medium sized (1-2mm) subhedral, grains whilst hornblende is a rare (~2%) component. The biotites are moderately magnesian ($Mg/Mg+Fe$ 0.6 - 0.75) with almost no octahedral Al and up to 2.5% fluorine. In this they are typical of the biotites of I-type granites (Chappell and White, 1984). Mannum differs from most of the other late-Delamerian A-type granites (cf. Foden *et al*, 1990) in that much more Fe-rich biotite is normal ($Mg\#$ 0.55- 0.30). Accessory phases in the granite include apatite and zircon both of which occur as early formed, euhedral stumpy prisms which are often included in biotite and the quartz and alkali feldspar phenocrysts. Fluorine forms late interstitial grains.

The fine grained (0.5 mm), stoped blocks are compositionally like the coarse granite except that the texture is equigranular. In fact they are equivalent to the matrix of the host granite though sphene is less abundant and quite late-stage forming anhedral poikilitic patches.

The dioritic enclaves show a variety of textures and compositions however chilled margins are not observed. Texturally the enclaves are quite equigranular (Figs. 5.1f & g), grain sizes being restricted to 0.1-0.3 mm though plagioclase laths may reach 0.5 mm and some display a faint trachytic texture suggesting flow alignment. They are composed of subhedral to anhedral plagioclase (60%), biotite (10%), hornblende (10%), sphene (8%) and opaques (2%). Sphene and zircon are common accessory minerals along with fine acicular apatite which may indicate some initial chilling of the mafic magma (Fig. 5.1h). The enclaves differ from the granite in their mode and texture but less so in the composition of their constituent minerals. As in the granite plagioclase has normally zoned albite-oligoclase compositions and the biotite is similarly magnesian ($Mg\#$ 65). The cores of the darker, least hybridized enclaves show some slight trachytic texture defined by elongate hornblende and plagioclase and in these mafic phases constitute up to 35%. However, towards the margins elongate plagioclase and hornblende are gradually

replaced by equant grains with feldspar and quartz increasing in abundance. Even where the contacts with the granite are quite sharp there is a partly gradational transition from diorite, with an increasing number of larger felsic inclusions, to the granite.

Sphene is a major accessory mineral (1-3 modal %) and occurs in both the enclaves and the granite. In the enclaves, sphene is relatively fine grained texturally late formed and sometimes even poikilitic. In the granite and the outer margins of the enclaves, it is more commonly of larger grain size and euhedral. The sphenes in the granite are very REE enriched and have over 2 wt % total REE (Table 5.2). There is a systematic decrease in the REE content of sphenes from granite to enclave rim and then to enclave core (Fig. 5.2a & b).

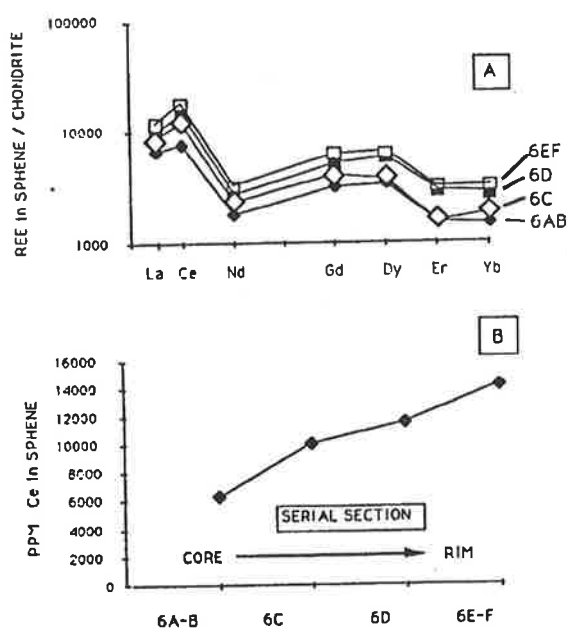


Figure 5.2a. Rare earth patterns of sphenes from the serially analysed xenolith (data from J. Foden).
5.2b. Cerium contents shown in Fig. 5.2a as a function of distance within the enclave.

Phenocrysts, reaching 15mm in diameter, of quartz and alkali feldspar are common inclusions in the enclaves and identical to the phenocrysts that must have been crystallizing early in the host granite. In the enclaves these phenocrysts show signs of corrosion consistent with initial disequilibrium in the presence of hotter mafic magma. The alkali feldspar cores are ubiquitously overgrown with broad (0.5-1 mm) rims of albite (Fig. 5.1f & g) which, along with overgrowths on the quartz phenocrysts, often contain abundant small inclusions of hornblende, plagioclase and sphene. These inclusions have the same composition and a similar or smaller grain size (0.1-0.2 mm) than those in the enclosing enclave (Fig. 5.1f) suggesting that they were nucleating against the phenocryst which subsequently overgrew them. Where the phenocrysts lie on

Table 5.2: Electron microprobe analyses of sphenes from the compositionally zoned enclave

	MG6A/B	MG6C	MG6D	MG6E/F
SiO₂	31.62	31.07	31.10	30.07
TiO₂	34.17	34.68	30.70	32.95
Al₂O₃	1.90	1.41	2.67	1.61
FeO	2.73	2.27	3.59	2.68
MnO	0.12	0.26	0.17	0.30
MgO	0.18	0.41	0.38	0.25
CaO	29.14	27.93	27.96	26.71
Na₂O	0.21	0.47	0.40	0.47
La₂O₃	0.255	0.344	0.349	0.442
Ce₂O₃	0.741	1.183	1.357	1.660
Nd₂O₃	0.128	0.131	0.175	0.231
Gd₂O₃	0.097	0.125	0.157	0.189
Dy₂O₃	0.146	0.132	0.238	0.226
Er₂O₃	0.038	0.038	0.072	0.080
Yb₂O₃	0.043	0.036	0.079	0.066
Nb₂O₅	0.290	0.530	0.890	0.770
Total	101.80	101.00	100.30	98.70

Note: each analysis is the average of between 3 and 7 spot analyses

the granite-enclave boundary the dioritic material is clearly moulded around them. Similar relationships have been described in detail by Vernon (1990) and are strong evidence that the phenocrysts were included into the enclaves under liquid state conditions. The pronounced development of rapakivi textures in the enclaves and the mesocratic hybrid zones is consistent with a magma mixing origin as suggested by Hibbard (1981) and Bussy (1990).

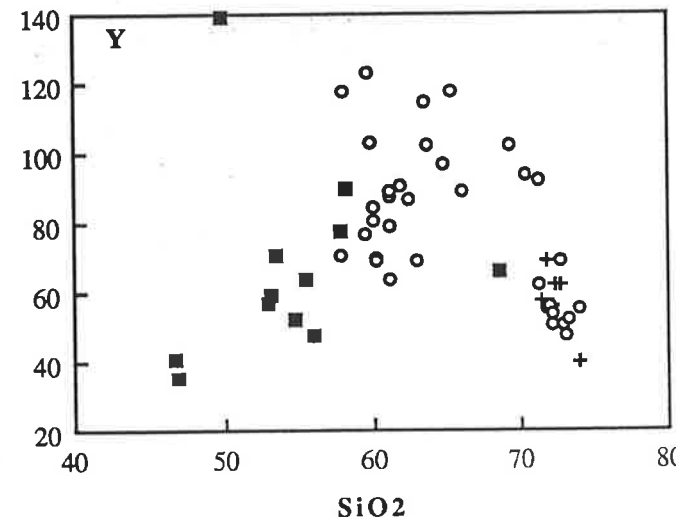
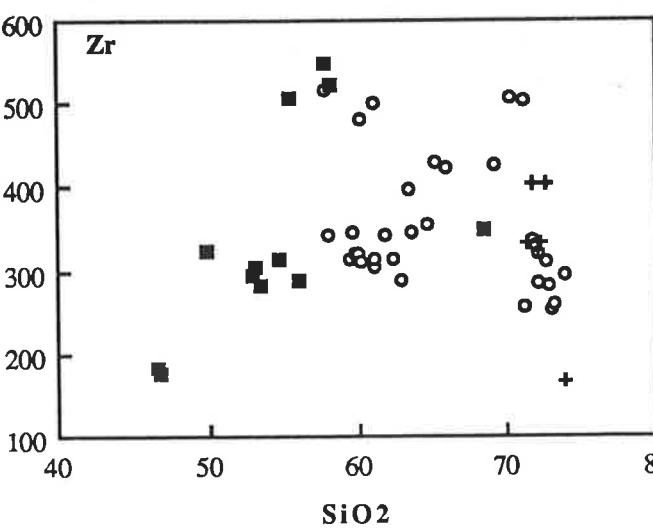
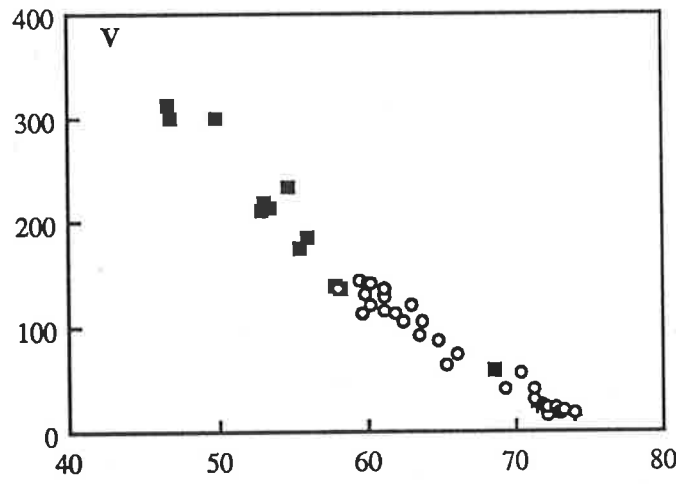
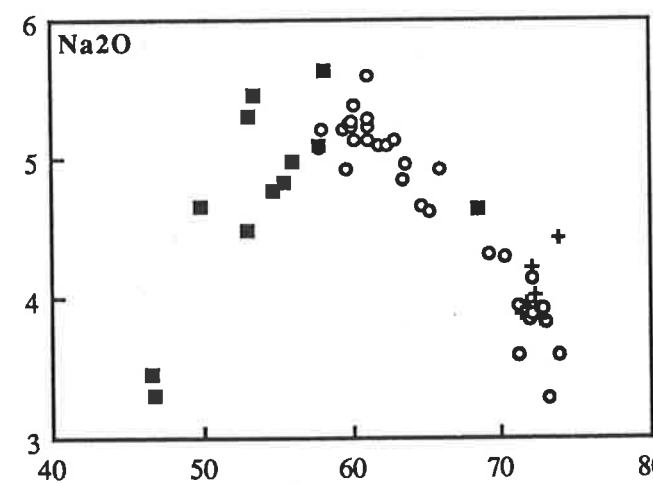
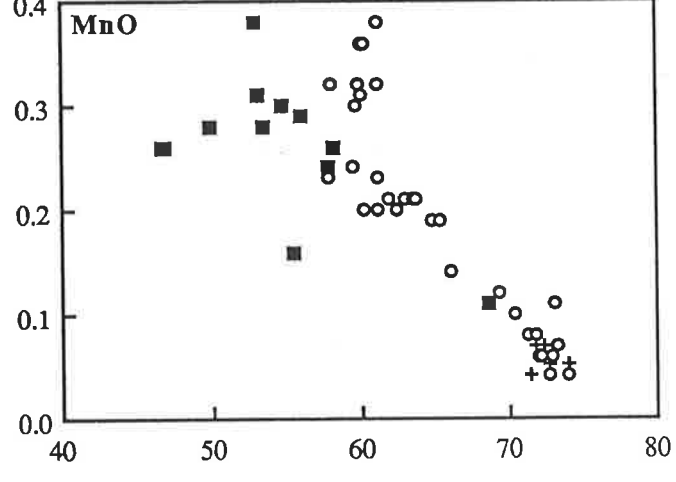
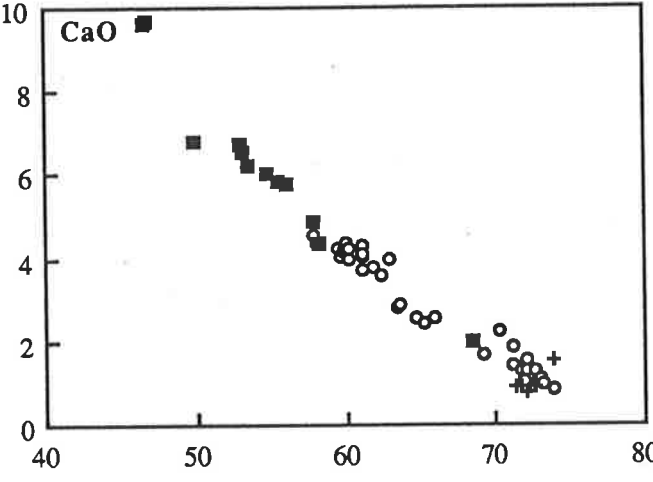
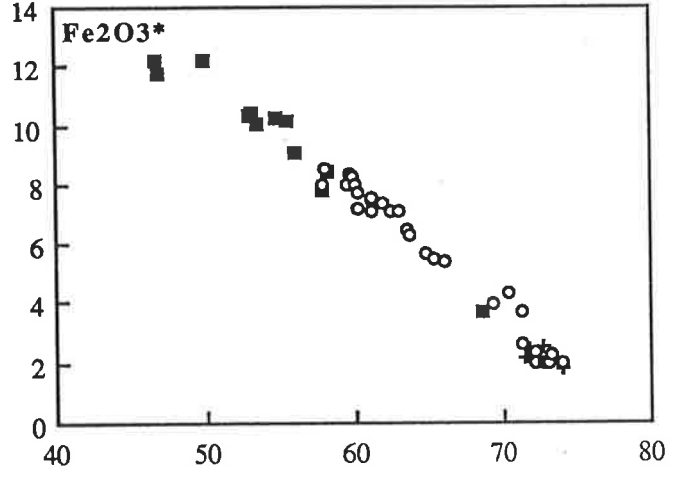
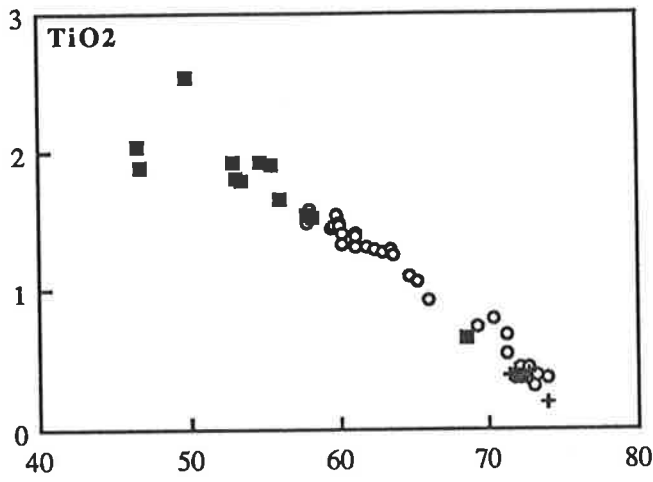
The dolerite dyke (hornblende 50%, plagioclase 46%) has a fine grained trachytic texture defined by the alignment of elongate (1 mm) plagioclase laths. These are set in a sub-ophitic groundmass comprised of more equant (0.2-0.3 mm diameter) plagioclase and hornblende. Glomeroporphyritic accumulations of hornblende are common whilst opaques (magnetite and pyrite) account for up to 4% of the rock. Sphene is unevenly distributed forming up to 0.5% in some sections whilst being absent in others. Compositionally this dyke is similar to the cores of the most mafic enclaves.

5.5. Geochemical and isotopic variation

The geochemical data in table 5.3 include representative analyses of the Mannum granite, a selection of enclaves including five serial sections and two analyses of the dyke. Table 5.4 contains rare earth element and isotopic analyses for the granite, enclaves, diorite dyke and two contemporaneous basaltic dykes from near Mannum at Black Hill and Reedy Creek (see Fig. 2.1).

Both the host granite and the fine grained marginal phase are diopside-normative with a silicic potassium-rich composition, relatively high Rb, Ba, LREE, Y, Zr and Nb contents and low CaO, Al₂O₃, V, Sc, Sr and Ni. In figure 5.4 the rare earth pattern for the granite has a large negative Eu-anomaly, which together with low Sr and very high Rb/Sr ratio, suggests protracted feldspar fractionation. Mg/Mg+Fe ratios are quite low (0.17) and Ga/Al ratios are high. Fluorine levels are quite high (300 ppm in the chilled blocks, 700 ppm in the coarse granite) and apatite, biotite and sphene all contain significant fluorine levels. All these are features attributed to A-type granites by Collins *et al* (1982) and Whalen *et al* (1987) and the Mannum pluton is one further example of an extensive S.E. South Australian province of Early Ordovician alkalic, late-orogenic magmatism (Foden *et al*, 1990). It is significant that these granitic rocks display a quite restricted compositional range. If these are highly fractionated granites then fractionation presumably took place in a magma chamber beneath the current exposure level. Isotopic

Overleaf Figure 5.3. SiO₂ variation diagrams for samples of the Granite (crosses), the dyke and enclaves (squares) and the analysed samples from the serially sectioned enclave (open circles). Note that the dispersion of the data in the plots corresponds closely to the interpretation in figure 5.10.



SiO₂

SiO₂

Table 5.3. Geochemistry of samples from Mannum

Sample	MG3 granite	SJF10 granite	M4 granite	861-93 granite	MG2 granite	861-95 chilled	779-63 enclave	779-60 enclave	1002 enclave	779-62 enclave	SJF8 enclave	MG9 enclave
SiO ₂	71.43	71.76	72.03	72.24	72.53	73.86	49.90	52.90	53.18	53.60	54.69	55.58
TiO ₂	0.38	0.43	0.36	0.38	0.41	0.19	2.54	1.93	1.81	1.79	1.92	1.91
Al ₂ O ₃	13.16	13.68	13.84	13.77	13.03	13.83	15.20	15.10	14.92	15.00	14.41	14.98
Fe ₂ O ₃ *	2.11	2.46	2.10	2.13	2.47	1.79	12.25	10.28	10.37	10.02	10.22	10.12
MnO	0.04	0.07	0.06	0.07	0.05	0.05	0.28	0.38	0.31	0.28	0.30	0.16
MgO	0.50	0.60	0.38	0.55	0.62	0.51	5.15	4.44	4.06	4.08	4.82	3.44
CaO	0.92	0.91	0.80	0.87	0.91	1.57	6.77	6.71	6.53	6.21	6.02	5.82
Na ₂ O	3.89	3.97	4.21	4.01	3.84	4.43	4.66	4.48	5.31	5.47	4.76	4.83
K ₂ O	5.12	5.44	5.43	5.66	4.95	3.56	1.85	1.41	2.02	1.98	2.39	1.60
P ₂ O ₅	0.06	0.10	0.07	0.08	0.08	0.05	0.68	0.52	0.45	0.45	0.49	0.79
LOI	0.47	0.29	0.21	0.36	0.52	0.72	1.70	1.80	0.44	1.10	1.11	0.38
Total	97.61	99.42	99.48	99.76	98.89	99.84	99.28	98.15	99.41	98.88	100.02	99.23
Cr	5	5	5	5	5	5	21	14	12	16	25	12
Ni	4	4	5	1	2	2	52	32	27	33	30	13
Sc	4.9	5.7	4.7	5.5	4.8	5	32	27	25	30	24.9	26
V	23	25	22	21	24	15	301	210	218	214	233	175
Pb	14	14	8	12	10	8	138	18	7	12	29	7
Rb	177	194	189	197	169	126	149	58	66	54	101	40
Sr	129	145	142	136	122	108	435	220	234	225	301	548
Ba	593	659	634	641	555	563	575	108	253	326	420	701
Ga	22	21		21	19	19	23	23		22	23	23
Nb	31	51	48	49	11.8	20.6	30	34	29	34	35	45
Zr	333	405	324	334	406	166	324	294	306	284	314	507
Y	58	69	56	62	62	40	139	57	59	71	52	64
Th	27	23	22	27	25	42	10	12	11	16	13	14
U	6.5	6.1	4	9.4	8.3	10	16	8.4	7	11	12	nd
La	74	85	63	91	71	79	180	67	62	61	71	94
Ce	145	150	138	152	143	106	565	108	111	114	116	183
Nd	58	61	45	57	59	34	177	43	42	44	44	83

Sample	MG8 enclave	779-64 enclave	779-61 enclave	MG1 enclave	MG7 dyke	MG10 dyke	MG6-A section	MG6-B section	MG6-C section	MG6-D section	MG6-E section	MG6-F section
SiO ₂	56.00	57.80	58.20	68.47	46.61	46.88	57.82	60.14	61.16	65.91	71.73	71.98
TiO ₂	1.65	1.53	1.52	0.66	2.03	1.88	1.48	1.33	1.30	0.93	0.37	0.38
Al ₂ O ₃	14.57	15.00	14.90	13.91	15.93	16.75	14.60	14.39	14.47	13.55	13.49	13.24
Fe ₂ O ₃ *	9.09	7.78	8.48	3.66	12.23	11.75	7.96	7.21	7.13	5.39	2.18	2.20
MnO	0.29	0.24	0.26	0.11	0.26	0.26	0.23	0.20	0.20	0.14	0.08	0.06
MgO	3.67	2.53	2.71	1.31	7.37	7.64	2.63	2.34	2.25	1.67	0.53	0.60
CaO	5.77	4.90	4.35	2.01	9.62	9.67	4.57	3.95	3.73	2.59	1.26	1.01
Na ₂ O	4.98	5.09	5.64	4.63	3.47	3.31	5.08	5.14	5.59	4.92	3.90	3.84
K ₂ O	2.40	3.55	1.78	3.86	0.75	0.93	3.17	2.93	2.18	2.90	5.03	5.08
P ₂ O ₅	0.39	0.69	0.73	0.16	0.37	0.35	0.67	0.60	0.58	0.38	0.07	0.07
LOI	0.37	1.10	1.50	0.42	0.69	0.37	0.93	0.62	0.60	0.62	0.73	0.44
Total	98.81	99.11	98.57	98.78	98.64	99.42	98.21	98.23	98.59	98.38	98.64	98.46
Cr	12	16	13	5	142	142	18	14	12	5	5	5
Ni	25	15	21	8	80	85	11	8	10	5	2	2
Sc	23	21	18	9.8	39	37	18	17.7	16.7	13.2	5.9	6.9
V	185	139	136	60	314	301	138	121	116	75	25	23
Pb	61	17	20	14	3	9	62	65	94	70	10	13
Rb	76	88	112	127	25	56	106	110	109	136	174	179
Sr	226	378	159	178	397	393	313	269	208	164	152	146
Ba	290	646	154	530	142	211	515	425	254	325	643	625
Ga	23	22	23	21	20	21	22	22	24	23	19	21
Nb	27	58	69	54	31	12.4	52	52	64	76	46	48
Zr	288	549	522	350	183	177	518	481	502	425	336	332
Y	48	78	90	66	41	35	71	70	89	89	55	56
Th	20	20	21	22	2.9	2.6	23	25	24	21	19	24
U	16	31	11	5	4.3	nd	31	48	99	29	4.1	3.8
La	54	112	142	77	21	29	101	103	121	109	52	64
Ce	81	198	259	149	42	70	176	179	211	205	121	139
Nd	26	81	88	53	30	30	66	69	84	80	49	44

Sample	861-96-1 section	861-96-2 section	861-96-3 section	861-96-4 section	861-96-5 section	861-96-6 section	90-300-1 section	90-300-2 section	90-300-3 section	90-300-4 section	90-300-5 section	90-300-6 section
SiO2	60.24	61.16	61.11	58.05	71.13	73.00	60.05	60.02	59.76	59.65	73.24	73.92
TiO2	1.40	1.39	1.40	1.57	0.53	0.30	1.47	1.48	1.53	1.47	0.39	0.36
Al2O3	14.63	14.26	14.36	15.03	13.46	13.24	14.49	14.54	14.58	14.52	12.90	13.02
Fe2O3*	7.68	7.55	7.51	8.57	2.64	1.93	7.95	8.01	8.26	8.31	2.27	2.01
MnO	0.36	0.38	0.32	0.32	0.08	0.11	0.36	0.31	0.32	0.30	0.07	0.04
MgO	3.10	3.00	2.90	3.13	0.92	0.53	3.07	3.14	3.21	3.01	0.70	0.43
CaO	4.22	4.11	4.07	4.38	1.43	1.07	4.35	4.15	4.18	4.04	0.98	0.83
Na2O	5.39	5.29	5.14	5.22	3.60	3.83	5.27	5.24	5.25	4.93	3.29	3.60
K2O	1.44	1.33	1.52	1.75	5.02	4.83	1.42	1.54	1.59	2.15	5.42	5.00
P2O5	0.34	0.33	0.33	0.38	0.12	0.09	0.35	0.35	0.37	0.35	0.08	0.07
LOI	0.67	0.69	0.68	0.90	0.51	0.52	0.45	0.47	0.51	0.68	0.30	0.20
Total	99.47	99.49	99.34	99.30	99.44	99.45	99.23	99.25	99.56	99.41	99.64	99.48
Cr	15	15	6	9	9	8	13	21	13	12	16	13
Ni	14	13	11	11	7	5	15	14	14	7	6.4	5.6
Sc	16	17	19	28	11	4	19	19	24	32	8	4
V	142	137	128	135	31	17	142	140	130	114	21	17
Pb	36	38	43	34	13	12	46	49	52	24	11	9.4
Rb	108	104	110	130	173	168	115	130	140	144	188	174
Sr	130	126	130	136	126	130	129	126	127	130	123	120
Ba	137	184	116	144	533	525	99	113	116	182	555	546
Ga	25	23	25	27	20	19	25	25	26	26	18	18
Nb	53	64	78	116	61	38	67	74	97	126	48	45
Zr	313	316	315	343	257	255	322	315	321	346	261	296
Y	69	79	88	118	62	48	81	85	103	123	52	55
Th	24	28	26	28	26	25	28	24	25	27	27	22
U	9.2	38	19	23	1.1	4.3	11.4	14	22	13.8	2.2	1.4
La	124	138	134	147	70	80	136	137	139	138	64	60
Ce	207	224	229	287	145	230	216	236	249	292	120	123
Nd	62	72	70	91	56	49	67	68	80	99	44	46

Sample	90-300-7 section	90-301-1 section	90-301-2 section	90-301-3 section	90-301-4 section	90-301-5 section	90-301-6 section	90-301-7 section	90-301-8 section	90-301-9 section	12163-1 section	12163-2 section
SiO2	72.00	71.10	70.34	61.78	62.88	61.03	59.43	62.26	72.12	72.54	63.55	64.70
TiO2	0.36	0.68	0.78	1.31	1.26	1.33	1.44	1.29	0.44	0.45	1.25	1.10
Al2O3	13.90	12.95	12.98	14.38	14.14	14.45	14.66	14.39	13.68	13.64	14.27	14.16
Fe2O3*	1.98	3.66	4.29	7.39	7.05	7.49	8.02	7.11	2.35	1.93	6.25	5.67
MnO	0.06	0.08	0.10	0.21	0.21	0.23	0.24	0.20	0.06	0.04	0.21	0.19
MgO	0.41	0.81	1.07	2.75	2.71	2.96	3.18	2.76	0.76	0.46	2.24	1.98
CaO	1.29	1.84	2.26	3.76	3.97	4.28	4.24	3.58	1.51	1.31	2.89	2.56
Na2O	3.88	3.95	4.28	5.10	5.14	5.23	5.21	5.10	4.13	3.92	4.96	4.65
K2O	5.22	3.81	2.85	1.95	1.34	1.49	1.84	1.82	4.19	4.64	2.74	3.24
P2O5	0.09	0.11	0.14	0.30	0.29	0.32	0.35	0.30	0.08	0.07	0.32	0.27
LOI	0.52	0.34	0.38	0.41	0.34	0.43	0.57	0.40	0.36	0.35	0.48	0.47
Total	99.71	99.33	99.47	99.34	99.33	99.24	99.18	99.21	99.68	99.35	99.16	98.99
Cr	5	11	15	14	15	16	23	12	9	13	18	10
Ni	1	10	13	8	10	11	11	4	7	7	6	5
Sc	5	7	10	18	16	16	16	18	3	1	16	16
V	16	41	57	114	120	132	144	105	23	22	106	88
Pb	10.3	10.1	10.2	21	18	19	22	17	13	11.3	43	34
Rb	181	137	105	126	103	104	130	134	146	155	154	160
Sr	141	146	142	155	156	160	160	158	165	165	125	131
Ba	571	483	333	173	105	129	151	153	520	620	16	329
Ga	19	20	21	26	24	25	25	26	20	20	25	23
Nb	43	80	90	103	73	66	78	101	48	51	99	93
Zr	287	503	508	342	288	306	314	314	320	313	347	357
Y	54	92	94	91	69	64	77	87	51	69	102	97
Th	23	24	23	26	23	24	23	21	16	28	26	20
U	2.1	5.4	6.4	12.3	6.6	5.6	7.3	10.8	2.8	1.6	49	42
La	86	75	83	119	107	106	119	111	56	63	119	110
Ce	136	160	182	231	189	186	215	214	104	125	236	221
Nd	50	62	71	73	54	50	62	70	37	55	81	74

Sample	12163-3 section	12163-4 section	12163-5 section	12163-6 section
SiO ₂	63.48	65.23	69.20	72.72
TiO ₂	1.28	1.06	0.73	0.35
Al ₂ O ₃	14.21	14.05	13.66	13.62
Fe ₂ O ₃ *	6.48	5.51	3.97	2.00
MnO	0.21	0.19	0.12	0.06
MgO	2.26	1.85	1.16	0.44
CaO	2.81	2.42	1.68	1.02
Na ₂ O	4.84	4.61	4.31	3.92
K ₂ O	3.08	3.32	3.78	4.80
P ₂ O ₅	0.32	0.27	0.15	0.07
LOI	0.44	0.47	0.33	0.33
Total	99.41	98.98	99.09	99.33
Cr	11	9	8	6
Ni	6	1	12	4
Sc	21	19	11	4
V	93	64	40	17
Pb	35	18	12.5	11.8
Rb	165	162	158	167
Sr	124	125	126	133
Ba	309	361	412	560
Ga	26	24	22	20
Nb	117	112	88	43
Zr	399	431	428	284
Y	115	118	102	51
Th	22	20	27	26
U	36	16	8.2	2.9
La	129	127	104	70
Ce	266	270	220	126
Nd	93	99	84	44

analyses of the host granite are quite primitive and variable with ϵNd -0.6 to -1.9 and initial $^{87}\text{Sr}/^{86}\text{Sr}$ 0.7048 to 0.7057 whilst a fine grained, quenched margin, granite block has ϵNd -7.7 and initial $^{87}\text{Sr}/^{86}\text{Sr}$ 0.7117 suggesting crustal contamination.

The enclaves are quartz-diorites and show a diverse range of compositions with a range of SiO_2 from 49.90 to 68.47% and MgO 5.15 to 1.31%. Their P_2O_5 , TiO_2 and REE contents are quite high and the most mafic and felsic end members approach the compositions of the dolerite dyke and host granite respectively. The serially sectioned enclaves show considerable chemical zonation resulting from chemical diffusion (see later discussion). A rare earth pattern from one of the more mafic enclaves is virtually indistinguishable from the host granite with the exception that it lacks a Eu anomaly (Fig. 5.4). This diagram also shows two of the contemporaneous basaltic dykes from outcrops nearby that are isotopically similar to the dolerite dyke at Mannum and have rare earth patterns of similar shape to the enclave. ϵNd (-0.4 to -3.1) and initial $^{87}\text{Sr}/^{86}\text{Sr}$ (0.7055 to 0.7060) values for the enclaves are similar to the host granite displaying a considerable isotopic range.

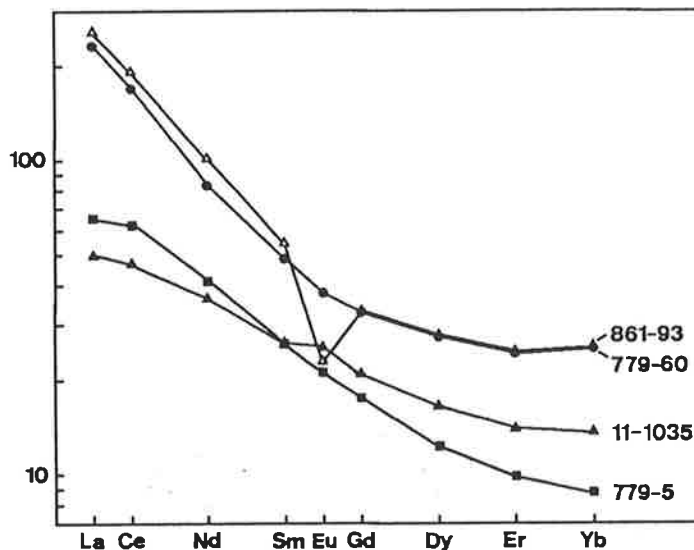


Figure 5.4. Chondrite normalized rare earth patterns for the Mannun Granite (861-93), an enclave (779-60), a basaltic dyke from Black Hill (11-1035) and a diorite dyke from Reedy Creek (779-5).

The dolerite dyke has a TiO_2 rich basaltic composition with high Fe_2O_3 , MgO , CaO , Cr , Ni , V , Sr and relatively low Ba , Zr , Nb , Y . K_2O , Na_2O and Rb are moderately enriched with the overall composition being similar to a moderately alkalic continental tholeiite. Isotopically it is clearly mantle derived with ϵNd +4 and initial $^{87}\text{Sr}/^{86}\text{Sr}$ 0.7041. These values are very like those inferred for the parental Black Hill magma in chapter 3 and the dyke is LREE enriched similar to this inferred composition and associated dykes nearby (Fig. 5.4).

Table 5.4.

Selected rare earth and isotopic analyses from Mannum

Sample	861-95	861-93	MG3	876-M4	779-60	MG9	MG6A	779-62
Locality	Mannum	Mannum	Mannum	Mannum	Mannum	Mannum	Mannum	Mannum
Lithology	chilled margin	granite	granite	granite	enclave	enclave	enclave	enclave
La		79.93			77.74			
Ce		155.36			138.37			
Nd	31.25	59.89	53.28	46.16	49.29	82.62	49.29	55.51
Sm	5.92	10.53	9.33	8.71	9.34	14.93	9.34	11.10
Eu		1.67			2.71			
Gd		8.60			8.60			
Dy		8.90			8.87			
Er		5.17			5.11			
Yb		5.29			5.27			
147Sm/144Nd	0.114546	0.106330	0.105926	0.114176	0.114616	0.109322	0.114623	0.121396
143Nd/144Nd	0.51199 +/-25	0.512295 +/-22	0.512325 +/-25	0.512287 +/-53	0.512361 +/-24	0.512249 +/-25	0.512223 +/-25	0.512373 +/-27
143Nd/144Nd (487Ma)	0.511625	0.511956	0.511987	0.511923	0.511995	0.511900	0.511857	0.512173
eps Nd	-7.67	-1.20	-0.59	-1.85	-0.43	-2.29	-3.13	-0.62
Tmod(dep)	1.30	1.08	1.04	1.17	1.07	1.17	1.23	0.84
Rb	126.0	189.8	178.9	181.7	61.2	39.6	108.0	55.7
Sr	108.0	133.3	131.1	139.0	213.1	559.1	321.6	221.5
87Rb/86Sr	3.379063	4.131658	3.954686	3.785607	0.830784	0.205317	0.973029	0.728905
87Sr/86Sr	0.735153	0.733774 +/-23	0.732300 +/-50	0.732017 +/-14	0.711337 +/-27	0.706897 +/-19	0.712320 +/-42	0.711093 +/-59
87Sr/86Sr (487Ma)	0.711704	0.705103	0.704857	0.705747	0.705572	0.705472	0.705568	0.706035

Sample	779-63	779-64	MG10	779-5	876-11-1035
Locality	Mannum	Mannum	Mannum	Reedy Creek	Black Hill
Lithology	enclave	enclave	diorite dyke	diorite dyke	basaltic dyke
La				20.40	15.63
Ce				50.63	38.75
Nd	209.53	96.93	26.37	24.51	21.94
Sm	40.47	15.92	4.56	4.93	4.97
Eu				1.53	1.83
Gd				4.56	5.44
Dy				3.99	5.32
Er				2.09	3.00
Yb				1.83	2.87
147Sm/144Nd	0.116837	0.099347	0.104602	0.126567	0.137145
143Nd/144Nd	0.512296 +/-47	0.512196 +/-34	0.512555 +/-23	0.512450 +/-27	0.512614 +/-20
143Nd/144Nd (487Ma)	0.511923	0.511879	0.512221	0.512045	0.512177
eps Nd	-1.84	-2.70	3.98	0.58	3.11
Tmod(dep)	1.19	1.14	0.73	1.06	0.90
Rb	154.9	98.7	25.9	43.0	38.7
Sr	432.9	373.0	406.2	882.0	368.8
87Rb/86Sr	1.036294	0.766672	0.184822	0.141025	0.303193
87Sr/86Sr	0.712315 +/-57	0.710922 +/-33	0.705390 +/-37	0.705610 +/-99	0.706257 +/-23
87Sr/86Sr (487Ma)	0.705124	0.705602	0.704107	0.704627	0.704153

5.6. Discussion of the origin of the enclaves

Various models have been proposed for the origin of mafic enclaves in granites including: they are country rock xenoliths; they represent restite; they formed by liquid immiscibility; they resulted from crystal accumulation; they were contemporaneous mafic magma which may or may not be genetically related to the host granite. Each of these will now be considered in turn.

The similar isotopic range for the granite and its enclaves argue for some genetic relationship between the two and the smooth, rounded shapes, textural homogeneity and coherent compositional array of the enclaves are inconsistent with them being accidental xenoliths of country rock. Likewise the regular compositional gradients within the enclaves (see later discussion) and the occurrence of phenocrysts from the granite within them argue against xenolithic origin.

I-type granites commonly carry populations of mafic to intermediate igneous or meta-igneous-textured xenoliths. These have been interpreted as solid inclusions either of restitic origin or as direct sampling of source rocks or modifications of source rocks (eg White and Chappell, 1977; Griffin *et al*, 1978; Chen *et al*, 1990). As angular, solid fragments it is probable that those enclaves differ significantly from the globular, plastic shaped, zoned inclusions described here. The same authors have suggested that zoned plagioclases with calcic cores represent restitic material. The plagioclases from Mannum however have only mildly calcic cores which are readily explicable by other processes (eg Wall *et al*, 1987). Linear unmixing arrays on variation diagrams are inherent in the restite model (eg Chappell *et al*, 1987), however as figure 5.3 shows, many elemental trends for the Mannum enclave-granite suite show curvilinear trends and some (Na_2O , Zr, Y) have clearly inflected trends. In summary the restite model is not applicable at Mannum.

Liquid immiscibility is also not a viable origin for the Mannum enclaves. Experimental studies in two liquid systems (eg Ryerson and Hess, 1978) indicate that the high field strength cations, transition metals and rare earth elements are partitioned into the mafic liquid and depleted in the silicic one. In terms of many of the bulk enclave compositions and the compositions of their cores, the opposite is true at Mannum (but see subsequent discussion of diffusion). Additionally immiscibility should produce enclaves in isotopic equilibrium with the granite yet both the granite and enclaves show a range of isotopic composition and isotopic equilibrium only occurs locally at the enclave margins.

An origin involving crystal accumulation would require an unknown mechanism for breaking up and redispersing a cumulate pile through the granite. The lack of cumulate textures in the enclaves and their finer grain size suggest they are unlikely to have resulted by crystal accumulation from the granite. The almost identical rare earth

patterns also argue against such a model and the enclave lacks a positive Eu anomaly to compliment the negative Eu anomaly in the granite.

None of the preceding models are applicable to the features seen at Mannum which we conclude are a consequence of co-mingling of contemporaneous magmas. It is suggested that the field and petrographic observations provide unequivocal evidence for their originally liquid state. Vernon (1984, 1990), Vernon *et al* (1988), Reid *et al* (1983) and Bender *et al* (1982) all describe globular inclusions like those at Mannum and conclude that they reflect a molten origin.

5.7. Enclave - granite interaction

This chapter is concerned with the interaction between the contemporaneous mafic and felsic magmas at Mannum. The evidence presented above suggests that the host coarse grained granite was an only partially crystalline magma and that the enclaves were at least very hot plastic solids and more probably magmas at the time of their interaction. Furthermore, the data suggest that complete mixing did not occur although the compositions of the enclaves became concentrically modified by diffusional exchange. In the experimental studies of Ryerson and Hess (1978) on two liquid systems the high field strength cations, transition metals and rare earth elements are partitioned into the mafic liquid and depleted in the silicic one. Although immiscibility is not a viable explanation for the Mannum enclaves, diffusion has occurred and it is certainly the case that some parts of the enclaves are enriched in Zr, Nb, REE, P_2O_5 , TiO_2 and transition metals by comparison with the granite (Fig. 5.5 and also compare MG6A - MG6D with MG3 in

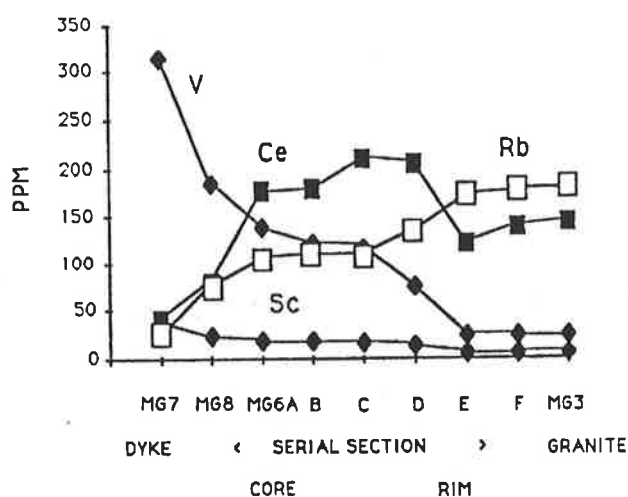


Figure 5.5. Trace element profiles from core to rim of the serially sectioned enclave (MG6A-F) with which are plotted the host granite (MG3), a very large xenolith (MG8) and the dolerite dyke that cuts the granite (MG7).

table 5.3). The physical and chemical diffusive aspects of this interaction will now be looked at in more detail.

5.7.1. Thermal and physical constraints on mixing

Recent studies on the thermal and fluid dynamic aspects of magmas have had important implications for our understanding of magmatic processes (e.g. McBirney, 1980, Huppert *et al*, 1984, 1986, Turner and Campbell, 1986). The plutonic complex of St. Kilda Scotland (Sparks and Marshall, 1986) for example shows very similar compositions and compositional ranges to the rocks at Mannum, the more mafic tholeiites being like the Mannum dyke and the granophyres equivalent to the Mannum Granite with a range of ferro-andesites and basalts similar to the Mannum enclaves. In the case of the St. Kilda rocks Sparks and Marshall (1986) show that only the magmas with less than 4% MgO were capable of mixing with silicic magma. Those which are more magnesian than this becoming too viscous to mix after thermal equilibration.

The process of mixing involves both physical shearing and reduction in the dispersed droplet or globule size, accompanied and followed by diffusional thermal and material exchange. The efficiency of the first phase depends on the vigor and turbulence of flow and on the viscosity contrast between the two phases. Sparks and Marshall (1986) note that thermal diffusion between mingled magmas is orders of magnitude quicker than chemical diffusion so that the tendency for complete mixing is dependant on the physical properties of the two after thermal equilibration. If there are very big differences in viscosity after thermal equilibration, then mixing will not become complete. In the situation where the equilibrated temperature of the mixture is low, a mafic magma may simply freeze to form xenoliths, while at the same temperature droplets of an intermediate magma may be well above their solidus and be fluid-enough to mix with the host granite. For this reason mixing between very mafic and very silicic magmas is not favoured.

The viscosity of a magma depends on a number of factors including temperature, crystallinity and composition. The inter-relationship of these factors has been modelled by McBirney and Murase (1984) and Shaw (1972). In a manner somewhat like that adopted by Sparks and Marshall (1986) and using the the relationships described by Frost and Lindsay (1988) a viscosity - temperature diagram has been constructed (Fig. 5.6) for the range of granite and enclave compositions at Mannum. This illustrates that only when temperatures were in excess of about 1000 °C would the core composition of the enclaves have a similar or lower viscosity to that of the host granite, allowing the two to freely mix. Due to its higher solidus temperature however, at lower temperatures, the viscosity of the mafic melt rapidly increases to greatly exceed that of the granite magma. When the temperature of the system is between about 850 and 930 °C the mafic magma is

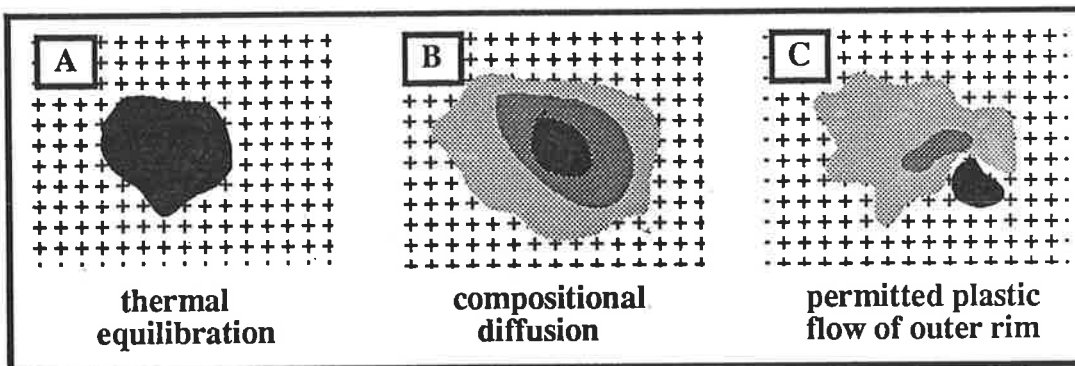
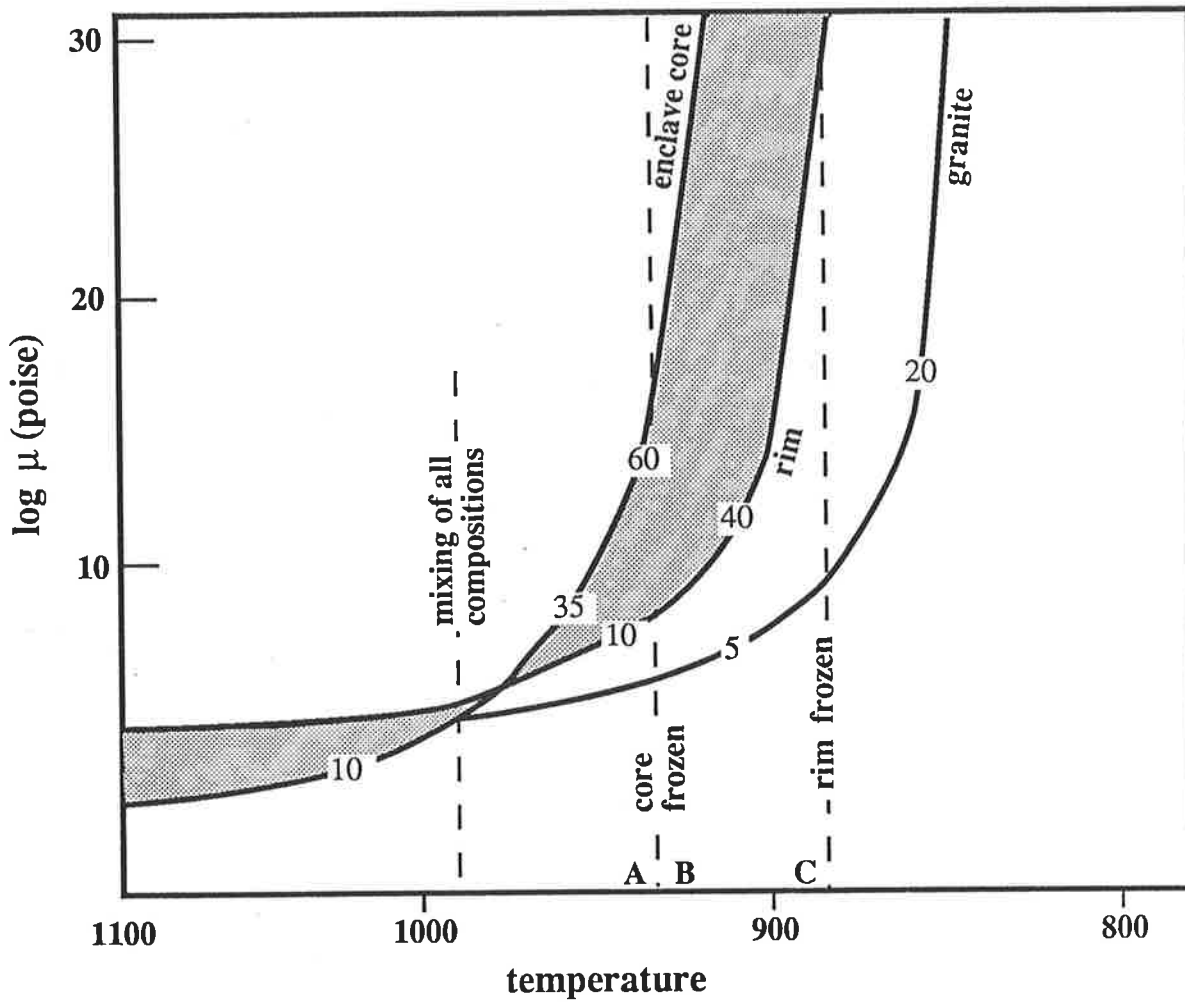


Figure 5.6. Calculated temperature - viscosity variation for compositions from Mannum (based on Frost and Lindsay, 1988; McBirney and Murase, 1984; and Shaw, 1972). The temperature at which the enclave core and marginal compositions become effectively solid are indicated (solid status is achieved at about $\log \mu = 15$) and the shaded region encompasses the range of viscosities shown by the enclave. Numbering on each curve indicates the % crystallization. Note that free mixing between the mafic and felsic compositions only occurs at temperatures above 980 degrees. The lower cartoon relates the observed variation of rheological behaviour of the enclaves during entrained flow in the granite magma with the temperature - viscosity relations from the diagram above.

effectively solid ($\mu > 15 - 20$ poise) whereas under these conditions the granite is still a viscous fluid and the two will be incapable of mixing. The composition of the enclave

will be progressively modified by diffusion and towards its rim will progressively tend towards the composition of the granite. Thus at temperatures less than about 980 °C, this change will progressively decrease the viscosity of the enclave outer margins.

Because the actual viscosity-temperature relationships calculated using Frost and Lindsay's (1988) model are quite dependent on the uncertain OH⁻ and F⁻ content of the magma the temperatures indicated in figure 5.6 are only approximate, although the general geometry of the illustrated relationships are true. This diagram was constructed for H₂O = 2%, consistent with the estimates in chapter 4 and with experimental work by Clemens *et al.* (1986), however, the effect of fluorine, which is likely to lower viscosities (eg Dingwell *et al.*, 1985) is not accounted for. Further, as the granite is by the far the majority phase at this intrusive site, the equilibration temperature of the mafic-felsic mixture will be that of the granite. The variable flow-induced deformation of some compositionally zoned enclaves (Fig. 5.6) appears to well illustrate the implications of the modelled composition-temperature-viscosity relationship (Fig. 5.6). The more hybridized parts of the enclaves certainly show plastic deformation implying $\mu < 20$ poise and thus temperatures > 890 °C (Fig. 5.6). Thermal diffusion is much faster than compositional diffusion and taken at face value this temperature must also represent the minimum equilibration temperature with the granite. This indication that the Mannum granite crystallized from a moderately dry, high temperature magma is supported by experimental data on A-type granites (Clemens *et al.*, 1986) and high temperature pyroxene assemblages from related A-type rocks from the Padthaway region to the southeast of Mannum (chapter 4).

Field observations indicate some of the enclave mafic cores behave as strong solids requiring that the physical separation illustrated in the lower cartoon of figure 5.6 took place at $T < 930$ °C. And yet it does appear that the dispersed drop-like form of the mafic enclaves requires that these were initially hot enough to exhibit fluid behaviour implying that this component was initially above 980 °C.

5.7.2. Post-mingling diffusion

As illustrated by the TiO₂ - SiO₂ variation in figure 5.3, the bulk composition of the granite appears unaffected by contamination by the dioritic enclaves possibly reflecting both the volumetric minority of the enclaves and the sluggishness of physical mixing. This would imply that viscosity contrasts between the enclave and granite were large enough to inhibit completely free mixing, though field observations indicate that the outer zones of many enclaves have achieved an extremely advanced state of hybridism, yielding pale-grey hybrid granite composition (see MG6E and MG6F, table 5.3). These are also the sites of the most advanced rapakivi texture. This evidence indicates that even though physical mixing was inhibited, diffusional exchange rates were fast.

In order to investigate the possible role of diffusion in the granite - enclave interaction, core to rim variation of several typical 20 cm diameter enclaves were investigated by means of approximately 1.5 cm thick serial sections. This data has also been presented together with the composition of the cross-cutting Mannum Quarry mafic dyke and an analysis of a very large 2-3 meter enclave included in the Mannum granite. It is apparent that in general compatible elements likely to be in high concentrations in a mafic magma show a trend of depletion from the dyke and enclave core to its rim. These elements include Ni, V, Sc, Mg, Cr and Sr. Conversely incompatible elements such as Rb and K₂O show reverse behaviour. These variations show the form and extent of variation consistent with diffusional control (eg. Hofmann, 1980).

Diffusion in one dimension is described by Fick's first law

$$J = - D \frac{\partial c}{\partial x}$$

where J is the flux of tracer, D is the distribution coefficient, c is the tracer concentration and x is the distance in the direction of diffusion. For a volume element of material with conservation of mass, Fick's second law states

$$\frac{\partial c}{\partial t} = D \frac{\partial^2 c}{\partial x^2}$$

The simplest solution of this is given by the following expression (Maaloe, 1985; Hofmann, 1980):

$$c(x,t) = \frac{c_1 - c_0}{2} \left(1 - \operatorname{erf} \left(\frac{x}{2\sqrt{Dt}} \right) \right) \dots\dots(1)$$

Where D is the diffusion constant (cm²/s), erf is error function, t is time and x distance, c(x,t) and (c₁-c₀)/2 expresses the average of the compositional difference between the starting concentrations of the same element in the two initial reservoirs. This is a simplified diffusional description of the probable situation at Mannum, however in principle it does illustrate the dependency of the process on the diffusion coefficient (D) and time.

Diffusion will take place down a concentration gradient (activity gradient?) and would not predict reversals in the sense of direction of the profile. For this reason, the variation of many elements in the enclave serial sections are not explicable by pure diffusional control. The REE, Y, Zr, Nb, U and P₂O₅ for instance, each have higher concentrations in the granite than in the mafic magma, yet they show real increases and concentration maxima within the enclave (Fig. 5.5). In figure 5.7 the result of a calculation for a diffusion coefficient of 10 cm² a⁻¹ and a time interval of 0.5 - 10⁶ years is shown. This profile is not unlike that illustrated for Rb (for instance) in figure 5.5. By

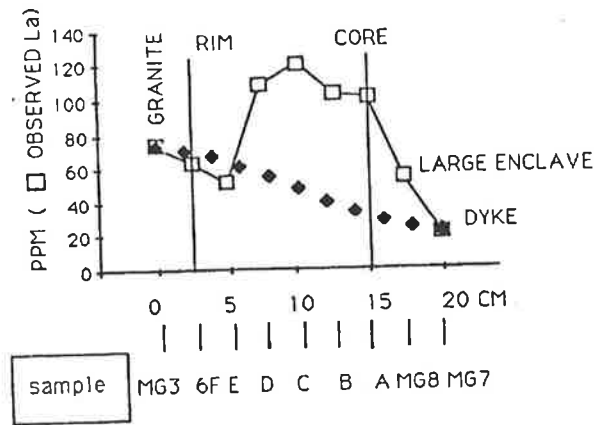


Figure 5.7. The curve composed of closed symbols represents the calculated diffusion profile using equation 1 which describes linear volumetric diffusion. At initial conditions the two magmas had 80 and 20 ppm of the element (see text for details). Superimposed on this profile is the analysed profile for La.

contrast, the concentration variation of La for the dyke-enclave-granite series has also been plotted on figure 5.7 and is representative of the situation for Y and the REE in general. This shows a very distinct concentration hump in the enclave and though the extremities of the profile seem to be in keeping with the diffusional model, some additional factor is clearly operating. It has already been mentioned that sphene is an abundant phase in the Delamerian granite province in general and that the Mannum enclaves are particularly sphene-rich. Accordingly it seems possible that the deviations of element concentration profiles away from the ideal diffusion-controlled model is due to reaction, mineral growth and the establishment of mineral sites to which trace and minor elements are partitioned.

The continuous increase in zirconium concentration towards the more mafic core of the serially sectioned xenolith (Fig. 5.8a) is intriguing as Zr is an essentially incompatible element in most magmatic systems until zircon saturation is achieved. The Zr concentrations in the xenolith core are more than twice those of the mafic dyke rocks, or of the large enclave (MG8, Table 5.3) and are also higher than those of the granite. The compositional and temperature dependency of zircon saturation have been calibrated in some detail (Harrison and Watson, 1983; Watson and Harrison, 1983, 1984). Figure 5.8b illustrates the isothermal (825 °C) Zr concentration at which zircon saturation occurs for each of the compositions from granite to enclave core calculated from the expression for zircon solubility generated by Watson and Harrison (1983):

$$\ln D_{Zr} \text{ zircon/melt} = \{-3.8 - [0.85 (M-1)]\} + 12900 / T \dots\dots(2)$$

Where D is the concentration ratio of Zr in the stoichiometric zircon and M is the cation ratio $(Na + K + 2Ca) / (Al + Si)$ the sum of these cations being 1. For the enclave, the calculated Zr concentration profile (Fig. 5.8b) coincides remarkably with both the form and the actual values of the measured profile.

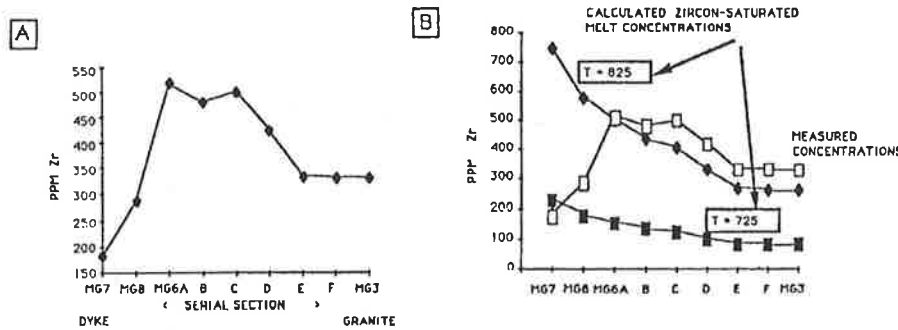


Figure 5.8a. Analysed concentration variation of Zr across the dyke-enclave granite profile.

5.8b. Zirconium concentrations required for zircon saturation of the bulk compositions in Fig. 5.8a (shown as open symbols) at 825 and 725 °C calculated using equation 2. The diagram suggests that in the smaller enclaves (10's cms in diameter) Zr concentrations are a function of the achievement of zircon saturation at temperatures in excess of 825 °C.

The enclave must have had a homogeneous Zr composition when it was first included and therefore the observed concentration gradient must have been established in its present site. U-Pb isotopic analysis of zircon separates from other granites of this late-Delamerian series by Foden *et al* (in prep) reveal that by contrast with the syn-tectonic Delamerian granites, zircons from this group are almost perfectly concordant. Given that the Zr concentration profile within the xenolith is exactly appropriate to that buffered by the zircon-saturated Zr concentration in the granite at 825 °C this indicates that granite melt evolution took place at or above temperatures required for zircon saturation (825 °C). In addition diffusion of Zr continued into the enclave at this temperature as long as a zirconium activity gradient existed, ceasing as soon as Zr concentrations sufficient for zircon saturation were achieved. If the enclaves were included as solids no Zr concentration profile is expected due to Zr-immobility in zircon-saturated rock

The contrasting behaviour of the high field strength trace elements Zr and Nb in the mafic-felsic magmatic interaction is interesting and may be a significant factor in the generation of the Nb-depleted lithophile element patterns that are a continental hallmark (eg Pearce, 1983). In the Mannum rocks sphenes are the major Nb and REE sites and those in the outer margins of the enclaves contain between 0.8 and 1.2 wt.% Nb₂O₅. The stability of sphene may be partly a function of development of a reaction front between the mafic and felsic magmas, its stability being enhanced by the diffusion of Ti and Ca from the enclave towards the granite and diffusion in the opposite sense of the REE, Nb, SiO₂ and F. This has resulted in a localised maximum in the amount of sphene, its grain-

size and its REE content (Figs. 5.2a & b), towards the outer margin of the enclave. The Zr profile is dictated by the greater isothermal solubility of zircon in more mafic compositions (Watson and Harrison, 1983; Harrison and Watson, 1984) and therefore must be imposed late in the mingled cooling history after a compositional profile in major elements had been established. The result is that the Zr/Nb ratios decrease from enclave core towards the granite (Fig. 5.9).

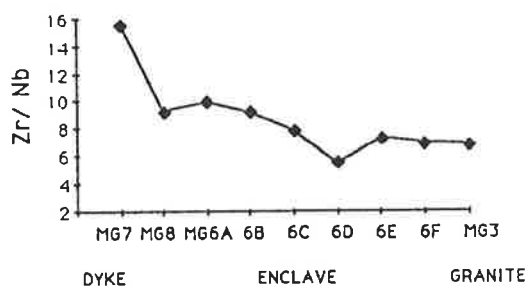


Figure 5.9. The variation in Zr/Nb ratios across the dyke-enclave-granite profile.

The more general implication of this may be that in many crustal situations where granitic liquids are evolving in contact with mafic wall rocks or cooling in layered magma chambers with mafic-felsic boundary layers, sphene growth by reaction may provide an important Nb site and hence relative depletion in the granitic liquid.

5.8. Compositional relationships between the enclaves and granite

An important question concerns the genetic relationship between the contemporaneous acid and mafic magmas at Mannum. Mafic enclaves have been used as evidence for a fundamental role for mantle magmas in granite genesis (eg Holden *et al.*, 1987). This role may often be primarily a thermal one in which mantle magmas promote fusion of crustal rocks to produce granitic melts (eg Huppert and Sparks 1988) and the systematic displacement of the mantle derived enclaves to higher ϵ_{Nd} values in some studies supports this scenario of largely separate source rocks for the granites and their enclaves (eg Holden *et al.*, 1987; Eberz *et al.*, 1990). However, in the case of Mannum where the isotopic values of the enclaves and the granite are similar, a possible interpretation is that the felsic magmas are compositionally related via fractionation to the mafic ones as indicated in chapters 3 and 4.

The data in Table 5.3 shows that the enclaves are compositionally variable. If simple two end member mixing (ie dilution by the granite) was responsible for all of this variation, linear element-element variation diagrams would be expected to result

(Langmuir *et al.*, 1978). This is certainly not the case when the relationships between TiO_2 , Na_2O , MnO , P_2O_5 , Zr or Y and SiO_2 are considered (Fig. 5.3) and the compositional variation must have existed prior to magma mingling. When the entire spectrum of compositions on the variation diagrams is considered, a surprisingly coherent tholeiitic-style of geochemical evolution is observed in which mafic magmas first fractionate pyroxenes and plagioclase to produce early TiO_2 -, MnO -, Na_2O - and P_2O_5 -enrichment, with ongoing large ion lithophile element (eg Zr, Y) and SiO_2 enrichment. This is followed by TiO_2 , MnO , Na_2O , P_2O_5 , Zr and Y depletion as sodic plagioclase, magnetite, ilmenite, apatite and zircon begin to precipitate. Throughout this fractionation, MgO and compatible trace elements such as Ni, Cr and Sc show continuous depletion.

The Mannum granite-enclave-mafic dyke data is remarkably like that from a number of strongly differentiated tholeiitic or sub alkaline basalt provinces worldwide (eg Iceland, McGarvie *et al.*, 1989). Amongst the best described of these is the Scottish Hebridean province, where ring-dyke and net-vein complexes appear to represent late-stage mingling of a range of the liquids from the tholeiite-granophyre fractionation series. These separate liquids formed initially in layered magma chambers (Bell, 1983; Marshall

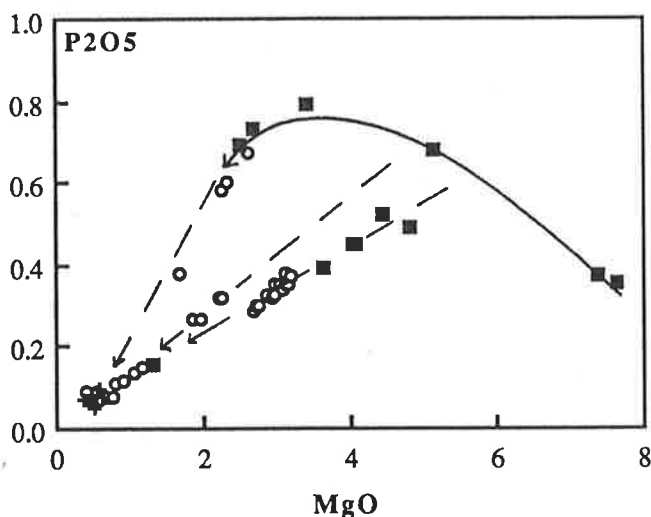


Figure 5.10. Plot of MgO vs P_2O_5 for the Mannum Quarry samples showing the tholeiitic style evolution (solid line) of the mafic rocks heading towards the granite composition and how diffusion (dashed lines) at various stages in this evolution also causes dispersion towards the granite composition.

and Sparks, 1984) and mixing took place when they were tapped to move to volcanic centres or dykes. Similarly it could be inferred that all the Mannum rocks are derived from a magma chamber that was compositionally zoned from basaltic at the base through intermediate compositions to rhyolitic at the top. Superimposed upon this variation is that resulting from diffusion and incorporation of granite phenocrysts causing linear dispersion of the enclaves towards the granite. This is well illustrated on a plot of MgO vs

P_2O_5 in figure 5.10 where the enclaves and enclave serial sections show linear dispersion towards the granite from a tholeiitic fractionation path. The same sort of behaviour is shown by Zr and Y in figure 5.3 where many of the outer zones of the sectioned enclaves are dispersed towards the granite from a curvilinear fractionation trend. Similar to the findings of Sparks and Marshall (1986), this dispersion does not occur with mafic magma that has $MgO > 5\%$.

On a ϵNd vs initial $^{87}Sr/^{86}Sr$ diagram (Fig 5.11) the enclaves do not show any systematic hyperbolic array with the granite that could be interpreted as a mixing curve. The enclaves show a range of isotopic values and, relative to the granite, some have higher ϵNd and some lower whilst the $^{87}Sr/^{86}Sr$ range is similar. This may partly reflect the greater diffusivity of Sr relative to the REE in a silicate melt (Hofmann, 1980) and as isotopic equilibration only occurred at the local scale of the enclave margins, the overall isotopic variation must reflect a primary variation in both the mafic and felsic magmas.

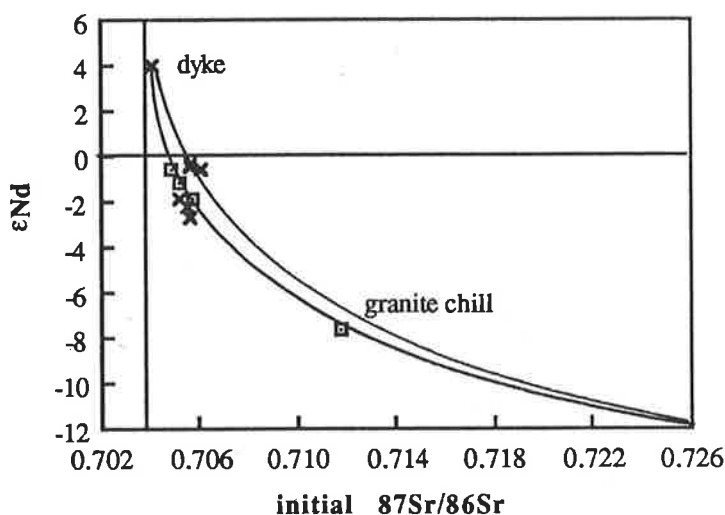


Figure 5.11. ϵNd vs initial $^{87}Sr/^{86}Sr$ for samples from Mannum Quarry with possible contamination hyperbolae between a mafic end member, taken to be the dyke, and the Kanmantoo metasediment from chapter 3.

The implication is that both the granite and the enclave magma were isotopically as well as compositionally heterogeneous which is best explained by varying degrees of crustal contamination of these magmas prior to mingling. In figure 5.11 analyses of the host granite and two groups of enclaves lie on separate but similar contamination hyperbolae between a mantle derived mafic end member, which could be the dolerite dyke or the Black Hill parental magma, and a crustal end member which is represented by an analysis of the local Kanmantoo Group country rock metasediments (from chapter 3). The group of enclaves with higher ϵNd are more magnesian whilst the lower MgO group also have lower ϵNd corresponding to greater contamination. The fine grained granite block interpreted to be a chilled margin lies much nearer the metasediment point consistent with the greatest degree of contamination at the margins of the magma body.

5.9. Conclusions and a model for the Mannum Granite

There have been numerous recent contributions to the literature in which dioritic enclaves are considered to represent contemporaneous globules of mafic magma (see Vernon, 1984 for a recent review) and the situation described in this paper from Mannum, South Australia appears similar. Mannum Quarry provides an excellent example of diffusion and mixing processes that occur when magmas mingle. It is clear that in fact the complete and efficient mixing of thermally and compositionally dissimilar magmas is surprisingly difficult and that under these circumstances diffusion is the main process by which compositional homogenization is approached. In the situation observed at Mannum large volumes of the granite are unaffected by the mafic contaminant while the mafic magma itself is being homogenised by diffusion and is producing hybrid patches whose size is of the order of twice the diameter of the original mafic droplets (~ 20-40 cm).

An interesting and important outcome of the observations made at Mannum Granite concerns the confirming evidence for the contemporary presence of both mafic and felsic magmas together at high crustal levels in the late-Delamerian period. This solves the problem of the source of heat required to generate the late-orogenic felsic magmas, at least in this terrane. The implication is that mantle derived magmas play a fundamental role in the genesis of A-type magmas to the extent that the two mingle at the site of intrusion. The preferred interpretation of the chemical and isotopic data is one of direct fractionation of the felsic (granitic) liquid from mafic parental magmas which also explains the high temperature nature of the granite (cf chapter 4).

Figure 5.12 illustrates a model suggested for the origin of the Mannum outcrop involving a magma chamber containing mantle derived mafic magma that was undergoing combined fractionation and assimilation such that it was both compositionally and isotopically layered. It is interesting that on the basis of the isotope data the degree of contamination of the host granite would appear to be no greater than that of the enclaves. This is similar to the data on the compositionally indistinguishable granophyres at Black Hill just north of the Mannum quarry (chapter 3) and the Padthaway Suite (chapter 4). One interpretation is that the magma chamber became insulated from further contamination by the solidification of a chilled margin. The upper zone of the magma chamber contained fractionated felsic magma that was also undergoing crystallization and already had a frozen cap of the most contaminated roof zone magma (the fine grained granite phase). Recent models for the development of compositionally layered magmachambers (McBirney, 1980; Turner and Campbell, 1986; Huppert and Sparks, 1988) are quite appropriate to this model. Subsequent remobilization of all or parts of this magma body, possibly triggered by the injection of a fresh pulse of mafic magma (eg

Sparks *et al.*, 1977), broke through and entrained parts of the frozen cap moving them to the site of the present outcrop. Density controlled draw-up (eg Blake and Ivey, 1986), entrained part of the lower, mafic layers from the magma chamber producing the screen of enclaves. Thermal and subsequent compositional diffusion controlled the final modification of these enclaves. This model is consistent with the presence of nearby large, contemporary, mafic plutons such as those at Black Hill which are compositionally and isotopically zoned (chapter 3). Drilling and geophysical evidence in the region in fact indicates that all of the A-type rocks of the late-orogenic suite are underlain by mafic magma (chapter 4).

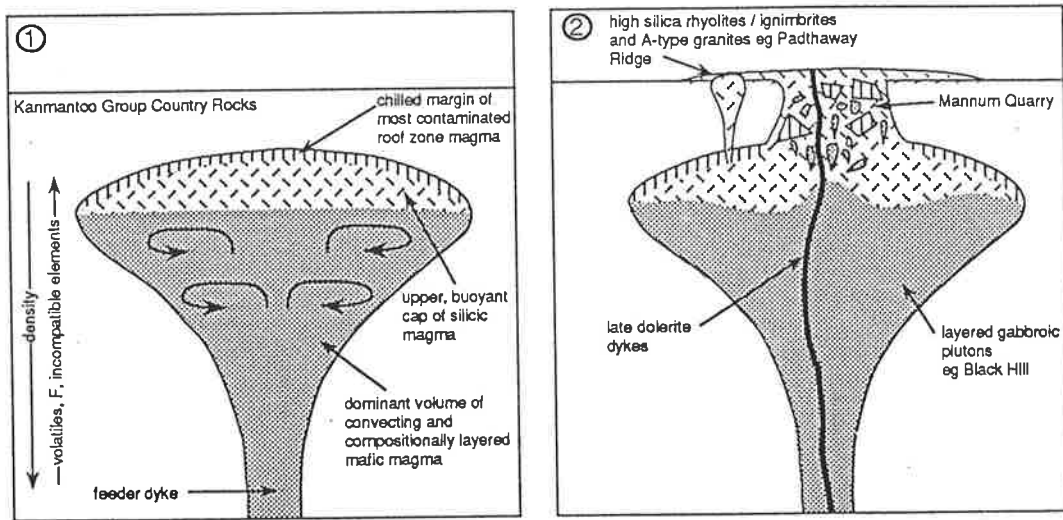


Figure 5.12. Cartoon illustrating a model for the features at Mannum and the interpreted relationships between the various elements of the late-orogenic, Delamerian magmatic suite.

As noted in chapter 1, at the beginning of this thesis, it is intriguing that the highest temperature magmas in the foldbelt appeared after the waning of deformation and metamorphism (at the observed levels of emplacement). Do pre-existing compressive orogenic forces and the presence of light, silicic, syn-orogenic magmas restrict these mafic magmas from rising through the lithosphere or is increased asthenospheric flux and mantle lithospheric thinning a natural successor to lithospheric thickening during orogenesis? These questions will now be considered in chapter 6.

Chapter 6. Some thermal and isostatic constraints on late-orogenic magmatism

6.1. Introduction

Many orogenic belts contain bimodal magmatic suites emplaced immediately following the cessation of convergent deformation (Table 4.5). Examples include the post-orogenic granites of Brown *et al.* (1981) from the Caledonides; the post-closure uplift granite-gabbro associations of Pitcher (1982); post-Acadian granite-gabbro associations from the Appalachians (Pitcher, 1982 and references therein); the A-type granite and gabbro associations from the Lachlan Fold Belt (Collins *et al.*, 1982); Tertiary bimodal volcanics from Queensland (Ewart, 1981); undeformed alkaline granites and mafic rocks from the Hercynian Pyrenees (Fourcade and Allegre, 1981); undeformed A-type granites and gabbros from southern Adelaide Foldbelt (this study).

A compositionally similar bimodal magmatic association occurs in areas undergoing crustal extension where lithospheric thinning is related to magma genesis and composition (McKenzie and Bickle, 1988). These include suites such as those at Loch Ba (Sparks, 1988) and St. Kilda (Marshall and Sparks, 1984) in the British Tertiary Province; the alkaline-ring complexes of the Nigerian and Kenyan rift valleys (Bonin and Giret, 1985; Bowden, 1985; Macdonald, 1987; Macdonald *et al.*, 1987); basalts and A-type granites from the Yeman Plateau (Capaldi *et al.*, 1987).

A common feature of all of the above magmatic suites is their bimodality and very frequently mingling is observed between the mafic and felsic magmas. The mafic magmas vary from alkalic to tholeiitic, often showing evidence of crustal assimilation, and may form dykes, layered gabbroic plutons or volcanics. Accompanying these are silicic plutons and volcanics which tend towards high temperature, high silica magmas with alkali, incompatible element- and LREE- enrichment that are characteristics of A-types (Collins *et al.*, 1982; Whalen *et al.*, 1987). Tectonically there is often a gradation between the late-orogenic and extensional suites with late-orogenic crustal relaxation leading into extension as in the Basin and Range province (Gans *et al.*, 1989).

Whilst there are various models for the distinctive chemistry of these late-orogenic magmatic suites, the critical geodynamic problems related to their genesis remain unanswered. The occurrence of these suites requires a significant perturbation in the thermal regime of the orogen and the coincident appearance of magmas with the cessation of deformation suggests that this is most likely linked to changes in the potential energy stored in the orogen. Changing or stopping the external tectonic driving forces is one way

of terminating deformation however this does not explain the thermal pulse. Another way of stopping convergent deformation is by producing major uplift, one result of which is to produce externally directed buoyancy forces which oppose those driving convergence (eg Turcotte, 1983; see discussion in section 6.2). Many of the late-orogenic suites do in fact seem to be associated with uplift (Pitcher, 1982; Bonnin, 1990; and discussion below on the southern Adelaide Foldbelt). This could result from increased topography built up by compressional deformation however this again provides no explanation for the thermal pulse. Thickening the lithosphere by injection of basalt from the asthenosphere would explain the thermal pulse and, given the correct density, could produce isostatic uplift eg 2.7 km uplift for an addition of 15 km of basalt into the lower crust (McKenzie, 1984) resulting in buoyancy forces that oppose and terminate compression. However it is not clear why large volume intrusions of basalt would be common to so many orogens nor why such intrusion would characteristically intrude after some finite amount of convergent strain.

An alternative is thinning of the lithospheric mantle (eg Houseman *et al.*, 1981). Such a scenario has been proposed for the Himalayan collision of India into Asia at about 40-50 Ma (England and Houseman, 1988, 1989). During the late Tertiary the Tibetan Plateau underwent a rapid increase in elevation and changed from a zone of compressive deformation to one of marked extensional deformation, despite the continuing convergence of India and Asia (England and Houseman, 1988). Geophysical data and numerical modelling suggests these events resulted from convective instability and removal of the lower lithospheric mantle (England and Houseman, 1989). Late-orogenic magmatism in the Tibetan Plateau consists of Late Tertiary to Quaternary bimodal volcanism involving incompatible element enriched basalts and rhyolites with A-type characteristics (Coulon *et al.*, 1986). In this model for late-orogenic magmatism the magmas may be expected to have a lithospheric mantle signature and be accompanied by uplift. The following section summarises the main consequences of lithospheric mantle thinning (Fig. 6.1).

6.2. Geophysical considerations

During convergent deformation both the continental crust and the sub-continental lithosphere undergo thickening with the result that cold, dense mantle lithosphere displaces warmer convecting asthenosphere. Theoretical considerations suggest that a thermally stabilized mantle lithosphere thickened during convergent deformation must, eventually, undergo thinning in order to balance heat loss through the lithosphere with heat supply to the base of the lithosphere (Houseman *et al.*, 1981; Sandiford and Powell, 1990). The thermal and mechanical evolution of the orogen is critically dependent on how fast this potential thermal energy balance is realized relative to the orogenic strain rate

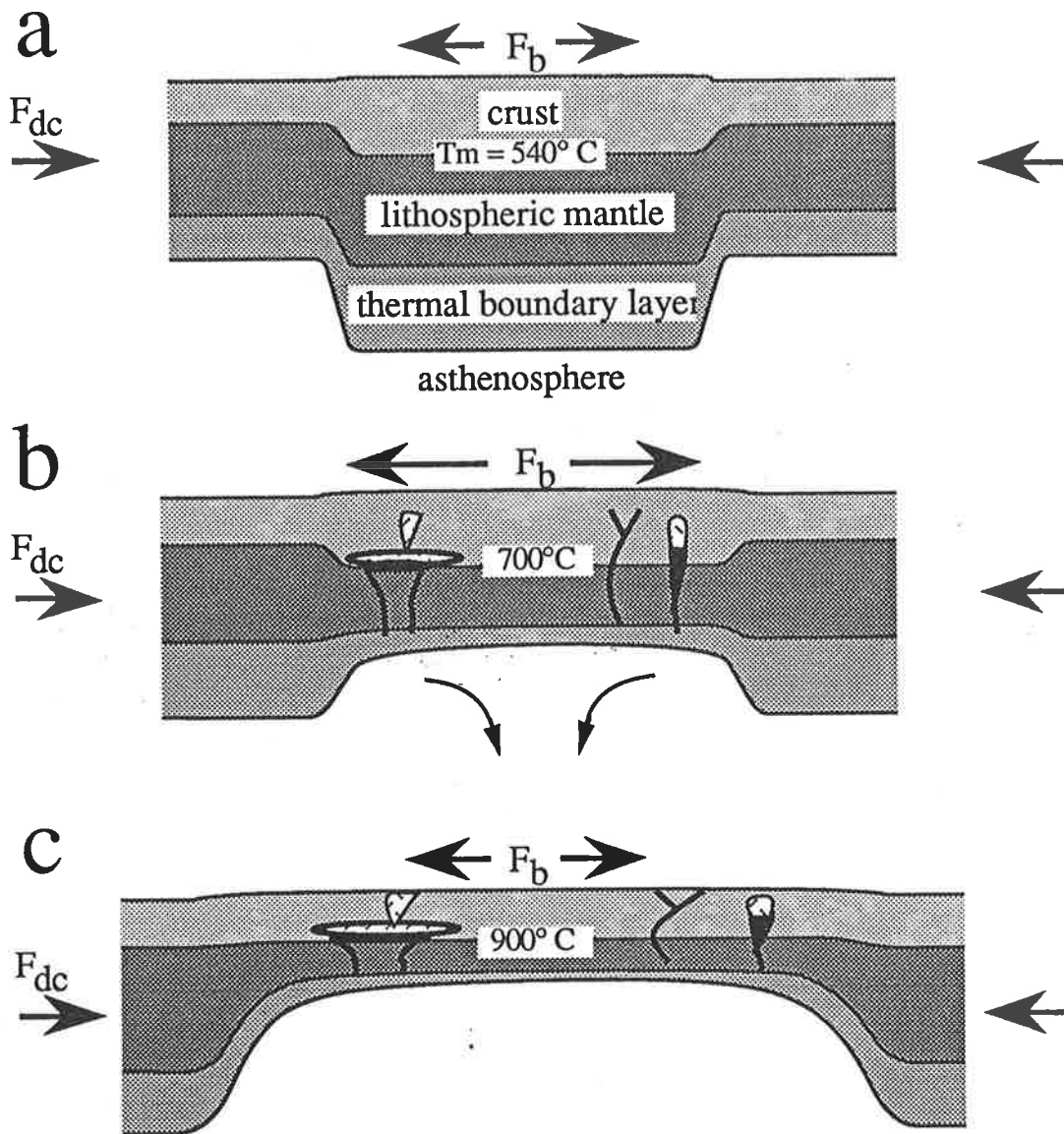


Figure 6.1. Cartoon illustrating the evolution of a convergent orogen subject to a driving force for convergence, F_{dc} , with the resultant development of horizontal buoyancy forces, F_b (the relative magnitude of the forces is indicated by the length of the arrows). Prior to any convective thinning of the mantle lithosphere the maximum elevation of the orogenic plateau is dictated by the balance between driving forces and buoyancy forces (Fig. 6.1a). An increase in the potential energy of the orogen consequent upon convective thinning of mantle lithosphere will preclude further compressional deformation (Fig. 6.1b) and may induce the extensional collapse of the orogen if the buoyancy forces exceed the driving force by an amount equivalent to the strength of the lithosphere to extensional failure (Fig. 6.1c). Magmas generated as a consequence of lithospheric thinning may appear either as post-orogenic (Fig. 6.1b) or extensional (Fig. 6.1c).

(Sandiford and Powell, 1990). Numerical experiments (Houseman *et al.*, 1981) suggest that convective processes may lead to very rapid thinning of a thickened mantle lithosphere after some initial critical thickening by processes such as thermal boundary layer detachment. The consequences of convective thinning of mantle lithosphere beneath a collision orogen are twofold, namely isostatic and thermal.

6.2.1. Isostatic consequences

The isostatic effect of mantle lithospheric thinning is to produce uplift and, consequently, an increase in the gravitational potential energy stored in the orogen. Assuming a linear geotherm where the temperature at the surface $T_s = 0^\circ\text{C}$ then the temperature at any depth z is:

$$T_z = T_1 \frac{z}{z_1} \quad (6.1)$$

where z_1 and T_1 are the depth and temperature at the base of the lithosphere, respectively. The density at depth z is given with reference to the density at temperature T_1 by:

$$\rho(z) = \rho[1 + \alpha(T_1 - T_z)] \quad (6.2)$$

Substituting (1) into (2) gives a density distribution in the crust, ρ_c , and mantle, ρ_l , respectively:

$$\begin{aligned} \rho_c(z) &= \rho_c \left(1 + \alpha T_1 \left(1 - \frac{z}{z_1} \right) \right) \\ \rho_l(z) &= \rho_l \left(1 + \alpha T_1 \left(1 - \frac{z}{z_1} \right) \right) \end{aligned} \quad (6.3)$$

For isostatic equilibrium the relative change in elevation, h , is obtained by equating the vertical stress of the crust and mantle lithosphere in the deformed and undeformed

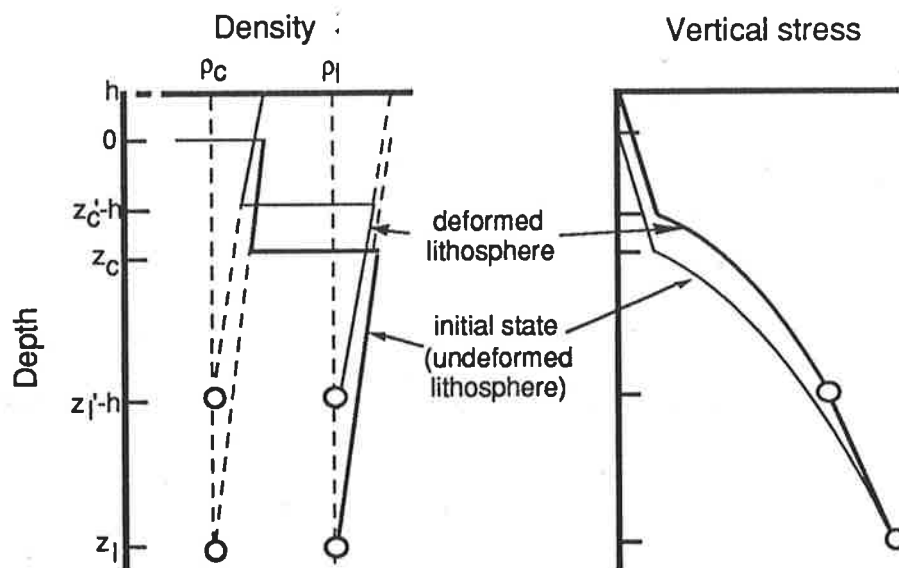


Figure 6.2. Schematic density, and vertical stress vs depth plots for an initial and deformed lithosphere. The elevation change (h) is found by equating the areas beneath the depth-density curves in the deformed and undeformed lithosphere respectively. The buoyancy force resulting from this topography is equal to the difference in the integrals of the vertical stress curves or the area between the two vertical stress curves for the deformed and undeformed lithosphere.

lithosphere respectively down to a common depth, the depth of isostatic compensation which is the greater of the thickness of the initial or deformed lithospheres (see figure 6.2). The vertical stress at depth z is given by:

$$\sigma_{zz} = \int_h^z g \rho_z dz \quad (6.4)$$

Adopting the simplifying assumption that $\rho_c \alpha = \rho_l \alpha$ and equating vertical stresses at depth z_l yields:

$$h = (z_c' - z_c) \left(1 - \frac{\rho_c}{\rho_l}\right) + \frac{(z_l - z_l') \rho_l \alpha T_l}{2} \quad (6.5)$$

Where z_c' and z_l' are the deformed thicknesses of the crust and mantle lithosphere. Following Sandiford and Powell (1990) it is useful to parameterise eqn 6.5 in terms of crustal (f_c) and lithospheric (f_l) thickening factors (ie $z_c' = z_c f_c$ and $z_l' = z_l f_l$) to give:

$$h = \left(1 - \frac{\rho_c}{\rho_l}\right) (z_c f_c + z_c) + \frac{T_l \alpha (f_l z_l - z_l)}{2} \quad (6.6)$$

A measure of the increase in potential energy is then provided by the horizontal buoyancy force per unit length of orogen, F_b , arising from gradients on density interfaces between the deformed and adjacent undeformed lithosphere. Following Turcotte (1983) and Sandiford and Powell (1990), F_b is approximated by the difference between the integrals of vertical stress, with respect to depth, between two regions, a and b, of different elevation, integrated from the Earth's surface down to a common depth beneath the lithosphere (z_l):

$$F_b = \int_{z_l}^0 g(\sigma_{zz}) dz - \int_{z_l}^{z_l+\Delta h} g(\sigma_{zz})' dz \quad (6.7)$$

Using the f_c - f_l parameterization of Sandiford and Powell (1990) this can be given to first approximation by:

$$\begin{aligned} \frac{F_b}{\rho_l z_c^2 g} = & \delta \frac{1 - \delta}{2} (f_c^2 - 1) - \frac{\alpha T_l}{6\psi^2} (f_l^2 - 1 - 3(1 - \delta)(f_c f_l - 1)) \\ & - \frac{\alpha^2 T_l^2}{8\psi^2} (f_l^2 - 1) \end{aligned} \quad (6.8)$$

Where $\delta = \rho_c/\rho_l$, and $\psi = z_c/z_l$. Figure 6.3a shows that thinning of a thick mantle lithosphere may produce substantial increases in the horizontal buoyancy forces in the orogen (by up to 10^{13} N m⁻¹). When the increase in the potential energy results in

horizontal buoyancy forces of a similar magnitude, but opposed, to the driving force for convergence (less by an amount related to the effective strength of the lithosphere, to convergent deformation) then convergent deformation will terminate or be partitioned elsewhere in regions of lower potential energy and/or strength. Continued lithospheric

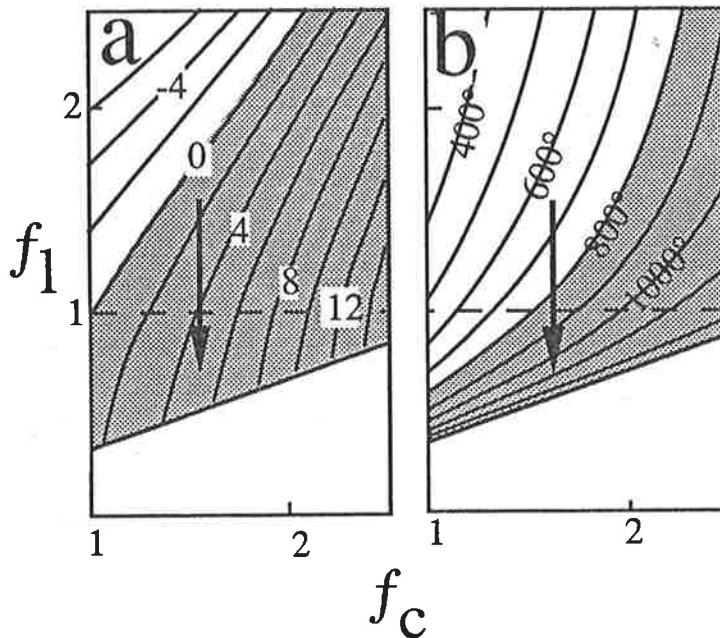


Figure 6.3. The parameterization of the vertical geometry of lithospheric deformation in convergent orogens in terms of the crustal thickening, f_c , and the lithospheric thickening, f_1 , allows the evaluation of the isostatic and thermal consequences of deformation paths involving processes such as convective thinning of the mantle lithosphere (arrows). Fig 6.3a shows the f_c - f_1 plane contoured for horizontal buoyancy forces arising from deformation induced gradients on density interfaces between a deformed and undeformed lithosphere. The stippled area shows the deformation geometries where buoyancy forces result extensional within the orogen. Initial parameters (see Sandiford, 1989; Sandiford and Powell, 1990) are $z_1 = 100$ km, $z_c = 35$ km, $\rho_c = 2800$ kg m $^{-3}$, $\rho_m = 3300$ kg m $^{-3}$, $\alpha = 10^{-5}$ °K $^{-1}$, $T_1 = 1280^\circ$ C. Note that thinning of the mantle lithosphere produces extensional buoyancy forces. Fig. 6.3b shows the f_c - f_1 plane contoured for potential Moho temperatures for the lithosphere modelled in Fig. 6.3a with heat source characteristics modelled to give an initial steady state Moho temperature of 500° C and a conductivity of 3 W m $^{-1}$ °K $^{-1}$. Note that thinning of the mantle lithosphere results in high potential moho temperatures.

thinning may cause horizontal buoyancy forces to exceed the driving forces; in which case, if the overshoot exceeds the driving force by an amount greater than the effective strength of the lithosphere to extensional deformation, then the orogen must begin to collapse (Fig. 6.4). Whether mantle lithospheric thinning is sufficient to induce extensional collapse is dependent largely on the timing of onset of mantle lithospheric thinning (Sandiford and Powell, 1990) and the strength of the lithosphere (Fig. 6.4).

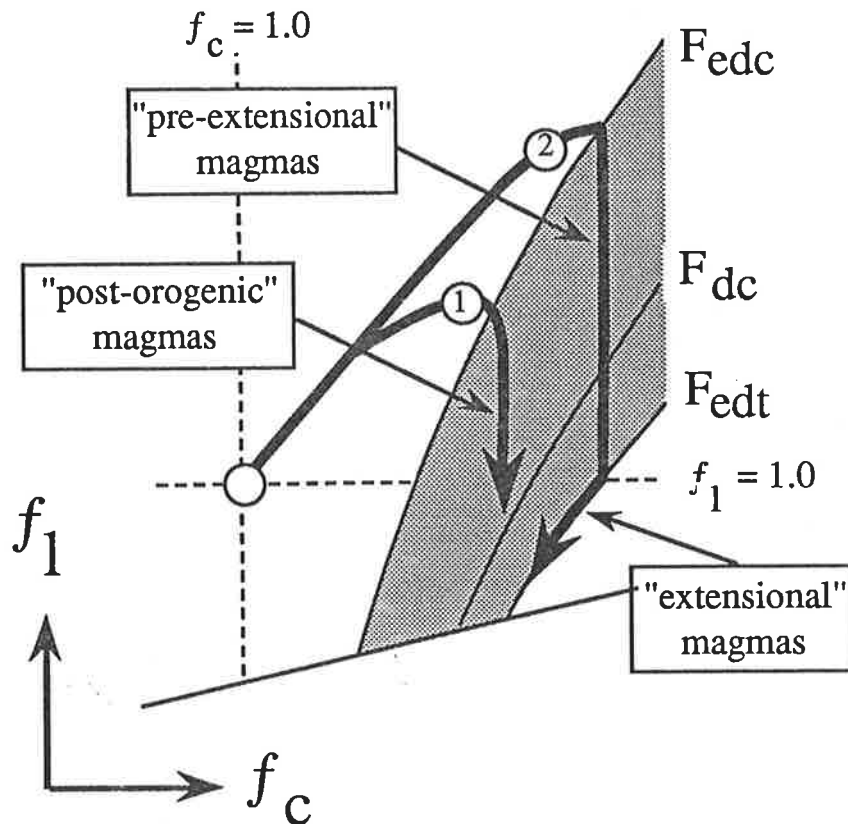


Figure 6.4. Schematic illustration of deformation ($f_c - f_1$) paths in an orogen subject to a driving force, F_{dc} , where the convective thinning of mantle lithosphere is initiated after some finite thickening. Initial homogeneous deformation ($f_c = f_1$) leads to the onset of convective thinning of mantle lithosphere ($f_c > f_1$), after small finite lithospheric thickening in Path 1 and larger finite lithospheric thickening in Path 2. Since the lithosphere has finite strength, convergent deformation and crustal thickening will cease when the buoyancy force is equal in magnitude to the effective driving force for compression, F_{edc} , given by the actual driving force minus the strength of the lithosphere in compression. Continued thinning of the mantle lithosphere will increase the buoyancy forces. If the buoyancy forces exceed the driving force by amount equivalent to the strength of the lithosphere in tension (F_{edt}) then extensional failure of the whole lithosphere may occur (Path 2). With respect to the strain history at their site of emplacement, magmas generated by thinning of the mantle lithosphere will appear as "post-orogenic" in path 1 and either "pre-extensional" or "extensional" in path 2.

6.2.2. Thermal consequences

The second important consequence of convective thinning of the mantle lithosphere is thermal. Temperature increases associated with mantle lithospheric thinning may be evaluated by solving the diffusion-advection equation in 1-dimension for model deformations. Temperature increases with depth due to the additive effects of heat flux from the mantle and that contributed by the heat producing elements that are concentrated in the crust (it is assumed for simplicity that heat production is constant with depth in the crust). For a steady state thermal gradient

$$k \frac{d^2T}{dz^2} + H_s = 0 \quad (6.9)$$

where k is the conductivity, and H_s is the surface heat production in the crust.

$$T = \frac{2 T_1 k z + H_s z^2 (z_c + z_1) - 2 H_s z z_c (z_c - z_1)}{2 k (z - z_c + z_1)} \quad (6.10)$$

Following Sandiford and Powell (1990) this can be parameterized in terms of crustal (f_c) and lithospheric (f_l) thickening factors. Let the initial ratio of the crustal/lithospheric thickness be Ψ ($= 0.35$), $p = \frac{z}{z_c}$ where p is the depth at which T is to be calculated, (\therefore for moho temperatures $p = 1$), z_c is the initial depth to the moho ($= 35000$ m), and $z = p z_c f_c$; $z_1 = f_l \frac{z_c}{\Psi}$, $z_c = z_c f_c$. Accordingly eqn 6.10 can be written for moho temperature as a function of varying crustal and lithospheric thickness:

$$T_m = \frac{f_c p (2 T_1 k \Psi + H_s f_c f_l (2 z_c^2 - p z_c^2) - H_s f_c^2 \Psi z_c^2 (2 - p))}{2 k (f_l - f_c \Psi + f_c p \Psi)} \quad (6.11)$$

The potential temperature of the Moho, T_m , calculated from eqn 6.11 in a crust with homogeneously distributed volumetric heat production is shown on the f_c - f_l plane in figure 6.3b. This shows that in order to generate the temperatures sufficient to induce melting in the lower crust and in low temperature melting fractions in the upper part of the mantle lithosphere on orogenic timescales (Sandiford and Powell, 1990) it is necessary to considerably thicken the crust and thin the mantle lithosphere beneath a thickened crust. Although both thick lithosphere ($f_l \sim 2$) and thick crust ($f_c \sim 2$) may also potentially result in very high lower crustal temperatures, the times required for attainment of these temperatures in thickened lithosphere are significantly greater than the expected orogen lifespans (Sandiford and Powell, 1990) and therefore are practically unobtainable.

6.3. Petrological considerations

A lithospheric mantle undergoing thinning has an increased potential for partial melting. The degree of partial melting and compositional heterogeneities will control magma compositions. Although the composition of the subcontinental mantle lithosphere cannot yet be quantitatively described it seems likely that the mantle lithosphere are enriched or veined by small percentage ($< 1\%$) partial melts from the convective mantle which are necessarily LREE and incompatible element enriched (Menzies and Murthy, 1980; Norry and Fitton, 1983; Hawkesworth *et al.*, 1983; O'Nions and McKenzie, 1988; McKenzie, 1989). Importantly parts of a mantle lithosphere previously enriched/veined by small partial melts from the asthenosphere will have a lower solidus than the subjacent convective mantle. Small degree melting of enriched lithospheric mantle at an early stage will produce alkaline liquids whilst larger proportion partial melts will be tholeiitic (Gast,

1968; McKenzie and Bickle, 1988). Resultant partial melt compositions will therefore be relatively anhydrous and primitive but with a LREE and incompatible element enriched signature. Isotopes may record a history relating to a period of lithospheric growth during which enrichment/veining occurred; for example, during extension of a continental margin prior to incorporation into a collisional orogen. For large magnitude thinning of the lithosphere, decompression may induce melting of depleted asthenospheric mantle beneath the orogen with initial compositions being a function of the degree of partial melting. Rising asthenospheric magmas may then become contaminated by the more fusible veins during passage through the overlying lithospheric mantle (eg. Thompson and Morrison, 1988). There is growing evidence to suggest that high silica magmas can result from extensive fractionation, with minor assimilation, from mantle derived parental magmas (Sparks, 1988; Foland *et al.*, 1988; Musselwhite *et al.*, 1989; Mahood and Halliday, 1988; this work) particularly under these relatively anhydrous conditions. Notably A-type magmas are invariably accompanied by mafic magmas and the granophyres found in layered mafic plutons typically have A-type compositions (cf Chapter 4).

6.4. Discussion

Once initiated convective thinning of a thickened mantle lithosphere may proceed very rapidly (Houseman *et al.*, 1981), with the consequence that the thermal response will be delayed with respect to the isostatic response. The melts generated as a consequence of the lithospheric thinning are therefore likely to postdate the termination of convergent deformation in any given part of the orogen (Fig. 6.1). The resulting magmas will, therefore exhibit the classic field relations of "post-orogenic" magmatism, although they certainly need not imply that convergent deformation elsewhere in the orogen has ceased. Moreover, if mantle lithospheric thinning continues to the stage where extensional collapse is initiated then magmas with the same geochemical imprint will preserve field relations which typify "pre-extensional" or "extensional" magmatic suites (Fig. 6.4). Extensive thinning, or even complete removal of the mantle lithosphere under such circumstances will result in very high Moho temperatures with the likelihood of crustal melting. In the Basin and Range province for example calc-alkaline magmatism may be the result of mixing of mantle and crustal melts (Gans *et al.*, 1989), and Nd isotopes indicate that the mantle lithosphere is indeed being progressively replaced by asthenosphere (Perry *et al.*, 1988).

Mantle lithosphere, enriched by small melt fractions from the mantle (O'Nions and McKenzie, 1987), is likely to be an important contributing component in many magmatic rocks (eg Hawkesworth *et al.*, 1990). O'Nions and McKenzie (1987) have argued that these small melt fractions play a fundamental role in producing the

composition of the continental crust. The model outlined here suggests that late-orogenic magmatism is a mechanism for crustal growth in which additions from the lithospheric mantle transfer these small partial melts and their signature to the crust.

6.5. Implications for the evolution of the late-orogenic bimodal province in the southern Adelaide Foldbelt

As documented in the preceding chapters, the southern Adelaide Foldbelt contains a suite of undeformed, A-type granites and rhyolites accompanied by tholeiitic gabbros and dykes that were emplaced during the late stages (ca. 487 Ma) of the Cambro-Ordovician Delamerian orogeny. These undeformed rocks were emplaced only a short time after a suite of deformed I- and S-type granites which intruded around 516-490 Ma (Foden *et al.*, 1990b). Compared with the temperatures deduced for the late-orogenic magmas in this thesis (900-1200 °C) the syn-orogenic tonalite-granite suite are likely to have only had temperatures of 700-850 °C in keeping with experimental constraints on hydrous phase breakdown (eg Vielzeuf *et al.*, 1990) and temperatures determined for I-type rocks (eg Hildreth, 1981; Wyborn *et al.*, 1981; White *et al.*, 1982). The late-orogenic suite clearly represents a significant thermal perturbation coincident with the cessation of deformation and there is evidence that this was associated with exhumation and possible uplift and that the magmas largely originated in the lithospheric mantle.

6.5.1. Evidence for exhumation and possible uplift

Geobarometry, the association with volcanics, and the presence of miarolitic cavities, granophyric intergrowths and embayed quartz phenocrysts in the granites indicates that the late-orogenic suite was intruded to very high crustal levels (ca. <1 kbar or < 4 kms). In contrast, yet at the same present structural level, are foliated sillimanite-kyanite bearing (ie ~4 kbar) metasediments (Sandiford *et al.*, 1990) intruded by similarly foliated granodiorites. Constraints cited by Sandiford *et al.* (1990) indicate that peak metamorphic temperatures and attendant porphyroblast growth require a thermal regime well in excess of that expected for tectonically thickened crust. Consequently these authors appeal to additional heat input from the syn-deformational magmas implying that their intrusion was coincident with peak metamorphism and also occurred at 4 kbar or 10-15 km depth. This necessitates at least 10 kms of exhumation in the minimal time (0-3 Ma; Foden *et al.*, 1990b) allowed between attainment of peak metamorphic grades (emplacement of syn-deformational intrusives) and emplacement of the late magmas which are both now exposed at the same level. Such evidence is consistent with uplift of rocks though not proof of surface uplift (England and Molnar, 1991).

Exhumation should be recorded by mineral cooling ages because the Rb-Sr and K-Ar systems in micas will pass through their closure temperatures during unroofing. In

the present case the postulated unroofing is at the time of, or just prior to intrusion of the late-orogenic magmas so intrusion and mineral cooling ages should be similar (~487 Ma). Although there is a tail of data extending to younger values the data do lend support to this. Milnes *et al.* (1977) report Rb-Sr biotite ages of 488-496 Ma for the Encounter Bay Granites at Victor Harbor, and 483 Ma for biotite from the Rathjen Gneiss, whilst the K-Ar age of a muscovite from Vivonne Bay on Kangaroo Island is 485 Ma and K-Ar on biotite from Black Hill gave 486 Ma. Webb (1976) gives K-Ar biotite ages from many of the Padthaway Ridge granites of 480-490 Ma.

Probable contiguity of the southern Adelaide Foldbelt, Antarctica, western Victoria and western Tasmania was mentioned in chapter 1, all of these areas containing undeformed Early Ordovician intrusives. Mineral cooling ages of around 480-500 Ma have been reported from all of these areas (Richards and Singleton, 1981; McDougall and Leggo, 1965; Adams and Kreuzer, 1984) though again younger ages also occur. In Tasmania, Cambrian metasediments similar to those of the Kanmantoo are overlain by the Ordovician aged transgressive Owen Conglomerate (eg. Williams, 1978) indicating rapid unroofing in this part of the orogen. Extensive westerly derived Ordovician turbiditic sequences in the Lachlan Foldbelt (eg. Cas, 1983) to the east of the Adelaide Foldbelt may represent the more distal deposits of such an unroofing event. Likewise an unroofing event implying some 10 kms of uplift and erosion at around 500 Ma has been proposed for parts of Antarctica (Stuwe and Powell, 1989; Stuwe and Oliver, 1989).

6.5.2. A lithospheric mantle source

Isotopic and chemical data from the late-orogenic suite suggests that both the mafic and silicic magmas evolved from enriched tholeiitic parental magma (chapters 3 & 4), whilst mingling between the mafic and silicic magmas (chapter 5) provides evidence of their close temporal and spatial proximity. Both these felsic and mafic end-members are LREE enriched and have Nd and Sr isotopic compositions similar to those of ocean island basalts derived from enriched mantle sources. Whilst some of the isotopic variation is due to crustal contamination, modelling is not consistent with simple crustal contamination of magma derived from the depleted mantle. To obtain the restricted range of isotopic values and generally constant incompatible element ratios such as Zr/Nb, La/Yb_N would seem to require a rather fortuitous contamination of asthenospheric magmas by just the appropriate amount of crustal material for each pluton. This is further complicated by the probable heterogeneous nature of the crust. It is intrinsically easier to explain the isotopic and incompatible element data through melting of a source which already possessed these characteristics, specifically, enriched subcontinental lithospheric mantle (K-rich layer of McKenzie, 1989). This is consistent with recent ideas about the sources of continental tholeiites and the composition of the subcontinental mantle lithosphere (Allegre *et al.*, 1981, 1982; Hawkesworth *et al.*, 1990). Mantle xenoliths (eg.

McDonough and McCulloch, 1987) demonstrate the existence of such an enriched mantle lithosphere beneath the Adelaide Foldbelt and show that it had appropriate isotopic characteristics to be the source for the late-orogenic magmas.

Finally the similarity of late-orogenic magmatic suites in many orogens and in some post-orogenic extensional environments affords the possibility that the model outlined in this thesis, for the southern Adelaide Foldbelt, may have more widespread application. In particular evidence from some of these other orogens may be able to further substantiate or negate the ideas put forward here.

References

- Anderson, J.L., 1983: Proterozoic anorogenic granite plutonism of North America. *Geol. Soc. Am. Mem.*, **161**: 133-154.
- Adams, C.J., and Kreuzer, H., 1984: Potassium-Argon age studies of slates and phyllites from the Bowers and Robertson Bay Terrains North Victoria Land, Antarctica. *Geol. Jb.*, **B60**: 265-288.
- Allegre, C.J., 1987: Isotope geodynamics. *Earth Planet. Sci. Lett.*, **86**: 175-203.
- Allegre, C.J., and Othman, D.B., 1980: Nd-Sr isotopic relationship in granitoid rocks and continental crust development: a chemical approach to orogenesis. *Nature*, **286**: 335-342.
- Allegre, C.J., Dupre, B., Lambret, B., and Richard, P., 1981: The subcontinental versus suboceanic debate, I. Lead-Neodymium-Strontium isotopes in primary alkali basalts from a shield area: the Ahaggar volcanic suite. *Earth Planet. Sci. Lett.*, **52**: 85-92.
- Allegre, C.J., Dupre, B., Richard, P., Rousseau, D., and Brooks, C., 1982: Subcontinental versus suboceanic mantle, II. Nd-Sr-Pb isotopic comparison of continental tholeiites with mid-ocean ridge tholeiites, and the structure of the continental lithosphere. *Earth Planet. Sci. Lett.*, **57**: 25-34.
- Arculus, R.J., 1987: The significance of source versus process in the tectonic controls of magma genesis. *J. Volc. Geotherm. Res.*, **32**: 1-12.
- Arculus, R.J., Ferguson, J., Chappell, B.W., Smith, D., McCulloch, M.T., Jackson, I., Hensel, H.D., Taylor, S.R., Knutson, J., and Gust, D.A., 1990: Eclogites and granulites in the lower continental crust: examples from eastern Australia and southwestern U.S.A. In: Smith, D.C., (Ed) *Eclogites and eclogite-facies rocks*. Elsevier, Amsterdam, pp. 335-380.
- Baille, P.W., 1985: A Palaeozoic suture in eastern Gondwanaland. *Tectonics*, **4**: 653-660.
- Baker, P.E., 1974: Peralkaline acid volcanic rocks of ocean islands. *Bull. Volcanol.*, **38**: 737-754.
- Barker, D.S., 1987: Tertiary alkaline magmatism in Trans-Pecos Texas. In: Fitton, J.G., and Upton, G.J., (Eds) *Alkaline Igneous Rocks*. Blackwell Scientific, Oxford, pp. 415-432.
- Bell, B.R., 1983: Significance of ferrodiortitic liquids in magma mixing processes. *Nature*, **306**: 323-327.
- Bender, J.F., Hanson, G.N.N., and Bence, A.E., 1982: The Cortland complex: evidence for large-scale liquid immiscibility involving granodiorite and diorite magmas. *Earth Planet. Sci. Lett.*, **58**: 330-344.
- Blake, S., and Ivey, G.N., 1986: Magma-mixing and the dynamics of withdrawal from stratified reservoirs. *J. Volc. and Geotherm. Res.*, **27**, 153-178.
- Blundy, J.D., and Holland, T.J.B., 1990: Calcic amphibole equilibria and a new amphibole-plagioclase geothermometer. *Contrib. Mineral. Petrol.*, **104**: 208-224.

- Bonin, B., 1990: From orogenic to anorogenic settings: evolution of granitoid suites after a major orogenesis. *Geol. J.*, **25**: 261-270.
- Bonin, B., Grelou-Orsini, C., and Vialette, Y., 1978: Age, origin and evolution of the anorogenic complex of Evisa (Corsica): a K-Li-Rb-Sr study. *Contrib. Mineral. Petrol.*, **65**: 425-432.
- Bonin, B., and Giret, A. J., 1985: Contrasting roles of rock-forming minerals in alkaline ring complexes. *J. Afr. Earth Sci.*, **3**: 41-49.
- Bowden, P., 1985: The geochemistry and mineralization of alkaline ring complexes in Africa (a review). *J. Afr. Earth Sci.*, **3**: 17-39.
- Bowden, P., Black, R., Martin, R.F., Ike, E.C., Kinnaird, E.C., and Batchelor, R.A., 1987: Niger-Nigerian alkaline ring complexes: a classic example of African Phanerozoic anorogenic mid-plate magmatism. In: Fitton, J.G., and Upton, G.J. (Eds), *Alkaline Igneous Rocks*. Blackwell Scientific, Oxford, pp 357-380.
- Brooks, C.K., and Nielsen, T.F.D., 1990: A discussion of Hunter and Sparks. *Contrib. Mineral. Petrol.*, **104**: 244-247.
- Brown, C.M., Tucker, D.H., and Anfiloff, V., 1988: An interpretation of the tectonostratigraphic framework of the Murray Basin region of southeastern Australia, based on an examination of airborne magnetic patterns. *Tectonophysics* **154**: 309-333.
- Brown, G.C., Cassidy, J., Locke, C.A., Plant, J.A., and Simpson, P.R., 1981: Caledonian plutonism in Britain: a summary. *J. Geophys. Res.*, **86**: 10502-10514.
- Buddington, A.F., and Lindsley, D.H., 1964: Iron-titanium oxide minerals and synthetic equivalents. *J. Pet.*, **5**: 310-357.
- Burnham, C.W., 1975: Water and magmas; a mixing model. *Geochim. Cosmochim. Acta.*, **39**: 1077-1084.
- Burt, D.M., Sheridan, M.F., Bikun, J.V., and Christiansen, E.H. 1982: Topaz rhyolites - distribution, origin and significance for exploration. *Ecc. Geol.*, **77**: 1818-1836.
- Bussy, F., 1990: The rapakivi texture of feldspars in a plutonic mixing environment: a dissolution-recrystallization process? *Geol. J.*, **25**: 319-324.
- Campbell, I.H., and Nolan, J., 1974: Factors effecting the stability field of Ca-poor pyroxene and the origin of the Ca-poor minimum in Ca-rich pyroxenes from tholeiitic intrusions. *Contrib. Mineral. Petrol.*, **48**: 205-219.
- Campbell, I.H., Naldrett, A.J., and Barnes, S.J., 1983: A model for the origin of the platinum-rich sulphide horizons in the Bushveld and Stillwater Complexes. *J. Pet.*, **24**: 133-165.
- Capaldi, G., Chiesa, S., Manetti, P., Orsi, G., and Poli, G., 1987: Tertiary anorogenic granites of the western border of the Yeman Plateau. *Lithos*, **20**: 433-444.
- Carmichael, I.S.E., Turner, F.J., and Verhoogen, J., 1974: *Igneous petrology*. McGraw-Hill, 739 pp.

- Cas, R., 1983: Palaeogeographic and tectonic development of the Lachlan Fold Belt southeastern Australia. *Geol. Soc. Aust. Spec. Publ. no. 10*.
- Chappell, B.W., 1984: Source rocks of I- and S-type granites in the Lachlan Fold Belt, southeastern Australia. *Phil. Trans. R. Soc. Lond.*, **A310**: 693-707.
- Chappell, B.W., and White, A.J.R., 1974: Two contrasting granite types. *Pacific Geol.*, **8**: 173-174.
- Chappell, B.W., and White, A.J.R., 1984: I- and S-type granites in the Lachlan Fold Belt, southeastern Australia. In: Xu Keqin and Tu Guangchi (Eds), *Geology and Granites and their Metallogenic Relations.*, pp. 87-101. Beijing Science Press.
- Chappell, B.W., and Stephens, W.E., 1988: Origin of infracrustal (I-type) granite magmas. *Trans. R. Soc. Edin.*, **79**: 71-86.
- Chappell, B.W., White, A.J.R., and Wyborn, D., 1987: The importance of residual source material (restite) in granite petrogenesis. *J. Pet.*, **28**: 1111-1138.
- Chen, Y.D., Price, R.C., White, A.J.R., and Chappell, B.W., 1990: Mafic inclusions from the Glenbog and Blue Gum granite suites, southeastern Australia. *J. Geophys. Res.*, **95**: 17757-17785.
- Clemens, J.D., Holloway, J.R., and White, A.J.R., 1986: Origin of an A-type granite: experimental constraints. *Am. Min.*, **71**: 317-324.
- Clemens, J.D., and Vielzeuf, D., 1987: Constraints on melting and magma production in the crust. *Earth. Planet. Sci. Lett.*, **86**: 287-306.
- Collerson, K.D., 1982: Geochemistry and Rb-Sr geochronology of associated Proterozoic peralkaline and subalkaline anorogenic granites from Labrador. *Contrib. Min. Petrol.*, **81**: 126-147.
- Collins, W.J., Beams, S.D., White, A.J.R., and Chappell, B.W., 1982: Nature and origin of A-type granites with particular reference to southeastern Australia. *Contrib. Mineral. Petrol.*, **80**: 189-200.
- Compston, W., and Chappell, B.W., 1979: Sr-isotope evolution of granitoid source rocks. In: McElhinny, M.W., (Ed), *The earth: Its origin, structure and evolution*. Academic Press, London, pp. 377-426.
- Cooper, P.F., Tuckwell, K.D., Gilligan, L. B., and Mears, R.M.D., 1974: Geology of the TORROWANGEE and FOWLERS GAP 1:100 000 sheets, 7135, 7235. *Geol. Surv. NSW*, Australia.
- Cooper, J.A., Jenkins, R.J.F., Compston, W., and Williams, I.S., 1990: Ion microprobe U-Pb zircon dating within the lower Cambrian of South Australia. *ICOG 7, Geol. Soc. Aust. Abst.*, **27**: 96.
- Coulon, C., Maluski, H., Bollinger, C., and Wang, S., 1986: Mesozoic and Cenozoic volcanic rocks from central and southern Tibet: ³⁹Ar-⁴⁰Ar dating, petrological characteristics and geodynamic significance. *Earth Planet. Sci. Lett.*, **79**: 281-302.

- Cox, K.G., and Hawkesworth, C.J., 1984: Relative contributions of crust and mantle to flood basalt magmatism, Mahabaleshwar area, Deccan Traps. *Phil. Trans. Roy. Soc. Lond.*, **A310**: 627-641.
- Cox, K.G., Bell, J.D., and Pankhurst, R.J., 1979: *The interpretation of igneous rocks*. George Allen and Unwin, London, 450 p.
- Crock, J.G., Lichte, F.E., and Wildeman, T.R., 1984: The group separation of the rare earth elements and Yttrium from geologic materials by cation-exchange chromatography. *Chem. Geol.*, **45**: 149-163.
- Daily, B., Firman, J.B., Forbes, B.G., and Lindsay, J.M., 1976: Geology. In: Twidale, C.R., Tyler, M.J., and Webb, B.P., (Eds), *Natural history of the Adelaide region*. Roy. Soc. S. Aust., pp. 17-18.
- Daly, S.J., and Fanning, C.M., 1990: Archaean geology of the Gawler Craton, South Australia. Int. Archaean Conf. Perth, 1990.
- Defant, J.M., and Nielsen, R.L., 1990: Interpretation of open system petrogenetic processes: Phase equilibria constraints on magma evolution. *Geochim. Cosmochim. Acta.*, **54**: 87-102.
- DePaolo, D.J., 1981: Trace element and isotopic effects of combined wallrock assimilation and fractional crystallization. *Earth Planet. Sci. Lett.*, **53**: 189-202.
- DePaolo, D.J., 1988: *Neodymium isotope geochemistry*. Springer-Verlag, Berlin. p. 187.
- Dick, H.J.B., and Bullen, T., 1984: Chromian spinel as a petrogenetic indicator in abyssal and alpine-type peridotites and spatially associated lavas. *Contrib. Mineral. Petrol.*, **86**: 54-76.
- Dickinson, J.E., and Hess, P.C., 1982: Zircon saturation in lunar basalts and granites. *Earth. Planet. Sci. Lett.*, **57**: 336-344.
- Didier, J., 1973: *Granites and their Enclaves*. Elsevier, Amsterdam. p. 393.
- Dingwell, D.B., Scarfe, C.M., and Cronin, D.J., 1985: The effect of fluorine on viscosities in the system $\text{Na}_2\text{O}-\text{Al}_2\text{O}_3-\text{SiO}_2$: implications for phonolites, trachytes and rhyolites. *Am. Min.*, **70**: 80-87.
- Dredge, C., 1979: Exploration License 401 - Meningie S Aust Dept Mines and Energy, Open File Env 3316 (unpubl.).
- Eberz, G.W., Nicholls, I.A., Maas, R., McCulloch, M.T., and Whitford, D.J., 1990: The Nd- and Sr-isotopic composition of I-type microgranitoid enclaves and their host rocks from the Swifts Creek Pluton, southeast Australia. *Chem. Geol.*, **85**: 119-134.
- Eby, G.N., 1990: The A-type granitoids: A review of the occurrence and chemical characteristics and speculations on their petrogenesis. *Lithos.*, **26**: 115-134.
- Ellam, R., and Cox, K.G., 1989: A Proterozoic lithospheric source for Karoo magmatism: evidence for the Nuanetsi picrites. *Earth Planet. Sci. Lett.*, **92**: 207-218.

- Ellis, D.J., 1980: Osumilite-sapphirine-quartz granulites from Enderby Land, Antarctica: P-T conditions of metamorphism, implications for garnet-cordierite equilibria and the evolution of the deep crust. *Contrib. Mineral. Petrol.* **74**: 201-210.
- England, P.C., and Houseman, G.A., 1988: The mechanics of the Tibetan Plateau. *Phil. Trans. R. Soc. Lond.*, **A326**: 301-320.
- England, P.C., and Houseman, G.A., 1989: Extension during continental convergence, with application to the Tibetan Plateau. *J. Geophys. Res.*, **94**: 17561-17579.
- England, P.C., and Molnar, P., 1990: Surface uplift, uplift of rocks, and exhumation of rocks. *Geology*, **18**: 1173-1177.
- Ewart, A., 1981: The mineralogy and chemistry of the anorogenic Tertiary silicic volcanics of S.E. Queensland and N.E. New South Wales, Australia. *J. Geophys. Res.*, **86** B11: 10242-10256.
- Fanning, C.M., 1975: Petrology, structure and geochronology of some high grade metamorphic rocks at Fishery Bay and Cape Carnot, Southern Eyre Peninsula. *Univ. Adelaide Hons. Thesis, (unpubl.)*.
- Fanning, C.M., Oliver, R.L., and Cooper, J.A., 1980: The Carnot Gneisses, southernmost Eyre Peninsula. *J. Geol. Soc. Aust.*, **27**: 47.
- Fletcher, C.J.N., and Beddoe-Stephens, B., 1987: The petrology, chemistry and crystallization history of the Velasco alkaline province, eastern Bolivia. *In*: Fitton, J.G., and Upton, G.J., (Eds), *Alkaline Igneous Rocks*. Blackwell Scientific, Oxford, pp. 403-414.
- Foden, J.D., Turner, S.P., and Morrison, R.S., 1990a: The tectonic implications of Delamerian magmatism in South Australia and western Victoria. *In*: Jago, J.B., and Moore, P.J., (Eds), *The evolution of a Late Precambrian-Early Cambrian Palaeozoic rift complex: The Adelaide Geosyncline*. *Geol. Soc. Aust. Spec. Publ.* no. 16, pp. 465-482.
- Foden, J.D., Williams, I., Compston, W., Michard, A. and Turner, S.P., 1990b: Some constraints on the timing of the Delamerian Orogeny in the Southern Adelaide Fold Belt: Implications for the evolution of the eastern margin of Gondwanaland. *In prep.*
- Foden, J.D., Michard, A. and Turner, S.P., 1990c: Late Proterozoic and early Palaeozoic crustal development in South Australia and Tasmania: Implications based on Nd- and Sr-isotopic results. *In prep.*
- Fodor, R.V., Corwin, C., and Roisenberg, A., 1985: Petrology of Serra Geral (Parana) continental flood basalts, southern Brazil: crustal contamination, source material and south Atlantic magmatism. *Contrib. Mineral. Petrol.*, **91**: 54-65.
- Foland, K.A., Raczek, I., Henderson, C.M.B., and Hofmann, A.W., 1988: Petrogenesis of the magmatic complex at Mount Ascutney, Vermont, U.S.A.: *Contrib. Mineral. Pet.*, **98**: 408-416.

- Fourcade, S., and Allegre, C.J., 1981: Trace elements behavior in granite genesis: A case study the calc-alkaline plutonic association from the Querigut Complex (Pyrenees, France). *Contrib. Mineral. Pet.*, **76**: 177-195.
- Frost, B.R., Lindsley, D.H., and Andersen, D.J., 1988: Fe-Ti oxide-silicate equilibria: Assemblages with fayalitic olivine. *Am. Min.*, **73**: 727-740.
- Frost, T.P., and Lindsay, J.R., 1988: MAGMIX: a BASIC program to calculate viscosities of interacting magmas of differing composition, temperature, and water content. *Comput. Geosci.*, **14**: 213-228.
- Fuhrman, M.L., Frost, B.R., and Lindsley, D.H., 1988: Crystallization conditions of the Sybille monzonite, Laramie Anorthosite Complex, Wyoming. *J. Pet.*, **29**: 699-729.
- Fuhrman, M.L., and Lindsley, D.H., 1988: Ternary feldspar modeling and thermometry. *Am. Min.*, **73**: 201-215.
- Gans, P.B., Mahood, G.A., and Schenner, E., 1989: Synextensional magmatism in the Basin and Range Province. *Geol. Soc. Am. Spec. Pap.*, 233.
- Gast, P.W., 1968: Trace element fractionation and the origin of tholeiitic and alkaline magma types. *Geochim. Cosmochim. Acta.*, **32**: 1057-1086.
- Gibson, I.L., 1974: A review of the geology, petrology and geochemistry of the volcano Fantale. *Bull. Volcanol.*, **38**: 791-802.
- Gray, C.M., 1984: An isotopic mixing model for the origin of granitic rocks in southeastern Australia. *Earth Planet. Sci. Lett.*, **70**: 47-60.
- Griffin, T.J., White, A.J.R., and Chappell, B.W., 1978: The Moruya Batholith and geochemical contrasts between the Moruya and Jindabyne suites. *J. Geol. Soc. Aust.*, **25**: 235-247.
- Griffin, W.L., O'Reilly, S.Y., and Stabel, A., 1988: Mantle metasomatism beneath western Victoria, Australia: II. Isotopic geochemistry of Cr-diopside lherzolites and Al-augite pyroxenites. *Geochim. Cosmochim. Acta.*, **52**: 449-459.
- Grove, T.L., and Baker, M.B., 1984: Phase equilibrium controls on the tholeiitic versus calc-alkaline differentiation trends. *J. Geophys. Res.*, **89**: 3253-3274.
- Grove, T.L., and Bryan, W.B., 1983: Fractionation of pyroxene-phyric MORB at low pressure: an experimental study. *Contrib. Mineral. Petrol.* **84**: 293-309.
- Grove, T.L., and Juster, T.C., 1989: Experimental investigations of low-Ca pyroxene stability and olivine-pyroxene-liquid equilibria at 1-atm in natural basaltic and andesitic liquids. *Contrib. Mineral. Petrol.*, **103**: 287-305.
- Harris, C., 1983: The petrology of lavas and associated plutonic inclusions of Ascension Island. *J. Pet.*, **24**: 424-470.
- Harris, N.B.W., Duyverman, H.J., and Almond, D.C., 1983: The trace element and isotope geochemistry of the Sabaloka Igneous Complex, Sudan. *J. Geol. Soc. Lond.*, **140**: 245-256.

- Harrison, T.M., and Watson, E.B., 1983: Kinetics of zircon dissolution and zirconium diffusion in granitic melts of variable water content. *Contrib. Mineral. Petrol.*, **84**: 66-72.
- Hawkesworth, C.J., Erlank, A.J., Marsh, J.S., Menzies, M.A., and van Calsteren, P., 1983: Evolution of the continental lithosphere: evidence from volcanics and xenoliths in southern Africa. In: Hawkesworth, C.J., and Norry, M.J., (Eds), *Continental basalts and mantle xenoliths*. Shiva, Nantwich, U.K., pp. 92-110.
- Hawkesworth, C.J., Kempton, P.D., Rogers, N.W., Ellam, R.M., and van Calsteren, P.W., 1990: Continental mantle lithosphere, and shallow level enrichment processes in the Earth's mantle. *Earth Planet. Sci. Lett.*, **96**: 256-268.
- Helz, R.T., 1982: Phase relations and compositions of amphiboles produced in studies of the melting behaviour rocks. In: Veblen, D.R., and Ribbe, P.H., (Eds), *Amphiboles: Petrology and Phase Relations*. Mineral. Soc. Am., Reviews in Mineralogy **9B** pp. 279-354.
- Henstridge, D.A., 1970: The petrology and geochemistry of the upper south east granites, South Australia. *University of Adelaide Hons thesis (unpubl.)*.
- Hergt, J.M., 1987: The origin and evolution of the Tasmanian dolerites. *Aust. Nat. Uni. Ph.D thesis (unpubl.)*.
- Hergt, J.M., Chappell, B.W., McCulloch, M.T., McDougall, I., and Chivas, A.R., 1989: Geochemical and isotopic constraints on the origin of the Jurassic dolerites of Tasmania. *J. Pet.* **30**: 841-883.
- Hibbard, M.J., 1981: The magma mixing origin of mantled feldspars. *Contrib. Mineral. Petrol.*, **76**: 158-170.
- Hildreth, W., 1981: Gradients in silicic magma chambers: implications for lithospheric magmatism. *J. Geophys. Res.*, **86** B11: 10153-10192.
- Hill, R.E., and Roeder, P.L., 1974: The crystallization of spinel from basaltic liquid as a function of oxygen fugacity. *J. Geol.*, **82**: 709-729.
- Hine, R., Williams, I.S., Chappell, B.W., and White, A.J.R., 1978: Contrasts between I- and S-type granitoids of the Kosciusko batholith. *J. Geol. Soc. Aust.*, **25**: 219-234.
- Hofmann, A.W., 1980: Diffusion in natural silicate melts: a critical review. In: Hargraves, R.B., (ed.), *Physics of magmatic processes*. Princeton Univ. Press, Princeton, N.J., pp. 385-417.
- Holden, P., Halliday, A.N., and Stephens, W.E., 1987: Neodymium and strontium isotope content of microdiorite enclaves points to mantle input to granitoid production. *Nature*, **330**: 53-56.
- Houseman, G.A., McKenzie, D.P., and Molnar, P.J., 1981: Convective instability of a thickened boundary layer and its relevance for the thermal evolution of continental convergent belts. *J. Geophys. Res.*, **86**: 6115-6132.
- Hudson, T., Arth, J.G., 1983: Tin granites of Seward Peninsula, Alaska. *Geol. Soc. Am. Bull.*, **94**: 768-790.

- Hunter, R.H., and Sparks, R.S.J., 1987: The differentiation of the Skaergaard Intrusion. *Contrib. Mineral. Petrol.*, **95**: 451-461.
- Hunter, R.H., and Sparks, R.S.J., 1990: Replies to McBirney and Naslund, Morse, and Brooks and Nielsen. *Contrib. Mineral. Petrol.*, **104**: 248-254.
- Huppert, H.E., and Sparks, R.S.J., 1980: The fluid dynamics of a basaltic chamber replenished by influx of hot, dense ultrabasic magma. *Contrib. Mineral. Petrol.*, **75**: 279-289.
- Huppert, H.E., and Sparks, R.S.J., 1985: Cooling and contamination of mafic and ultramafic magmas during ascent through continental crust. *Earth Planet. Sci. Lett.*, **74**: 371-386.
- Huppert, H.E., and Sparks, R.S.J., 1988: The generation of granitic magmas by intrusion of basalt into continental crust. *J. Pet.*, **29**: 599-624.
- Huppert, H.E., Sparks, R.S.J., and Turner, J.S., 1984: Some effects of viscosity on the dynamics of replenished magma chambers. *J. Geophys. Res.*, **89**: 6857-6877.
- Huppert, H.E., Sparks, R.S.J., Whitehead, J.A., and Hallworth, M.A., 1986: The replenishment of magma chambers by light inputs. *J. Geophys. Res.*, **91**: 6113-6122.
- Ike, E.C., Bowden, P., and Martin, R.F., 1984: Fayalite and clinopyroxene in the porphyries of the Tibchi anorogenic ring-complex, Nigeria: postmagmatic initiation of a peralkaline trend. *Can. Min.*, **22**: 401-409.
- Irvine, T.N., 1970: Crystallization sequences in the Muskox Intrusion and other layered intrusions. *Geol. Soc. S. Afr. Spec. Publ.* #1., pp. 441-476.
- Irvine, T.N., 1979: Rocks whose composition is determined by crystal accumulation and sorting. In: Yoder, H.S., (Ed.), *The Evolution of the Igneous Rocks, Fiftieth Anniversary Perspectives*. Princeton, NJ: Princeton University Press, pp. 245-306.
- Irvine, T.N., 1980: Magmatic infiltration metasomatism, double diffusive fractional crystallization and adcumulus growth in the Muskox intrusion and other layered intrusions. In: Hargraves, R.B., (Ed.), *Physics of Magmatic Processes*. Princeton, N.J.: Princeton University Press, pp. 325-384.
- Jackson, N.J., Walsh, J.N., and Pegram, E., 1984: Geology, geochemistry and petrogenesis of Late Precambrian granitoids in the Central Hizaz Region of the Arabian Shield. *Contrib. Mineral. Petrol.*, **87**: 205-219.
- Jacobsen, S.B., and Wasserburg, G.J., 1979: Nd and Sr isotopic study of the Bay of Islands ophiolite complex and the evolution of the source of midocean ridge basalts. *J. Geophys. Res.*, **84**: 7429-7445.
- Jenkins, R.J.F., 1986: Ralph Tate's enigma - and the regional significance of thrust faulting in the Mt Lofty Ranges. *Geol. Soc. Aust., Abstr.* 15, pp. 101.
- Jenkins, R.J.F., 1990: The Adelaide Foldbelt: tectonic reappraisal. In: Jago, J.B., and Moore, P.J., (eds), *The evolution of a Late Precambrian - Early Palaeozoic rift complex: The Adelaide Geosyncline*. Geol. Soc. Aust. Spec. Publ. 16 pp. 396-420.

- Johnson, M.C., and Rutherford, M.J., 1989: Experimental calibration of the aluminium-in-hornblende geobarometer with application to Long Valley caldera (California) volcanic rocks. *Geol.* **17**: 837-841.
- Keays, R.R., Hamlyn, P.R., and Reeves, S.J., 1990: Ore genesis and exploration for platinum-group element mineralization in layered mafic/ultramafic intrusions. *Geol. Soc. Aust. Abst. Vol. 10 A.G.C., Hobart.*
- Kennedy, R.J., 1989: A 3-D gravity and aeromagnetic interpretation of the Black Hill - Cambrai Region. *University of Adelaide Hons. Thesis, (unpubl.).*
- Kleemann, G.J., and Twist, D., 1989: The compositionally-zoned sheet-like granite pluton of the Bushveld Complex: Evidence bearing on the nature of A-type magmatism. *J. Pet.* **30**: 1383-1414.
- Kudo, A.M., and Weill, D.F., 1971: An igneous plagioclase thermometer. *Contrib. Mineral. Petrol.* **25**: 52-65.
- Laird, M.G., and Grindley, G.W., 1982: *Antarctica*. Spec. Publ. Geol. Soc. Aust., **9**: 17-22.
- Langmuir, C.H., Vocke, Jr., R.D., Hanson, G.N., and Hart, S.R., 1978: A general mixing equation with applications to Icelandic basalts. *Earth Planet. Sci. Lett.*, **37**: 380-392.
- Leake, B.E., 1978: Nomenclature of amphiboles. *Am. Min.*, **63**: 1023-1052.
- Liegeois, J.P., Black, R., 1987: Alkaline magmatism subsequent to collision in the Pan-African belt of the Adrar des Iforas (Mali). In: Fitton, J.G., and Upton, G.J., (Eds) *Alkaline Igneous Rocks*. Blackwell Scientific, Oxford, pp. 381-402.
- Lindsley, D.H., 1983: Pyroxene thermometry. *Am. Min.*, **68**: 477-493.
- Loiselle, M.C., and Wones, D.R., 1979: Characteristics and origin of anorogenic granites. *Geol. Soc. Am. Bull. Abs. Prog.*, **92**: 468.
- Lynch, J., 1978: Report on North Broken Hill Ltd. exploration licence # 204. SADME open file env., 2631.
- Maaloe, S., 1985: *Igneous Petrology*. Springer-Verlag, Berlin -Heidelberg, pp. 374.
- Macdonald, R., 1987: Quaternary peralkaline silicic rocks and caldera volcanoes of Kenya. In: Fitton, J.G., and Upton, B.G.J., (eds), 1987. *Alkaline igneous rocks*. Geol. Soc. Spec. Publ. # 30, pp. 313-333.
- Macdonald, R., Davies, G.R., Bliss, C.M., Leat, P.T., Bailey, D.K., and Smith, R.L., 1987: Geochemistry of high-silica peralkaline rhyolites, Naivasha, Kenya Rift Valley. *J. Pet.*, **28**: 979-1008.
- Macdonald, R., McGarvie, D.W., Pinkerton, H., Smith, R.L., and Palacz, Z.A., 1990: Petrogenetic evolution of the Torfajokull Volcanic Complex, Iceland I. Relationship between the magma types. *J. Pet.*, **31**: 429-459.
- Mahood, G.A., and Halliday, A.N., 1988: Generation of high-silica rhyolite: A Nd, Sr, and O isotopic study of Sierra La Primavera, Mexican Neovolcanic belt. *Contrib. Mineral. Petrol.*, **100**: 183-191.

- Mancktelow, N.S., 1979: The structure and metamorphism of the southern Adelaide fold belt. *University of Adelaide PhD thesis, (unpubl.)*.
- Manning, D.A.C., and Pichavant, M., 1983: The role of fluorine and boron in the generation of granitic melts. *In: Atherton, M.P., and Gribble, C.D., (Eds), Migmatites, melting and metamorphism*. Shiva pp. 94-110.
- Margaritz, M., and Hofmann, A.W., 1978: Diffusion of Sr, Ba and Na in obsidian. *Geochim. Cosmochim. Acta.*, **42**: 595-605.
- Marshall, L.A. and Sparks, R.S.J. 1984: Origin of some mixed-magma and net-veined ring intrusions. *J. Geol. Soc. London.*, **141**: 171-182.
- Martin, R.F., and Bonin, B., 1976: Water and magma genesis: the association hypersolvus granite-subsolvus granite. *Can. Min.* **14**: 228-237.
- Mathez, E.A., 1973: Refinement of the Kudo-Weill plagioclase thermometer and its application to basaltic rocks. *Contrib. Mineral. Petrol.* **41**: 61-72.
- Mawson, D., and Dallwitz, W.B., 1944: Palaeozoic igneous rocks of lower south-eastern South Australia. *Trans. Roy. Soc. S.A.*, **68** (2): 191-209.
- Mawson, D., and Parkin, L.W., 1943: Some granitic rocks of south-eastern South Australia. *Trans. Roy. Soc. S.A.*, **67**: 233-243.
- Mawson, D., and Segnit, E.R., 1945: Granites of the Tintinara district. *Trans. Roy. Soc. S.A.*, **69**: 263-276.
- McBirney, A.R., 1975: Differentiation of the Skaergaard Intrusion. *Nature*, **253**: 691-694.
- McBirney, A.R., 1980: Mixing and unmixing of magmas. *J. Volcanol. Geotherm. Res.*, **7**: 357-371.
- McBirney, A.R., and Noyes, R.M., 1979: Crystallization and layering of the Skaergaard Intrusion. *J. Pet.* **20**: 487-554.
- McBirney, A.R., and Murase, T., 1984: Rheological properties of magmas. *Ann. Rev. Earth Planet. Sci.*, **12**: 337-357.
- McBirney, A.R., and Naslund, H.R., 1990: The differentiation of the Skaergaard Intrusion, a discussion of Hunter and Sparks. *Contrib. Mineral. Petrol.*, **104**: 235-240.
- McBirney, A.R., Baker, B.H., and Nilson, R.H., 1985: Liquid fractionation. Part 1: Basic principles and experimental simulations. *J. Volc. Geotherm. Res.*, **24**: 1-24.
- McCulloch, M.T., 1987: Sm-Nd isotopic constraints on the evolution of Precambrian crust in the Australian continent. *In: Kroner, A., (Ed.), Proterozoic lithospheric evolution. Am. Geophys. Union. Geodynamics series, #17 pp. 115-130.*
- McCulloch, M.T., Arculus, R.J., Chappell, B.W., and Ferguson, J., 1982: Isotopic and geochemical studies of nodules in kimberlite have implications for the lower continental crust. *Nature*, **300**: 166-169.
- McCulloch, M.T., and Chappell, B.W., 1982: Nd isotopic characteristics of S- and I-type granites. *Earth Planet. Sci. Lett.*, **58**: 51-64.

- McDonough, W.F., and McCulloch, M.T., 1987: The southeast Australian lithospheric mantle: isotopic and geochemical constraints on its growth and evolution. *Earth Planet.Sci. Lett.*, **86**: 327-340.
- McDonough, W.F., McCulloch, M.T., and Sun, S.S., 1985: Isotopic and geochemical systematics in Tertiary-Recent basalts from southeastern Australia and implications for the evolution of the subcontinental lithosphere. *Geochim. Cosmochim. Acta.*, **49**: 2051-2067.
- McDougall, I., 1962: Differentiation of the Tasmanian Dolerites: Red Hill dolerite-granophyre association. *Geol. Soc. Am. Bull.*, **73**: 279-316.
- McDougall, I., and Leggo, P.J., 1965: Isotopic age determinations on granitic rocks from Tasmania. *J. Geol. Soc. Aust.*, **12**: 295-332.
- McGarvie, D.W., Macdonald, R., Pinkerton, H., and Smith, R.L., 1989: Petrogenetic evolution of the Torfajökull volcanic complex, Iceland II. The role of magma mixing. *J. Pet.*, **31**: 461-481.
- McKenzie, D.P., 1984: A possible mechanism of epeirogenic uplift. *Nature*, **307**: 616-618.
- McKenzie, D.P., 1985: The extraction of magma from the crust and mantle. *Earth. Planet. Sci. Lett.*, **74**: 81-91.
- McKenzie, D.P., 1989: Some remarks on the movement of small melt fractions in the mantle. *Earth Planet.Sci. Lett.*, **95**: 53-72.
- McKenzie, D.P., and Bickle, M.J., 1988: The volume and composition of melt generated by extension of the lithosphere. *J. Pet.*, **29**: 625-679.
- McKenzie, D.P., and O'Nions, R.K., 1983: Mantle reservoirs and ocean island basalts. *Nature*, **301**: 229-231.
- Menzies, M., and Murthy, V.R., 1980: Enriched mantle: Nd and Sr isotopes in diopsides from kimberlite nodules. *Nature*, **283**: 634-636.
- Menzies, M.A., 1983: Mantle ultramafic xenoliths in alkaline magmas: evidence for mantle heterogeneity modified by magmatic activity. In: Hawkesworth, C.J., and Norry, M.J., (Eds), *Continental basalts and mantle xenoliths*. Shiva, Nantwich, U.K., pp. 92-110.
- Menzies, M.A., Leeman, W.P., and Hawkesworth, C.J., 1984: Geochemical and isotopic evidence for the origin of continental flood basalts with particular to Snake River Plain Idaho, U.S.A. *Phil. Trans. R. Soc. Lond. A* **310**: 643-660.
- Milnes, A.R., Compston, W., and Daily, B., 1977: Pre- to syn-tectonic emplacement of early Palaeozoic granites in southeastern South Australia. *J. Geol. Soc. Aust.*, **24**: 87-106.
- Milnes, A.R., 1982: The Encounter Bay Granites and their relationship to the Kanmantoo Group. In: Oliver, R.L., and Gatehouse, C.G. (Eds), *Guide to excursions B1, B2, B3, B4, Geology of the Adelaide Region, Fourth Int. Symp. on Antarctic Earth Sciences*, pp 16-29.
- Mitchell, S.F., 1990: S-type granite formation at Vivonne Bay, Kangaroo Island. *Univ. of Adelaide Hons. thesis (unpubl)*.

- Moeller, T., 1980: The petrology and geochemistry of the Reedy Creek granitoids and migmatites. *Univ. of Adelaide Hons. thesis (unpubl.)*.
- Molnar, P., 1984: Structure and tectonics of the Himalaya: constraints and implications of geophysical data. *Ann. Rev. Earth. Planet. Sci.*, **12**: 489-518.
- Morrison, R.S., 1989: Igneous intrusive rocks of the Peake and Denison Ranges within the Adelaide Geosyncline. *Univ. Adelaide PhD thesis (unpubl.)*.
- Morse, S.A., 1979: Kiglapait geochemistry 1: systematics, sampling and density. *J. Pet.*, **20**: 555-590.
- Morse, S.A., 1990: A discussion of Hunter and Sparks. *Contrib. Mineral. Petrol.*, **104**: 240-244.
- Mortimer, G.E., 1984: Granitoids and basaltic dykes, southern Eyre Peninsula. *University of Adelaide PhD thesis (unpubl.)*.
- Murase, T., and McBirney, A.R., 1973: Properties of some common igneous rocks and their melts at high temperatures. *Bull. Geol. Soc. Am.*, **84**: 3563-3592.
- Musselwhite, D.S., DePaolo, D.J., and McCurry, M., 1989: The evolution of a silicic magma system: isotopic and chemical evidence from the Woods Mountains Volcanic Center, eastern California. *Contrib. Mineral. Petrol.*, **101**: 19-29.
- Naslund, H.R., 1989: Petrology of the Basistoppen Sill, East Greenland: A calculated magma differentiation trend. *J. Pet.*, **30**: 299-319.
- Nathan, H.D., and Van Kirk, 1978: A model of magmatic crystallization. *J. Pet.*, **19**: 66-94.
- Nesbitt, H.W., 1980: Genesis of the New Quebec and Adirondack granulites: evidence for their production by partial melting. *Contrib. Mineral. Petrol.*, **72**: 303-310.
- Nielsen, R.L., 1988a: A model for the simulation of combined major and trace element liquid lines of descent. *Geochim. Cosmochim. Acta.*, **52**: 27-38.
- Nielsen, R.L., 1988b: TRACE.FOR: A program for the calculation of combined major and trace element liquid lines of descent for natural magmatic systems. *Comput. Geosci.*, **14**: 15-35.
- Nielsen, R.L., 1989: Phase equilibria constraints on liquid lines of descent generated by paired assimilation and fractional crystallization: trace elements and Sr and Nd isotopes. *J. Geophys. Res.*, **94**: 787-794.
- Nishiyama, T., 1983: Steady diffusion model for olivine-plagioclase corona growth. *Geochim. Cosmochim. Acta.*, **47**: 283-294.
- Noble, D.C., 1970: Loss of sodium from crystallized comendite welded tuffs of the Miocene Grouse Canyon Member of the Belted Range Tuff, Nevada. *Bull. Geol. Soc. Am.* **81**: 2677-2687.
- Norry, M.J., and Fitton, J.G., 1983: Compositional differences between oceanic and continental basic lavas and their significance. In: Hawkesworth, C.J., and Norry, M.J., (Eds), *Continental Basalts and Mantle Xenoliths* (Shiva) p. 5-20.

- Offler, R., and Fleming, P.D., 1968: A synthesis of folding and metamorphism in the Mt Lofty Ranges, South Australia. *J. Geol. Soc. Aust.*, **15**: 245-266.
- O'Nions, R.K., 1984: Isotopic abundances relevant to the identification of magma sources. *Phil. Trans. Roy. Soc. Lond.*, **A310**: 591-603.
- O'Nions, R.K., and McKenzie, D.P., 1988: Melting and continent generation. *Earth. Planet. Sci. Lett.*, **90**: 449-456.
- O'Reilly, S.Y., and Griffin, W.L., 1988: Mantle metasomatism beneath western Victoria, Australia: I. Metasomatic processes in Cr-diopside lherzolites. *Geochim. Cosmochim. Acta.*, **52**: 433-447.
- Pearce, J.A., 1983: The role of sub-continental lithosphere in magma genesis at active continental margins. In: Hawkesworth, C.J., and Norry, M.J., (Eds), *Continental Basalts and Mantle Xenoliths*, Shiva Geology Series, pp. 230-249.
- Pearce, J.A., and Norry, M.J., 1979: Petrogenetic implications of Ti, Zr, Y and Nb variations in volcanic rocks. *Contrib. Mineral. Petrol.*, **69**: 33-47.
- Pearce, J.A., Harris, N.B.W., and Tindle, A.G., 1984: Trace element discrimination diagrams for the tectonic interpretation of granitic rocks. *J. Pet.*, **25**: 956-983.
- Perry, F.V., Baldrige, W.S., and DePaolo, D.J., 1988: Chemical and isotopic evidence for lithospheric thinning beneath the Rio Grand rift. *Nature*, **332**: 432-434.
- Pitcher, W.S., 1982: Granite type and tectonic environment, In: Hsu, K.J., (ed.), *Mountain Building Processes*. (Academic Press) p.19-40.
- Ponader, C.W., and Brown, G.E., 1989: Rare earth elements in silicate glass/melt systems: II. Interactions of La, Gd and Yb with halogens. *Geochim. Cosmochim. Acta.*, **53**: 2905-2914.
- Powell, R., and Holland, T.J.B., 1988: An internally consistent dataset with uncertainties and correlations: 3. Applications to geobarometry, worked examples and a computer program. *J. Met. Geol.*, **6**: 173-204.
- Preiss, W.V. (Compiler), 1987: The Adelaide Geosyncline: Late Proterozoic stratigraphy, sedimentation, palaeontology and tectonics. *Bull. Geol. Surv. S. Aust.*, **53**.
- Rahaman, M.A., van Breeman, O., Bowden, P., and Bennet, J.N., 1984: Age migrations of anorogenic ring complexes in northern Nigeria. *J. Geol.*, **92**: 173-184.
- Rasmussen, E., Neumann, E-R., Andersen, T., Sundvoll, B., Fjerkingstad, V., and Stabel, A., 1988: Petrogenetic processes associated with intermediate and silicic magmatism in the Oslo Rift, southeast Norway. *Min. Mag.*, **52**: 293-307.
- Reid, J.B., Evans, O.C. and Fates, D.C., 1983: Magma mixing in granitic rocks of the central Sierra Nevada California. *Earth Planet. Sci. Lett.*, **66**: 243-261.
- Richard, P., Shimizu, N., and Allegre, C.J., 1976: $^{143}\text{Nd}/^{144}\text{Nd}$, a natural tracer: an application to oceanic basalts. *Earth Planet. Sci. Lett.*, **31**: 269-278.

- Richards, J.R., and Singleton, O.P., 1981: Palaeozoic Victoria, Australia: igneous rocks, ages and their interpretation. *J. Geol. Soc. Aust.*, **28**: 395-421.
- Robert, J.L., 1976: Phlogopite solid solutions in the system K_2O -MgO- Al_2O_3 - SiO_2 - H_2O . *Chem. Geol.*, **17**: 195-212.
- Rochow, K.A., 1971: NARACOORTE, South Australia. Explanatory Notes, 1:250 000 Geological Series. *Geol. Surv. S. Aust.*
- Rudnick, R.L., and Presper, T., 1990: Geochemistry of intermediate/- to high-pressure granulites. In: Vielzuef, D., and Vidal, Ph., (Eds), *Granulites and crustal evolution*. NATO ASI series C 311, Kluwer Academic Publishers, Netherlands pp, 523-550.
- Rushmer, T., 1989: Granulites as residues of partial melting: experimental constraints. *Terra Abstracts*, **1**: 302.
- Ryerson, F.J., and Hess, P.C., 1978: Implications of liquid-liquid distribution coefficients to mineral-liquid partitioning. *Geochim. Cosmochim. Acta.*, **42**: 921-932.
- Sandiford, M., Oliver, R.L., Mills, K.J., and Allen, R.V., 1990: A cordierite-staurolite-muscovite association, east of springton, Mt Lofty Ranges; implications for the metamorphic evolution of the Kanmantoo Group. In: Jago, J.B., and Moore, P.J., (eds), *The evolution of a Late Precambrian - Early Palaeozoic rift complex: The Adelaide Geosyncline*. Geological Society of Australia, Special Publication no. 16 pp. 483-495.
- Sandiford, M., and Powell, R., 1990: Some isostatic and thermal consequences of the vertical strain geometry in convergent orogens. *Earth Planet. Sci. Lett.*, **98**: 154-165.
- Sandiford, M., 1989: Secular trends in the thermal evolution of metamorphic terrains. *Earth Planet. Sci. Lett.*, **95**: 85-96.
- Schilling, J.G., Bergeron, M.B., and Evans, R., 1980: Halogens in the mantle beneath the North Atlantic. *Phil. Trans. R. Soc. Lond.*, **297**: 147-178.
- Shaw, H.R., 1972: Viscosities of magmatic silicate liquids: an empirical method of prediction. *Am. J. Sci.*, **272**: 870-893.
- Shaw, S.E., Flood, and R.H., 1981: The New England Batholith, eastern Australia: geochemical variations in time and space. *J. Geophys. Res.*, **86**: 10530-10544.
- Sparks, R.S.J., 1988: Petrology and geochemistry of the Loch Ba ring-dyke, Mull (N.W. Scotland): an example of the extreme differentiation of tholeiitic magmas. *Contrib. Mineral. Petrol.*, **100**: 446-461.
- Sparks, R.S.J., Huppert, H.E., Kerr, R.C., McKenzie, D.P., and Tait, S.R., 1985: Post cumulus processes in layered intrusions. *Geol. Mag.*, **122**: 555-568.
- Sparks, R.S.J., Sigurdsson, H., and Wilson, L., 1977: Magma mixing: a mechanism for triggering acid explosive eruptions. *Nature*, **267**: 315-318.
- Sparks, R.S.J., Huppert, H.E., and Turner, J.S., 1984: The fluid dynamics of evolving magma chambers. *Phil. Trans. R. Soc. Lond.*, **A310**: 511-534.

- Sparks, R.S.J., and Marshall, L.A., 1986: Thermal and mechanical constraints on mixing between mafic and silicic magmas. *J. Volcanol. Geotherm. Res.*, **29**: 99-124.
- Spear, F.S., and Kimball, C., 1984: RECAMP - a Fortran IV program for estimating the Fe³⁺ contents in amphiboles. *Comput. Geosci.*, **10**: 317-325.
- Stewart, B.W., and DePaolo, D.J., 1990: Isotopic studies of processes in mafic magma chambers: II The Skaergaard Intrusion, East Greenland. *Contrib. Mineral. Petrol.*, **104**: 125-141.
- Stewart, K.P., and Foden, J.D., 1990: The fundamental role of mantle derived magma in the production of a large volume felsic volcanic province, Gawler Ranges, South Australia. *ICOG 7, Geol. Soc. Aust. Abs.*, **27**: 96.
- Stolper, E., 1980: A phase diagram for mid-ocean ridge basalts: preliminary results and implications for petrogenesis. *Contrib. Mineral. Petrol.*, **74**: 13-27.
- Stuwe, K., and Oliver, R., 1989: Geological history of Adelie Land and King George V Land, Antarctica: Evidence for a polycyclic metamorphic evolution. *Precam. Res.*, **43**: 317-334.
- Stuwe, K., and Powell, R., 1989: Low-pressure granulite facies metamorphism in the Larsemann Hills area, East Antarctica; petrology and tectonic implications for the evolution of the Prydz Bay area. *J. Met. Geol.*, **7**: 465-483.
- Sylvester, P.J., 1989: Post-collisional alkaline granites. *J. Geol.* **97**: 261-280.
- Tait, R.E., and Harley, S.L., 1988: Local processes involved in the generation of migmatites within mafic granulites. *Trans. R. Soc. Edin.*, **79**: 209-222.
- Taylor, S.R., 1965: The application of trace element data to problems in petrology. *Phys. Chem. Earth.*, **6**: 133-214.
- Taylor, S.R., and McClelland, S.M., 1985: *The continental crust: its composition and evolution*. Hallam, A. (Ed). Blackwell Scientific Publications, 312pp.
- Thompson, B.P., 1969: The Kanmantoo Group and Early Palaeozoic tectonics. In: Parkin L.W. (Ed), *Handbook of South Australian Geology. Geol. Surv. S. Aust.*, pp 97-108.
- Thompson, R.N., 1983: Thermal aspects of the origin of Hebridean Tertiary acid magmas. II. Experimental melting behaviour of the granites at 1 kbar PH₂O. *Min. Mag.*, **47**: 111-121.
- Thompson, R.N., Morrison, M.A., Dickin, A.P., and Hendry, G.L., 1983: Continental flood basalts...arachnids role OK? In: Hawkesworth, C.J., and Norry, M.J., (Eds), *Continental basalts and mantle xenoliths*. Shiva, Nantwich, pp. 158-185.
- Thompson, R.N., Morrison, M.A., Dickin, A.P., Gibson, I.L., and Harmon, R.S., 1986: Two contrasting styles of interaction between basic magmas and continental crust in the British Tertiary Province. *J. Geophys. Res.*, **91**: 5985-5997.
- Thompson, R.N., and Morrison, M.A., 1988: Asthenospheric and lower-lithospheric mantle contributions to continental extensional magmatism: an example from the British Tertiary Province. *Chem. Geol.*, **68**: 1-15.
- Turcotte, D.L., 1983: Mechanisms of crustal deformation. *J. Geol. Soc. Lond.*, **140**: 701-724.

- Turcotte, D.L., and Schubert, G., 1982: Geodynamics - applications of continuum physics to geological problems. Wiley, New York, p. 450.
- Turner, J.S., and Campbell, I.H., 1986: Convection and mixing in magma chambers. *Earth Sci. Rev.* **23**: 255-352.
- Turner, S.P., 1986: Early Palaeozoic magmatism in western Victoria and eastern South Australia: implications. *Uni. Adelaide Hons. thesis (unpubl.)*.
- Turner, S.P., Foden, J.D., and Cooper, J., 1989: Post-Delamerian magmatism: tectonic controls on magma chemistry and evidence for post-Delamerian extension. *Geol. Soc. Aust. Abst.* **24**: 155-156.
- Turner, S.P., Foden, J.D. 1990a: Post Delamerian magmatism - is lithospheric thinning guilty? *Geol. Soc. Aust. Abst. 10th AGC*, pp. 262-263.
- Turner, S.P., and Foden, J.D., 1990b: The nature of mafic magmatism through the evolution of the Adelaide Foldbelt and subsequent Delamerian Orogeny. *Proceedings Volume, 2nd Int Dyke Conf.*
- Turner, S.P., Adams, C., and Flottmann, T., 1991: Geology, geochemistry and geochronology of the Glenelg River Complex, western Victoria. (*in prep.*).
- Tuttle, O.F., and Bowen, N.L., 1958: Origin of granite in the light of experimental studies in the system $\text{NaAlSi}_3\text{O}_8\text{-KAlSi}_3\text{O}_8\text{-SiO}_2\text{-H}_2\text{O}$. *Geol. Soc. Amer. Mem.*, **74**.
- Upton, B.G., and Emeleus, C.H., 1987: Mid-Proterozoic alkaline magmatism in southern Greenland: the Gardar province. *In*: Fitton, J.G., and Upton, G.J., (Eds), *Alkaline Igneous Rocks*. Blackwell Scientific, Oxford, pp. 449-472.
- Van Der Laan, S.R., Flower, M.F.J., and Van Groos, A.F.K., 1989: Experimental evidence for the origin of boninites: near liquid phase relations to 7.5 kbar. *In*: Crawford, A.J., (Ed), *Boninites and related rocks*. Unwin Hyman, London, pp. 113-145.
- Vernon, R.H., 1984: Microgranitoid enclaves in granites- globules of hybrid magma quenched in a plutonic environment. *Nature*, **309**:438-439.
- Vernon, R.H., 1990: Crystallization and hybridism in microgranitoid enclave magmas: microstructural evidence. *J. Geophys. Res.*, **95**: 17849-17859.
- Vernon, R.H., Etheridge, M.A., and Wall, V.J., 1988: Shape and microstructure of microgranitoid enclaves: indicators of magma mingling and flow. *Lithos*, **22**: 1-11.
- Vielzeuf, D., and Vidal, Ph., 1990: *Granulites and crustal evolution*. NATO ASI series C 311, Kluwer Academic Publishers, Netherlands.
- Vielzeuf, D., Clemens, J.D., Pin, C., and Moinet, E., 1990: Granites, granulites and crustal differentiation. *In*: Vielzeuf, D., and Vidal, Ph., (Eds), *Granulites and crustal evolution*. NATO ASI series C 311, Kluwer Academic Publishers, Netherlands pp 59-85.
- Villari, L., 1974: The island of Pantelleria. *Bull. Volcanol.*, **38**: 680-724.
- Von der Borch, C.C., 1980: Evolution of Late Proterozoic to Early Palaeozoic Adelaide Foldbelt, Australia: comparisons with post-permian margins. *Tectonophysics*, **70**: 115-134.

- Wager, L.R., and Brown, G.M., 1968: *Layered Igneous Rocks*. Edinburgh: Oliver and Boyd.
- Walker, D., Shibata, T., and DeLong, S.F., 1979: Abyssal tholeiites from the Oceanographer Fracture Zone II: Phase equilibrium and mixing. *Contrib. Mineral. Petrol.*, **70**: 111-125.
- Wall, V.J., Clemens, J.D., and Clarke, D.B., 1987: Models for granitoid evolution and source compositions. *J. Geol.*, **95**: 731-749.
- Walsh, J.N., Beckinsale, R.D., Skelhorn, R.R., and Thorpe, R.S., 1979: Geochemistry and petrogenesis of Tertiary granitic rocks from the island of Mull, northwest Scotland. *Contrib. Mineral. Petrol.*, **71**: 99-116.
- Ware, N.G., 1981: Computer programs and calibration with the PIBS technique for quantitative electron probe analysis using a lithium-drifted silicon detector. *Comput. Geosci.*, **7**: 167-184.
- Watson, E.B., 1982: Basalt contamination by continental crust: some experiments and models. *Contrib. Mineral. Petrol.*, **80**: 73-87.
- Watson, E.B. and Harrison, T.M., 1983: Zircon saturation revisited : temperature and composition effects in a variety of crustal magma types. *Earth Planet. Sci Lett.*, **64**: 295-304.
- Watson, E.B. and Harrison, T.M., 1984: Accessory minerals and the geochemical evolution of crustal magmatic systems: a summary and prospectus of experimental approaches. *Phys. Earth Planet. Int.*, **35**: 19-30.
- Weaver, B.L., and Tarney, J., 1980: Continental crust composition and nature of the lower crust: constraints from mantle Nd-Sr isotope correlation. *Nature*, **286**: 342-346.
- Weaver, B.L., and Tarney, J., 1981: Lewisian geochemistry and Archean crustal development models. *Earth Planet. Sci. Lett.*, **55**: 171-180.
- Webb, A.W., 1976: Geochronology of the granitic rocks of south-eastern South Australia. *Amdel Rept. No.* 1138.
- Webb, A.W., Thompson, B.P., Blissett, A.H., Daly, S.J., Flint, R.B., and Parker, A.J., 1986: Geochronology of the Gawler Craton, South Australia. *Aust. J. Earth. Sci.*, **33**: 119-143.
- Wegmann, D., 1980: Pre-Tertiary geology of the Black Hill region in the western Murray Basin of South Australia; with special emphasis on the petrology and geochemistry of the gabbroic rocks. *Univ. Adelaide Hons. Thesis, (unpubl.)*.
- Whalen, J.B., Currie, K.L., and Chappell, B.W., 1987: A-type granites: geochemical characteristics, discrimination and petrogenesis. *Contrib. Mineral. Petrol.*, **95**: 407-419.
- White, A.J.R., and Chappell, B.W., 1977: Ultrametamorphism and granitoid genesis. *Tectonophysics*, **43**: 7-22.
- White, A.J.R., and Chappell, B.W., 1983: Granitoid types and their distribution in the Lachlan Fold Belt, southeastern Australia. *Geol. Soc. Am. Mem.*, **159**: 21-34.

- White, A.J.R., Collins, W.J., and Chappell, B.W., 1982: Influence of melt structure on the trace element composition of granites. *In: Geology of granites and their metallogenetic relations. Proc. Int. Symp., Nanjing Uni. China* pp. 737-751.
- White, A.J.R., Clemens, J.D., Holloway, J.R., Silver, L.T., and Chappell, B.W., 1986: S-type granites and their probable absence in southwestern North America. *Geology*, **14**: 115-118.
- White, R.S., and McKenzie, D.P., 1989: Magmatism at rift zones: the generation of volcanic continental margins and flood basalts. *J. Geophys. Res.*, **94**: 7685-7730.
- White, W., 1985: Source of oceanic basalts: Radiogenic isotopic evidence. *Geol.*, **13**: 115-118.
- Williams, E., 1978: Tasman foldbelt system in Tasmania. *Tectonophysics*, **48**: 159-205.
- Wilson, M., 1989: *Igneous Petrogenesis, a global tectonic approach*. Unwin Hyman, UK, p. 466.
- Wones, D.R., 1972: Stability of biotite: a reply. *Am. Min.*, **57**: 316-317.
- Wones, D.R., and Gilbert, C.M., 1982: Amphiboles in the igneous environment. *In: Veblen, D.R., and Ribbe, P.H., (Eds), Amphiboles: Petrology and experimental phase relations. Min. Soc. Am., Reviews in Mineralogy* 9B, 355-389.
- Woolley, A.R., and Jones, G.C., 1987: The petrochemistry of the northern part of the Chilwa alkaline province, Malawi. *In: Fitton, J.G., and Upton, G.J., (Eds), Alkaline Igneous Rocks. Blackwell Scientific, Oxford*, pp. 335-356.
- Wright, T.L., and Doherty, P.C., 1970: A linear programming and least squares computer method for solving petrologic mixing problems. *Bull. Geol. Soc. Am.*, **81**: 1995-2008.
- Wyborn, D., Chappell, B.W., and Johnston, R.M., 1981: Three S-type volcanic suites from the Lachlan Fold Belt, southeast Australia. *J. Geophys. Res.*, **86**: 10335-10348.
- Wyllie, P.J., 1984: Constraints imposed by experimental petrology on possible and impossible magma sources and products. *Phil. Trans. Roy. Soc. Lond.*, **A310**: 439-456.

Appendix A. Analytical techniques and uncertainties

Electron microprobe analyses

Polished sections were coated with approximately 250 μm of carbon. Multiple analyses of each grain were carried out using a KEVEX 7000 series energy dispersive system (EDS) attached to a JEOL 733 analyser.

Analysis conditions used were 15 KV accelerating voltage and 5 nA electron beam current. Data was corrected on-line using PIBS style software (Ware, 1981). Calibration of the EDS system was carried out using pure copper as a primary standard and olivine and kaersutite as secondary standards.

Fluorine and chlorine analyses were carried out using the JEOL wave length dispersive system (WDS). WDS analysis conditions were 15 KV accelerating voltage and 2 nA electron beam current.

Detection limits are:

Element	Detection limit (wt%)
Na ₂ O	0.0511
MgO	0.0517
Al ₂ O ₃	0.0590
SiO ₂	0.0623
P ₂ O ₅	0.0750
SO ₃	0.1037
Cl	0.0406
Fe ₂ O ₃	0.0072
K ₂ O	0.0565
CaO	0.0737
TiO ₂	0.1191
V ₂ O ₃	0.1216
Cr ₂ O ₃	0.1366
MnO	0.1435
NiO	0.2412
F	0.0479 - 0.0870

Whole rock chemical analysis

Samples were trimmed to remove weathered edges and crushed using a jaw crusher. Crushed samples were then ground in a Siebtechnik tungsten carbide mill. Powders for major element analysis were ignited overnight at 960 °C; for each sample 280 mg of ignited sample, 20 mg of sodium nitrate and 1.5 g of flux were mixed and used to produce a fused button.

SiO₂, Al₂O₃, Fe₂O₃, MnO, MgO, CaO, K₂O, TiO₂ and P₂O₅ concentrations were determined using a programable Siemens SRS XRF calibrated on international standards. Na₂O analyses were performed on 50-60 mg of sample digested and made up to 100 ml. Concentrations were determined by atomic absorption on a Varian Techtron atomic absorption spectrophotometer. In-house standards were run with all samples and the following is given as a guide to the precision of the major element analyses:

Element	+/- %
SiO ₂	0.6 rel.
TiO ₂	1.5 rel. +/- 0.01% abs.
Al ₂ O ₃	1.0 rel.
Fe ₂ O ₃	1.0 rel.
MnO	+/- 0.01% abs.
MgO	1.0 rel +/- 0.10% abs.
CaO	0.5 rel. +/- 0.02% abs.
Na ₂ O	2.2 rel.
K ₂ O	1.5 rel. +/-0.01 abs.
P ₂ O ₅	+/- 0.01% abs.

Trace elements abundances (Sr, Rb, Y, Zr, Nb, Ba, Sc, Ni, V, Ga, La, Ce, Nd, U, Pb, Th, Cr) were determined on a Siemens XRF using pressed pellets produced using approximately 5 g of unignited powder. For trace element analyses, the lower limit of detection (LLD) is used as a measure of the precision of the data. It is defined statistically as that concentration which gives a count-rate equal to three times the standard deviation of the nett count-rate for peak minus background. This means that if an element is present in this amount, then there is a 99.7% probability of it being detected. Obviously, with less stringent statistical criteria the LLD values will be reduced. Because the LLD is dependent on the mass absorption of the individual sample the following LLD's are given

for a typical gabbro (A876-7-510) and a typical granite (A876-15-301) from the thesis work.

Element	LLD (+/- ppm)	
	7-510	15-301
Cr	5.6	5.2
Ni	2.9	2.1
Sc	1.1	0.9
V	2.3	1.6
Pb	2.9	2.3
Rb	1.1	0.9
Sr	1.0	0.8
Ba	3.9	2.7
Ga	2.2	1.7
Nb	1.7	1.4
Zr	2.1	1.7
Y	1.2	1.1
Th	2.5	2.0
U	3.1	2.4
La	4.1	2.8
Ce	8.6	6.2
Nd	5.0	3.7

Fluorine abundances were determined by specific ion electrode analysis. This involved fusing 1.0 g of unignited sample with 8.0 g of Na₂CO₃ in a platinum crucible. The contents were then digested in 1.5 M HCl and 5 ml aliquots mixed with 50 ml of TISAB (Total Ionic Strength Adjustment Buffer). F⁻ concentrations were determined on these solutions by standard addition technique. The detection limit is 100 ppm and the error range ± 50 ppm.

Rare earth element analysis

Selected samples were analysed for the rare earth elements (REE) La, Ce, Nd, Sm, Eu, Gd, Dy, Er and Yb. 500 mg of sample was spiked with a multi element spike and dissolved for several days in a teflon bomb using HF and HCl₄O. The REE were separated following the cation exchange column techniques of Crock *et al.* (1984), firstly on a HNO₃ based column and then on a HCl based column. The samples were run, at The University of Adelaide Department of Geology and Geophysics, on a Thompson thermal ion solid source mass spectrometer. The mass spectrometry methods are described in:

Nesbitt, R.W., and Stanley, J., (Eds), Compilation of analytical geochemistry reports 1973-1979, Research Report #3, 1980. The Department of Geology and Geophysics, University of Adelaide.

In-run ratio variance was less than 0.2% and the following results were obtained for BCR-1:

La	25.29
Ce	54.33
Nd	27.82
Sm	6.25
Eu	1.90
Gd	6.45
Dy	6.07
Er	3.48
Yb	3.25

Rb-Sr and Nd-Sm isotope analysis

The same samples run for rare earths were also analysed for their Nd and Sr isotopic compositions. Approximately 100 mg of unspiked sample was digested for several days in a teflon bomb using HF and then converted to a chloride using 3 N HCl. Sr and Nd were then separated from the sample solution using a two stage cation exchange column procedure essentially the same as that described by Richard *et al.* (1976). The resulting Sr and Nd samples were loaded onto single tantalum and double rhenium filaments (respectively) and analysed for their isotopic compositions, at the University of Adelaide Department of Geology and Geophysics, on a Finnigan Mat 261 thermal ion, solid source, mass spectrometer. Data blocks of 10 scans each were run until acceptable in run statistics were achieved (8-16 blocks for Sr using a double collector, and 15-35 blocks for Nd using a single collector). The following results were obtained for duplicate samples and standards where (n) indicates the number of analyses (errors quoted are 2 standard errors of the mean of in-run statistics):

	143Nd/144Nd (measured) error	87Sr/86Sr (measured) error
La Jolla	0.511838 ± 0.000021 (3)	
E & A		0.708001 ± 0.000037 (1)
NBS SRM 987		0.710234 ± 0.000025 (10)
BHVO-1	0.512968 ± 0.000035 (2)	0.703426 ± 0.000027 (2)
BCR-1	0.512507 ± 0.000024 (1)	0.704679 ± 0.000044 (2)
A779-60	0.512363 ± 0.000025	
Duplicate	0.512361 ± 0.000024	
BHN-II		0.711419 ± 0.000039
Duplicate		0.711422 ± 0.000019

Average procedural blanks during the course of isotope analysis were as follows:

Rb	0.5 ng
Sr	1.1 ng
Nd	0.09 ng
Sm	0.06 ng

$^{147}\text{Sm}/^{143}\text{Nd}$ was calculated using the concentrations obtained from the rare earth analyses. $^{87}\text{Rb}/^{86}\text{Sr}$ was calculated from accurate Rb and Sr analyses obtained from an extended XRF routine.

Constants used in isotope work are:

$$^{87}\text{Rb}/^{85}\text{Rb} = 0.38571$$

$$^{88}\text{Sr}/^{86}\text{Sr} = 8.3752$$

$$\lambda_{\text{Rb}} = 1.42 \times 10^{-11} \text{y}^{-1}$$

$$\text{Bulk Earth } ^{87}\text{Rb}/^{86}\text{Sr} = 0.0827$$

$$\text{Bulk Earth } ^{87}\text{Sr}/^{86}\text{Sr} = 0.7045$$

$$\text{Bulk Earth } ^{147}\text{Sm}/^{143}\text{Nd} = 0.1967$$

$$\text{Depleted mantle } ^{147}\text{Sm}/^{143}\text{Nd} = 0.2157$$

$$\lambda_{\text{Sm}} = 6.54 \times 10^{-12} \text{y}^{-1}$$

$$\text{Bulk earth } ^{143}\text{Nd}/^{144}\text{Nd} = 0.512638$$

$$\text{Depleted mantle } ^{143}\text{Nd}/^{144}\text{Nd} = 0.513108$$

$$\text{Nd isotopic compositions normalized to } ^{146}\text{Nd}/^{144}\text{Nd} = 0.721903$$

Average error in $\epsilon\text{Nd} \pm 0.5$, error in Nd model age < 40Ma.

Appendix B. Complete listing of analyses of Black Hill gabbros

Sample #	876-5-727	876-5-742	876-19-467	876-5-575	876-5-756	876-5-719	876-5-473	876-5-572
Rock Type	peridotite	peridotite	ol-cumulate	ol-gabbro	troctolite	troctolite	troctolite	troctolite
SiO2	36.68	40.51	41.03	42.95	43.76	44.22	44.46	44.77
TiO2	0.78	0.43	0.26	0.17	0.14	0.16	0.18	0.21
Al2O3	4.37	7.29	8.25	17.32	18.99	18.56	19.28	20.55
Fe2O3*	16.06	13.33	14.40	9.52	7.25	7.37	7.44	7.39
MnO	0.23	0.20	0.19	0.13	0.11	0.10	0.11	0.10
MgO	31.60	29.35	23.75	16.93	15.98	15.98	14.36	12.62
CaO	3.03	4.38	4.21	9.23	9.34	9.42	10.28	10.88
Na2O	0.49	0.93	0.4	1.31	1.68	1.69	1.69	1.81
K2O	0.08	0.16	0.20	0.09	0.06	0.06	0.08	0.11
P2O5	0.04	0.10	0.07	0.02	0.02	0.02	0.03	0.03
LOI	4.87	2.84	6.39	1.30	1.70	1.81	1.73	0.10
Total	98.23	99.52	99.15	98.97	99.03	99.39	99.64	98.57
Mg#	79.69	81.44	76.68	78.00	81.46	81.21	79.37	77.30
Cr	8487	1738	526	115	510	369	717	132
Ni	1249	1176	876	609	635	627	493	527
Sc	16	12.5	15	9.5	8.1	10.2	11.3	10
V	179	80	41	27	25	28	36	33
Pb	1	4	1	12	nd	1	1	nd
Rb	2	5.9	7.9	2.3	1.8	1.4	1.4	3
Sr	57	90	67	347	288	283	312	367
Ba	16	26	28	44	23	22	34	47
Ga	6	6	6	12	11	12	11	13
Nb	2.6	2.9	2.3	0.9	0.5	0.9	0.8	1
Zr	48	58	32	11.6	11.1	9.6	10	8
Y	10.9	9.3	5.8	1.6	2.1	2.6	2.1	4
Th	1.5	0.6	1.3	0.9	nd	0.9	1.2	1.6
U	1.2	nd	nd	0.5	2.4	0.6	1	1.8
La	8	4	3	3	nd	1	1	3
Ce	16	18	23	24	4	9	7	3
Nd	16	4	7	3	nd	1	1	3

Sample #	876-5-760	876-2-856	876-5-395	876-5-544	876-3-834	876-3-851	876-2-830	876-2-823
Rock Type	aug-troctolite	ol-pyroxenite	ol-gabbro	troctolite	troctolite	troctolite	troctolite	pyroxenite
SiO2	44.80	45.31	45.49	45.49	46.48	46.51	47.38	48.26
TiO2	0.15	0.20	0.22	0.29	0.48	0.54	0.35	0.36
Al2O3	18.55	19.47	20.02	22.35	19.22	17.38	18.16	20.76
Fe2O3*	7.61	8.25	7.11	6.59	8.55	9.54	8.14	7.10
MnO	0.11	0.11	0.11	0.09	0.12	0.15	0.11	0.11
MgO	17.00	11.00	12.42	9.84	10.62	12.76	10.82	8.17
CaO	9.23	9.72	11.35	10.65	9.80	9.58	10.35	10.70
Na2O	1.82	2.15	1.75	2.22	2.32	2.07	2.31	2.47
K2O	0.08	0.33	0.10	0.16	0.31	0.25	0.31	0.40
P2O5	0.02	0.04	0.04	0.04	0.07	0.07	0.07	0.06
LOI	0.10	1.00	0.10	1.78	1.32	0.71	0.60	1.09
Total	99.43	97.58	98.71	99.50	99.29	99.56	98.60	99.48
Mg#	81.66	72.66	77.69	74.85	71.23	72.73	72.60	69.64
Cr	727	123	194	11	336	257	51	248
Ni	769	nd	426	291	463	300	481	330
Sc	8	14	15	7.3	15	19	22	15
V	1	41	44	41	89	90	67	64
Pb	nd	8	1	2	3	1	5	2
Rb	3	13	3	4.6	9.1	6.8	10	10.5
Sr	282	356	362	411	319	295	332	402
Ba	24	79	33	49	66	67	78	109
Ga	10	15	14	15	14	14	6	16
Nb	1	0.5	1	1.8	2.9	3	3	2.9
Zr	8	23	11	26	36	33	31	35
Y	3	4	4	3.4	9.9	10	7	8.2
Th	nd	0.2	2.2	nd	1.6	nd	1.7	nd
U	1.2	1.3	2	2	4	3.4	0.5	1.3
La	4	6	4	2	9	7	9	8
Ce	3.5	9	3	10	15	21	10	26
Nd	3	3	3	1	12	14	3	9

Sample #	876-19-824	876-5-451	876-18-426	876-2-620	876-5-429	876-7-707	876-3-801	876-6-440
Rock Type	pyroxenite	pyroxenite	f.g. gabbro	gabbronorite	coarse zone	coarse zone	gabbronorite	gabbronorite
SiO ₂	49.48	49.60	41.98	46.08	46.69	46.93	47.60	47.75
TiO ₂	0.86	0.84	1.66	0.25	0.58	2.31	0.63	2.00
Al ₂ O ₃	6.86	12.23	18.66	19.63	15.40	14.19	17.09	15.99
Fe ₂ O ₃ *	13.26	6.18	14.70	6.88	8.29	15.78	7.59	11.54
MnO	0.23	0.14	0.20	0.13	0.14	0.19	0.14	0.22
MgO	14.08	10.58	7.29	9.54	13.90	6.44	9.05	6.52
CaO	11.83	15.09	12.78	10.08	12.07	10.05	11.47	9.06
Na ₂ O	1.21	1.72	1.20	2.54	1.62	2.72	2.19	3.65
K ₂ O	0.44	0.50	0.29	0.46	0.13	0.60	0.75	0.90
P ₂ O ₅	0.09	0.15	0.10	0.03	0.04	0.12	0.06	0.52
LOI	0.87	2.19	1.00	3.61	1.42	0.30	1.67	0.55
Total	99.21	99.22	99.86	99.23	100.28	99.63	98.24	98.70
Mg#	67.92	77.34	49.71	73.43	76.97	44.86	70.39	52.97
Cr	575	1332	31	198	397	32	996	156
Ni	322	137	14	233	455	161	170	93
Sc	41	74	36	13	34	44	35	31
V	192	58	446	45	125	548	149	248
Pb	2	4	3	5	2	5	5	4
Rb	17	20	7	19	2.2	18.3	47	17
Sr	103	199	672	323	250	272	302	400
Ba	101	69	66	63	54	149	90	290
Ga	10	11	22	14	12	21	15	20
Nb	6.3	4.1	2	2.8	2.3	6.8	2.6	24
Zr	77	76	26	28	42	84	50	314
Y	30	30	7	5	15.4	27	15.8	51
Th	2.2	2	0.5	1.1	1.4	3	0.9	3.6
U	0.7	0.8	3.1	0.2	0.5	1.7	1	4.2
La	15	9	8	8	8	13	4	46
Ce	48	25	15	17	26	41	26	85
Nd	18	15	6	9	10	21	10	46

Sample #	876-6-441	876-5-501	876-2-590	876-6-377	876-11-875	876-2-451	876-19-768	876-9-364
Rock Type	gabbronorite	coarse zone	gabbronorite	gabbronorite	hb-bt-gabbro	gabbronorite	gabbronorite	sheared gabbro
SiO2	48.46	48.54	48.55	48.57	48.83	48.89	49.56	49.62
TiO2	1.86	0.88	0.38	1.87	0.44	0.44	0.94	2.79
Al2O3	16.42	13.79	19.00	16.22	19.17	18.54	15.33	14.98
Fe2O3*	11.35	5.83	6.74	11.43	7.26	6.74	8.99	12.57
MnO	0.18	0.13	0.12	0.21	0.13	0.12	0.15	0.22
MgO	6.76	9.46	8.56	6.19	9.17	8.89	8.95	4.06
CaO	9.31	16.45	11.24	8.98	9.44	11.41	10.77	7.77
Na2O	3.57	1.78	2.24	3.63	2.71	2.59	2.84	4.20
K2O	0.83	0.24	1.11	1.10	0.73	0.28	0.54	1.34
P2O5	0.45	0.10	0.05	0.42	0.08	0.07	0.14	1.41
LOI	0.30	1.50	1.29	0.40	1.00	0.30	0.50	1.00
Total	99.49	98.70	99.28	99.02	98.96	98.27	98.71	99.96
Mg#	54.28	76.39	71.69	51.91	71.57	72.45	66.50	39.17
Cr	189	682	379	157	174	517	344	7
Ni	21	153	207	71	240	293	218	10
Sc	33	58	26	32	15	34	38	32
V	248	194	83	246	67	100	185	220
Pb	3	5	5	4	3	7	5	6
Rb	13.9	6.6	74	28	26	4	17	36
Sr	404	254	350	396	330	318	254	427
Ba	274	108	97	292	105	76	113	368
Ga	21	13	15	22	16	15	15	23
Nb	18.5	3.7	3.3	17.6	5	4	7	28
Zr	280	67	30	282	47	40	82	327
Y	46	19.2	11.2	50	11	13	23	78
Th	5.5	4.4	1.3	2.7	3.6	2.2	4.4	3.4
U	1.4	nd	nd	3.3	2.2	1.1	2	3.5
La	41	6	8	41	14	13	13	89
Ce	94	17	27	83	17	18	26	152
Nd	42	11	16	40	9	6	15	82

Sample #	876-7-510	876-19-536	876-19-1031	876-7-554	876-19-900	876-5-629	876-7-634	876-7-569
Rock Type	gabbronorite	gabbronorite	gabbronorite	gabbronorite	gabbronorite	f.g. gabbro	gabbronorite	gabbronorite
SiO2	49.91	50.25	50.26	50.45	50.54	50.68	50.93	51.04
TiO2	0.94	0.70	1.01	0.96	0.88	1.59	0.30	1.09
Al2O3	16.14	16.94	16.46	17.30	16.17	15.60	15.66	17.07
Fe2O3*	10.25	7.74	8.47	9.28	5.00	11.07	10.14	10.37
MnO	0.17	0.13	0.15	0.15	0.14	0.19	0.16	0.18
MgO	8.40	8.69	7.74	7.33	8.66	6.60	6.84	7.31
CaO	9.34	11.02	11.34	9.47	10.23	9.01	10.15	9.02
Na2O	2.88	2.82	2.79	2.87	2.90	2.97	2.92	3.05
K2O	0.65	0.43	0.45	0.52	0.67	1.19	0.70	0.62
P2O5	0.14	0.07	0.13	0.14	0.12	0.24	0.16	0.14
LOI	0.44	0.30	0.59	0.40	0.20	0.33	0.55	0.11
Total	99.26	99.09	99.38	98.87	95.51	99.47	98.51	100.00
Mg#	62.03	69.12	64.56	61.16	77.54	54.31	57.35	58.42
Cr	136	243	701	36	398	176	227	52
Ni	151	149	96	109	163	78	81	126
Sc	29	36	40	30	34	36	42	26
V	163	160	191	162	176	291	250	184
Pb	3	nd	1	4	11	6	2	3
Rb	19.9	10	14.5	12	26	38	22	19.4
Sr	337	282	262	350	270	290	306	351
Ba	169	94	108	149	122	265	159	172
Ga	17	14	17	18	17	20	17	18
Nb	8.3	4	5.6	8	7	13.2	9	6.5
Zr	115	69	96	65	49	169	108	71
Y	24.4	18	24	19	22	39	29	20.7
Th	4	nd	1.5	3.2	3.9	3.5	2.2	3.6
U	2	1.7	0.3	1.9	1.1	1.7	2.8	1.8
La	14	13	9	16	15	22	17	14
Ce	39	18	44	29	25	53	34	31
Nd	18	5	20	12	10	26	17	12

Sample #	876-19-1310	876-19-801	876-19-1233	876-11-938	876-19-1278	876-12-391	876-10-550	876-7-743
Rock Type	gabbronorite	qz-gabbronorite	gabbronorite	diorite	gabbronorite	diorite	diorite	hb-bt-gabbro
SiO2	51.31	51.78	52.08	52.73	52.76	52.83	53.62	53.97
TiO2	0.55	0.72	0.61	0.79	1.07	1.20	2.01	1.57
Al2O3	17.29	17.34	17.44	16.22	14.91	17.69	15.26	15.10
Fe2O3*	6.91	7.38	6.41	6.72	9.13	8.31	9.68	10.29
MnO	0.13	0.13	0.11	0.14	0.17	0.15	0.20	0.16
MgO	8.52	8.59	7.39	8.27	8.77	4.45	3.49	5.21
CaO	10.47	9.35	10.76	8.10	8.73	7.66	5.37	7.35
Na2O	2.70	2.66	2.93	2.69	2.57	4.00	4.50	4.02
K2O	0.52	0.57	0.49	1.15	0.79	1.56	2.36	0.41
P2O5	0.07	0.12	0.06	0.09	0.13	0.37	0.66	0.27
LOI	1.36	0.63	0.50	2.31	0.85	0.59	1.40	0.75
Total	99.83	99.27	98.78	99.21	99.88	98.81	98.75	99.10
Mg#	71.08	69.88	69.68	71.04	65.69	51.63	41.82	50.23
Cr	329	184	339	306	296	44	5	55
Ni	144	65	95	136	163	41	12	77
Sc	32	27	34	29	34	22	24	30
V	107	119	124	120	176	182	189	249
Pb	4	6	4	3	2	5	6	8
Rb	18.1	19.7	15	53	30	41	104	52
Sr	294	303	301	253	253	1190	375	302
Ba	97	114	98	161	153	592	484	302
Ga	15	15	16	15	18	22	23	19
Nb	4.1	6.1	5	9.2	8.9	18.1	53	23
Zr	53	82	56	115	129	154	455	224
Y	14.8	16.5	13	22	24	25	67	51
Th	3	5.9	3.6	7	4.4	2.9	12	9.4
U	0.7	1.1	1	3.5	3	1.9	4.4	1.8
La	11	12	11	18	17	27	60	33
Ce	27	32	18	47	48	61	100	75
Nd	10	13	8	18	16	36	48	41

Sample #	876-7-676	876-4-225	876-18-677	876-11-750	876-5-590	876-5-417	876-5-482	876-5-514
Rock Type	gabbro	diorite	diorite	diorite	ol-gabbro	ol-gabbro	ol-gabbro	ol-gabbro
SiO2	54.94	56.17	56.97	60.52	43.45	44.05	44.46	46.02
TiO2	2.48	1.42	0.70	0.64	0.16	0.27	0.11	0.41
Al2O3	15.12	17.66	16.20	15.19	18.56	13.56	19.69	17.47
Fe2O3*	10.63	2.96	6.21	5.58	9.91	11.10	7.49	8.22
MnO	0.23	0.03	0.11	0.09	0.14	0.16	0.11	0.13
MgO	3.19	5.18	4.43	4.45	15.43	20.13	14.01	12.71
CaO	6.89	9.06	8.23	6.11	9.95	8.60	10.25	11.57
Na2O	3.74	5.23	3.52	3.81	1.34	1.21	1.62	1.80
K2O	1.19	0.34	1.93	1.14	0.10	0.07	0.10	0.12
P2O5	0.52	0.56	0.13	0.11	0.02	0.04	0.02	0.07
LOI	0.57	0.58	1.07	1.67	0.79	1.23	1.62	1.00
Total	99.50	99.19	99.50	99.31	99.85	100.42	99.48	99.52
Mg#	37.43	77.72	58.71	61.39	75.63	78.33	78.85	75.50
Cr	5	25	31	251	196	131	204	396
Ni	16	16	13	66	484	674	474	347
Sc	33	40	20	19	8.4	16.6	9.7	21
V	217	203	159	97	27	192	23	67
Pb	6	6	9	3	2	2	5	1
Rb	58	14.2	189	45	1.5	1.3	2.3	1.7
Sr	273	688	419	236	339	227	351	311
Ba	130	82	315	245	63	26	28	49
Ga	23	21	25	18	11	10	12	14
Nb	34	21	25	21	nd	1.6	0.4	2.5
Zr	233	297	88	168	8.7	15.3	6.3	33
Y	72	40	19.4	51	0.5	4.3	0.8	7.8
Th	9.5	31	9.8	17	1	1.7	0.3	1.6
U	4	6	4	6.7	1.4	0.2	nd	2.7
La	43	41	32	30	6	1	3	4
Ce	96	90	50	64	25	10	16	12
Nd	40	52	12	27	8	1	5	2

Sample #	876-19-495	876-5-738	876-3-726	876-19-714	876-3-750	876-2-543	876-2-648	876-2-732
Rock Type	ol-gabbro	ol-gabbro	ol-gabbro	ol-gabbro	ol-gabbro	ol-gabbro	ol-gabbro	ol-gabbro
SiO ₂	46.84	47.08	47.95	48.36	48.48	48.88	48.94	49.05
TiO ₂	0.62	0.13	0.64	0.70	0.58	0.32	0.33	0.42
Al ₂ O ₃	16.74	28.04	16.88	16.35	18.85	20.52	19.58	20.20
Fe ₂ O ₃ *	9.45	2.69	8.27	9.25	7.09	6.66	6.32	6.75
MnO	0.15	0.04	0.14	0.16	0.10	0.11	0.11	0.12
MgO	13.24	4.25	10.25	10.49	8.87	7.88	8.18	8.73
CaO	8.66	13.21	10.55	9.39	10.79	11.20	11.47	11.35
Na ₂ O	2.41	2.53	2.22	2.69	2.93	2.67	2.56	2.31
K ₂ O	0.29	0.12	0.83	0.44	0.29	0.51	0.27	0.34
P ₂ O ₅	0.07	0.01	0.07	0.09	0.07	0.07	0.04	0.06
LOI	1.10	1.54	1.64	0.50	0.30	0.70	0.86	0.70
Total	99.57	99.64	99.37	98.42	98.35	99.52	98.66	100.03
Mg#	73.64	75.90	71.19	69.33	71.38	70.23	72.07	72.05
Cr	150	484	195	453	179	414	354	348
Ni	336	156	161	203	135	138	185	186
Sc	20	5.7	32	27	25	23	23	20
V	105	22	133	130	102	66	67	74
Pb	nd	3	3	2	nd	4	2	3
Rb	7.2	3.1	47	113	9	15	8.4	10.7
Sr	272	440	318	274	362	354	355	361
Ba	66	33	87	94	77	95	71	99
Ga	14	16	16	16	13	14	15	17
Nb	3.8	0.4	2.8	6	4	2	2.8	4.1
Zr	59	10.4	29	71	229	29	41	44
Y	14.2	1	10.7	16	8	9	8	10.4
Th	1.4	2.5	1.9	1.3	nd	4.7	0.2	3.7
U	1.1	0.8	2.1	2.7	1	2.1	1.1	1.4
La	4	1	5	9	7	13	5	9
Ce	35	8	15	24	14	14	31	27
Nd	12	5	11	10	4	3	14	10

Sample #	876-11-1081	876-2-790	876-19-458	876-BHG-1	876-BHN-2	876-4-894	876-4-926	876-4-807
Rock Type	ol-gabbro	ol-gabbro	ol-gabbro	K-gabbronorite	K-gabbronorite	anorthosite	anorthosite	px-monzonite
SiO2	49.09	49.47	49.81	47.30	52.26	52.38	52.98	53.83
TiO2	0.84	0.39	0.63	1.20	1.29	1.19	1.08	1.43
Al2O3	16.41	19.90	17.74	15.64	16.77	19.58	20.51	17.36
Fe2O3*	9.45	5.70	8.97	10.81	10.10	7.38	7.34	9.40
MnO	0.15	0.10	0.14	0.18	0.17	0.12	0.12	0.16
MgO	10.42	7.69	11.09	6.14	4.55	2.19	2.17	3.66
CaO	8.99	12.74	8.65	10.15	8.69	7.87	8.46	7.31
Na2O	2.75	2.38	2.62	2.18	2.60	3.03	3.22	2.96
K2O	0.53	0.28	0.59	1.37	2.51	3.52	3.04	3.47
P2O5	0.09	0.04	0.05	0.34	0.43	0.48	0.49	0.67
LOI	0.72	1.07	0.15	4.07	0.00	0.40	0.12	-0.15
Total	99.44	99.76	100.44	99.38	99.39	98.14	99.53	100.10
Mg#	68.73	72.90	71.14	53.10	48.49	37.17	37.08	43.70
Cr	194	458	193	103	117	17	11	25
Ni	228	143	249	41	37	23	12	15
Sc	24	28	19	30	28	19	15.8	21
V	145	82	100	328	143	146	108	192
Pb	1	2	2	6	23	19	16	16
Rb	17.3	7	19	75	148	221	182	219
Sr	273	380	294	596	564	621	676	547
Ba	104	86	107	338	635	798	558	1059
Ga	15	15	14	19	23	23	23	22
Nb	6	2.9	7	5.9	10	17	12.4	15.2
Zr	84	34	57	81	127	218	279	208
Y	17.9	11	20	22	24	24	23.5	33
Th	3.2	1.6	3	8.6	13	22	21	24
U	2.3	1.2	2.3	4.1	5.9	8.7	5.7	5.3
La	10	8	9	23	32	43	33	45
Ce	25	27	23	55	69	79	72	107
Nd	12	6	11	25	34	34	36	47

Sample #	876-4-991	876-4-1044	876-4-879	876-4-428	876-4-348	876-4-201	876-4-265	876-4-565
Rock Type	anorthosite	anorthosite	anorthosite	px-monzonite	px-monzonite	px-monzonite	px-monzonite	px-monzonite
SiO2	53.90	54.01	54.33	54.81	54.87	54.92	54.98	55.02
TiO2	0.75	0.92	0.92	1.37	1.34	1.29	1.39	1.32
Al2O3	22.01	20.79	20.86	16.79	16.63	17.28	16.64	17.12
Fe2O3*	5.43	6.52	6.02	8.88	8.90	8.66	8.16	8.45
MnO	0.08	0.11	0.09	0.13	0.16	0.15	0.12	0.13
MgO	2.26	1.90	1.89	2.89	2.95	3.01	3.25	2.65
CaO	8.60	8.55	8.01	6.44	6.35	7.06	7.42	6.43
Na2O	3.01	3.16	3.39	2.90	2.87	3.07	3.54	3.08
K2O	3.24	2.58	3.30	4.23	4.13	3.90	3.16	4.07
P2O5	0.47	0.49	0.27	0.55	0.55	0.56	0.60	0.53
LOI	0.35	0.20	0.30	0.20	0.28	0.26	0.53	0.20
Total	100.10	99.23	99.38	99.19	99.03	100.16	99.79	99.00
Mg#	45.35	36.75	38.49	39.35	39.79	40.93	44.26	38.47
Cr	11	16	12	27	20	21	26	22
Ni	12	17	6	23	13	12	12	22
Sc	11	15	14.2	21	22	23	27	20
V	107	179	219	179	182	184	129	173
Pb	17	19	18	18	18	19	11	20
Rb	207	195	211	253	273	238	180	252
Sr	784	679	734	494	484	535	545	493
Ba	395	247	843	813	861	982	707	828
Ga	25	26	24	20	20	22	20	22
Nb	10.8	17	11.1	21	17.7	14.5	16.7	20
Zr	77	172	70	158	194	170	136	192
Y	19.2	24	17.3	27	34	31	33	36
Th	22	39	28	26	26	22	21	28
U	6.3	11	7.1	6	6.3	9.1	6.4	6.1
La	34	44	27	52	51	39	46	53
Ce	77	88	57	98	98	87	97	96
Nd	33	41	23	45	48	40	47	44

Sample #	876-4-387	876-4-180	876-4-340	876-4-634	876-4-726	876-19-877	876-19-835	876-11-716
Rock Type	px-monzonite	px-monzonite	px-monzonite	px-monzonite	px-monzonite	norite	norite	norite
SiO2	55.17	55.39	55.50	56.09	56.41	48.69	50.20	50.58
TiO2	1.37	1.28	1.28	1.20	1.22	1.19	0.76	0.95
Al2O3	17.25	17.47	16.60	17.53	17.06	15.38	6.18	15.46
Fe2O3*	8.75	8.45	8.05	7.86	8.12	11.04	12.33	8.87
MnO	0.15	0.14	0.13	0.13	0.13	0.16	0.21	0.16
MgO	3.03	2.83	2.87	2.94	2.40	8.60	14.61	8.66
CaO	6.60	6.73	6.92	6.27	6.08	10.85	10.14	9.78
Na2O	2.99	2.99	3.47	3.02	3.15	2.54	1.19	3.04
K2O	3.99	3.71	3.34	4.29	4.44	0.28	0.57	0.52
P2O5	0.54	0.51	0.55	0.51	0.52	0.05	0.11	0.15
LOI	-0.19	-0.11	0.41	0.08	0.20	0.73	1.20	0.40
Total	99.65	99.39	99.12	99.92	99.73	99.51	97.50	98.57
Mg#	40.84	40.04	41.55	42.72	37.08	60.83	70.26	66.06
Cr	26	25	25	20	20	277	789	457
Ni	14	12	16	11	20	117	631	105
Sc	20	19	23	18	19	43	40	38
V	175	167	178	149	147	297	169	184
Pb	15	19	14	19	19	3	7	1
Rb	252	252	209	274	298	6.2	24	12
Sr	497	501	527	504	477	271	91	264
Ba	798	793	672	851	837	77	116	112
Ga	20	21	19	22	20	17	7	16
Nb	20	18	17.5	17.2	20	3.8	10	7
Zr	212	273	235	181	231	48	79	93
Y	33	32	34	30	28	22	23	21
Th	24	31	27	22	29	3.5	4.2	1
U	5.4	8.1	7.8	6.1	8.5	1.9	1.9	0.6
La	50	42	48	48	53	6	16	15
Ce	107	100	105	103	94	34	22	30
Nd	48	46	48	42	48	16	6	15

Sample #	876-11-1064	876-11-687	876-19-1411	876-19-1366	876-11-910	876-19-635	876-19-1349	876-11-903
Rock Type	bt-norite	qz-norite	norite	bt-norite	norite	norite	qz-norite	norite
SiO2	50.87	51.50	51.74	51.91	52.23	52.28	52.62	52.65
TiO2	0.74	1.07	0.69	0.66	0.61	0.67	0.73	0.74
Al2O3	14.80	15.39	16.09	14.19	6.79	15.50	15.73	16.42
Fe2O3*	8.94	9.16	7.23	9.12	13.79	7.73	7.79	7.17
MnO	0.16	0.17	0.15	0.17	0.25	0.16	0.14	0.16
MgO	11.75	8.56	8.70	11.04	19.04	9.25	8.60	9.08
CaO	7.78	9.60	10.90	8.41	4.12	10.44	9.16	7.31
Na2O	2.50	2.87	2.62	2.65	1.18	2.47	2.65	3.01
K2O	0.53	0.55	0.44	0.46	0.53	0.45	0.67	1.00
P2O5	0.10	0.14	0.07	0.07	0.11	0.08	0.11	0.21
LOI	0.30	0.62	1.26	0.20	0.20	0.20	1.48	1.45
Total	98.47	99.63	99.89	98.88	98.85	99.23	99.68	99.20
Mg#	72.38	65.07	70.58	70.70	73.35	70.46	68.76	71.63
Cr	580	403	345	318	647	280	237	275
Ni	238	98	120	184	638	107	197	184
Sc	29	40	40	35	33	40	33	25
V	136	198	143	135	125	148	131	119
Pb	3	1	7	5	7	2	3	3
Rb	20	18.4	13.9	13	21	14.7	25	39
Sr	243	273	284	254	96	266	266	278
Ba	109	111	98	100	101	105	131	154
Ga	15	18	17	14	9	16	16	15
Nb	7	6.9	3.6	5	7	5.6	6.8	8.8
Zr	73	96	60	49	74	64	73	124
Y	18	26	18.6	15	17	18.5	17.8	22.4
Th	4.6	1.6	3.5	0.8	2.7	3.1	3.5	5
U	1.3	4.1	0.6	3.1	0.7	0.9	1.3	2.4
La	14	10	8	11	11	14	11	14
Ce	17	32	35	16	22	28	32	38
Nd	13	17	12	6	3	15	10	14

Sample #	876-11-1027	876-11-997	876-11-963	876-11-941
Rock Type	bt-norite	norite	norite	norite
SiO2	52.82	53.15	53.20	54.96
TiO2	0.74	0.59	0.67	1.13
Al2O3	9.78	16.99	7.00	10.91
Fe2O3*	10.98	7.37	11.81	10.26
MnO	0.20	0.16	0.23	0.18
MgO	15.44	9.22	18.08	10.67
CaO	6.13	7.90	5.36	4.57
Na2O	1.86	2.78	1.31	2.57
K2O	0.56	0.65	0.60	1.29
P2O5	0.09	0.08	0.09	0.28
LOI	0.20	1.17	0.35	2.25
Total	98.80	100.06	98.70	99.07
Mg#	73.71	71.38	75.32	67.46
Cr	968	240	701	336
Ni	331	162	360	246
Sc	36	24	38	28
V	153	108	158	137
Pb	1	5	3	6
Rb	23	24.3	22	59
Sr	164	295	95	202
Ba	115	127	104	194
Ga	12	16	11	16
Nb	6	5	7	15
Zr	70	70	84	165
Y	16	15.6	21	34
Th	3.4	4.9	2.8	7.3
U	3.8	1.8	2.6	2.4
La	13	9	14	22
Ce	23	24	19	48
Nd	18	10	15	24

**Appendix C. Complete listing of analyses of
granites and granophyres from Black Hill**

Sample	9-364	19-1310	3-513	11-938	12-391	10-550	15-597	3-661	7-637	11-954	19-919
Rock Type	diorite	diorite	gneiss	diorite	diorite	diorite	tonalite	tonalite	tonalite	granodiorite	granodiorite
SiO ₂	49.62	51.31	51.88	52.73	52.83	53.62	57.53	57.58	57.83	59.34	62.73
TiO ₂	2.79	0.55	1.33	0.79	1.20	2.01	0.69	1.55	1.71	1.63	1.35
Al ₂ O ₃	14.98	15.29	15.79	16.22	17.69	15.26	13.45	13.69	14.47	14.82	14.56
Fe ₂ O ₃ *	12.57	6.91	9.71	6.72	8.31	9.68	6.71	9.67	10.41	8.31	7.12
MnO	0.22	0.13	0.16	0.14	0.15	0.20	0.23	0.20	0.16	0.16	0.15
MgO	4.06	8.52	6.38	8.27	4.45	3.49	6.33	4.36	3.19	2.16	1.97
CaO	7.77	10.47	8.91	8.10	7.66	5.37	6.60	6.39	5.89	4.88	4.14
Na ₂ O	4.20	2.70	3.30	2.69	4.00	4.50	3.41	3.98	3.86	4.13	3.90
K ₂ O	1.34	0.52	1.11	1.15	1.56	2.36	1.92	1.24	1.35	2.42	2.89
P ₂ O ₅	1.41	0.07	0.18	0.09	0.37	0.66	0.28	0.21	0.34	0.44	0.35
LOI	1.00	1.36	0.44	2.31	0.59	1.40	1.44	0.49	0.25	0.86	0.25
Total	99.96	99.83	99.19	99.21	98.81	98.55	98.59	99.36	99.46	99.15	99.41
Cr	7	329	156	306	44	5	298	80	5	5	nd
Ni	10	144	77	136	41	12	92	29	11	6	3
Sc	32	32	33	29	22	24	22	32	26	24	19
V	220	107	232	120	182	189	183	205	234	133	110
Pb	6	4	6	3	5	6	6	7	5	8	11
Rb	36	18.1	41	53	41	104	77	40	63	80	106
Sr	427	294	266	253	1190	375	992	160	255	317	271
Ba	368	97	194	161	592	484	543	145	181	522	585
Ga	23	15	16	15	22	23	17	21	25	23	21
Nb	28	4.1	11.3	9.2	18.1	53	13.9	39	24.3	24.4	23
Zr	327	53	131	115	154	455	127	202	127	300	320
Y	78	14.8	39	22	25	67	23.2	84	39	58	53
Th	3.4	3	5.5	7	2.9	12	6.3	7.4	6.4	15	15
U	3.5	0.7	2.1	3.5	1.9	4.4	4.6	2.8	1.9	6.7	6.2
La	89	11	29	18	27	60	36	54	24	39	45
Ce	152	27	63	47	61	100	81	112	49	74	81
Nd	82	10	27	18	36	48	42	49	24	33	34

Sample	10-400	12-366	15-311	5-677	15-387	7-722	19-980	7-716	3-716	11-808	1-881
Rock Type	tonalite	tonalite	granite	granodiorite	granite	granite	granite	granophyre	granophyre	granophyre	rhyolite
SiO ₂	63.29	63.84	66.28	67.16	68.88	69.56	69.78	70.05	72.21	72.79	73.38
TiO ₂	0.77	0.66	0.47	0.84	0.35	0.71	0.27	0.36	0.31	0.17	0.11
Al ₂ O ₃	16.30	16.75	15.94	13.96	14.63	13.87	15.34	15.38	13.84	13.47	13.28
Fe ₂ O ₃ *	5.13	4.64	3.93	5.11	2.22	3.72	2.40	1.90	1.73	1.12	1.64
MnO	0.10	0.07	0.10	0.10	0.04	0.06	0.05	0.03	0.02	0.04	0.03
MgO	2.52	2.05	1.22	2.41	0.33	1.00	0.71	0.40	0.60	0.14	0.15
CaO	4.60	4.80	3.20	3.21	0.78	3.01	2.63	1.93	1.17	1.32	1.03
Na ₂ O	3.90	4.35	5.19	4.17	3.64	3.74	5.11	3.91	3.91	3.75	4.79
K ₂ O	2.42	1.52	1.85	1.95	6.76	3.19	2.07	5.08	4.48	4.91	3.99
P ₂ O ₅	0.30	0.19	0.19	0.15	0.03	0.18	0.09	0.08	0.05	0.05	0.02
LOI	0.85	0.85	0.82	0.39	0.20	0.41	0.33	0.49	0.20	1.32	0.85
Total	100.18	99.72	99.19	99.45	97.86	99.45	98.78	99.61	98.52	99.08	99.27
Cr	19	15	5	43	5	nd	nd	5	7	5	5
Ni	23	20	4	21	20	5	1	3	16	2	0
Sc	13	13	10.1	14.9	8	11	5.7	3.9	4	4.4	1.6
V	110	97	57	112	10	65	24	25	16	16	3
Pb	9	8	8	8	12	8	8	11	12	5	11
Rb	94	51	114	96	146	65	59	92	85	121	151
Sr	659	760	361	131	58	199	406	224	94	118	62
Ba	1140	598	360	191	277	528	301	1031	569	580	92
Ga	20	20	21	22	20	19	20	20	18	16	44
Nb	18	14	23.7	34	27	29	50	14.5	22	18	123
Zr	193	153	186	210	375	494	168	327	245	158	372
Y	21	14	34	66	146	107	44	53	21	23	128
Th	6.8	6.2	6.2	29	17	7.1	15	7.2	9	22	50
U	4	3.4	2.9	4.3	3.2	1.9	9.2	2.2	1.4	6.3	16
La	28	30	21	31	98	45	20	48	68	32	79
Ce	58	41	43	64	213	111	50	93	113	57	164
Nd	21	11	19	30	125	65	23	35	43	20	75




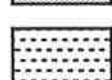





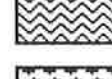
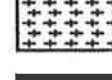

Sample	5-625	15-301	14-539	5-540	5-619	10-650	19-964	6-456	16-803
Rock Type	granophyre	granophyre	granophyre	granophyre	granophyre	granophyre	granophyre	granophyre	granophyre
SiO ₂	73.75	73.80	73.97	74.20	74.20	74.98	75.19	76.63	77.76
TiO ₂	0.19	0.31	0.20	0.25	0.25	0.04	0.10	0.05	0.16
Al ₂ O ₃	13.60	13.07	12.20	13.47	12.85	13.36	13.42	12.70	11.37
Fe ₂ O ₃ *	1.67	1.64	1.35	1.98	2.05	0.64	0.71	0.39	1.31
MnO	0.05	0.05	0.01	0.03	0.05	0.03	0.01	0.00	0.00
MgO	0.40	0.01	0.30	0.38	0.29	0.13	0.31	0.58	0.23
CaO	1.40	0.51	0.30	1.29	0.99	0.74	1.30	0.61	0.40
Na ₂ O	3.73	3.52	3.01	4.39	3.82	3.55	3.72	3.45	3.51
K ₂ O	3.81	6.20	6.12	3.46	4.31	5.32	4.32	5.50	4.94
P ₂ O ₅	0.04	0.02	0.01	0.05	0.00	0.01	0.03	0.00	0.01
LOI	0.49	0.30	0.15	0.22	0.35	0.55	0.31	0.01	0.01
Total	99.13	99.43	97.62	99.72	99.16	99.35	99.42	99.92	99.70
Cr	nd	5	5	5	5	nd	6	6	5
Ni	4	3	14	4	5	2	2	13	15
Sc	4	4.7	6	6.3	5.7	2.7	2.7	3	2
V	13	7	4	17	17	4	8	1	3
Pb	16	9	10	14	14	22	9	40	5
Rb	167	163	189	125	173	238	113	236	173
Sr	132	24	12	101	87	93	222	13	61
Ba	586	116	81	356	412	256	789	24	89
Ga	17	19	20	17	18	18	16	15	19
Nb	23	30	31	38	26	51	15.6	23	39
Zr	146	236	208	185	181	71	61	75	122
Y	38	142	85	52	43	28	21	36	88
Th	28	18	23	38	34	27	11	33	27
U	9.6	6.9	9	12	8.8	34	5	3.8	8
La	30	59	62	42	37	7	10	11	37
Ce	61	148	128	83	73	22	28	21	59
Nd	22	99	66	33	30	8	7	7	37

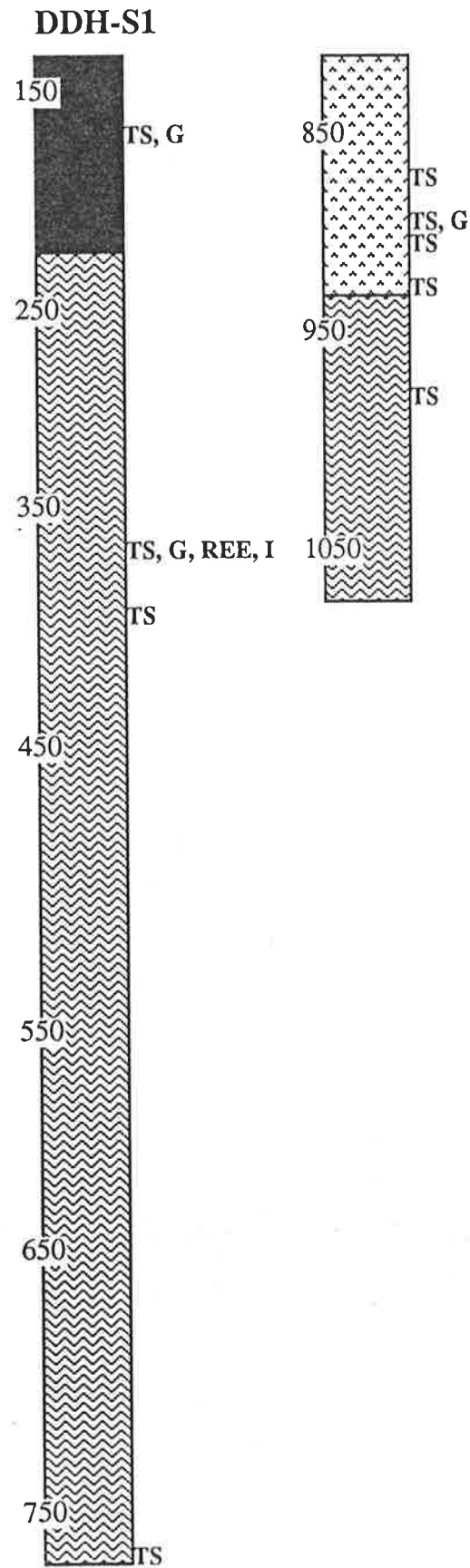
Appendix D. Black Hill Drill Core Logs

Legend

- TS Thin section
- P Probe analysis
- REE Rare earth analysis
- G Geochemistry
- I Isotopic analysis

(Depth in feet)











-  gabbronorite
-  pyroxene monzonite
-  anorthosite
-  norite
-  olivine gabbro
-  peridotite
-  troctolite
-  granophyre
-  metasediment
-  granite
-  metabasalt
-  metarhyolite



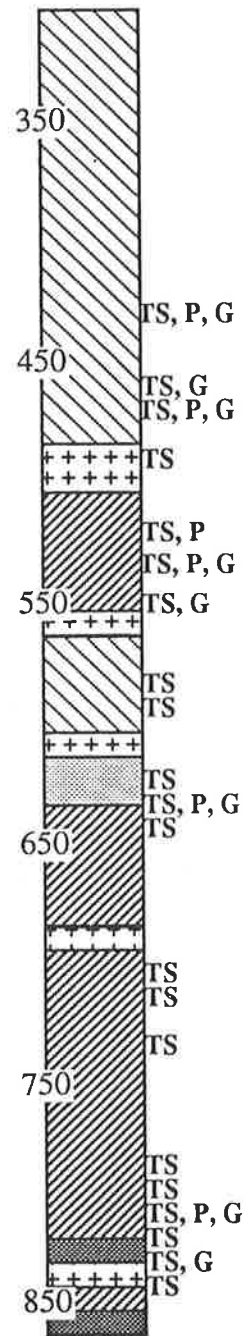
Legend

- TS Thin section
- P Probe analysis
- REE Rare earth analysis
- G Geochemistry
- I Isotopic analysis

(Depth in feet)

-  gabbronorite
-  pyroxene monzonite
-  anorthosite
-  norite
-  olivine gabbro
-  peridotite
-  troctolite
-  granophyre
-  metasediment
-  granite

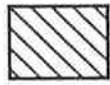

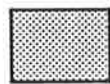
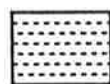





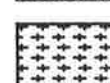
DDH-S2

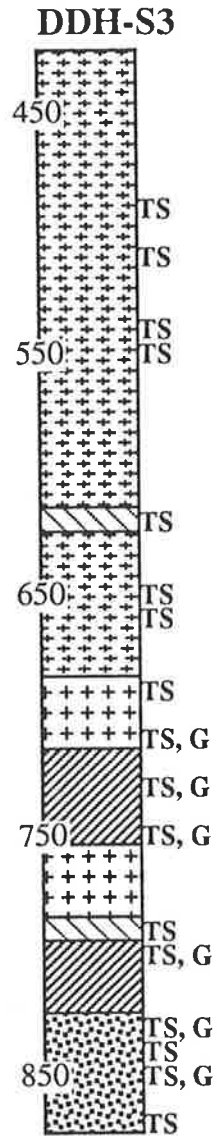


Legend

- TS Thin section
- P Probe analysis
- REE Rare earth analysis
- G Geochemistry
- I Isotopic analysis

(Depth in feet)



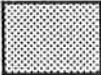
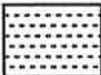



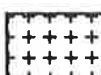


-  gabbronorite
-  pyroxene monzonite
-  anorthosite
-  norite
-  olivine gabbro
-  peridotite
-  troctolite
-  granophyre
-  metasediment
-  granite

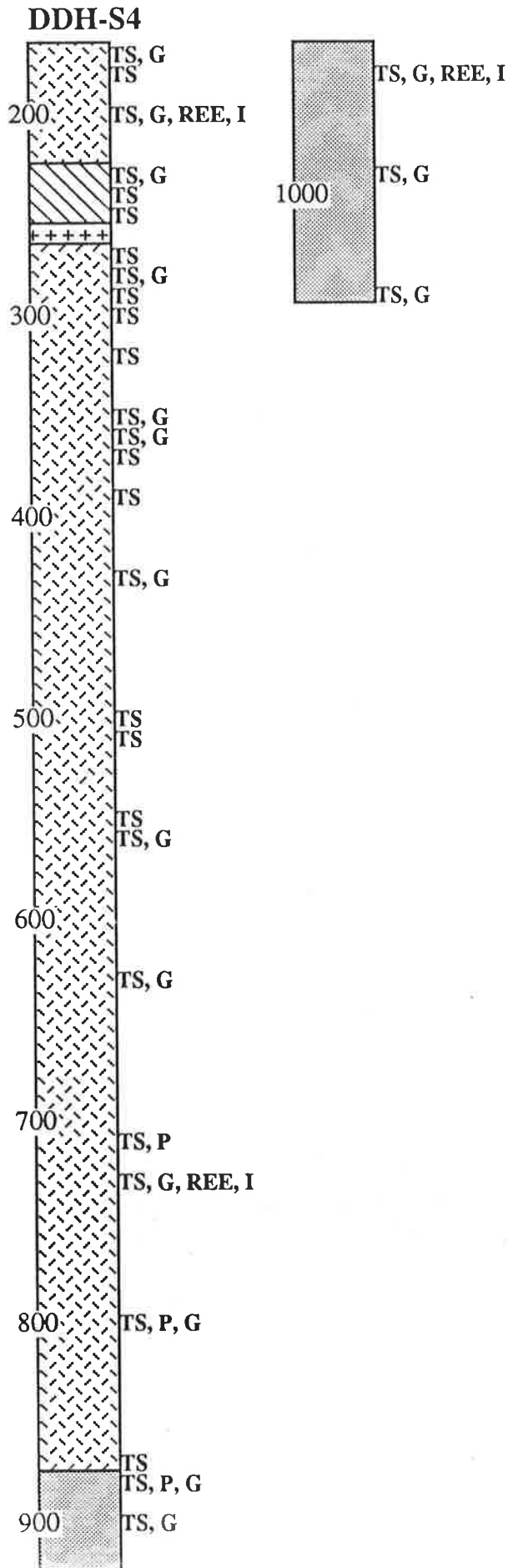


Legend

- TS Thin section
- P Probe analysis
- REE Rare earth analysis
- G Geochemistry
- I Isotopic analysis

(Depth in feet)

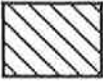

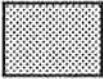
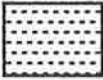

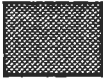
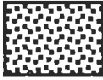
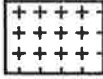

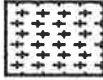
-  gabbronorite
-  pyroxene monzonite
-  anorthosite
-  norite
-  olivine gabbro
-  peridotite
-  troctolite
-  granophyre
-  metasediment
-  granite

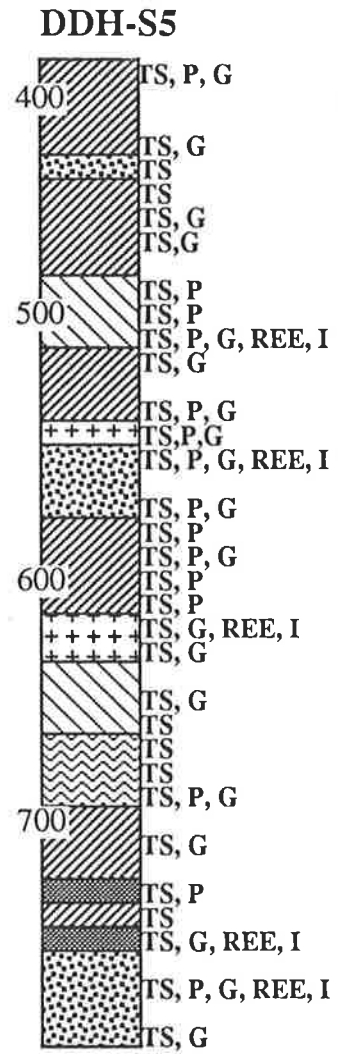


Legend

- TS Thin section
- P Probe analysis
- REE Rare earth analysis
- G Geochemistry
- I Isotopic analysis

(Depth in feet)



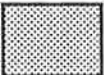
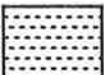






-  gabbronorite
-  pyroxene monzonite
-  anorthosite
-  norite
-  olivine gabbro
-  peridotite
-  troctolite
-  granophyre
-  metasediment
-  granite

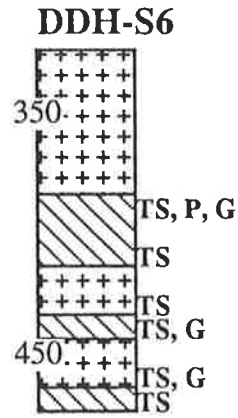


Legend

- TS Thin section
- P Probe analysis
- REE Rare earth analysis
- G Geochemistry
- I Isotopic analysis

(Depth in feet)



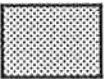
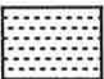






-  gabbronorite
-  pyroxene monzonite
-  anorthosite
-  norite
-  olivine gabbro
-  peridotite
-  troctolite
-  granophyre
-  metasediment
-  granite

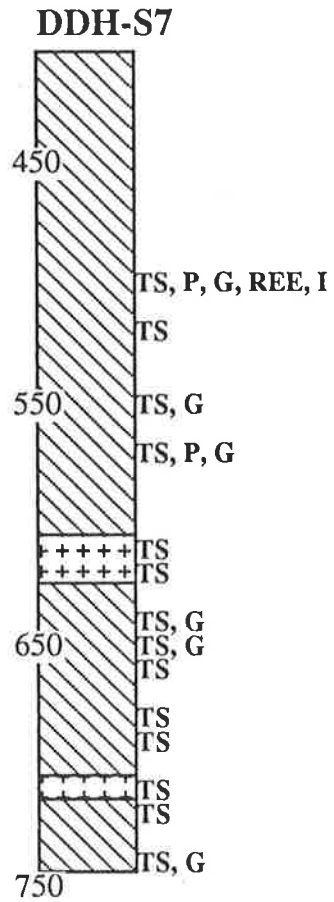


Legend

- TS Thin section
- P Probe analysis
- REE Rare earth analysis
- G Geochemistry
- I Isotopic analysis

(Depth in feet)



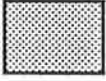
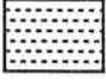



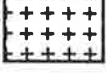


-  gabbronorite
-  pyroxene monzonite
-  anorthosite
-  norite
-  olivine gabbro
-  peridotite
-  troctolite
-  granophyre
-  metasediment
-  granite

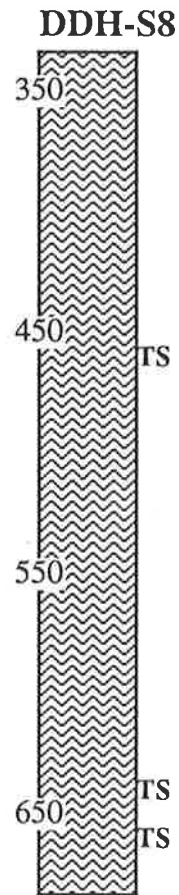


Legend

- TS Thin section
- P Probe analysis
- REE Rare earth analysis
- G Geochemistry
- I Isotopic analysis

(Depth in feet)








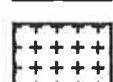
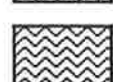
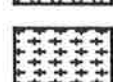
-  gabbronorite
-  pyroxene monzonite
-  anorthosite
-  norite
-  olivine gabbro
-  peridotite
-  troctolite
-  granophyre
-  metasediment
-  granite

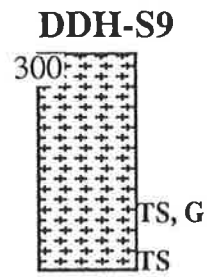


Legend

- TS Thin section
- P Probe analysis
- REE Rare earth analysis
- G Geochemistry
- I Isotopic analysis

(Depth in feet)



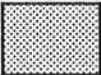
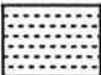


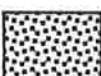


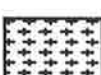
-  gabbronorite
-  pyroxene monzonite
-  anorthosite
-  norite
-  olivine gabbro
-  peridotite
-  troctolite
-  granophyre
-  metasediment
-  granite



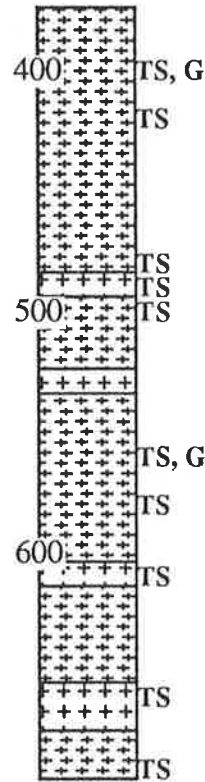
Legend

- TS Thin section
- P Probe analysis
- REE Rare earth analysis
- G Geochemistry
- I Isotopic analysis

(Depth in feet)

-  gabbronorite
-  pyroxene monzonite
-  anorthosite
-  norite
-  olivine gabbro
-  peridotite
-  troctolite
-  granophyre
-  metasediment
-  granite



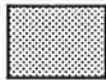
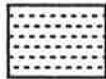
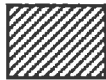

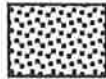
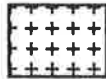

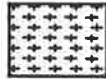
DDH-S10

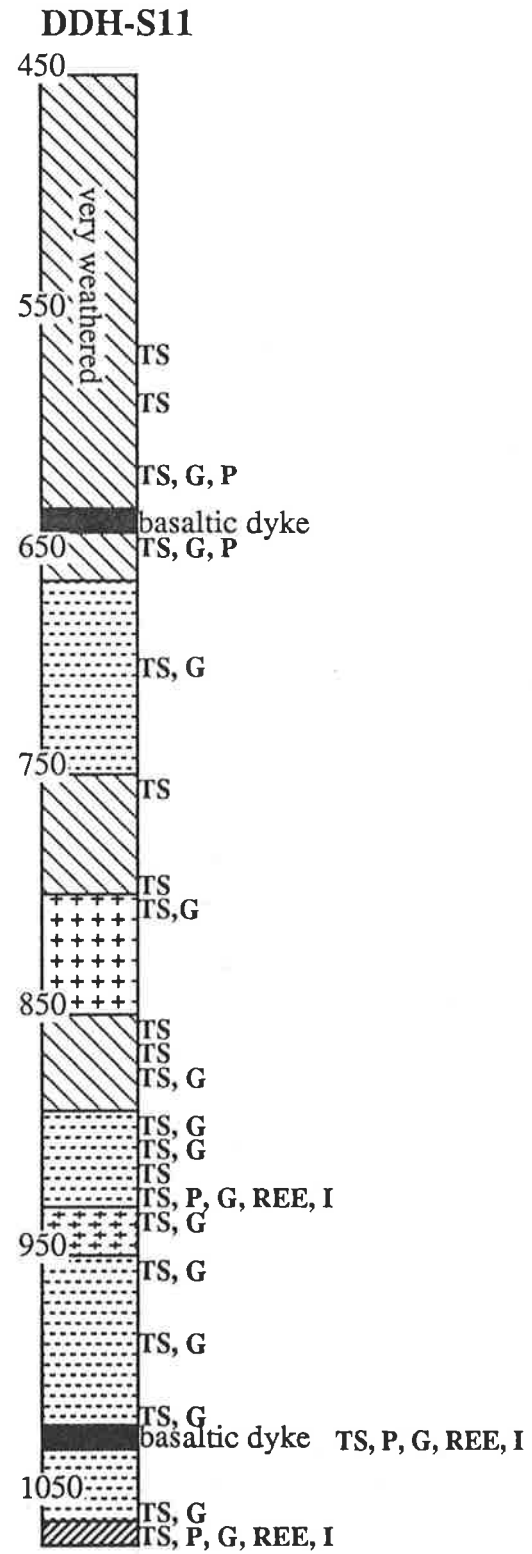


Legend

- TS Thin section
- P Probe analysis
- REE Rare earth analysis
- G Geochemistry
- I Isotopic analysis

(Depth in feet)



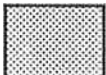
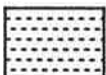



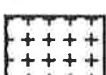


-  gabbronorite
-  pyroxene monzonite
-  anorthosite
-  norite
-  olivine gabbro
-  peridotite
-  troctolite
-  granophyre
-  metasediment
-  granite



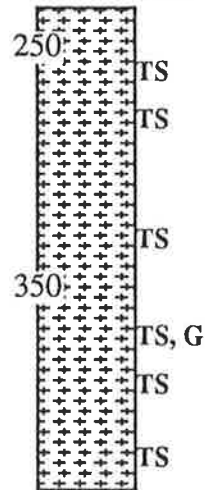
Legend

- TS Thin section
- P Probe analysis
- REE Rare earth analysis
- G Geochemistry
- I Isotopic analysis

(Depth in feet)

-  gabbronorite
-  pyroxene monzonite
-  anorthosite
-  norite
-  olivine gabbro
-  peridotite
-  troctolite
-  granophyre
-  metasediment
-  granite



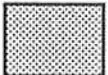
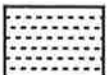






DDH-S12

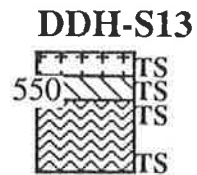


Legend

- TS Thin section
- P Probe analysis
- REE Rare earth analysis
- G Geochemistry
- I Isotopic analysis

(Depth in feet)



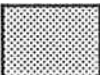
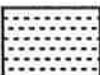






-  gabbronorite
-  pyroxene monzonite
-  anorthosite
-  norite
-  olivine gabbro
-  peridotite
-  troctolite
-  granophyre
-  metasediment
-  granite

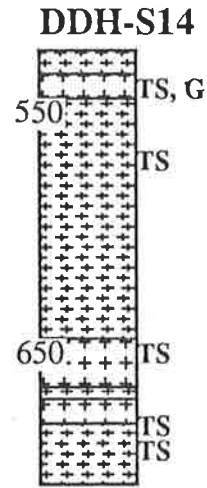


Legend

- TS Thin section
- P Probe analysis
- REE Rare earth analysis
- G Geochemistry
- I Isotopic analysis

(Depth in feet)

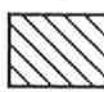

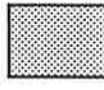
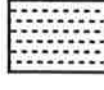


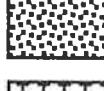



-  gabbronorite
-  pyroxene monzonite
-  anorthosite
-  norite
-  olivine gabbro
-  peridotite
-  troctolite
-  granophyre
-  metasediment
-  granite

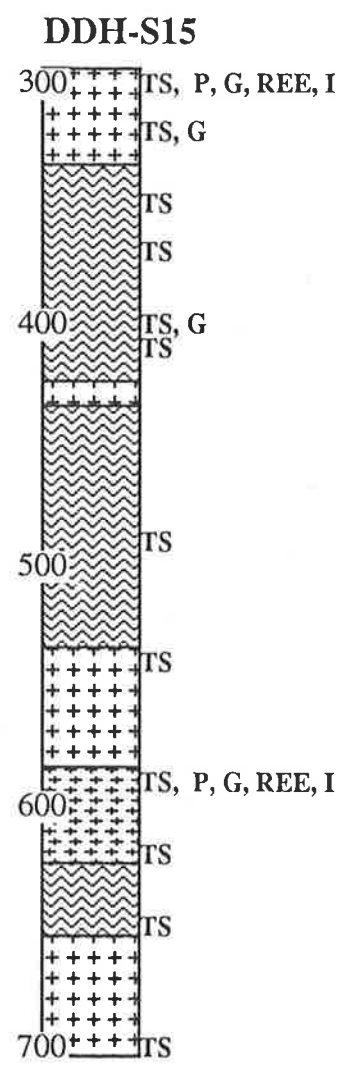


Legend

- TS Thin section
- P Probe analysis
- REE Rare earth analysis
- G Geochemistry
- I Isotopic analysis

(Depth in feet)

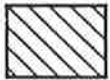

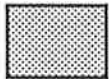
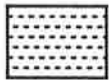
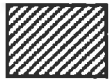
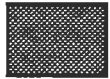
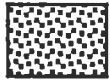
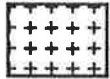

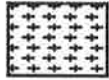
-  gabbronorite
-  pyroxene monzonite
-  anorthosite
-  norite
-  olivine gabbro
-  peridotite
-  troctolite
-  granophyre
-  metasediment
-  granite

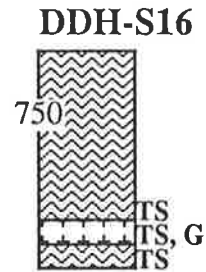


Legend

- TS Thin section
- P Probe analysis
- REE Rare earth analysis
- G Geochemistry
- I Isotopic analysis

(Depth in feet)

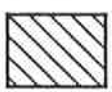
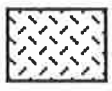
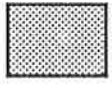







-  gabbronorite
-  pyroxene monzonite
-  anorthosite
-  norite
-  olivine gabbro
-  peridotite
-  troctolite
-  granophyre
-  metasediment
-  granite



Legend

- TS Thin section
- P Probe analysis
- REE Rare earth analysis
- G Geochemistry
- I Isotopic analysis

(Depth in feet)

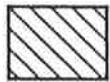


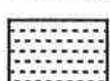



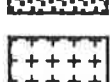
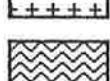

-  gabbronorite
-  pyroxene monzonite
-  anorthosite
-  norite
-  olivine gabbro
-  peridotite
-  troctolite
-  granophyre
-  metasediment
-  granite

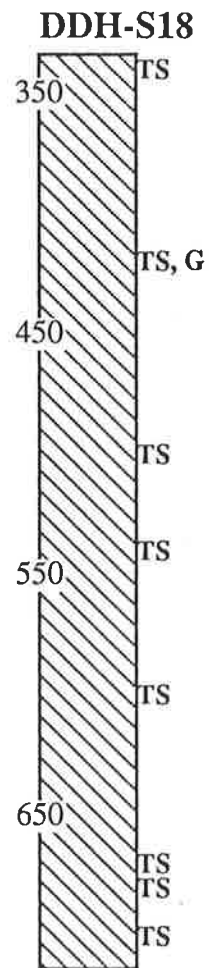


Legend

- TS Thin section
- P Probe analysis
- REE Rare earth analysis
- G Geochemistry
- I Isotopic analysis

(Depth in feet)



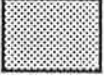




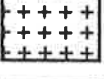


-  gabbronorite
-  pyroxene monzonite
-  anorthosite
-  norite
-  olivine gabbro
-  peridotite
-  troctolite
-  granophyre
-  metasediment
-  granite

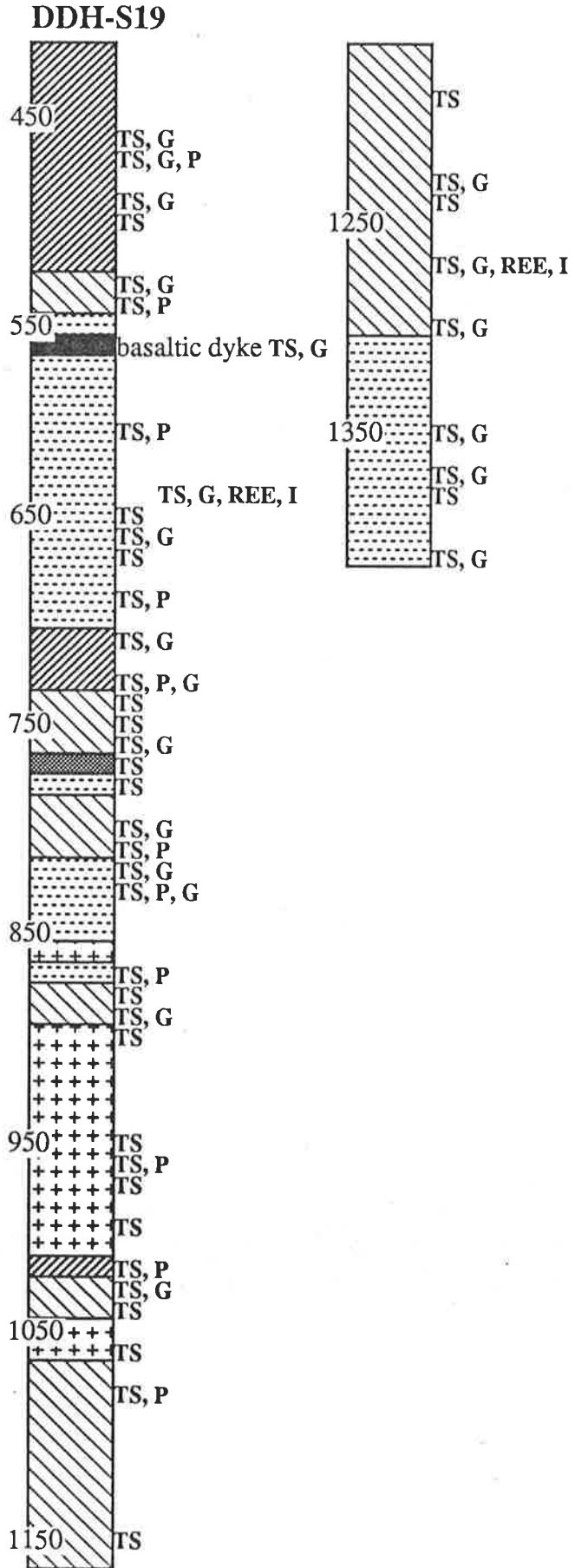


Legend

- TS Thin section
- P Probe analysis
- REE Rare earth analysis
- G Geochemistry
- I Isotopic analysis

(Depth in feet)

-  gabbronorite
-  pyroxene monzonite
-  anorthosite
-  norite
-  olivine gabbro
-  peridotite
-  troctolite
-  granophyre
-  metasediment
-  granite



Appendix E. Copies of papers and abstracts

Foden, J.D., Turner, S.P., and Morrison, R.S., (2000) The tectonic implications of Delamerian magmatism in South Australia and western Victoria.
In: Jago, J.B., and Moore, P.J., (eds.) *The evolution of a Late Precambrian-Early Cambrian Palaeozoic rift complex: the Adelaide Geosyncline*. Geological Society of Australia Special Publication, v. 16, pp. 465-482.

NOTE:

This publication is included in the print copy
of the thesis held in the University of Adelaide Library.

Turner, S., Foden, J., and Cooper, J., (1989) Post Delamerian magmatism: tectonic controls on magma chemistry and evidence for post Delamerian extension. *Specialist Group in Tectonics and Structural Geology, Geological Society of Australia Abstract no. 24, pp. 155-156.*

NOTE:

This publication is included in the print copy
of the thesis held in the University of Adelaide Library.

Foden, J., Turner, S., and Michard, A., (1989) Geochemical and isotopic characteristics of igneous activity in the Adelaide fold belt; implications for mechanisms of crustal growth.
Specialist Group in Tectonics and Structural Geology, Geological Society of Australia Abstract no. 24, pp. 47-48.

NOTE:

This publication is included in the print copy
of the thesis held in the University of Adelaide Library.

Turner, S., and Foden, J., (1990) Post Delamerian magmatism: is lithospheric thinning guilty?

Tenth AGC, Geological Society of Australia Abstract no. 25, pp. 263-263.

NOTE:

This publication is included in the print copy
of the thesis held in the University of Adelaide Library.

Foden, J., and Turner, S., (1990) Proterozoic lithospheric enrichment and its profound influence on the isotopic composition of Phanerozoic magmas.
Seventh International Conference on Geochronology, Cosmochronology and Isotope Geology, Geological Society of Australia Abstract no. 27, p. 34.

NOTE:

This publication is included in the print copy
of the thesis held in the University of Adelaide Library.

Turner, S.P., and Foden, J.D., (1990) The nature of mafic magmatism during the development of the Adelaide geosyncline and the subsequent delamerian orogeny. In: Parker, A.J., Rickwood, P.C., and Tucker, D.H., (eds.) *Mafic Dykes and Emplacement Mechanisms, Proceedings of the 2nd International Dykes Conference*, pp. 431-434.

NOTE:

This publication is included in the print copy
of the thesis held in the University of Adelaide Library.